UNIVERSITÉ DE STRASBOURG

THÈSE présentée par :

Dariush JAVANI

Soutenue le : **12 Juillet 2023**

Pour obtenir le grade de : **Docteur de l'université de Strasbourg**

Discipline/ Spécialité : Géophysique

Modélisation des variations de vitesse des ondes P liées au glissement asismique dans un réservoir fracturé

THÈSE dirigée par :
  SCHMITTBUHL Jean   Directeur de Recherche CNRS, université de Strasbourg

RAPPORTEURS :   Chercheur, BRGM
  Mme. MAURY Julie   Chercheur, TNO Geological Survey of the Netherlands
  M. CANDELA Thibault

AUTRES MEMBRES DU JURY :   Professeur, université de Strasbourg
  [M. FOND Christophe]   Coordinateur de Projet, TotalEnergies
  [M. POURPAK Hamid]   Chercheur, Helmotz Center Potsdam
  [M. BLÖCHER Guido]

To My Wife Solmaz

and My Son Karen

Résumé

La stimulation hydraulique joue un rôle important dans l'amélioration de la conductivité hydraulique du réseau de fractures autour des puits d'injection et de production dans les réservoirs géothermiques. Il est donc important de caractériser le comportement hydromécanique des discontinuités face à l'injection de fluide. Le site de Soultz-sous-Forêts (France) a été un site pilote EGS où plusieurs stimulations hydrauliques majeures ont été réalisées et sont bien documentées (https://cdgp.u-strasbg.fr/ et https://tcs.ah-epos.eu/).

Ici, nous avons utilisé l'outil de modélisation numérique 3DEC (Itasca) pour analyser la stimulation en 2000 du puits GPK2 pour lequel des anomalies sismiques à grande échelle ont été mises en évidence pendant les différentes étapes de la stimulation en utilisant la tomographie 4D d'onde P (Calo et al, 2011). La spécificité de l'approche est de combiner deux modélisations à différentes échelles. Tout d'abord, un modèle à petite échelle (100x100x100 m^3) est construit pour analyser la réponse mécanique effective d'un réseau de fractures discrètes stochastique (DFN) en suivant les caractéristiques statistiques du réseau de fractures observé (Massart et al, 2010). Deuxièmement, un modèle numérique à grande échelle du réservoir de Soultz-sous-Forêts (5000x5000x5000 m^3) hébergeant les plus grandes failles du réservoir définies par Sausse et al, 2010, est développé en incluant les contraintes régionales. L'objectif est de contraindre les propriétés mécaniques à grande échelle de la matrice environnante autour de la faille à partir du modèle à petite échelle, en particulier, son comportement hydromécanique en termes de réponse élastique non linéaire liée à la DFN stochastique.

La simulation numérique d'une stimulation hydraulique à grande échelle de l'anné 2000 réalisée sur le GPK2 de Soultz-sous-Forêts est effectuée pour mieux caractériser la propagation de la pression des fluides à travers un plan de faille. La méthode des éléments distincts (DEM) 3DEC d'Itasca a été utilisée pour stimuler la fracture FZ4770 encastrée dans un bloc de granite élastique, homogène, isotrope et imperméable par injection d'eau pendant 24 heures à un débit constant. Les résultats indiquent qu'un front de pression de fluide existe et migre en fonction de √t lorsqu'un débit d'injection constant est imposé. Le même comportement a été observé dans l'ouverture hydraulique de la fracture où un débit constant a entraîné une propagation de l'ouverture de la fracture avec une fonction de racine carrée du temps. Au contraire un débit augmentant linéairement, a entraîné une migration de l'ouverture de la fracture avec une tendance linéaire dans le temps.

Les résultats des deux scénarios d'injection susmentionnés ont été comparés au modèle introduit par Lengliné et al, en 2017 pour la stimulation d'un puits voisin à Rittershoffen. Ce modèle est un modèle de décollement supposant une ouverture constante le long de la partie ouverte de la fissure et un front net entre la partie ouverte et la partie fermée de la fissure sans diffusion de la pression. Il exprime que c'est l'évolution de l'ouverture qui est le mécanisme moteur de la sismicité et non la diffusion de la pression. Nous avons essayé de généraliser le modèle à nos résultats numériques en utilisant les valeurs d'ouverture des fractures dérivées des simulations 3DEC pendant la période d'injection. Ces valeurs d'ouverture varient dans le temps et dans l'espace et, ici, une valeur moyenne d'ouverture dans l'espace à un moment donné a été substituée dans le modèle de Lengliné et al. 2017. Les résultats ont montré une bonne concordance entre les deux modèles, indiquant le fait qu'il existe un front de pression de fluide lié au front d'ouverture hydraulique qui se propage dans une tendance de type diffusion le long du plan de fracture.

Pour mieux comprendre le comportement de la fracture face à la stimulation hydraulique, une série d'analyses de sensibilité a été réalisée et a montré que parmi les rigidités normales et de cisaillement de la fracture, la taille, le pendage et l'orientation, seules la rigidité normale et la taille de la faille influencent de manière significative son comportement élastique. On constate que l'augmentation de l'ouverture de la faille pendant l'injection présente une

relation linéaire avec la pression du fluide, sensible à l'ampleur de la rigidité normale de la fracture ainsi qu'à la taille de la fracture.

On constate également que la prise en compte de l'effet du glissement de cisaillement de la fracture basé sur la loi de glissement de Coulomb a diminué la vitesse de migration pression/ouverture de l'ouverture, cependant le processus de propagation présente une loi de puissance, avec une légère réduction de l'exposant par rapport au comportement diffusif (0,4). En outre, cette vitesse de propagation est supérieure d'un ordre de grandeur aux vitesses de migration des événements sismiques survenus en 1993 lors de la stimulation du puits GPK1 à Soultz-sous-Forêts, mentionnées dans Bourouis et Bernard, 2007.

Dans un deuxième temps, il s'agissait de déterminer numériquement les propriétés mécaniques effectives (module d'Young et coefficient de Poisson) d'un bloc de roche fracturée de 100x100x100 m^3 dans lequel les rigidités normales et de cisaillement des fractures sont définies sur la base des équations non linéaires introduites par Bandis et al. en 1983. Pour ce faire, le code 3DEC d'Itasca a été utilisé pour effectuer des tests de vérification du comportement non linéaire des fractures. Cette phase était composée d'un bloc rocheux de 1x1x2 m^3 contenant une fracture finie circulaire de 0,5 m de diamètre avec un pendage et une direction de pendage de 45° et 90°, respectivement. Les courbes de contrainte normale-déplacement (pour les joints imbriqués et non imbriqués) et de contrainte de cisaillement-déplacement ont ensuite été comparées aux courbes analytiques (Bandis et al. 1983) pour vérifier le comportement du modèle développé. Ce modèle a ensuite été généralisé à un bloc de 100x100x100 m^3 abritant deux fractures afin de vérifier la cohérence du code développé lorsqu'un DFN est le cas d'étude. Après cette vérification, le code développé a été appliqué au bloc fracturé avec différents exemples de DFN soumis à des scénarios de perturbation de la contrainte dans l'état de contrainte in situ du réservoir géothermique de Soultz-sous-Forêts à une profondeur d'environ 500 m, 2,3 km et 4,7 km afin d'évaluer les modules élastiques de la masse rocheuse fracturée. Les résultats ont ensuite été comparés aux solutions analytiques existantes telles que l'absence d'interaction, l'auto-cohérence, le schéma différentiel, et enfin à la méthode introduite par Davy et al. en 2018.

Les trois méthodes de non-interaction, d'auto-consistance et de schéma différentiel sont basées sur l'énergie de déformation élastique stockée d'Eshelby, 1957. L'approche la plus simple pour obtenir la perturbation de l'énergie dans un milieu contenant des fractures/vides causés par une contrainte de confinement/cisaillement, consiste à négliger l'interaction fracture-fracture/pore et à calculer l'effet de chaque fracture/pore comme s'il s'agissait d'une fracture/pore isolée dans une roche intacte infinie, puis à additionner toutes ces perturbations de l'énergie pour toutes les fractures/pores. Cette simplification a entraîné une divergence significative entre les résultats des trois méthodes susmentionnées et ceux de Davy et al. 2018 et de 3DEC.

Les résultats de Davy et al. (2018) étaient les plus proches de ceux de la méthode 3DEC. La raison en est que cette méthode prend en compte le champ de contrainte à distance, l'orientation de la fracture par rapport au champ de contrainte à distance appliqué et les paramètres de rigidité de la fracture. Cependant, les différences peuvent résulter du fait que Davy et al. 2018 ne prend pas en compte la perturbation de la contrainte causée par les fractures et les interactions entre les fractures, de sorte qu'une diminution précoce ainsi qu'une surestimation des modules effectifs ont été observées dans les résultats.

Les modules élastiques numériques résultants ainsi que ceux de la méthode de Davy et al. 2018 ont ensuite été utilisés pour obtenir la vitesse des ondes P à travers les modèles synthétiques de masse rocheuse fracturée, normalisée par la vitesse des ondes P le long de la roche intacte. La variation de la vitesse des ondes P normalisée en fonction du paramètre de densité de fracture à trois niveaux de contrainte différents, a montré le même schéma que celui des modules élastiques. À de faibles densités de fracture, les méthodes analytiques et numériques, quel que soit le type de rigidité de la fracture, étaient indépendantes du paramètre de densité de fracture et du niveau de contrainte appliqué. D'autre part, pour les résultats analytiques de la vitesse des ondes P à travers la masse rocheuse fracturée basés sur la méthode de Davy et al. 2018, là encore quel que soit le type de rigidité de la fracture, l'écart par rapport à la vitesse de la roche intacte s'est produit pour un paramètre de rigidité de la fracture plus faible par rapport au modèle numérique

; probablement en raison du fait que la méthode analytique ne prend pas en compte les interactions entre fracture et les perturbations de contrainte associées.

En considérant le milieu à faible perméabilité traité par Weidler et al. (2002), en plus de l'existence d'un front de pression de fluide/ouverture de fracture qui se propage le long de la fracture plus rapidement que la diffusion de fluide dans le milieu environnant la fracture, comme démontré dans cette étude, on peut affirmer que la surpression générée par le fluide injecté dans la fracture agit comme une composante additive à la pression de confinement de la masse rocheuse, au lieu de jouer le rôle d'une augmentation de la pression interstitielle. Dans cette situation, et selon la littérature déjà mentionnée, en particulier Todd et Simmons (1972), toute augmentation de la pression de confinement peut entraîner une augmentation de la vitesse des ondes P.

La présente étude s'est concentrée sur l'évaluation de l'influence que des fractures sèches peuvent avoir sur les modules élastiques effectifs d'une masse rocheuse fracturée. Il serait intéressant, en tant que perspective, d'effectuer cette étape en ajoutant un fluide dans le système afin d'étudier l'effet des fractures saturées en fluide sur les modules élastiques effectifs d'une masse rocheuse.

Abstract

Hydraulic stimulation of pre-existing fractures and faults plays a significant role in improving hydraulic conductivity of the fracture network around injection and production wells in geothermal reservoirs. It is therefore important to characterize the hydro-mechanical behavior of discontinuities against fluid injection. The Soultz-sous-Forêts site (France) has been an EGS pilot site where several major hydraulic stimulations have been performed and are well documented (https://cdgp.u-strasbg.fr/ and https://tcs.ah-epos.eu/).

Here, we used the 3DEC numerical modeling tool (Itasca) to analyze the year 2000 stimulation of GPK2 well for which large scale seismic anomalies have been evidenced during the different stages of the stimulation using 4D-P-wave tomography (Calo et al, 2011). The specificity of the approach is to combine two modeling at different scales. First, a small-scale model (100x100x100 m^3) is built to analyze the effective mechanical response of a stochastic discrete fracture network (DFN) following the statistical features of observed fracture network (Massart et al, 2010). Second, a large-scale numerical model of the Soultz-sous-Forêts reservoir (5000x5000x5000 m^3) hosting the largest faults of the reservoir defined by Sausse et al., 2010, is developed including regional stresses. The objective is to constrain the large-scale mechanical properties of the surrounding matrix around the fault from the small-scale model, in particular, its hydro-mechanical behavior in terms of non-linear elastic response related to the stochastic DFN.

Numerical simulation of large-scale hydraulic stimulation of the year 2000 performed on GPK2 of Soultz-sous-Forêts is carried out to better characterize fluid pressure propagation throughout a fault plane. The 3DEC distinct element method (DEM) of Itasca was used to simulate the stimulation of FZ4770 fracture embedded in an elastic, homogeneous, isotropic, and impermeable block of granite by injection of water for 24 hours at a constant flow rate. The results indicated that a fluid pressure front exists and migrates as a function of $\sqrt{t}$ when a constant injection rate is imposed. Then, a complementary simulation with variable flow rate was performed and found that the fluid pressure propagated as a function of t. The same behavior was also observed in the fracture's hydraulic aperture where a constant flow rate yield a fracture opening propagation with a time square root function and a linearly increasing flow rate resulted in a fracture opening migration with a linear trend in time.

The findings of both aforementioned injection scenarios were compared to the model introduced by Lengliné et al., 2017. This model is a lift-off model assuming a constant aperture along the open part of the crack and a sharp front between open and close part of the crack with no diffusion of the pressure. It

expresses that it is the aperture evolution which is the driving mechanism of seismicity not the pressure diffusion. We tried to generalize the model to our numerical results by using the fracture aperture values derived from the 3DEC simulations during injection period. Such aperture values were varying in the time and space and here an average value of aperture over space in any given time were substituted in the Lengliné et al., 2017 model. The outcome showed a good agreement between the two models indicating the fact that there exist a front in fluid pressure related to the hydraulic aperture front that propagates in a diffusion-like trend along the fracture plane.

To better understand the behavior of the fracture against hydraulic stimulation, a series of sensitivity analysis are carried out and found that among the fracture's normal and shear stiffnesses, size, dip and strike, only the normal stiffness and size of the fault significantly influence its elastic behavior. It is found that the increase of the aperture of the fault during the injection shows a linear relationship with fluid pressure sensitive to the magnitude of the fracture normal stiffness as well as the size of the fracture.

It is also found that, taking into account the effect of shear slip of the fracture based on Coulomb slip law decreased the pressure/aperture opening migration velocity, however the propagation process still remained power-low, but now, with a little reduction in the magnitude of the exponent in merely downward migration (0.4). In addition, this propagation velocity compared to the seismic event velocities of 1993 stimulation of GPK1 well at Soultz-sous-Forêts, mentioned in Bourouis and Bernard, 2007, are one order of magnitude larger.

In second step, it was aimed to numerically determine the effective mechanical properties (Young's modulus and Poisson ratio) of a 100x100x100 m^3 fractured rock block in which the fractures' normal and shear stiffnesses are defined based on non-linear equations introduced by Bandis et al., 1983. For that, the 3DEC of Itasca was used to first do some verification tests on the implemented non-linear fracture behavior. This phase was composed of a rock block of 1x1x2 m^3 containing a 0.5 m diameter circular finite fracture with dip and dip direction of 45° and 90°, respectively. Normal Stress-displacement (for both interlocked and mismatched joints) and shear stress-displacement curves were then compared to the analytical curves (Bandis et al., 1983) to verify the behavior of developed model. This model was then generalized to a block of 100x100x100 m^3 hosting two fractures to verify consistency of the developed code when a DFN is the case of study. After this verification, the developed code was applied to the block fractured with various DFN examples undergoing some stress perturbation scenarios when were at the in-situ stress state of Soultz-sous-Forêts geothermal reservoir at a depth of approximately 500 m, 2.3 km, and 4.7 km in order to evaluate elastic moduli of the fractured rock mass. The results were then compared to the existing analytical solution such as no-interaction, self-consistent, differential scheme, and finally to the method introduced by Davy et al., 2018.

Three methods of no-interaction, self-consistent, and differential scheme are based on stored elastic strain energy of Eshelby, 1957. The simplest approach to obtain energy perturbation in a fracture/void containing medium caused by confining/shear stress is to neglect fracture-fracture/ pore-pore interaction and calculate the effect of each fracture/pore as if it were an isolated fracture/pore in an infinite intact rock, and then sum up all these energy perturbations for all fractures/pores. This simplification caused significant divergence of results of three above mentioned methods from those of Davy et al., 2018, and 3DEC.

The Davy et al., 2018, results were closest to those of 3DEC. The reason was that this method considered the remote stress field, fracture's orientation relative to the applied remote stress field, and fracture stiffness parameters. But, the differences may resulted from the fact that Davy et al., 2018, does not take into account the stress perturbation caused by fractures and also fracture interactions; so that an early stage decrease as well as overestimated effective moduli were seen in the results.

Resulting numerical elastic moduli as well as those of Davy et al., 2018 method were then utilized to obtain P-wave velocity through the synthetic fractured rock mass models normalized by the P-wave velocity along the intact rock. Variation of the normalized P-wave velocity versus fracture density parameter at all three stress levels demonstrated the same pattern as that for the elastic moduli. At low fracture densities, both the analytical and the numerical methods, regardless of the fracture stiffness type, were independent of the fracture density parameter and the applied stress level. On the other hand, for the analytical results of P-wave velocity through the fractured rock mass based on Davy et al., 2018 method, again regardless of the fracture stiffness type, deviation from the intact rock velocity occurred in lower fracture stiffness parameter compared to the numerical scheme; probably due to the fact that the analytical method does not take the fracture interaction and corresponding stress perturbation factors into the account.

Considering the low permeability medium addressed by Weidler et al. (2002), in addition to the existence of a fluid pressure/fracture opening front that propagates along the fracture faster than fluid diffusion in the fracture surrounding medium, as demonstrated in this study, it can be stated that the overpressure generated by the injected fluid in the fracture acts as an additive component to the confining pressure of the rock mass, instead of playing the role of pore pressure enhancement. In this situation, and according to the literature already mentioned, especially Todd and Simmons (1972), any increase in confining pressure can cause an increase in P-wave velocity.

The second step of the present work focused on assessment of the influence the dry fracture may had on the effective elastic moduli of a fractured rock mass. It would be of interest, as perspective, to perform this step by adding fluid into the system so as to investigate the effect of wet fractures on the effective elastic moduli of saturated rock mass.

Acknowledgment

An immense thank you to my PhD supervisors: Jean Schmittbuhl and late François Cornet. Support and guidance throughout the project from you has been invaluable. Jean in particular you've been a fantastic primary supervisor, always being there when I needed your support, reviewing my progress constantly, and guiding me through my PhD studies. Thank you and Maria also to all the efforts you made to help me get to this stage. The late François Cornet was a huge influence and without which I would have never followed this path. He provided me with the opportunity to be a part of this project. He may rest in peace.

It has been an amazing experience working at ITI GeoT research group, thanks to everyone from the ITES/EOST I've worked with and from whom I've learned so much. A special thanks to Hamid Pourpak (a sincere and supportive comrade), Atef Onaisi, and Jean-Philippe Matheiu from TotalEnergies who have been closely followed my progress on this project. Thank you of course to the Itasca C.G. team I've working on this project with: Rima Ghazal, Jim Hazzard, and Caroline Darcel.

I am grateful to my colleagues and friends who supported me during my PhD since first days of my arrival to Strasbourg up to now encompassing an exhaustive list: Lachin, Sina, Agnès, Damian, Franck (an exceptional comrade), Qinglin, Weiwei, Cindy, and many others whom I apologize to if I forget to add them to this list but they will always be in my mind.

And finally, but the most importantly, I would like to thank my lovely wife, Solmaz, for her relentless and persistent support as well as to my son, Karen, for his childish patience when I was not been around enough to play with him. I would also like to extend my thanks to my parents and parents in law for all they've done for us during our life. I would like to highlight two truly exceptional people, Joseph and Catherine, who have not spared any efforts to help us.

Table of Contents

List of Tables

List of Figures

xxv

Chapter 1

1 Introduction

1.1 Background

Hydraulic stimulation is a widely used method for enhancing permeability of reservoir rocks and improving connectivity of injection and production wells in geothermal reservoirs (Zimmermann and Reinicke, 2010; Darnet et al, 2005; Baria et al,1999). Enhanced Geothermal Systems (EGS), formerly called Hot Dry Rock (HDR) systems, were first conceptualized at Los Alamos National Laboratory at Fenton Hill, New Mexico (USA) in the 1970s (Mc Clure, 2012; Genter et al., 2009). Since then, these projects have attracted a lot of attention as a potential, abundant and widespread source of green energy (free from emission of greenhouse gases (Tester, 2007)). Soultz-sous-Forêts site in France, Rosemanowes site in UK, Ogachi and Hijiori sites in Japan, Cooper Basin in Australia, and Desert Peak in USA are examples of EGS around the world (Mc Clure, 2012). In spite of being a green source of energy, EGS developments are often involved with induced seismicity generated from alteration of subsurface stress or fluid pressure during hydraulic stimulation. In recent years, some large earthquakes induced by fluid injections are documented. The 2011 Mw 5.7 and 5.0 earthquakes near Prague in Oklahoma, United States (Keranen et al., 2013), the Mw 5.8 Pawnee, Oklahoma, in 2016 (Yeck et al., 2017), or the 2017 Mw 5.5 earthquake near an EGS in Pohang, South Korea (Grigoli et al., 2018; Kim et al., 2018; Lee et al., 2019) are large induced seismic events caused from fluid injection into the underground formation (Wynantes-Morel et al., 2020). The 2003 Mw 2.9 Soultz-sous-Forêts, France (Evans et al., 2012), the 2006 Mw 3.4 Basel, Switzerland (Evans et al., 2012), the 2019 Mw 3.0 and the 2020 Mw 3.6 and 3.3 Vendenheim, France, are some examples of relatively large earthquake felt by local population and caused definitive project abandonment (Schmittbuhl et al., 2021). Therefore, EGS development demands a high level of responsibility against ever-growing concerns in terms of human-felt seismic events, which demands sufficient understanding about the mechanism of induced seismicity.

1.2 Soultz-sous-Forêts Geothermal Reservoir

Soultz-sous-Forêts geothermal reservoir is located in upper Rhine Graben, North-East of France (Dezayes et al., 2010) (Figure 1.1.a) which is laid under a 1.4 km of sedimentary layers and consisting of a 2.5 km porphyritic granite followed by a two mica granite till depth of interest at approximately 5 km (Vallier et al., 2019) (Figure 1.1.b).

This reservoir is one of the "Enhanced Geothermal System" (EGS) sites in the world. It hosted drilling of many observational and operational wells among which a 1400 m well called 4550 was one of the seismic observation wells. Well EPS1 fully cored down to 2230 m, GPK2, GPK3, and GPK4 constitute the European geothermal pilot plant, which extended beyond 5000 m and, finally, well GPK1 drilled down to approximately 3600 m dedicated to first hydraulic tests (Sausse et al., 2010).
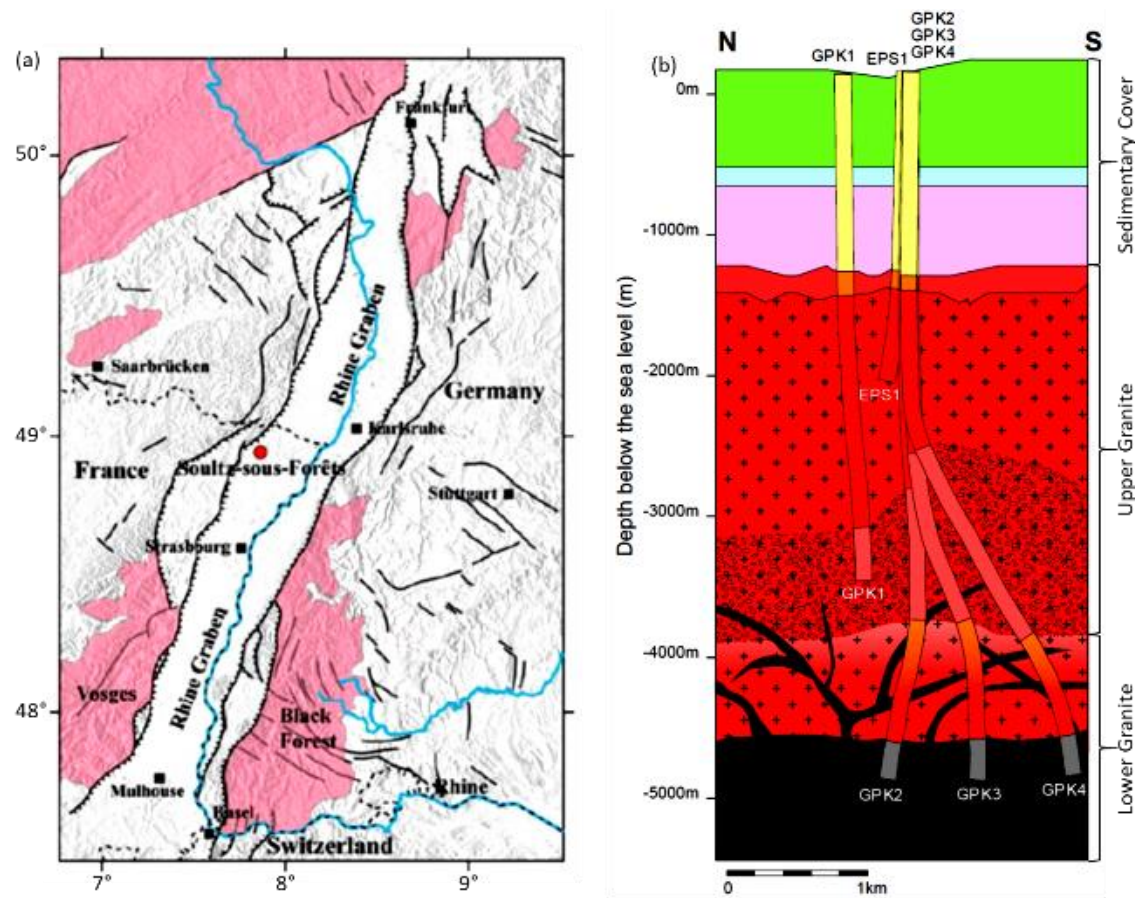
Figure 1.1. (a) Location map of Soultz-sous-Forêts (Dorbath et al., 2009), (b) Horizontal cross section of the EGS site (reproduced after Dezayes et al., 2005)
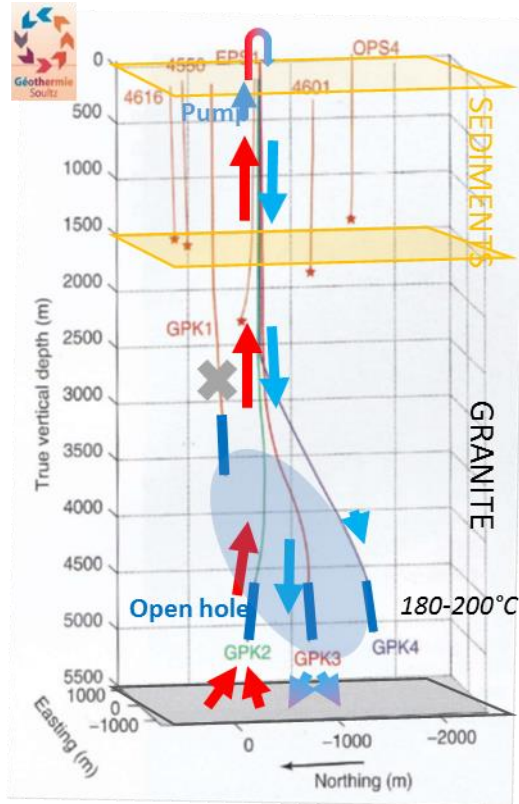
Figure 1.2. Schematic view of EGS site and drilled observation and operation wells (reproduced after Schmittbuhl, 2018)

1.3   Question of the Thesis

This thesis is about modeling of P-wave velocity variation during hydraulic stimulation of GPK2 well. The purpose of stimulation was to enhance hydraulic conductivity of reservoir by stimulating pre-existing fractures and faults or creating new fractures to ensure efficient hydraulic exchange between injection and production wells (Calo et al., 2011). This operation was monitored seismically using down-hole and surface receiver networks, enabling 4-D P-wave tomography mapping of the reservoir. Figure 1.3 demonstrates stimulation procedure of GPK2 well in terms of wellhead pressure and injection rate against time. The operation time is divided to four sets and fourteen subsets based on changes occurring in injection rate and wellhead pressure (Calo et al., 2011).

Injection flow rate at first day (subsets 1 and 2) of stimulation was 30 liter per second that increased to 40 l/s in second day (subsets 3, 4, and 5). Stimulation was continued from beginning of third day to end of sixth day by injection flow rate of 50 l/s and the dropped to zero by the end of the operation. While well-head pressure in beginning of injection in days one and two were approximately 12 MPa gradually decreasing to about 11 MPa at the end of days and before enhancing flow rate, it build up from 12 to about 13 MPa by progress of injection operation in third stage of stimulation from day 3 to end of day 6. An instance decrease of about 3 MPa experienced by shut-in the injection and gradually dropped to 3 MPa at day 10 of operation. It is worth mentioning that, precise analyses of shut-in pressure change with respect to time will be useful in building geomechanical model including stress state, fracture gradient, focal mechanism, and injection pressure.

3
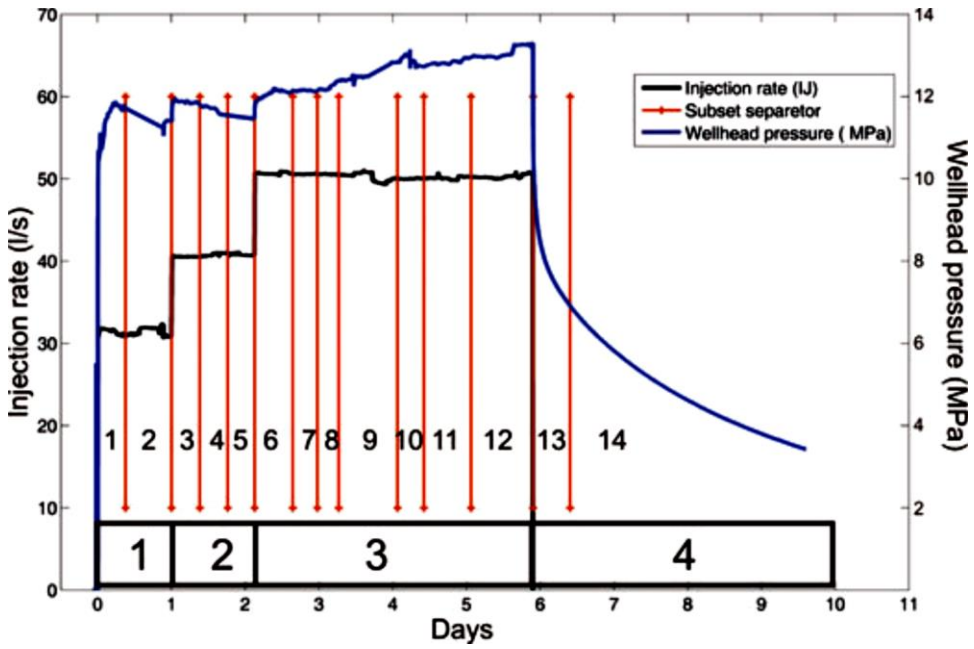
Figure 1.3. stimulation procedure of well GPK2; Black line of graph shows injection rate in each day in terms of liter per second, blue line corresponds well-head pressure during stimulation operation in terms of MPa, and red lines are subset separators (Calo et al., 2011).

The 4-D tomography showed the temporal and spatial evolution of the P-wave velocity during and after fluid injection. Figure 1.4 illustrates evolution of P-wave velocity at depth of 4.6 km during stimulation of GPK2. Each image demonstrates P-wave velocity change in corresponding subset from 1 to 14, respectively. Looking at figures reveals two points:

1) With the exception of sets 3 and 6, all the sets share a low-velocity anomaly that is larger than the seismic cloud and primarily located near the region where microseismic activity occurs. On the map view, the velocity anomaly is circular and appears right after the start of injection (set 1). During set 2, it lengthens in the direction of N145-N150E, and this direction does not change after that.

2) Trends of P-wave velocity change during stimulation; first, at early stages of fluid injection (subsets one and two), decrease in P-wave velocity happens as expected from pore pressure increase caused by fluid injection, but then, at subset 3, enhancing injection flow rate results in disappearance of P-wave velocity anomaly which is vice versa with expectation as is discussed in next two paragraphs. The same pattern is repeated from subset 4 through 6. This V_p evolution is, as mentioned by Calo et al., 2011, a fast and extended change, where a rapid change in seismic velocity of over 1000 m in 3 h was observed.

Lockner et al. [1977] performed a laboratory experiment on a Granite sample. They put the sample in a cell equipped circumferentially with P- and S-wave source and receivers positioned parallel and perpendicular with respect to the sample axis. Confining stress was set on a fixed magnitude while axial stress gradually increased until rock failure occurs. P- and S-wave velocity was monitored during loading process and the results were drew in terms of V/V_0 (ratio of velocity to initial velocity at hydrostatic pressure) and percent of failure strength (percentile proportion of applied axial stress from rock failure strength) as figure 1.5. Looking at their derived graph reveals that under axial loading of approximately 35% of failure strength and subsequently closure of horizontal micro-cracks, the P-wave and perpendicular S-wave velocities

experience less increase comparing to parallel S-waves. By progression of the loading and initiation of vertical fractures P-wave and perpendicular S-wave, velocities experience more drop compared with parallel S-waves until rock failure moment.
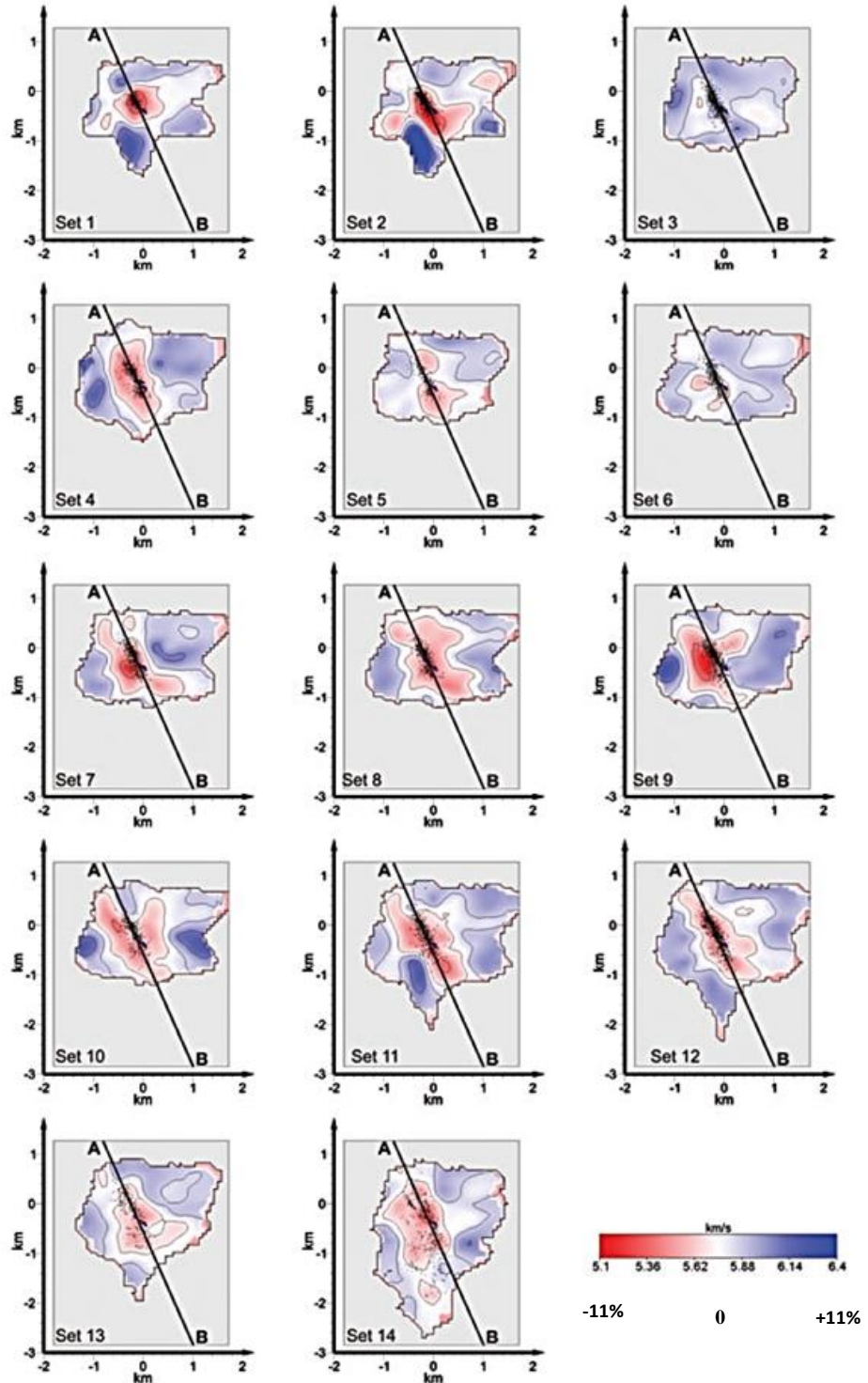
Figure 1.4. Map view of evolution of P-wave velocity in each subset of stimulation operation of well GPK2 (reproduced after Calo et al., 2011)

5
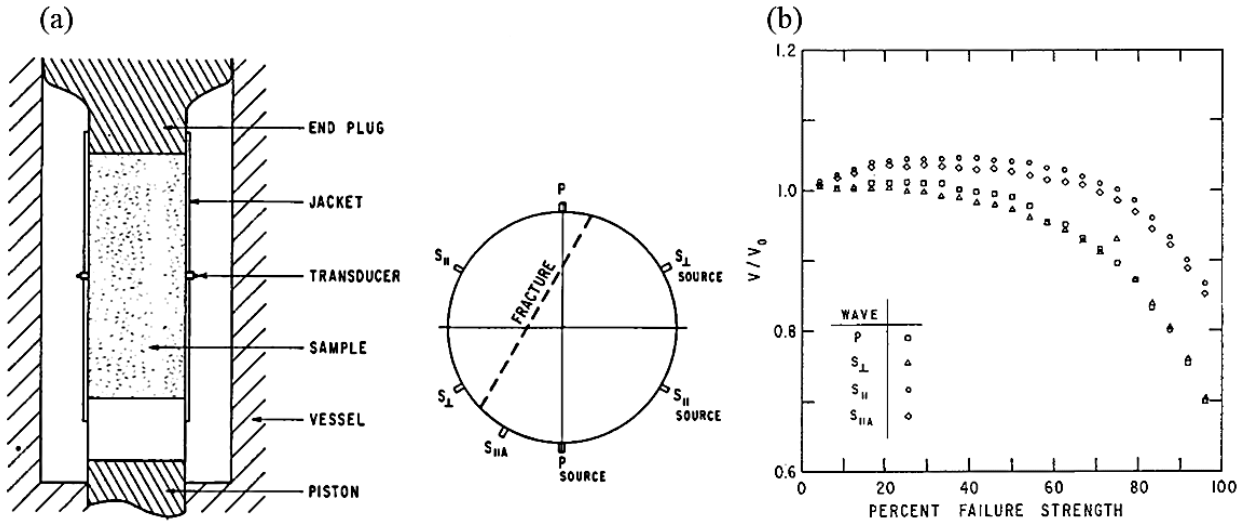
Figure 1.5. (a) This picture illustrates experiment machine and horizontal cross section of sample equipped with seismic wave sources and receivers, (b) the graph of changes in seismic wave velocities with respect to change in axial loading (Lockner et al., 1977)

Rummel (1991) also performed some experimental studies about physical properties of the granite samples cored from GPK1 well of Soultz-sous-Forêts. He investigated P-wave velocity evolution due to lithostatic pressure change and found that P-wave velocity increases as pressure enhances (figure 1.6). According to his findings the rate of increase in P-wave velocity happens in initial stages of pressure increase. He suggests that this may be due to closure of micro-cracks, which were open during core relaxation from in-situ stress situation. The outcomes of P-wave 4D tomography of GPK2 stimulation demonstrated in figure 1.4 are consistent with the results of Lockner et al, 1977 and Rummel, 1991 experiment except for subsets 3 and 6 in which the P-wave velocity increases by enhancing injection flow rate (and in consequence enhancing pore pressure and water content of system which can be either within discontinuity or rock), being vice versa with the Lockner's derivations probably due to existence of non-linear behavior of discontinuities under stress as explained by Bandis et al. at 1983.

Linear diffusion of pore pressure in porous media has hydraulic diffusivity as a central parameter (Jaeger et al., 2007):

$$\frac{\partial p}{\partial t} = D\nabla^2 p \quad (1)$$

in which temporal evolution of the pore pressure ($\frac{\partial p}{\partial t}$) is related to the spatial evolution of the pore pressure ($\nabla^2 p$) by a proportionality factor of hydraulic diffusivity (D) (Jaeger et al. 2007; Wang 2000; Rozhko 2010). In fact, hydraulic diffusivity is a ratio of transport (permeability) to storage (specific storage capacity) properties, which in turn, depend on properties of rock (geometrical characteristics of flow conduits and deformation characteristics) and fluid (compressibility and viscosity) (Deng et al., 2021).

Shapiro et al., 1997, evaluated spatio-temporal distribution of approximately over 400 microseismic events induced during hydraulic fracturing experiment of KTB borehole in Germany in order to estimate permeability. At their study, fluid injection in KTB was approximated by a point source fluid injection into an infinite homogeneous, isotropic, poroelastic, and saturated medium for which the pore pressure diffusion

6

can be considered as the mechanics of poroelastic media, analogous with present simulation. Shapiro and associates, by ignoring all non-mechanical (e.g. chemical and electro-chemical) solid –fluid interactions, solved pore pressure diffusion equation (equation (1)) for their simulated model assuming a boundary condition as an initial pore pressure perturbation being supplied as a function of time, $p_0(t)$, on a tiny spherical surface of radius a, with the injection point at its center. It is found that the initial seismic triggerings may take place at t_0 for the very first occurrences as

$$t_0 \leq r_0\sqrt{t_0/(4\pi D)} \quad (2)$$

This disparity leads to the following

$$D \leq \frac{r_0^2}{4\pi t_0} \quad (3)$$

Using above arguments on about 9000 seismic events induced during hydraulic stimulation of GPK1 well of Soultz-sous-Forêts at 1993, Shapiro et al., 2002, estimated an effective hydraulic diffusivity of 0.05 m²/s at depths of 2500 to 3500 m. The diffusion distance of pore pressure perturbation from injection point can then be obtained by manipulation and reordering of equation (3) as

$$r = \sqrt{4\pi Dt} \quad (4)$$

Substituting t=3 h and D=0.05 m²/s in this model leads to pressure evolution distance of 82 m, which is by far less than the Calo et al., 2011, observation of over 1000 m in 3 h.
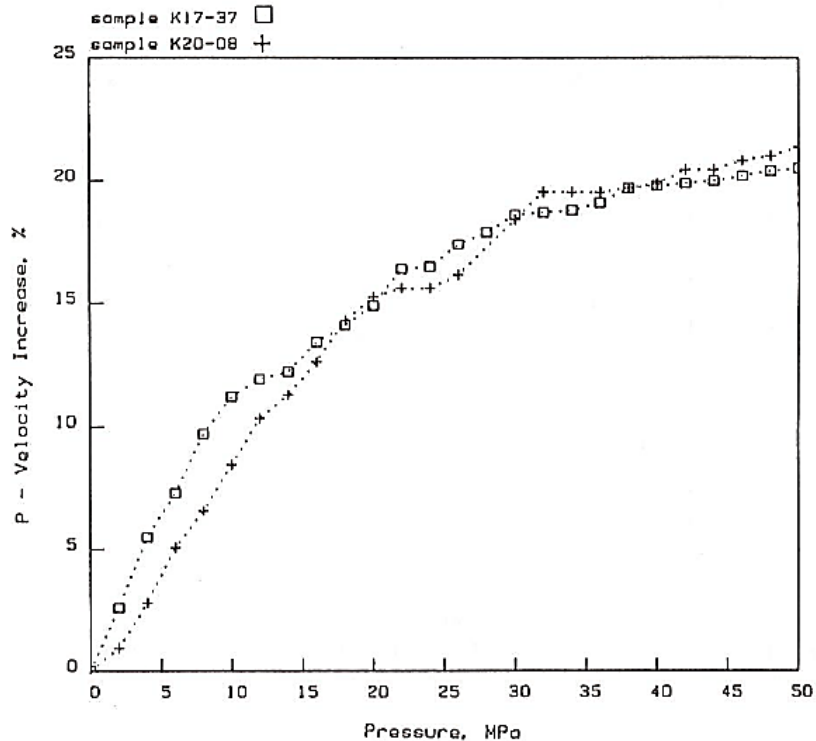
Figure 1.6. P-wave velocity evolution versus lithostatic pressure of two granite sample of GPK1 well of Soultz-sous-Forêts reservoir (Rummel, 1991)

7

In conclusion, a large-scale P-wave velocity variation is observed during and after the hydraulic stimulation of GPK2 in 2000, part of which, as shown in Figure 1.7, is associated with the effective normal stress change in the vicinity of the injection point and is accompanied by microseismicity associated with fluid diffusion; but the larger part of this V_p variation, which is still associated with the effective normal stress change, is not accompanied by microseismicity and rather reflects the occurrence of large-scale aseismic motions and/or elastic response of fractures. These unexpected behaviors are studied in this thesis.

1.1 Methodology

According to previous section, the aim of this thesis is numerical modeling of non-linear hydro-mechanical coupling of discontinuities encountered in GPK2 stimulation test. To achieve this goal, 3DEC discrete element modeling software of ITASCA Consulting group as a powerful tool in numerical modeling of discontinuum environment is chosen.

To account for the observed non-linear behavior, a description of the fracture network is required which may be achieved by definition of Discrete Fracture Network (DFN). In addition of assigning a DFN to the numerical model of target area, the model must be built applying mechanical properties of the intact rock and fractures, pore pressure, and in-situ stress field using ITASCA 3DEC software (Version 5.2). The next step will be to simulate the observed velocity anomaly for the maximum possible stress drop during GPK2 stimulation (possibly discussing the lack of velocity anomaly during GPK3 stimulation).

1.1.1 Discrete Fracture Network (DFN)

A DFN can be characterized with fracture position or density, fracture orientation (dip and dip direction), fracture size, and fracture thickness or hydraulic aperture each of which can be determined using borehole data such as image logs, vertical seismic profiles (VSP) as well as microseismic events. Figure 1.8 illustrates some characteristics of a fracture. The dip of a discontinuity is the angle between its plane and horizontal plane and the direction of its plane is dip direction.

A DFN can be characterized in stochastic and deterministic approaches. In stochastic type, fractures and faults are presented statistically as a set of planes in which their characteristics are related to a distribution model such as log normal, gamma law, or power law. In deterministic version, each fracture and fault is presented as a plane with specific characteristics of dip, dip direction, size, position, and aperture.

1.1.2 Numerical Modeling (3DEC)

Numerical models are used when empirical methods cannot be extrapolated to new situations and when no other methods (such as analytical or limit equilibrium) are available or the available methods are too simplistic and lead to underestimation of the actual situation. Their advantage is that they can be used to explain observed physical behavior such as collapse and multiple options can be analyzed such as different design hypothesis.

Numerical models are divided into two categories of continuum and discontinuum. Continuum methods which are suitable for modeling of continuum materials such as soils are categorized in types of finite element, finite difference/finite volume, and boundary elements. On the other hand, discontinuum methods are divided into two categories of implicit and explicit methods which are applicable in discontinuum medium such as rocks.
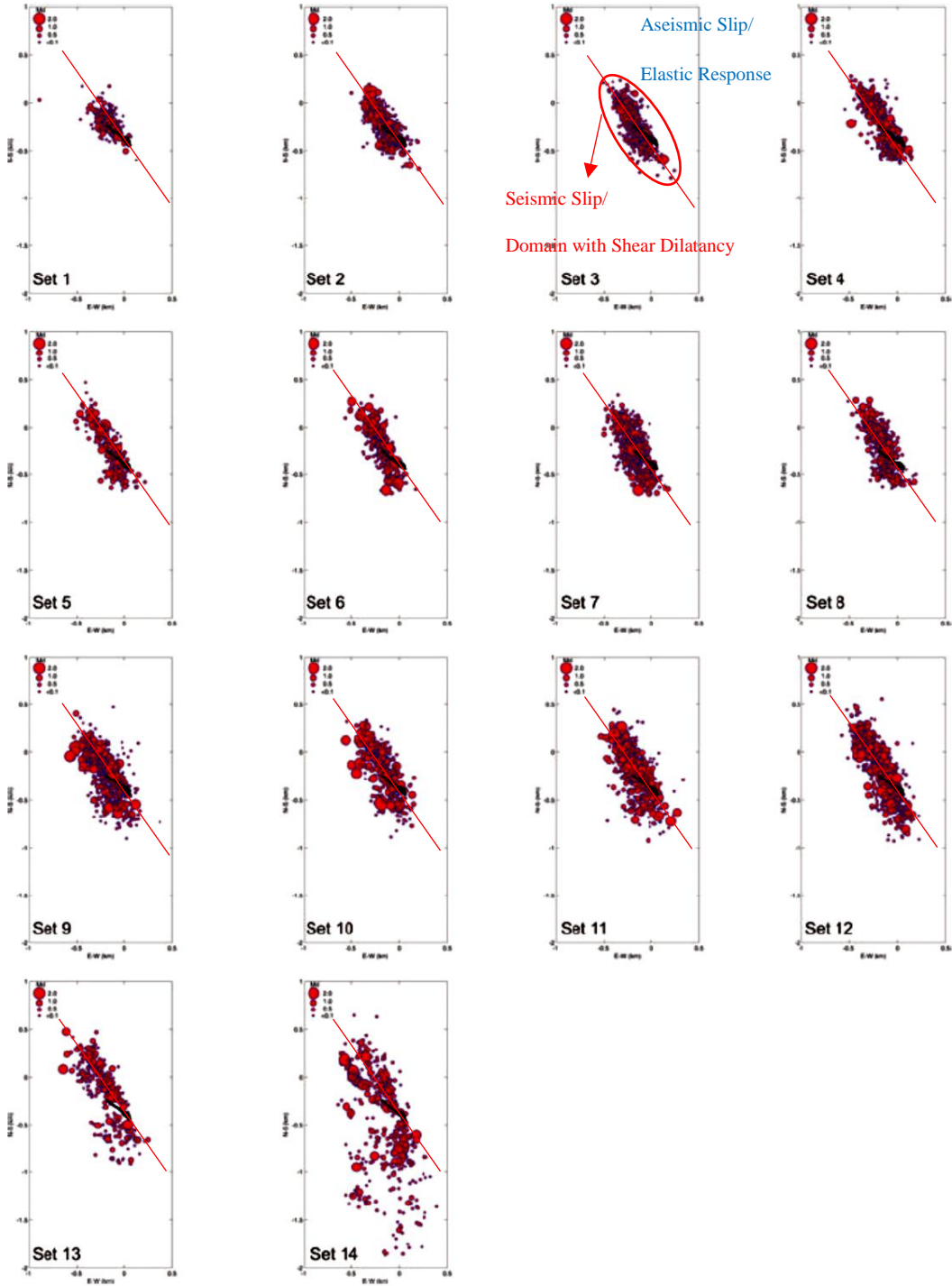
Figure 1.7. Map view of evolution of the microseismic cloud. Each picture shows, in chronological order comparable with those shown in figure 1.4, the final event positions after the computation of the local tomography. The radius of each circle is proportional to the magnitude and the projection of the injection well is indicated as a black line. Red line is approximate illustration of fault surface passing through stimulation area. X-axis is E-W direction and Y-axis is N-S direction, both in kilometers.
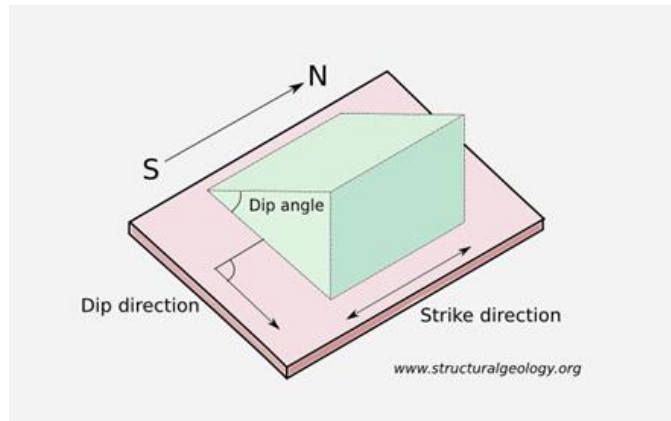
Figure 1.8. Characteristics of a discontinuity (www.structuralgeology.org)

UDEC/3DEC, FLAC2D/3D, and PFC 2D/3D of ITASCA Consulting and Engineering Group are commonly used software in numerical modeling of geological projects. Among these tools, FLAC is best fit to modeling of projects in shallower depth projects performed in soils such as urban railway tunnels. PFC is suitable for activities related to particle flows such as block caving mining method. UDEC/3DEC is mostly used in modeling of problems in rocks such as slopes, tunnels, and wellbores because of its ability to model discontinuous materials that show non-linear behavior.

3DEC is a Distinct Element Method (DEM) for discontiuum environment and can simulate the interaction between blocks. It is best suited to model discontinuous materials that show non-linear behavior. It comprises of many built-in constitutive models for blocks and joints and provides an option for user-written models by introducing FISH scripting language. In addition, of representing or importing of any shape of geometries, it can carry out static and dynamic analysis and considers thermal stress and time-dependent behavior of geomaterial.

To account for the observed non-linear behavior, a description of the fracture network is required which may be achieved by definition of a Discrete Fracture Network (DFN). In addition, of assigning a DFN to numerical model of the target area, it must be built applying mechanical properties of the intact rock and fractures, pore pressure, and in-situ stress field.

What to keep in mind about 3DEC is that the Biot theory is not implemented in that. Therefore, the fluid flow is restricted to the fracture network and pore pressure evolution of the system due to fluid dissipation from fracture to the rock matrix is independent from applied stress.

1.1.3   Nonlinear fracture stiffness

Bandis et al., 1983, performed a series of experiments on fresh and weathered locked joints of some samples of five rock types under normal and shear loading condition. Normal deformability was studied by conducting loading/unloading and repeated load cycling tests and shear deformability was studied by performing direct shear tests under a range of normal stresses. In both normal and shear loading methods, deformability of samples demonstrated nonlinear behavior irrespective of joint and rock type (figure 1.9) indicating the influence of discontinuities on mechanical behavior of rock mass under loading condition. Comparison tests were also carried out on mismatched joints where two faces of the joints were relatively

dislocated by 0.5-1.0 mm. The normal stress versus closure curves of the dislocated joints showed a similar behavior as when loaded in a fully locked position.
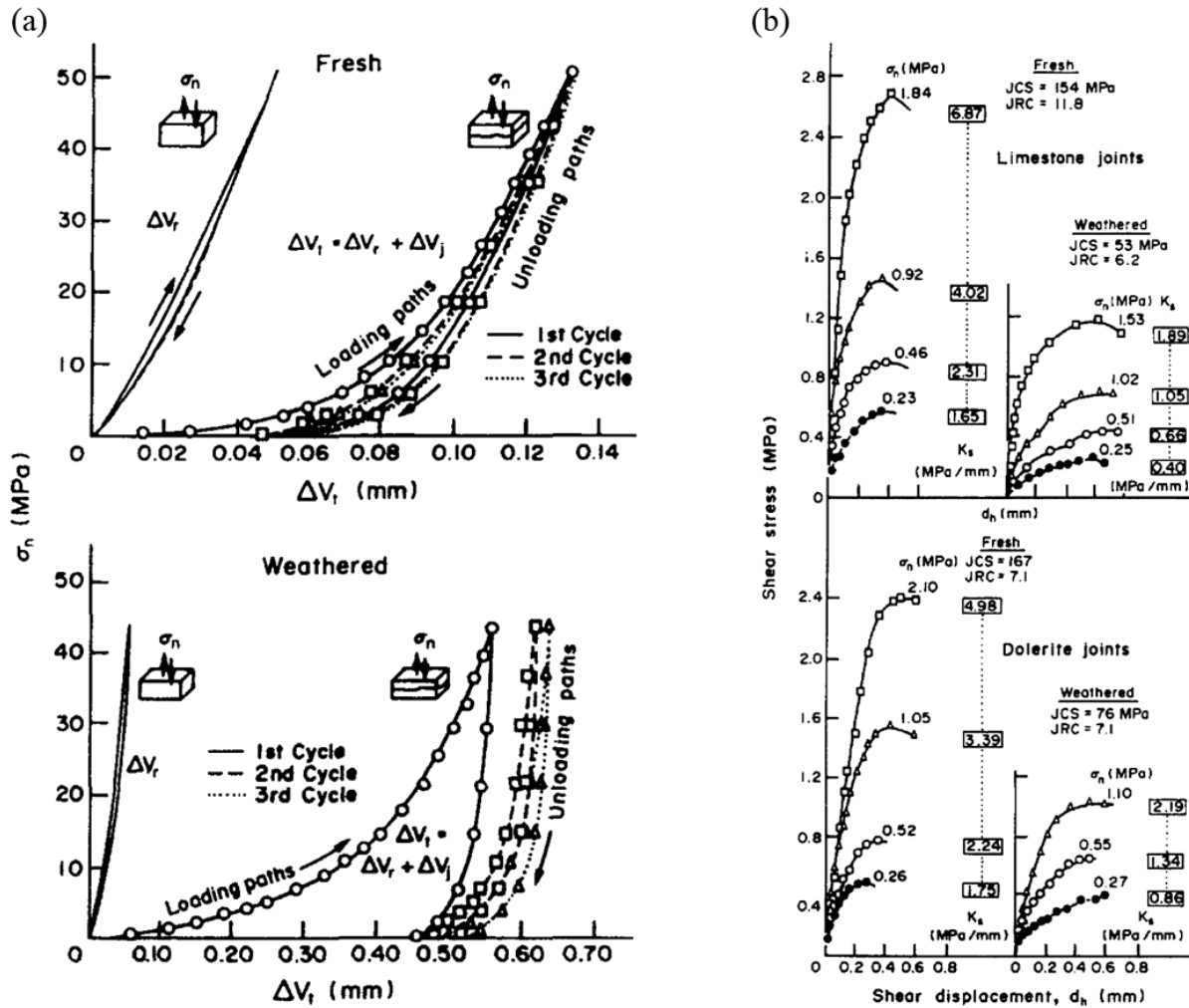
Figure 1.9. (a) Total deformation of fresh and weathered joints in Dolerite under repeated normal loading condition and (b) Joint shear displacement in Limestone and Dolerite; in both cases the graphs demonstrating a nonlinear behavior being described with a hyperbolic function (Bandis et al., 1983)

1.2 Overview of the thesis and State-of-the-Art

To model the response of geomaterial around injection point during stimulation of GPK2, it is necessary to take the role of both small fractures and large faults into account. According to Cornet (2015), a rock sample bearing small fractures under triaxial loading condition demonstrates elastic behavior until it reaches to plastic domain. This is shown in figure 1.10 in which change in effective normal stress causes some reversible strain in rock. This is related to the initial stages of fluid injection into a rock mass where subsequent pressure increase in pore space of fractures will cause decrease in effective normal stress and subsequent increase in fracture hydraulic aperture that, in turn, will result in decrease in P-wave velocity. Then continuous increase in pore pressure will cause shear slip of preexisting fractures or generation of fresh fractures depending on mechanical properties of rock mass and stress state. Activation of preexisting

11

fractures is bearing reaction of fracture stiffness to changes in effective normal stress, which is controlled by fracture roughness (Joint Roughness Constant or JRC as defined by Barton, 1976), fracture wall strength (Joint wall Compressive Strength or JCS as defined by Barton, 1976), and fluid flow within fracture.
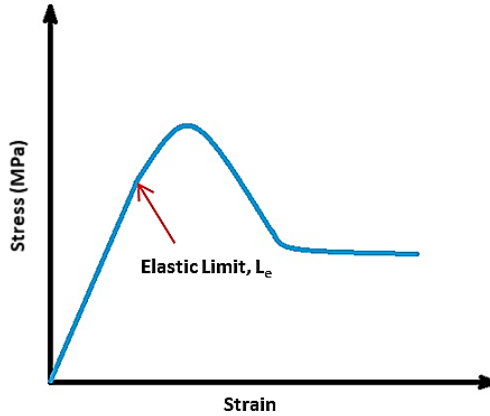
Figure 1.10. Deformation of rock mass under different stress magnitudes

Figure 1.11 illustrates the evolution of shear stiffness with respect to effective normal stress in which shear stiffness shows a non-linear trend with respect to change in effective normal stress. This non-linear behavior can be simplified to a bilinear trend (figure 1.11). However, and according to the author's best of knowledge, the fractures' shear and normal stiffness in the literature is always considered constant (e.g. Cappa et al., 2006; Guglielmi et al., 2008; Farmahini-Farhani and Ghassemi, 2016; Yin et al., 2020; Wynants-Morel et al., 2020 & 2021) with some exceptions such as Darcel et al., 2021. In the current work, we will try to account for the nonlinearity of normal and shear stiffness, as shown in Figure 1.8, and study its effect on the elastic response of fractures.
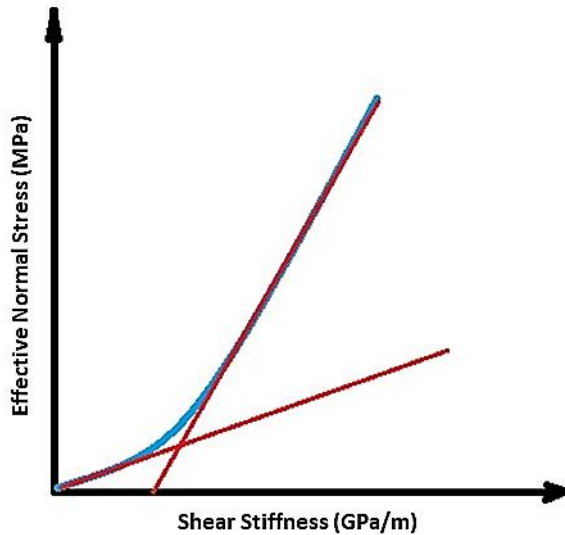
Figure 1.11. The shear stiffness of a fracture is strongly dependent on effective normal stress and shows non-linear behavior

Based on the above explanations, the aim of this work is to numerically simulate the fluid flow along the main fault of the Soultz-sous-Forêts reservoir and the nonlinear hydromechanical coupling of the discontinuities encountered during the GPK2 stimulation test, in order to characterize the observed anomaly in the P-wave velocity variation, as shown in Figure 1.4. For that, first the effect of fluid flow along a large fracture passing through the seismic cloud resulted from hydraulic stimulation of the study area, as shown in figure 1.7, will be assessed. Then, the elastic behavior of the rock mass fractured by a DFN in a 100x100x100 m^3 block will be studied, taking into account the nonlinear fracture stiffness. The models will be characterized with appropriate physical properties, in-situ stress state, and normal and shear stiffness of fractures. The elastic response of the block to different scenarios of applied stress will be evaluated in terms of the evolution of P-wave velocity.

Chapter 2

2 Numerical Benchmarking Modeling of Mechanical Behavior of an Intact Rock Block

To effectively model the response of geomaterial around the injection point as well as far field during stimulation of GPK2, it is necessary to take the role of both intact rock and discontinuities into account. In this chapter, by utilizing 3DEC the mechanical behavior of an intact rock block of 100x100x100 m³ was assessed through a set of benchmarking tests.

2.1 Benchmarking Tests

In order to check that 3DEC is used properly, first the mechanical behavior of a homogeneous, isotropic, and elastic block of 100x100x100 m³ was assessed. The model was characterized with proper mechanical and physical properties, as well as stress and velocity (displacement) boundary conditions. Elastic responses of blocks in different cases of Uniaxial Stress, Uniaxial Strain, and Polyaxial Stresses were investigated. Figures 2.1 and 2.2 show three different tests of benchmarking where the gravity was neglected and was considered, respectively.
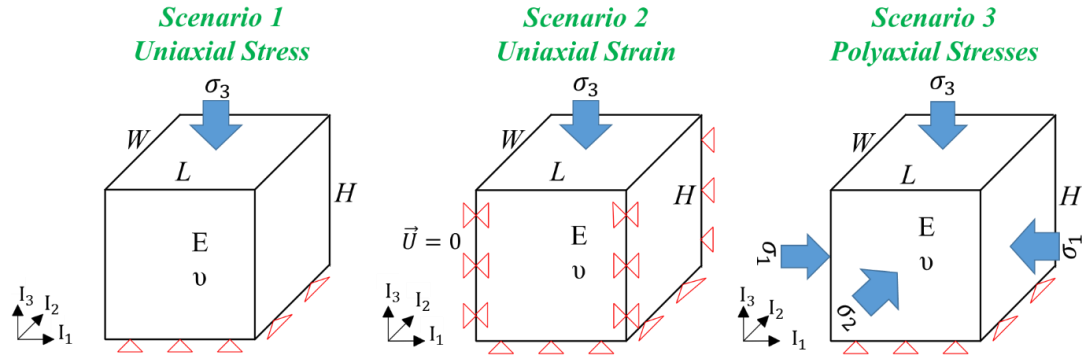
Figure 2.1. Three different cases in which mechanical benchmarking were conducted when the gravity is not considered
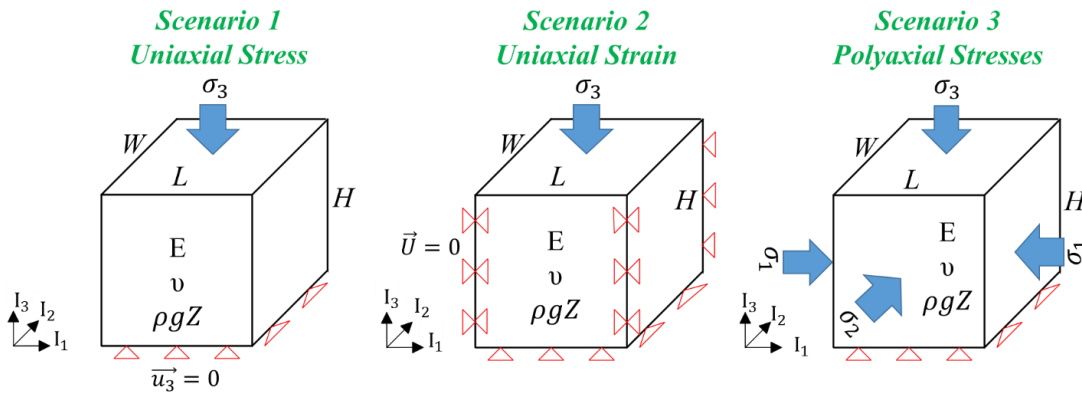
Figure 2.2. Three different cases of Uniaxial Stress, Uniaxial Strain, and Polyaxial Stress in which mechanical benchmarking were conducted when the gravity is considered

2.1.1   Numerical Solution (Distinct Element Method-3DEC)

The distinct element method (Cundall, Strack 1979b) is a method for simulating the mechanical behavior of systems consisting of isolated blocks or particles. The shapes of the particles can be freely chosen; any particle can interact with any other; and there are no restrictions on the displacement or rotation of the particles. Blocks can be modeled in 3DEC in two distinct ways: rigid blocks with six degrees of freedom (including translational and rotational degrees) or deformable blocks with three degrees of freedom in a tetrahedron (or node) at each vertex. The rigid block motion is sufficient for stability studies where the stress state applied is low in comparison to the intact rock strength and the motion is focused along the structural features. In deformable block formulae, each block is divided into a finite difference mesh composed of tetrahedron elements of constant-strain. The resulting mesh is an explicit large-strain mesh, and the block material is modeled using elastic models as well as elastoplastic models. The logic of deformable blocks is similar to the two-dimensional block logic, as formulated by Lemos et al. (1987).

3DEC takes into account the deformability of blocks and the failure of intact material. In 3DEC, each polyhedron block is divided into an inner finite difference mesh made up of tetrahedron elements of constant strain. The resulting mesh is an explicit large strain mesh. The model for the block is an elastic model and the model for the elasto model is an elasto plastic model. The logic of the deformable block is similar to the two-dimensional block logic, as described by Lemos, (1987).

3DEC uses a dynamic (time domain) algorithm to solve the equations of motion for the block system using the explicit finite difference method (see Cundall 1987). Solution schemes based on equations of motion are better suited to identify potential failure modes for discontinuum systems, as opposed to schemes that do not take into account velocities or inertial forces (for example, successive over-relaxation). The law of motion and constitutive equations are used at each timestep. For both rigid blocks and deformable blocks the sub-contact force displacement relations are prescribed. Integrating the law of motion gives the new block positions and hence the contact displacement increments (or velocities). Sub-contact force displacement law is used to obtain the additional sub-contact forces to be applied on the blocks in the following timestep. Figure 2.3 shows the cycle of mechanical calculations.
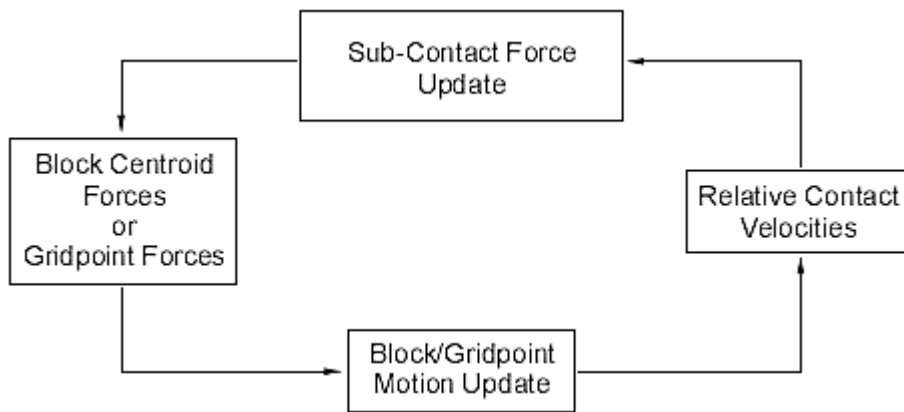
Figure 2.3. Cycle of mechanical calculations in 3DEC

In most cases, it's impossible to ignore the deformations of individual blocks (you can't just assume that blocks are solid). In 3DEC, fully deformable blocks are designed to allow you to deform each block in your model internally.

15

These deformable blocks are divided into tetrahedral blocks with a finite difference. The amount of deformation you can get depends on how many elements you have to divide the blocks into. Using tetrahedral blocks means you don't have to worry about deformations like the hourglass* that can happen when you're working with a polyhedron constant-strain finite-difference.

The vertices in the tetrahedron are called gridpoints, and the motion equations for each gridpoint are given as follows:

$$\ddot{u}_i = \frac{\int_s \sigma_{ij} n_j ds + F_i}{m} + g_i \quad (2.1)$$

where s is the surface enclosing the mass, m, lumped at the gridpoint, σ_{ij} is the zone stress tensor, n_j is the unit normal to s, F_i is the resultant of all external forces applied to the gridpoint (from block sub-contacts or otherwise), and g_i is the gravitational acceleration.

Gridpoint forces are obtained as a sum of three terms as

$$F_i = F_i^z + F_i^c + F_i^l \quad (2.2)$$

where F_i^l is the external applied load. F_i^c is the result of the sub contact forces. F_i^c exists only for gridpoints along the block boundaries. The forces from sub contacts along the two adjacent faces to the gridpoint contribute to F_i^c. Because the displacements along any face are assumed to be linearly distributed, the impact of sub-contact forces along a face can be represented by static equivalent forces applied on the face endpoints. The contribution of internal stresses in adjacent zones is calculated as

$$F_i^z = \int_C \sigma_{ij} n_j ds \quad (2.3)$$

where n_j is the unit outward normal to the contour, C, which follows the closed polygonal surface defined by the straight segments which bisect the zone faces converging on the gridpoint under consideration.

At each gridpoint, a net nodal force, $\sum F_i$, is calculated. The net nodal force includes the contributions of applied loads, as mentioned above, and the contributions of body forces caused by gravity. Gravitational forces, $F_i^{(g)}$, are computed from

$$F_i^{(g)} = g_i m_g \quad (2.4)$$

where m_g is the lumped gravitational mass at the gridpoint and equal to the one third of the masses of tetrahedral connected to the gridpoint. If the body is in equilibrium or in a steady-state flow (for example, plastic flow), $\sum F_i$ on the node is zero. If not, the node is accelerated according to Newton's second law of motion as

$$\dot{u}_i^{(t+\frac{\Delta t}{2})} = \dot{u}_i^{\left(t - \frac{\Delta t}{2}\right)} + \sum F_i^{(t)} \frac{\Delta t}{m} \quad (2.5)$$

where the superscripts denote the time at which the corresponding variable is evaluated.

During each timestep, strains and rotations are related to nodal displacements in the usual fashion:

16

$$\dot{\epsilon}_{ij} = \frac{1}{2}(\dot{u}_{i,j} + \dot{u}_{j,i}) \quad (2.6)$$

$$\dot{\theta}_{ij} = \frac{1}{2}(\dot{u}_{i,j} - \dot{u}_{j,i}) \quad (2.7)$$

Notice that, because of incremental treatment, equations (2.6) and (2.7) do not imply a restriction to small strains.

The constitutive laws for deformable blocks are used in an incremental form so that it is easy to implement on non-linear problems. The form in which these equations are actually expressed is

$$\Delta\sigma_{ij}^e = \lambda\Delta\epsilon_v\delta_{ij} + 2\mu\Delta\epsilon_{ij} \quad (2.8)$$

where λ and μ are Lame constants, $\Delta\sigma_{ij}^e$ are the elastic increments of the stress tensor, $\Delta\epsilon_{ij}$ are the incremental strains, $\Delta\epsilon_v = \Delta\epsilon_{11} + \Delta\epsilon_{22} + \Delta\epsilon_{33}$ is the increment of volumetric strain, and δ_{ij} is the Kronecker delta function.

Nonlinear and post-peak strength models are easy to implement directly in the code without using tools like equivalent stiffnesses or starting strains, which must be introduced into matrix oriented programs to maintain the linearity imposed by matrix formulation. In explicit programs, however, it is much easier: After each time step, we know the strain state for each zone. Then, we need to know the stress for each zone to continue to the next time step. The stress is unique to the stress and strain model, whether it be a linear elastic relation or a more complex, nonlinear and post-peak strength model.

2.1.1.1 Sign Conventions in 3DEC

The sign conventions in 3DEC are as follows and must be followed when entering input or evaluating results (Itasca, 2016).

Block motion: Positive motion is in the positive coordinate axes directions.

Direct stress: Positive stresses indicate tension; negative stresses indicate compression. It is the same as the convention in continuum mechanics (Cornet, 2015).

Shear stress: Referring to Figure 2.4, a positive shear stress points in the positive direction of the coordinate axis of the second subscript if it acts on a surface with an outward normal in the positive direction. Conversely, if the outward normal of the surface is in the negative direction, the positive shear stress points in the negative direction of the coordinate axis of the second subscript. The shear stresses shown in Figure 2.4 are all positive. The stress tensor is symmetric (i.e., complementary shear stresses are equal).

Direct strain: Positive strain indicates extension; negative strain indicates compression.

Shear strain: Shear strain follows the convention of shear stress (see above).

Pore pressure: Fluid pore pressure is positive in compression.

Dip, dip direction: – Dip and dip direction assume that the x-direction corresponds to "East," the y-direction corresponds to "North," and the z-direction corresponds to "Up." The dip angle is measured in the negative

z-direction from the global xy-plane. The dip direction angle is measured in the global xy-plane, clockwise from the positive y-axis.

Note that the x, y, and z components of vector quantities (such as forces, displacements, and velocities) are positive when they point in the directions of positive x, y, and z coordinate space.
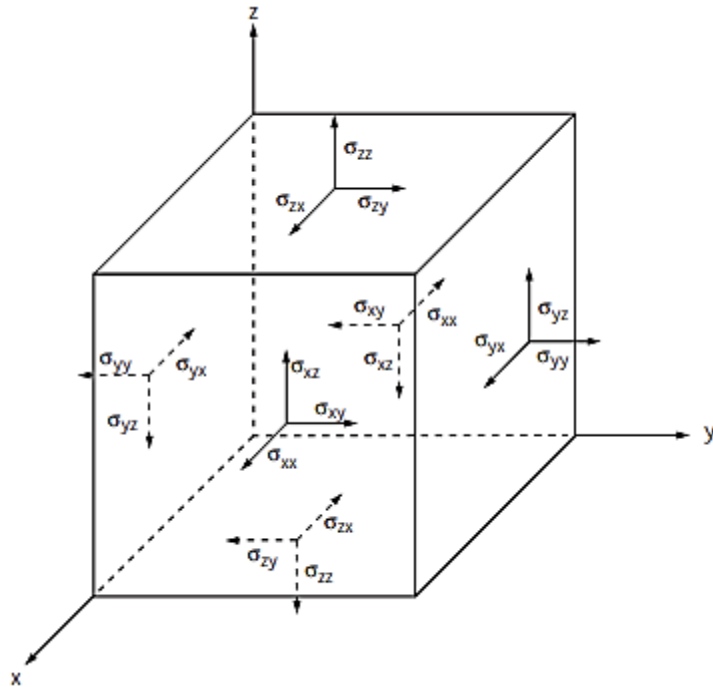
Figure 2.4. Sign convention for positive stress components

2.1.2 Analytical Solution

Below, you can find analytical solution to calculate displacement components in abovementioned block for Polyaxial Stresses case when the gravity is not considered. Its generalization to the other two cases of Uniaxial Stress and Uniaxial Strain is straightforward.

If u_3 and u_1 in figure 2.5 are displacement components in I_3 and I_1 principal directions (I_2 is inward normal to the page), the strain components will be:

$$\varepsilon_1 = \frac{u_1}{l} \quad (2.9)$$

$$\varepsilon_2 = \frac{u_2}{l} \quad (2.10)$$

$$\varepsilon_3 = \frac{u_3}{l} \quad (2.11)$$
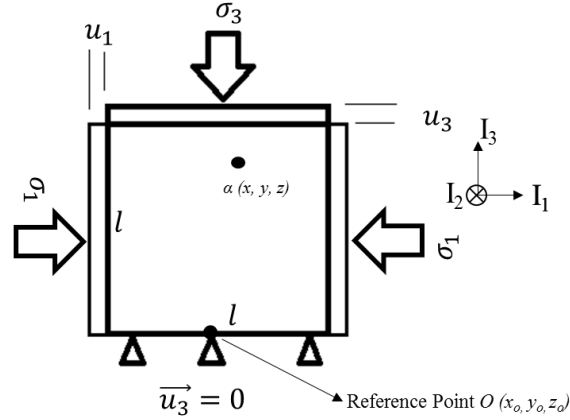
Figure 2.5. Schematic cross section of block with side size of l for Polyaxial Stresses case

To determine strain at any point such as α in the block, the side length of l should get very small, for the strain is assumed to be uniform in the block. Then:

$$\varepsilon_1^\alpha = \lim_{l \to 0} \left(\frac{u_1}{l} \right) \equiv \frac{du_1^\alpha}{dl} \quad (2.12)$$

$$\varepsilon_2^\alpha = \lim_{l \to 0} \left(\frac{u_2}{l} \right) \equiv \frac{du_2^\alpha}{dl} \quad (2.13)$$

$$\varepsilon_3^\alpha = \lim_{l \to 0} \left(-\frac{u_3}{l} \right) \equiv \frac{du_3^\alpha}{dl} \quad (2.14)$$

Substituting Hooke's law in strain relations 2.12-2.14 at a point and solving in terms of displacement will yield to:

$$du_1^\alpha = \left[\frac{\sigma_1}{E} - \frac{\vartheta}{E}(\sigma_2 + \sigma_3) \right] dl \quad (2.15)$$

$$du_2^\alpha = \left[\frac{\sigma_2}{E} - \frac{\vartheta}{E}(\sigma_1 + \sigma_3) \right] dl \quad (2.16)$$

$$du_3^\alpha = \left[\frac{\sigma_3}{E} - \frac{\vartheta}{E}(\sigma_1 + \sigma_2) \right] dl \quad (2.17)$$

In which E and v are Young's modulus and Poisson's ratio, respectively. Integration of above relations will yield to displacement magnitudes in principal directions in the cube of side size l:

$$u_1 = \int du_1^\alpha = \int_0^l \left[\frac{\sigma_1}{E} - \frac{\vartheta}{E}(\sigma_2 + \sigma_3) \right] dl \quad (2.18)$$

$$u_2 = \int du_2^\alpha = \int_0^l \left[\frac{\sigma_2}{E} - \frac{\vartheta}{E}(\sigma_1 + \sigma_3) \right] dl \quad (2.19)$$

$$u_3 = \int du_3^\alpha = \int_0^l \left[\frac{\sigma_3}{E} - \frac{\vartheta}{E}(\sigma_1 + \sigma_2) \right] dl \quad (2.20)$$

To conclude displacement magnitudes in Uniaxial Stress case, it should be noticed that Hooke's law for this case is:

19

$$\varepsilon_3 = \frac{\sigma_3}{E} \quad (2.21)$$

$$\varepsilon_1 = \varepsilon_2 = -\vartheta\varepsilon_3 \quad (2.22)$$

Substituting equations 2.21 and 2.22 in equations 2.12 to 2.14 and doing the same derivation steps as earlier case will yield to following displacement components:

$$u_3 = \int du_3^\alpha = -\int_0^l \frac{\sigma_3}{E} dl \quad (2.23)$$

$$u_1 = \int du_1^\alpha = -\int_0^l \vartheta \frac{\sigma_3}{E} dl \quad (2.24)$$

$$u_2 = \int du_2^\alpha = -\int_0^l \vartheta \frac{\sigma_3}{E} dl \quad (2.25)$$

For the Uniaxial Strain, lateral strains are equal to zero. Hooke's law will be as equation 2.26 due to effect of Poisson's ratio:

$$\varepsilon_3 = \frac{\sigma_3}{E} - \frac{\vartheta}{E}(\sigma_1 + \sigma_2) \quad (2.26)$$

$$\varepsilon_1 = \varepsilon_2 = 0 \quad (2.27)$$

Similarly, substituting equations 2.26 in equations 2.14 and doing the same derivation steps as Polyaxial Stresses case will yield to following vertical displacement value:

$$u_3 = \int du_3^\alpha = -\int_0^l \left[\frac{\sigma_3}{E} - \frac{\vartheta}{E}(\sigma_1 + \sigma_2)\right] dl \quad (2.28)$$

Taking the gravity into consideration, a gradient of the Gravitational loading (which is equal to $\rho g Z$; ρ is bulk density in Kg/m³, g is gravitational acceleration in m/s², and Z is depth in m which is variable from 0 to 100 m in current benchmarking modeling) will be directly added to constant magnitude of σ_3 from top to bottom of the block. Consequently, lateral principal stresses will be changed corresponding to change in vertical stress value.

An example for comparison of numerical displacement magnitudes to analytical values and corresponding errors can be found in figures 2.6 and 2.7 respectively for Polyaxial Stresses and Uniaxial Stress cases when the gravity is ignored or considered in calculations, respectively. To find complete sets of results, interested readers can refer to Appendix A2.1. The relative error in terms of percent is determined as below:

$$error = \frac{Numerical\ Value - Analytical\ Value}{Analytical\ Value} * 100 \quad (2.29)$$

By above definition of error calculation, it is obvious that in some points of the block where the analytical displacement is zero, magnitude of the error will tend to a very high value due to division to zero. This can be seen in the central axis of the block for lateral displacements (figures A2.6, A2.7, A2.9, A2.10, A2.13, and A2.14 of appendix A2.1).
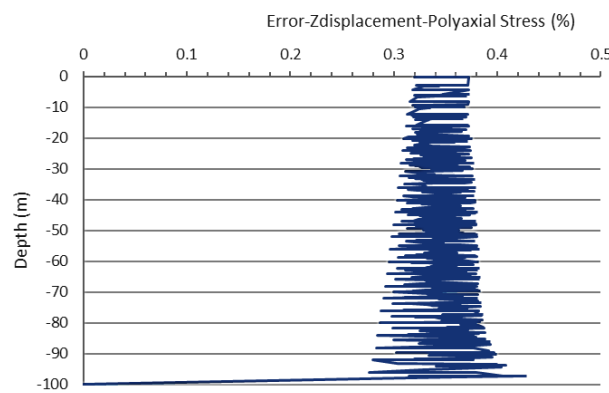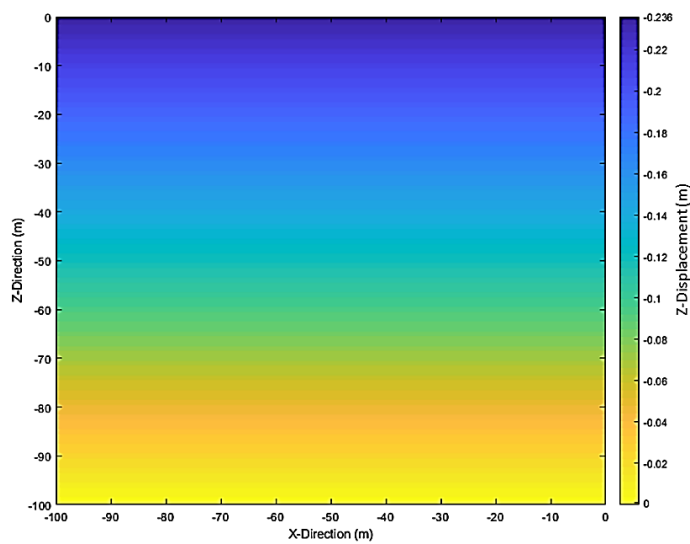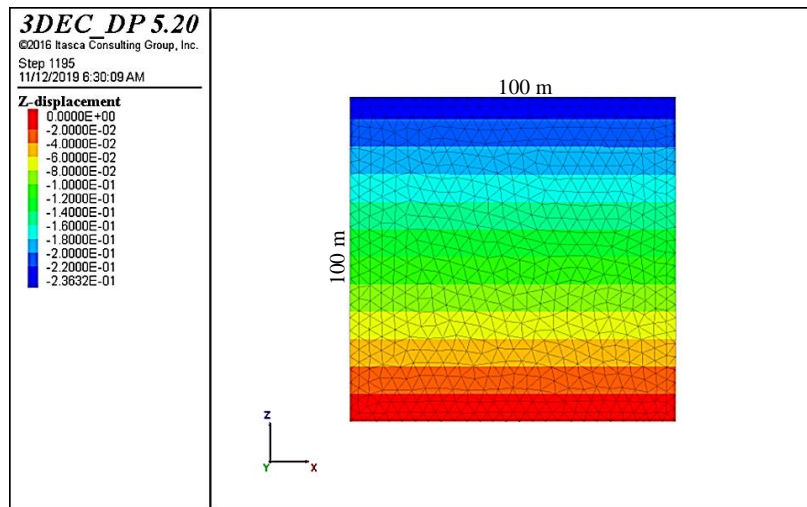
Figure 2.6. Numerical (upper) and analytical (middle) vertical displacement magnitudes and corresponding error (lower) for Polyaxial Stresses case when gravity is not considered
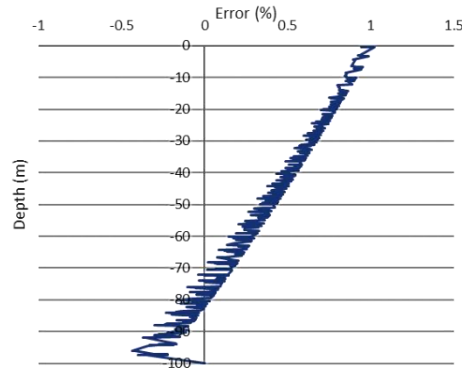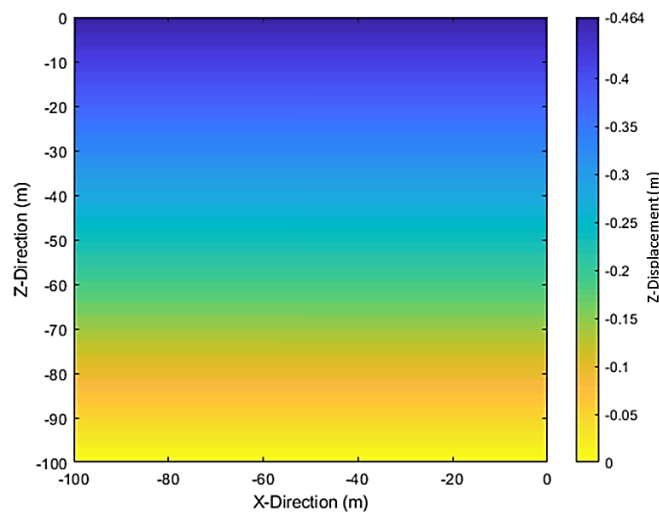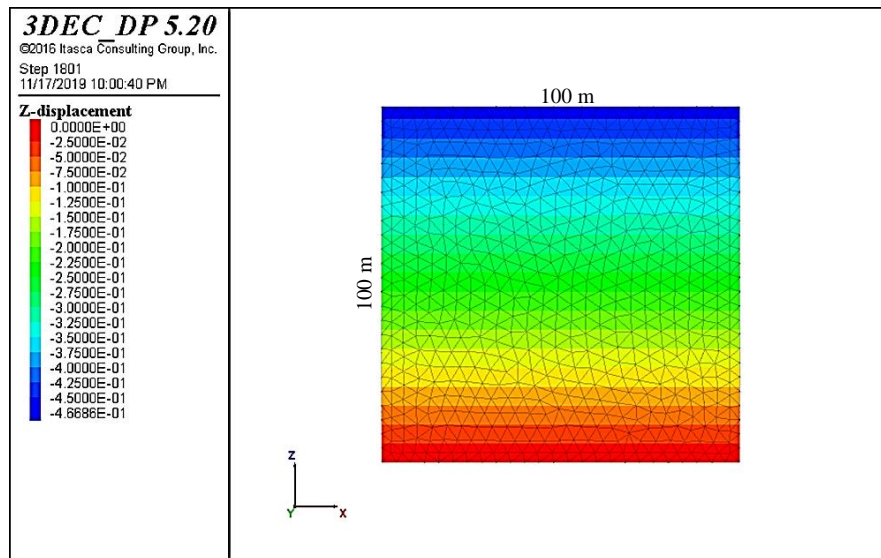
Figure 2.7. Numerical (upper) and analytical (middle) vertical displacement magnitudes and corresponding error (lower) for Uniaxial Stress case when gravity is considered

It is worth mentioning that, the accuracy of numerical results generally increases with decreasing mesh size. However, with an extremely fine mesh size, substantial computational time will be consumed. Therefore, it is necessary to determine a reasonable mesh size to achieve a balance between computation efficiency and accuracy (Chen et al., 2000b). Magnitudes of absolute error, which is difference between analytical and numerical displacement components, at two points of A and B shown in figure 2.8 versus mesh sizes of 2, 3, 4, 5, and 10 meters, when the gravity is taken into account, are shown in tables 2.1 to 2.3 and figures 2.9 to 2.11.
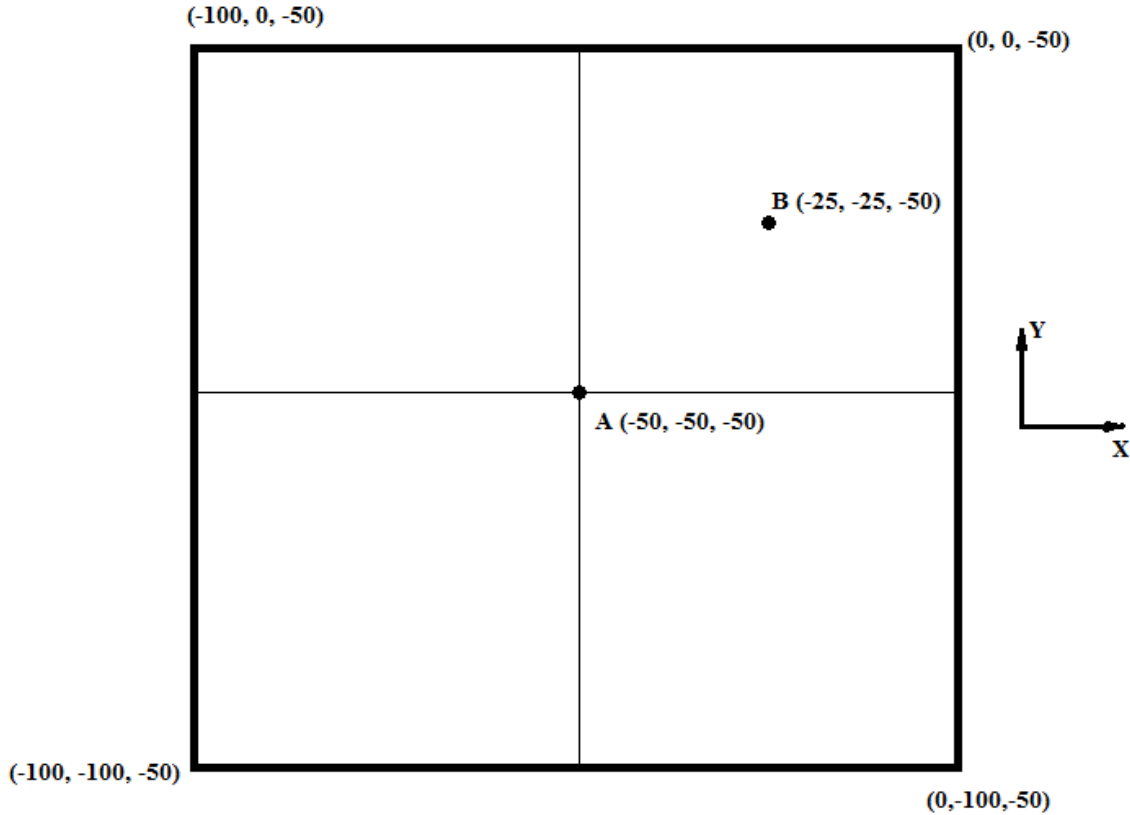
Figure 2.8. Plane view of the block of benchmarking modeling at the depth of -50 m where A and B are the points in which, respectively, the vertical and both lateral components of displacement are evaluated and compared with analytical values

Table 2.1. Absolute error values of numerical displacement components versus discretization mesh size at point A (for vertical displacement) and point B (for lateral displacements) in the block for Uniaxial Stress case when the gravity is considered

Mesh Size (m)	Absolute Errors		
	Vertical Displacement (m)	Lateral Displacement (X Direction) (m)	Lateral Displacement (Y Direction) (m)
2	-3.775E-03	3.354E-04	1.207E-04
3	-8.065E-03	-1.273E-03	2.517E-03
4	-7.338E-03	-5.820E-04	2.228E-03
5	-1.639E-02	3.230E-04	1.293E-03
10	-2.638E-02	3.430E-03	-1.153E-02

Table 2.2. Absolute error values of numerical vertical displacement versus discretization mesh size at point A in the block for Uniaxial Strain case when the gravity is considered

Mesh Size (m)	Absolute Error
	Vertical Displacement (m)
2	-2.393E-03
3	-5.581E-03
4	-5.035E-03
5	-1.177E-02
10	-1.923E-02

Table 2.3. Absolute error values of numerical displacement components versus discretization mesh size at point A (for vertical displacement) and point B (for lateral displacements) in the block for Polyaxial Stresses case when the gravity is considered

Mesh Size (m)	Absolute Error		
	Vertical Displacement (m)	Lateral Displacement (X Direction) (m)	Lateral Displacement (Y Direction) (m)
2	-1.47E-03	2.86E-04	-2.08E-04
3	-3.22E-03	-3.68E-04	-5.27E-03
4	-3.29E-03	6.18E-07	-4.69E-03
5	-7.91E-03	2.15E-04	-2.63E-03
10	-1.30E-02	1.22E-03	2.47E-02

Looking at the results of the error analysis and considering the physical time of block discretization, in most cases the 4 meter mesh size has the lowest absolute error compared to other sizes. Therefore, the discretization mesh size of 4 may be the most efficient size for benchmarking modeling when both error and computation time are considered.
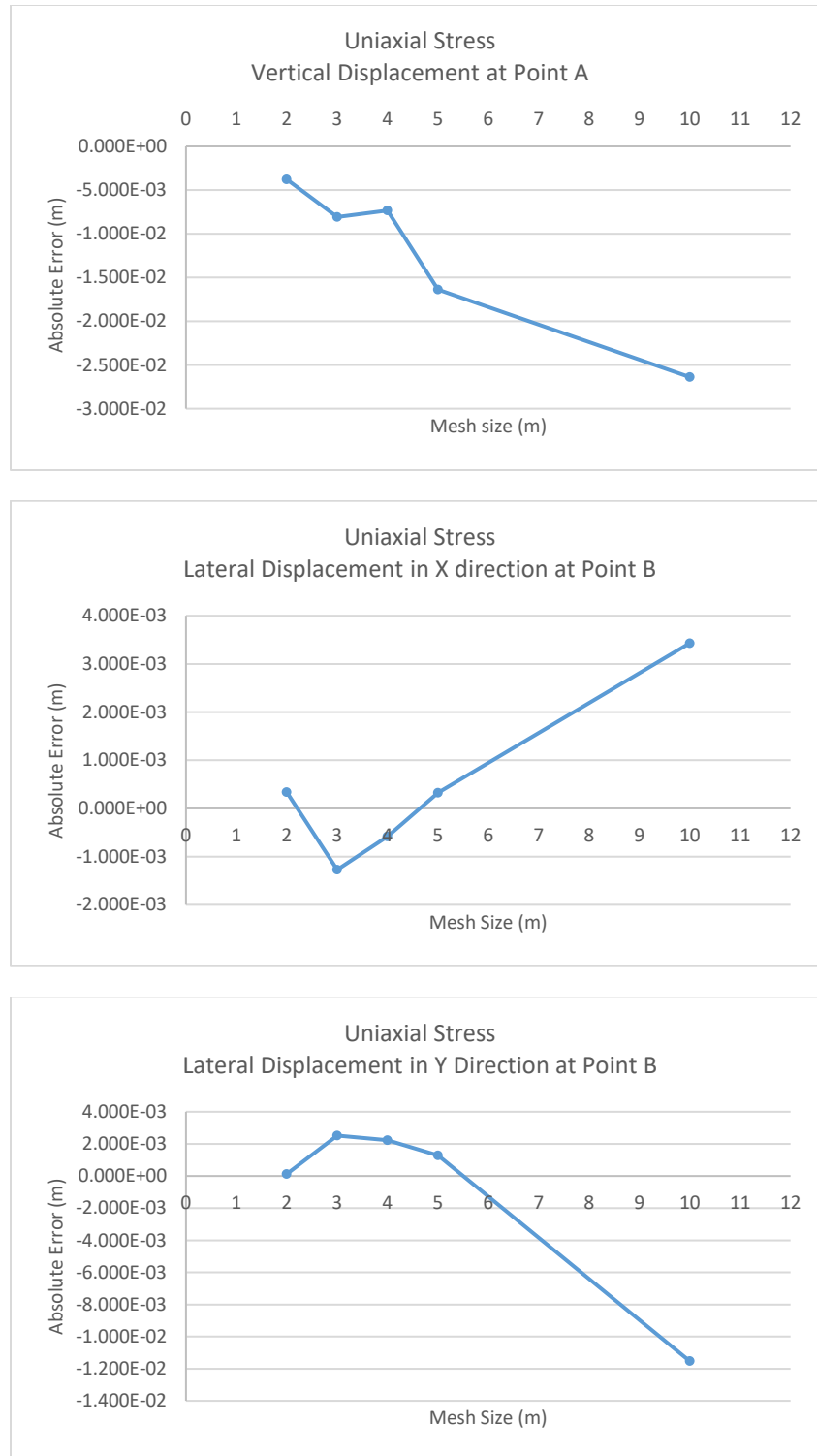
Figure 2.9. Absolute errors of displacement components versus mesh size in Uniaxial Stress case when the gravity is considered in computation; (a) for vertical displacement at Point A, (b) for lateral displacement in X direction at point B, and (c) for lateral displacement in Y direction at point B
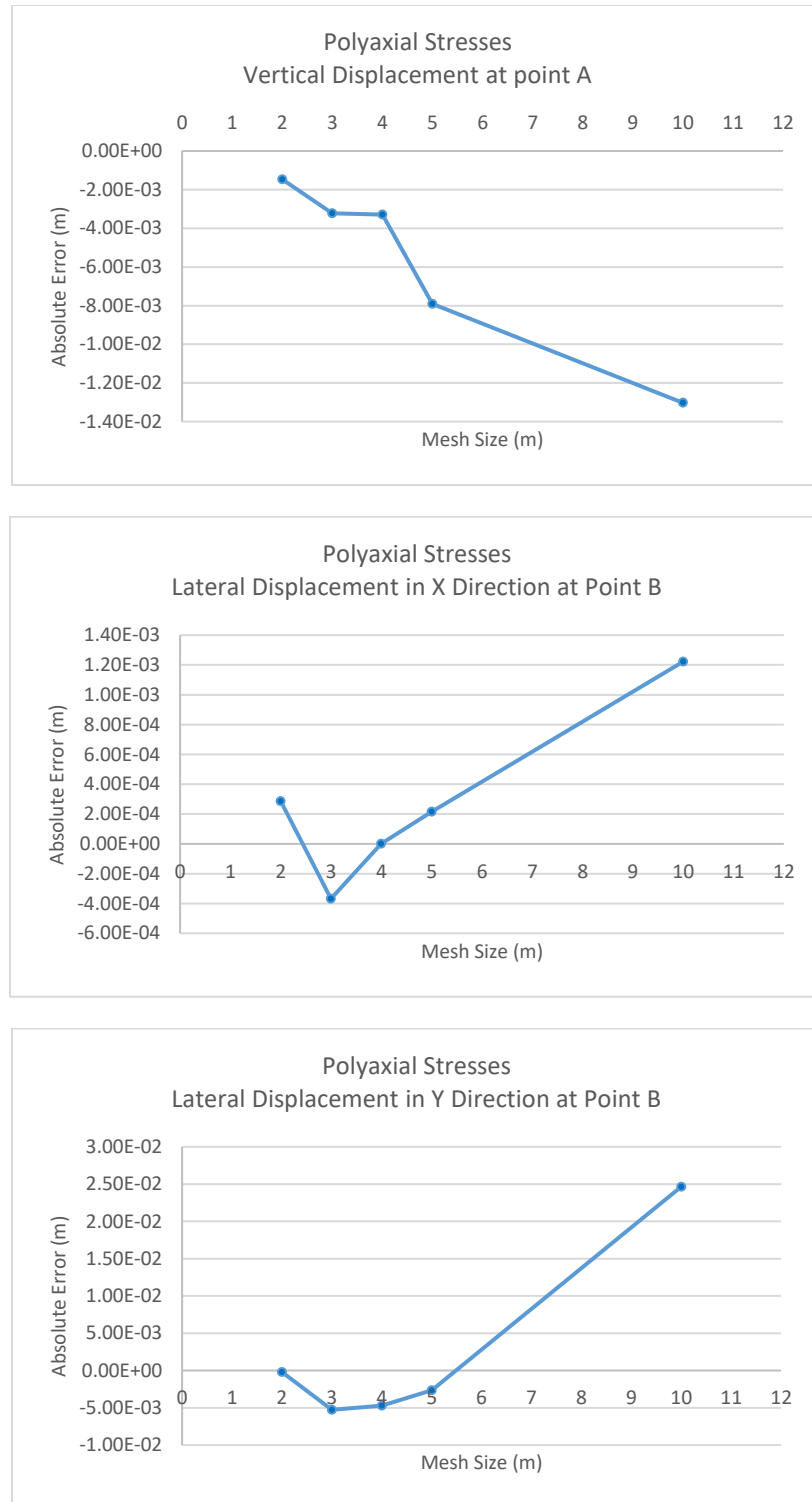
Figure 2.10. Absolute errors of displacement components versus mesh size in Polyaxial Stresses case when the gravity is considered in computation; (a) for vertical displacement at point A, (b) for lateral displacement in X direction at point B, and (c) for lateral displacement in Y direction at point B
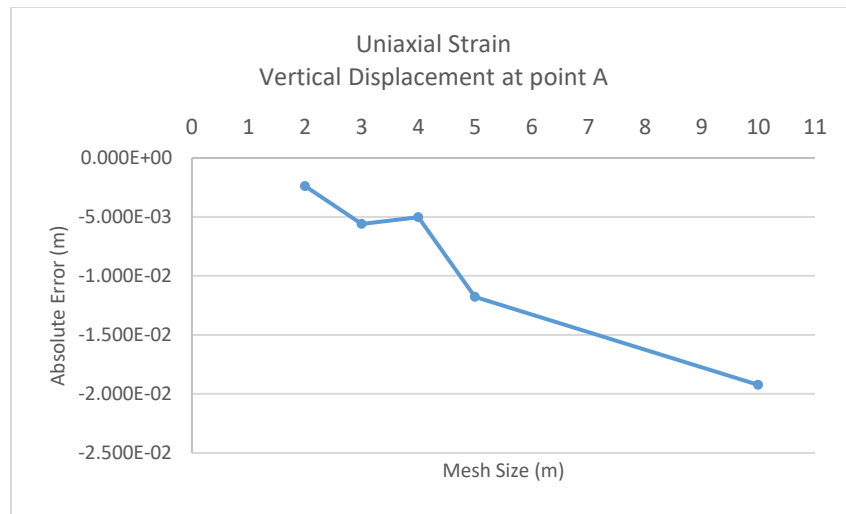
Figure 2.11. Absolute error of vertical displacement at point A versus mesh size in Uniaxial Strain case when the gravity is considered in computation

Chapter 3

3 Benchmarking modeling of hydro-mechanical effect of fluid flow in a fracture embedded in a rock matrix

Therefore, the decision was made to consider the well-known problem of fluid flow through a single fracture modeled by two parallel plates. In fact, the problem at this step aimed to numerically assess transient as well as steady-state fluid flow through a parallel-plate fracture. This flow generated by pressure gradient between two ends of the fracture and the results were then compared to the analytical values. After that, a uniform normal stress field was added to the problem in order to investigate the influence of the effective normal stress and normal stiffness of the fracture on deformation of the fracture and rock matrix as well as on the fluid flow results achieved in the first step.

3.1 Fluid flow through a rigid parallel plate fracture

This section aims to assess one dimensional fluid flow through a fracture intersecting a cubic block of homogeneous, impermeable, and rigid material. A pressure difference has been imposed to two ends of the fracture in x-direction. On the one hand, as the material is rigid, then the imposed fluid pressure gradient will not cause any deformation in the material. On the other hand, the fracture can be stiff enough to avoid normal displacement of that due to fluid pressure by defining a very large value of normal stiffness. Then, the analyses can merely be restricted to fluid flow through a fracture with a given aperture. Figure 3.1 is schematic illustration of the block, the fracture, initial and boundary conditions.
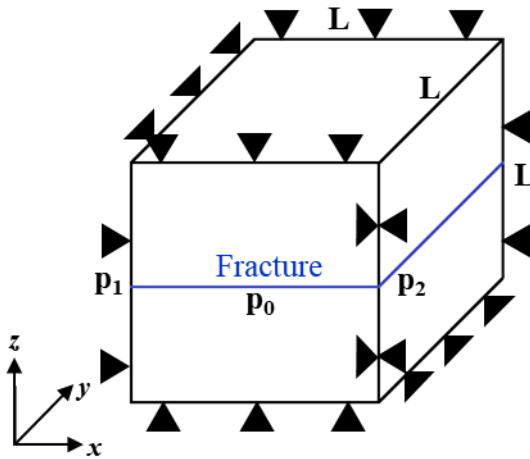
Figure 3.1. Schematic view of the block and the fracture in the middle of the block

The initial and boundary conditions for fluid flow in x-direction are as

Initial condition:

$$p(x, 0) = p_0 \quad for \quad 0 \leq x \leq L$$

Boundary conditions:

$$p(0,t) = p_1 \quad for \quad t > 0$$

$$p(L,t) = p_2 \quad for \quad t > 0$$

It should again be denoted that there is no flow in *y*-direction. The objectives are numerically assessing steady-state and transient fluid flow through parallel plate fracture and are also validating the numerical achievements with analytical results.

3.1.1   Governing Equations

The flow of a fluid in a fracture is governed by Navier-Stokes equation (Jaeger et al., 2007)

$$\frac{\partial}{\partial t} \boldsymbol{v} + (\nabla \boldsymbol{v})\boldsymbol{v} = -\frac{1}{\rho} \nabla p + \frac{\mu_d}{\rho} \nabla^2 \boldsymbol{v} + \boldsymbol{b} \qquad (3.1)$$

Where $\boldsymbol{v}$ is the velocity vector, $\boldsymbol{b}$ is body force per unit volume, ρ is fluid density, μ_d is fluid's dynamic viscosity, and p is the pressure. The first term on the left-hand side of equation (3.1) represents the acceleration of a fluid particle that is due to the fact that, at a fixed point in space, the velocity may vary with time. The second term is the advective acceleration term, which accounts for the fact that, even in steady-state flow, a given fluid particle may change its velocity (i.e., be accelerated) by virtue of moving to a position at which there is a different velocity (Zimmerman & Bodvarsson, 1996). The terms on the right-hand side represent the applied pressure gradient, the viscous forces, and the applied body force, respectively (Jaeger et al., 2007). The ratio between inertial forces and viscous forces also known as Reynold's number which is a dimensionless parameter and specifies the onset of turbulent flow (Cornet, 2015, pp. 159) and is defined as (Streeter et al., 1975)

$$Re = \frac{\rho VL}{\mu_d} \qquad (3.2)$$

where V is characteristic velocity and L is characteristic length, such as aperture of fracture, h. Iwai (1976) determined that the critical Reynolds number for a rock joint is 100, while Louis (1974) determined the critical number to be 2300.

Equation (3.1) represents a vector equation or three scalar equations for four unknowns including three velocity components and the pressure. Then, an additional equation which is conservation of mass or continuity equation is required to have four equations for four unknowns as

$$\frac{\partial \rho}{\partial t} + div(\rho \boldsymbol{v}) = 0 \qquad (3.3)$$

Steady-State Fluid Flow

In steady-state fluid flow, there is no dependence on time, then in conservation of mass equation, $\partial \rho / \partial t = 0$ and it can be concluded that $div (\rho \boldsymbol{v}) = 0$. On the other hand, for an incompressible fluid, which is reasonable assumption for fluids under typical subsurface conditions, the conservation of mass takes the form (Zimmerman and Bodvarsson, 1996) of

$$div \, \boldsymbol{v} = \nabla.\boldsymbol{v} = v_{x,x} + v_{y,y} + v_{z,z} = 0 \qquad (3.4)$$

Also, for the steady-state case since there is no dependence on time, the Navier-Stokes equation will be (Jaeger et al., 2007)

$$\mu_d \nabla^2 \boldsymbol{v} - \rho(\nabla \boldsymbol{v})\boldsymbol{v} = \nabla p \quad (3.5)$$

The relevant boundary condition for Navier-Stokes equation is "no slip" condition, meaning that at any boundary between fluid and solid, the velocity vector of the fluid should be equal to that of the solid. It specifies that for the fixed fracture walls (Poisseuille flow), both components of fluid velocity, either normal or tangential, must be equal to zero.

Parallel plate model such as figure 3.2 is the simplest form of a fracture for which the exact calculation of the link between velocity and pressure is possible (Zimmerman and Bodvarsson, 1996). Considering a steady (no time dependence) and laminar ($Re < 1$ or in sufficiently low velocities) flow of an incompressible fluid in *x*-direction (direction of the pressure gradient) and between two parallel and smooth plates implies that the solution does not depend on *y*-direction ($v_y = 0$).
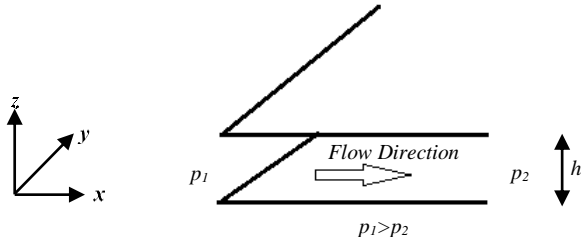
Figure 3.2. Steady-state fluid flow between two parallel plates

In this situation, equations (3.4) and (3.5) become

$$\mu_d\left(v_{x,xx} + v_{x,zz}\right) - \rho\left(v_{x,x}v_x + v_{x,z}v_z\right) = p_{,x} \quad (3.6)$$

$$\mu_d\left(v_{z,xx} + v_{z,zz}\right) - \rho\left(v_{z,x}v_x + v_{z,z}v_z\right) = p_{,z} \quad (3.7)$$

$$v_{x,x} + v_{z,z} = 0 \quad (3.8)$$

Since the fracture is assumed to be with uniform aperture of *h* and on the other hand, fractures show a very small aspect ratio (ratio of aperture to length of the fracture), then velocity component in *z*- direction will be zero, too ($v_z = 0$). Thereafter, from equation (3.8) it can be concluded that $v_{x,x} = 0$; meaning that the x-component of the velocity does not vary in x-direction and equations (3.6) and (3.7) will reduce to

$$\mu_d v_{x,zz} = p_{,x} \quad (3.9)$$

$$p_{,z} = 0 \quad (3.10)$$

One can find mathematical derivation of solution for equations (3.9) and (3.10) in Cornet (2015) for both Couette and Poisseuille flow. The final solution for Poisseuille flow (Cornet, 2015) is

$$v_x = -\frac{1}{2\mu_d}p_{,x}[(h/2)^2 - (z - h/2)^2] \quad (3.11)$$

Equation (3.11) reveals that the flow velocity exhibits a parabolic profile between the fracture walls. The total fluid flow in a fracture with width of *w* in *y*-direction, normal to the pressure gradient, can be determined by integrating the velocity as

30

$$Q = w \int_0^h v_x dz = -\frac{w}{2\mu_d} p_{,x} \int_0^h [(h/2)^2 - (z - h/2)^2] dz = -\frac{wh^3}{12\mu_d} p_{,x} \quad (3.12)$$

This equation is known as cubic law in which

$$T = \frac{wh^3}{12} \quad (3.13)$$

is known as Transmissivity. Recalling Darcy's law for flow in porous media, which in one dimension can be written as (Kranz et al., 1979)

$$Q = -\frac{kA}{\mu_d} p_{,x} \quad (3.14)$$

and comparing of that with equation (3.12) reveals that $h^2/12$ can be defined as permeability of the fracture. Q in Darcy's law is flow rate, k is permeability, and A is cross-sectional area through which fluid flows and is equal to wh.

Equation (3.12) is consistent with achievements of many researches such as Oron and Berkowitz (1998), Zimmerman and Yeo (2000), Skjetne et al. (1999) and Hasegawa and Izuchi (1983). They analyzed the relation between the volumetric flux and pressure gradient using various approaches and proved that this relation is approximately linear for Reynolds number less than about 10.

Zimmerman and Bodvarsson (1996) showed that if the flow is governed by the Stokes equation, even for fractures with variable aperture, the relation between volumetric flux and pressure gradient will be linear, as $Q = -(T/\mu_d)\nabla p$, homologous with equation (3.12). They reduced Navier-Stokes equation to Stokes equation by doing the order of magnitude analysis and taking some assumptions. Here, their approach is manipulated for a fracture with uniform aperture through which a laminar flow occurs.

Assuming that the advective acceleration terms in the Navier-Stokes equation is negligible compared to the viscous terms will yield the Navier-Stokes equation to the Stokes equation. If V is considered to be characteristic velocity like the mean velocity in the direction of the pressure gradient, since the in-plane velocity varies quasi-parabolically from zero at the upper and lower boundaries to some maximum value in the order of V in the interior, as concluded from equation (3.11), the magnitude of the viscous term can be estimated as

$$|\mu_d \nabla^2 \boldsymbol{v}| \approx |\mu_d v_{x,zz}| \approx \frac{\mu_d V}{h^2} \quad (3.15)$$

The order of magnitude of the advective acceleration term or inertia term can be determined as

$$|\rho(\nabla \boldsymbol{v})\boldsymbol{v}| \approx \frac{\rho V}{\Lambda} \quad (3.16)$$

where Λ is a characteristic dimension in the direction of the flow, which we assume that Λ is fracture length. Referring to the assumption that the inertia forces being negligible compared to the viscous forces will read

$$\frac{\rho V}{\Lambda} \ll \frac{\mu_d V}{h^2}, \quad \text{or} \quad Re^* \equiv \frac{\rho V h^2}{\mu_d \Lambda} \ll 1 \quad (3.17)$$

where Re^* is reduced Reynolds number being a product of the traditional Reynolds number, $\frac{\rho V h}{\mu_d}$, and the geometric parameter $\frac{h}{\Lambda}$. The $\frac{h}{\Lambda}$ identifies aspect ratio of the fracture which is always a very small value, then the condition (3.17) is satisfied and the Navier-Stokes equation reduces to the Stokes equation as

$$\mu_d \nabla^2 \boldsymbol{v} = \nabla p \quad (3.18)$$

or

$$v_{x,xx} + v_{x,yy} + v_{x,zz} = \frac{1}{\mu_d} p_{,x} \quad (3.19)$$

$$v_{y,xx} + v_{y,yy} + v_{y,zz} = \frac{1}{\mu_d} p_{,y} \quad (3.20)$$

$$v_{z,xx} + v_{z,yy} + v_{z,zz} = \frac{1}{\mu_d} p_{,z} \quad (3.21)$$

It can be seen, the Stokes equations are linear and more tractable than nonlinear Navier-Stokes equation. In current benchmarking modeling the flow is considered to be only in x-direction, then y component of the velocity will be zero. Additionally, very small aspect ratio also implies that velocity component in z-direction is negligible in comparison with x component of fluid; reducing Stokes equation to Reynolds lubrication equation according to Zimmerman and Bodvarsson (1996). The magnitude of the second derivatives in equation (3.19) can be estimated as

$$\left|v_{x,xx}\right| \approx \left|v_{x,yy}\right| = \frac{V}{\Lambda^2}, \quad \left|v_{x,zz}\right| = \frac{V}{h^2}, \quad (22)$$

If $(h/\Lambda)^2 \ll 1$, the derivatives within the plane (derivatives with respect to x and y) will be negligible compared to the derivative with respect to the z, and equation (3.19) can be replaced by

$$v_{x,zz} = \frac{1}{\mu_d} p_{,x} \quad (3.23)$$

Integration of this equation with respect to the z, with the previous knowledge of the no-slip boundary condition at the top and bottom walls of the fracture, $z=0$ and $z=h$, reads

$$v_x = \frac{1}{2\mu_d} p_{,x}(z^2 - zh) \quad (3.24)$$

This is essentially the same parabolic velocity profile as occurs for flow between parallel plates.

As $\nabla \cdot \boldsymbol{v} = 0$, therefore the integral of it with respect to z must be zero, too. If the velocity satisfies the no-slip boundary condition, the interchanging the order of the divergence and integration operations will show that the divergence of the z-integrated velocity or $\overline{\boldsymbol{v}}$, must also be zero. Then,

$$\frac{\partial h v_x}{\partial x} = 0, \quad \text{so} \quad \frac{\partial}{\partial x}\left[h^3 p_{,x}\right] = 0 \quad (3.25)$$

which is Reynolds lubrication equation.

Considering that fracture thickness or mechanical aperture (h) in fluid flow analysis through a parallel plate fracture may be equal to hydraulic aperture, h_H, then the transmissivity and flow rate per unit width of fracture can be given by:

$$T = \frac{wh_H^3}{12} \quad (3.26)$$

$$Q_w = \frac{Q}{w} = -\frac{h_H^3}{12\mu_d}p_{,x} \quad (3.27)$$

where Q_w is flow rate per unit width of the fracture ($m^3/s.m$).

Transient Fluid Flow

So far, the steady-state fluid flow, in which the time has not effect on variation of pressure and velocity, has been introduced. Now, governing equation for pressure evolution with time or transient flow in a porous medium will be explained. Generalization of the results to transient flow through a parallel plate fracture is straightforward.

As stated before, conservation of mass equation for fluid flow in a porous medium is

$$\frac{\partial \rho}{\partial t} + \nabla.(\rho \boldsymbol{v}) = 0 \quad (3.28)$$

By multiplying both terms in porosity, n, we have

$$\frac{\partial n\rho}{\partial t} + \nabla.(\rho n \boldsymbol{v}) = 0 \quad (3.29)$$

In a homogeneous medium, we know that

$$\boldsymbol{v} = \frac{q}{n} \quad (3.30)$$

where $\boldsymbol{q}$ is fluid flux vector. Then,

$$\frac{\partial n\rho}{\partial t} + \nabla.(\rho \boldsymbol{q}) = 0 \quad (3.31)$$

Using product rule, we will have

$$n\frac{\partial \rho}{\partial t} + \rho\frac{\partial n}{\partial t} + \rho\nabla.\boldsymbol{q} + \boldsymbol{q}.\nabla\rho = 0 \quad (3.32)$$

With the knowledge that the density and porosity are a function of the pressure (p), we can use chain rule and factoring out the $n\rho$ of first two terms in the left-hand side (LHS) of the equation (3.32), then it will read

$$n\rho\left[\frac{1}{\rho}\frac{\partial \rho}{\partial p}\frac{\partial p}{\partial t} + \frac{1}{n}\frac{\partial n}{\partial p}\frac{\partial p}{\partial t}\right] + \rho\nabla.\boldsymbol{q} + \frac{\partial \rho}{\partial p}\nabla p.\boldsymbol{q} = 0 \quad (3.33)$$

If the both sides are divided by ρ, and substituting fluid and rock compressibility as $c_f = \frac{1}{\rho}\frac{\partial \rho}{\partial p}$ and $c_r = \frac{1}{n}\frac{\partial n}{\partial p}$, then

$$n[c_f + c_r]\frac{\partial p}{\partial t} + \nabla.\boldsymbol{q} + c_f\nabla p.\boldsymbol{q} = 0 \quad (3.34)$$

33

The relation between fluid flux vector and pore pressure in any anisotropic porous medium by vector form of the Darcy's Law is (Bear, 1988) as

$$\boldsymbol{q} = -\frac{\boldsymbol{k}}{\mu_d}\boldsymbol{\nabla}(p - \rho\boldsymbol{g}.\boldsymbol{x}) \quad (3.35)$$

where $\boldsymbol{k}$ is permeability tensor, μ_d is dynamic viscosity of the fluid, and $\boldsymbol{g}$ is the gravity vector and assuming isotropic and homogeneous permeability beside the assumption of horizontal fluid flow (i.e., there is no gravitational effect on fluid flow) and the knowledge of $c_t = c_f + c_r$ in a fully saturated fluid-solid system (Jaeger et al. 2007), equation (3.34) will lead to

$$nc_t\frac{\partial p}{\partial t} - c_f\,\nabla p.\left(\frac{k}{\mu_d}\nabla p\right) - \nabla.\left(\frac{k}{\mu_d}\nabla p\right) = 0 \quad (3.36)$$

Some manipulations will read

$$\frac{\mu_d nc_t}{k}\frac{\partial p}{\partial t} - c_f\,\nabla p.\,(\nabla p) - \nabla.\,(\nabla p) = 0 \quad (3.37)$$

Assumption of negligible fluid compressibility compared to the rock compressibility (for example, as the compressibility of water is only $4.9e-10/\text{Pa}$ (Batchelor, 1967), a pressure change of 1 MPa will cause a change of 0.05% in density of the water (Zimmerman & Bodvarsson, 1996)) gives

$$\frac{\mu_d nc_t}{k}\frac{\partial p}{\partial t} - \nabla.\,(\nabla p) = 0 \quad (3.38)$$

or

$$\frac{\partial p}{\partial t} = \frac{k}{\mu_d nc_t}\nabla.\,(\nabla p) \quad (3.39)$$

which is pressure diffusion equation. For 1D problem in *x*-direction, the equation will be

$$\frac{\partial p}{\partial t} = Dp_{,xx} \quad (3.40)$$

In which

$$D = \frac{k}{\mu_d nc_t} \quad (3.41)$$

is hydraulic diffusivity (Jaeger et al. 2007). In current case with initial and boundary conditions explained at the beginning and by assuming rigid matrix ($c_r = 0$ then $c_t = c_f$) and porosity of 1 for the fracture and knowledge of that the permeability of a single fracture is $u_h^2/12$ the magnitude of hydraulic diffusivity for fractures will be

$$D = \frac{u_h^2}{12\mu_d c_f} \quad (3.42)$$

34

For 1-D fluid flow in which the initial pressure is p_0 (initial condition) and pressures at the beginning and end of the tube are respectively p_1 and p_2 (boundary conditions), the pressure evolution at any point of x in time t can be determined as explained below.

To facilitate solving the pressure diffusion equation, it is permissible to homogenize the boundary conditions by substituting $p(x,t)$ with $u(x,t)$ as

$$u(x,t) = p(x,t) - \left[p_1 + \frac{x}{L}(p_2 - p_1)\right] \quad (3.43)$$

Then, the equation (3.40) and its related initial and boundary conditions will change to

$$\frac{\partial u}{\partial t} = D\frac{\partial^2 u}{\partial x^2} \quad (3.44)$$

Initial Condition: $u(x,0) = p(x,0) - \left[p_1 + \frac{x}{L}(p_2 - p_1)\right] = p_0 - \left[p_1 + \frac{x}{L}(p_2 - p_1)\right] = f^*(x) \quad (3.45)$

$$\text{Boundary Conditions: } \begin{cases} u(0,t) = 0 \\ u(L,t) = 0 \end{cases}$$

As it is obvious, the boundary conditions are homogenized to be zero. Left-hand side of equation (3.44) is t derivation of function u and right-hand side of it is second degree x derivation of function u. These two derivatives will be equal to each other merely in a condition that both of them be a floating value such as λ. λ can be zero ($\lambda = 0$), or positive ($\lambda > 0$), or negative ($\lambda < 0$). Considering these three possibilities and solving equation (3.16), the general solution will be as below

$$u(x,t) = \begin{cases} (a_0 x + b_0) & for\ \lambda = 0 \\ (a_1 cosh\lambda x + b_1 sinh\lambda x)e^{D\lambda^2 t} & for\ \lambda > 0 \\ (a_2 cos\lambda x + b_2 sin\lambda x)e^{-D\lambda^2 t} & for\ \lambda < 0 \end{cases} \quad (3.46)$$

For homogeneous boundary conditions where in two points the $u(x,t)=0$, the third form of the equation (3.46) where λ is negative will be the solution of partial differential equation (PDE), because the other two possibilities only will have one zero point for any amount of x and t. Then, benefiting from separation of variables (Tsay and Weinbaum, 1991) will read

$$u(x,t) = F(x)G(t) \Rightarrow \begin{cases} F(x) = (a_2 cos\lambda x + b_2 sin\lambda x) \\ G(t) = e^{-D\lambda^2 t} \end{cases} \quad (3.47)$$

Let us to consider the boundary conditions

$$F(0) = 0 \Rightarrow a_2 \cos(0) + b_2 \sin(0) = 0 \Rightarrow a_2 = 0$$

$$F(L) = 0 \Rightarrow b_2 \sin(\lambda L) = 0 \Rightarrow \sin(\lambda L) = 0 \Rightarrow \lambda L = n\pi \Rightarrow \lambda = \frac{n\pi}{L} \quad (3.48)$$

By substituting above results in $F(x)$ of equation (3.47) we have

$$F(x) = b_2 sin\left(\frac{n\pi}{L}x\right) \quad (3.49)$$

35

Then, for $u(x,t)$ we can conclude that

$$u(x,t) = b_2 \sin\left(\frac{n\pi}{L}x\right)e^{-D\lambda^2 t} \quad (3.50)$$

or in general expression

$$u_n(x,t) = \sum_{n=1}^{\infty} b_n \sin\left(\frac{n\pi}{L}x\right)e^{-D\lambda^2 t} \quad (3.51)$$

Considering the initial condition, we will have

$$u_n(x,0) = \sum_{n=1}^{\infty} b_n \sin\left(\frac{n\pi}{L}x\right) = f^*(x) \quad (3.52)$$

In which b_n can be determined benefiting from Fourier series as

$$b_n = \frac{2}{L}\int_0^L f^*(x)\sin\left(\frac{n\pi}{L}x\right)dx \quad (3.53)$$

By substituting $f^*(x)$ from equation (3.18), above integration will be

$$b_n = \frac{2}{L}\int_0^L \left(p_0 - \left[p_1 + \frac{x}{L}(p_2 - p_1)\right]\right)\sin\left(\frac{n\pi}{L}x\right)dx \quad (3.54)$$

The solution of above integration will be

$$b_n = \frac{2}{L}\left[\frac{(p_2 - p_0)\cos(n\pi)}{n\pi/L} - \frac{(p_1 - p_0)\cos(0)}{n\pi/L}\right]$$

Doing some manipulations will read

$$b_n = \frac{-2}{n\pi}[(p_1 - p_0) - (p_2 - p_0)\cos(n\pi)]$$

In which magnitude of b_n depends on magnitude of $\cos(n\pi)$ as

$$b_n = \begin{cases} \dfrac{-2}{n\pi}(p_1 + p_2 - 2p_0) & for\ n = 1,3,5,\dots \\ \dfrac{-2}{n\pi}(p_1 - p_2) & for\ n = 2,4,6,\dots \end{cases}$$

Or, in cumulative form,

$$b_n = \frac{-2}{n\pi}(p_1 + (-1)^{1+n}p_2 + (-1 + (-1)^n)p_0) \quad for\ n \geq 1 \quad (3.55)$$

Substituting (3.55) in (3.51) yields to

$$u_n(x,t) = \sum_{n=1}^{\infty}\frac{-2}{n\pi}(p_1 + (-1)^{1+n}p_2 + (-1 + (-1)^n)p_0)\sin\left(\frac{n\pi}{L}x\right)e^{-D\lambda^2 t} \quad (3.56)$$

Then, $p(x,t)$ will be

36

$$p(x,t) = p_1 + \frac{(p_2 - p_1)x}{L} + \sum_{n=1}^{\infty} \frac{-2}{n\pi}(p_1 + (-1)^{1+n}p_2 + (-1 + (-1)^n)p_0)\sin\left(\frac{n\pi}{L}x\right)e^{-D\left(\frac{n\pi}{L}\right)^2 t} \quad (3.57)$$

The characteristic time is

$$t^* = \frac{L^2}{D} \quad (3.58)$$

When $t \gg t^*$, the pressure evolution is expected to obey the below equation

$$p(x) = p_1 + (p_2 - p_1)\frac{x}{L} \quad (3.59)$$

which is pressure gradient calculation solution in steady-state fluid flow. For $t < t^*$, the pressure evolution, can be calculated using equation (3.57).

3.1.2   Numerical Approach

In the 3DEC numerical approach, the flow domain is fully saturated (Itasca, 2016) and discretized into tetrahedral zones defined by four nodes as same discretizing method as mechanical and thermal calculations (Itasca, 2016). This flow domain is indicated by flow plane, which is major geometrical element of the flow model and always is a plane extended to the boundaries of the block (Itasca, 2016). The flow plane is a two dimensional surface in which flow is occurring through its thickness. Therefore, flow planes are planar polygons and are connected along the edges, which are straight-line segments called a flow pipe (Itasca, 2016). The geometric elements of the flow model are (Itasca, 2016):

1. Flow plane- a planar polygon corresponding to a face-to-face contact between solid blocks
2. Flow plane zone- a triangular discretization element of the flow plane
3. Flow plane vertex- vertex of a flow plane zone, generally corresponding to a sub-contact between solid blocks
4. Flow plane edge- a straight line that defines each segment on the periphery of a flow plane
5. Flow plane edge segment- a sub-segment of the flow plane edge
6. Flow pipe- the intersection between two or more flow planes
7. Flow pipe vertex- the vertex (end) of the flow pipe
8. Flow knot- the same as a flow plane vertex except along the flow plane intersects, in which case one flow knot corresponds to two or more co-locational flow plane vertices from the intersecting flow planes. The flow knot stores the fluid pressure; hence, the pore pressure is a nodal variable.

Figure 3.3 illustrates some of these structures. Figure 4 represents the hierarchical and adjacency relations between elements in the data structures in both directions. In this figure, hierarchical relations are shown with vertical solid arrows, adjacency relations are indicated by horizontal solid arrows and dashed arrows are pointers to the list (or loop) of the indicated elements (Itasca, 2016).
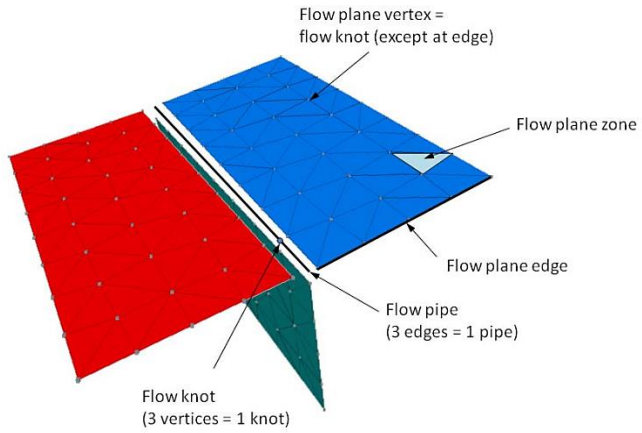
Figure 3.3. Flow structures for the intersection of three flow planes. The flow planes are actually connected but have been exploded for visualization (Itasca, 2016)
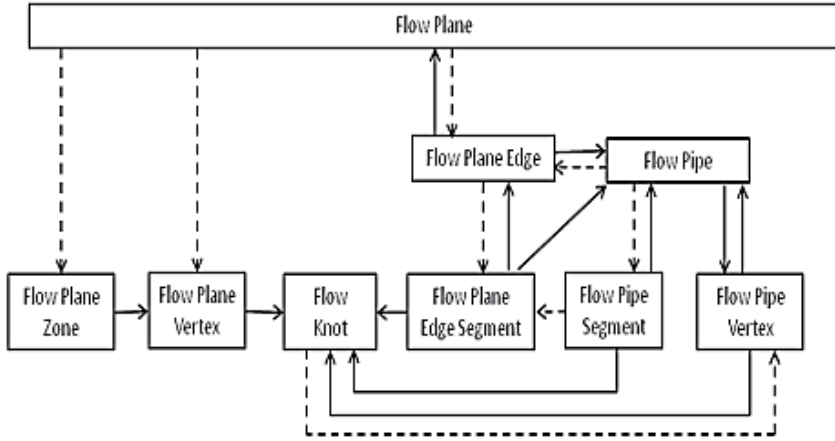
Figure 3.4. Links between data structure of the geometrical elements of the flow model (Itasca, 2016)

As it is shown in figure 3.4, once a pointer to a flow plane has been obtained, all other structures are accessible (Itasca, 2016). In this figure, a dashed arrow indicates that the higher structure contains a pointer to a linked list of the lower structure. For example, the flow plane contains a pointer to a linked list of flow plane zones. In addition, the solid arrows represent a pointer to a single instance of the corresponding object. For instance, a flow plane edge contains a pointer to its flow plane (Itasca, 2016). There are some important exceptions (Itasca, 2016) as

- Each flow plane points to the flow-plane edge list, which is a doubly linked list of flow-plane edges. The double-linked data structure allows traversal of the loop in the both directions. This is essentially an infinite loop in which the last element links to the first element.
- A flow pipe points to two flow pipe vertices indicating the ends of the pipe.
- A flow pipe segment points to two flow knots; one on each end of the segment.

It is worth to note that the link between fluid flow data structures and the solid model is made through relations between the flow plane and its corresponding face-to-face contact of the solid blocks and between the flow plane vertex and the corresponding sub-contact between the solid blocks (Itasca, 2016). At flow plane locations, one

flow-knot or flow plane vertex indicates two or more coincident gridpoints, so that the joint flow and matrix flow is connected (Itasca, 2016).

In 3DEC, the numerical scheme for fluid flow analysis relies on a finite difference nodal formulation of the continuity equation and the resulting ordinary differential equations will be solved using an explicit mode of discretization in time (Itasca, 2016).

Fluid flow through fractures in 3DEC, is governed by simplified Navier-Stokes equation; which is Reynolds lubrication equation for incompressible fluid through two parallel and impermeable surfaces (Itasca, 2016) as

$$\left(\frac{h^3}{12\mu_d}p_{,x}\right)_{,x} = 0 \quad (3.60)$$

This equation is valid only for laminar flow. From equation (3.60), fluid flow rate per unit width of the fracture may be determined (Itasca, 2016) as

$$Q_w = -\frac{h^3}{12\mu_d}p_{,x} \quad (3.61)$$

which is well-known cubic law. Note that in fractures introduced by two parallel plates, aperture of fracture is equal with hydraulic aperture; therefore, equation (3.61) will yield to equation (3.27).

As already mentioned, a fluid flow analysis may be transient or steady state. In 3DEC, the solution is always transient. If steady-state solution is desired, the transient solution will run until no change in pore pressures being observed, at which time it is assumed that the steady state has been achieved (Itasca, 2016).

The rate of pressure propagation in a saturated medium (in 3DEC the joints and rock matrix are assumed to be fully saturated) is dictated by the fluid diffusivity (Itasca, 2016)

$$c = \frac{k_H}{S_t} \quad (3.62)$$

in which k_H is hydraulic conductivity defined as $\rho g h_H^3 / 12\mu_d$, and S_t is the storage which may be obtained (Itasca, 2016) as

$$S_t = \rho g \left(\frac{c_f h_H}{s} + \frac{1}{K+4/3G}\right) \quad (3.63)$$

where s is spacing between fractures, G and K are shear and bulk moduli of the surrounding rock. If the rock is assumed rigid, then the second term in the parenthesis will be equal to zero (Itasca, 2016).

Pressures are calculated and stored in a data structure called flow-knot and are updated subsequent to flow rate calculations, considering the net flow into the flow-knot. Then, the new flow-knot pressure for uncoupled fluid flow (no mechanical effect is taken into account) will be (Itasca, 2016)

$$p = p_0 + \frac{Q}{c_f}\frac{\Delta t}{V} \quad (3.64)$$

where p_0 is the flow-knot pressure in the preceding time-step, Q is the sum of flow rates into the flow-knot from all surrounding contacts, Δt is time-step, and V is flow-knot volume which is constant in flow-only analysis (no

39

hydromechanical coupling) but can vary in hydromechanical analysis. For such case (i.e., hydromechanical coupling) a third term as $-\frac{1}{c_f}\frac{\Delta V}{V_m}$ will be added to the right-hand side of the equation (3.64) in which

$$\Delta V = V - V_0 \quad (3.65)$$

And

$$V_m = (V + V_0)/2 \quad (3.66)$$

Where V and V_0 are the new and old flow-knot volumes respectively. Therefore, equation (3.64) will take the form of (Itasca, 2016)

$$p = p_0 + \frac{Q}{c_f}\frac{\Delta t}{V} - \frac{1}{c_f}\frac{\Delta V}{V_m} \quad (3.67)$$

If the new pressure calculated from equation (3.67) is negative, then the pressure will be set to zero; meaning that the negative pore pressure cannot exist (Itasca, 2016).

3.1.3   Benchmarking

In present benchmarking modelling, fluid flow through a stiff fracture with aperture of 1 mm embedded in a rigid cubic block, which initially was dry ($p_0 = 0$ Pa in figure 3.1), was investigated. The side size of the block, L, and consequently length of the fracture was assumed to be equal to 10 m. To have a stiff fracture, its normal stiffness was set to 1e20 MPa/m. Initial fluid pressure in the fracture plane was zero ($p_0 = 0$ Pa in figure 3.1) and flow was generated by imposing differential fluid pressure of 1e3 Pa and zero ($p_1 = 1000$ Pa and $p_2 = 0$ Pa in figure 3.1), respectively, to left-hand side and right-hand side of the fracture in x-direction shown in figure 3.1. Fluid in this test was water with density of 1e3 Kg/m^3, dynamic viscosity of 1e-3 Pa.s, and bulk modulus of 2e9 Pa.

In 3DEC, governing equation for the fluid flow through fractures is Navier-Stokes equation simplified to Reynolds lubrication equation for incompressible fluid through two parallel and impermeable surfaces. This equation is valid only for laminar flow and from which fluid flow rate per unit width of the fracture may be determined by equation (3.27). Reynolds number for current test was determined equal to 12.5 using equation (3.2) by substitution of relevant parameters as $\rho = 1e3$ Kg/m^3, $L = h = 1e - 3$ m, $\mu_d = 1e - 3$ Pa. sec and $V = 1.25e - 2$ m/s calculated at the middle of the fracture aperture ($z=h/2$) using equation (3.11) with the knowledge that $p_{,x} = 1e2$ Pa/m. Hence, according to both Iwai (1976) and Louis (1974) determinations, the flow holds laminar condition. Therefore, Reynolds lubrication equation can be utilized to analyze fluid flow. Figure 3.5 illustrates numerical pressure profile along the fracture length compared with analytical counterparts determined from equation (3.57).
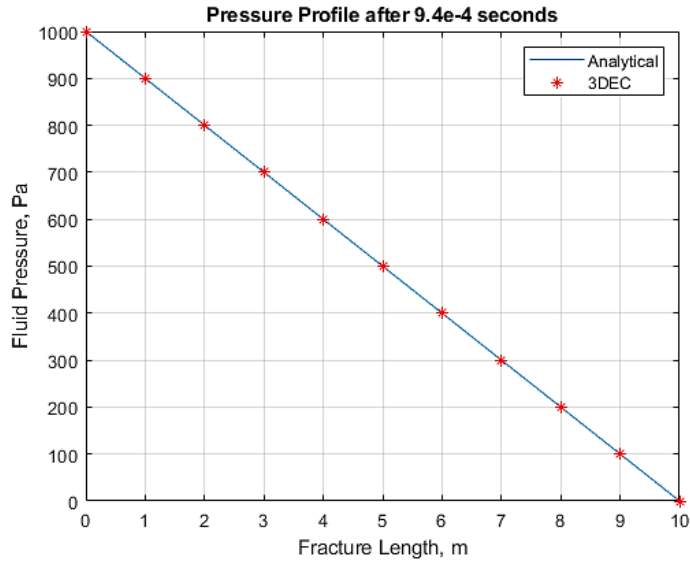
Figure 3.5. 3DEC and analytical fluid pressure profile along fracture length

Figure 3.6 shows 3DEC flow rate per unit width of fracture mainly equal to 8.3333e-6 m^2/sec, but ranging from 8.32208e-6 to 8.3632e-6 m^2/sec in some areas; showing good agreement with analytical value of 8.33e-6 m^2/sec achieved from equation (3.27).
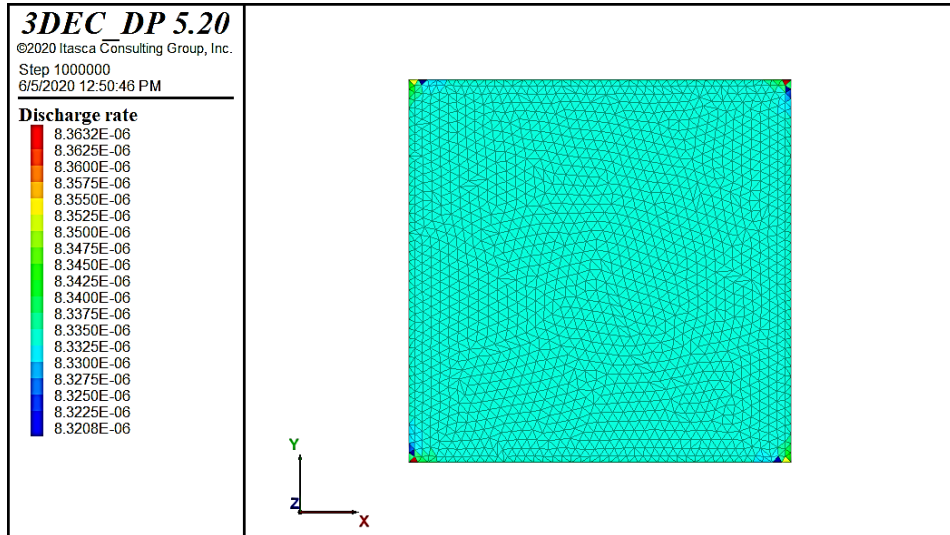
Figure 3.6. Flow rate per unit width of the fracture derived by 3DEC

To compare numerical transient flow solution to analytical one, fluid pressure profile along fracture length in various time values were extracted and plotted. In analytical transient solution of current problem, since $p_2 = p_0 = 0$, then p_0 was replaced by p_2 and factoring out of $(p_2 - p_1)$ in second and third terms in right-hand side of equation (3.57) read

$$p(x,t) = p_1 + (p_2 - p_1)\left[\frac{x}{L} + \frac{2}{\pi}\sum_{n=1}^{\infty}\frac{1}{n}sin\left(\frac{n\pi}{L}x\right)e^{-D\left(\frac{n\pi}{L}\right)^2 t}\right] \quad (3.68)$$

Calculating hydraulic diffusivity of $D=0.167e6$ m^2/sec from equation (3.42), and substituting values of fluid pressure and fracture length in equation (3.68) yielded to

$$p(x,t) = 1000 - 1000 \left[\frac{x}{10} + \frac{2}{\pi} \sum_{n=1}^{\infty} \frac{1}{n} sin\left(\frac{n\pi}{10}x\right) e^{-0.167e6\left(\frac{n\pi}{10}\right)^2 t} \right]$$

Figure 3.7 illustrates numerical and analytical results of fracture fluid pressure evolution in time through fracture length. It may be approximated from figure 3.6 that in both numerical and analytical solutions the flow approaches steady state at 6e-4 seconds which is consistent with characteristic time of 6e-4 seconds determined from equation (3.58) for present test; however, it is worth mentioning that in figure 3.6 the flow numerically reaches to steady-state in 0.94 milliseconds compared to 1.106 milliseconds of analytical solution.

Accuracy of 3DEC results is, to some extent, dependent of mesh size; the smaller the mesh size the higher the density of zones in the block. The user should be careful not to create zones that have a high aspect ratio; a practical limit on aspect ratio is approximately 1:5 for reasonable solution accuracy (Itasca, 2016).

To compare agreement of 3DEC results and analytical values against discretization size, the Sum of Squared Error (SSE) method was utilized. In this method, the sum of square of difference between analytical and numerical pressure values at each point through the fracture length (x=1, 2, 3… 10; for $L=10$ m) were calculated as

$$SSE = \Sigma\left(P_a(x,t) - P_n(x,t)\right)^2 \quad (3.69)$$

where subscripts a and n represents, respectively, analytical and numerical pressure values in time. Figure 3.8 illustrates how magnitude of SSE drastically decreases versus the decrease of discretization size from 1 meter to 0.25 meter.

Discrepancy of 3DEC results from analytical values may also be caused by the size of fluid timestep. Fluid timestep in 3DEC is calculated automatically; however a maximum limit can directly be introduced by the user, but it cannot exceed the critical timestep which is equal to minimum value of the fluid timestep over all flow-knots in the analysis (Itasca, 2016) as

$$\Delta t_f = min\left[\frac{c_f V}{\Sigma_i k_i}\right] \quad (3.70)$$

where the summation of the permeability factors, k_i, is extended to all contacts surrounding the flow-knot. The minimum value of Δt_f over all flow-knots is the critical timestep in the analysis. From equation (3.70) it can be concluded that fluid timestep is function of the fluid bulk modulus and an inverse function of the joint transmissivity. Joint transmissivity is proportional to the hydraulic aperture cubed as introduced by equation (3.26). Hence, any change in hydraulic aperture and consequently in hydraulic diffusivity will cause reverse effect on fluid timestep. Therefore, keeping the length of the fracture constant and changing the hydraulic aperture from 2 mm to 0.5 micrometer will provide a possibility to assess the influence of hydraulic diffusivity (or hydraulic aperture) and corresponding fluid timestep on accuracy of the numerical calculations. Table 3.1 summarizes fluid flow characteristic parameters for various hydraulic apertures. As it can be seen from table 3.1, fluid flow in all fracture geometry combinations falls into the laminar flow regime, and any decrease in hydraulic aperture also causes an increase in the 3DEC fluid timestep, accompanied by an increase in the analytical characteristic time obtained from equation (3.58).
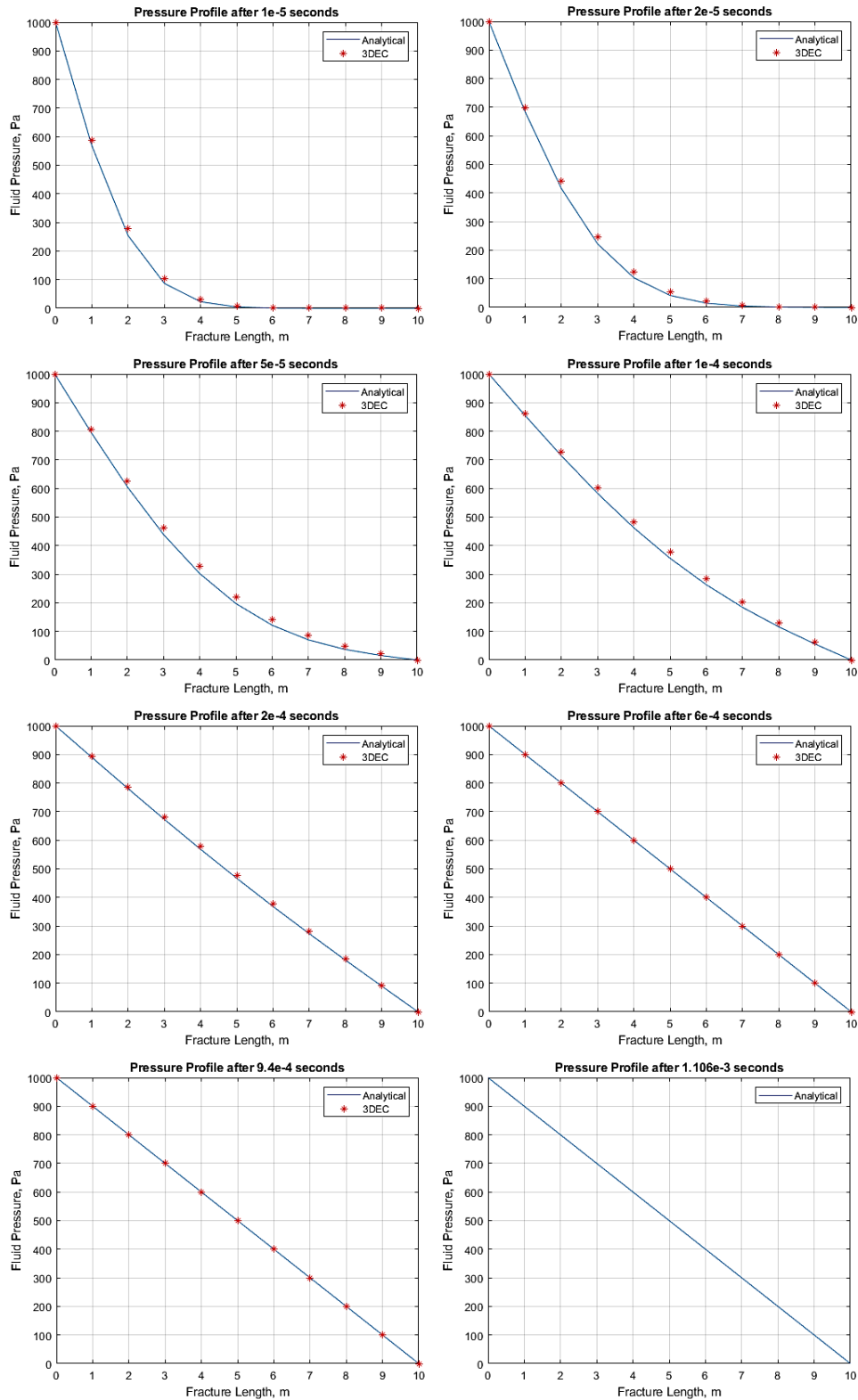
Figure 3.7. Numerical and analytical fluid pressure evolution in time along the fracture length of 10 m (hydraulic aperture of 1 mm, numerical discretization size of 0.25 m)
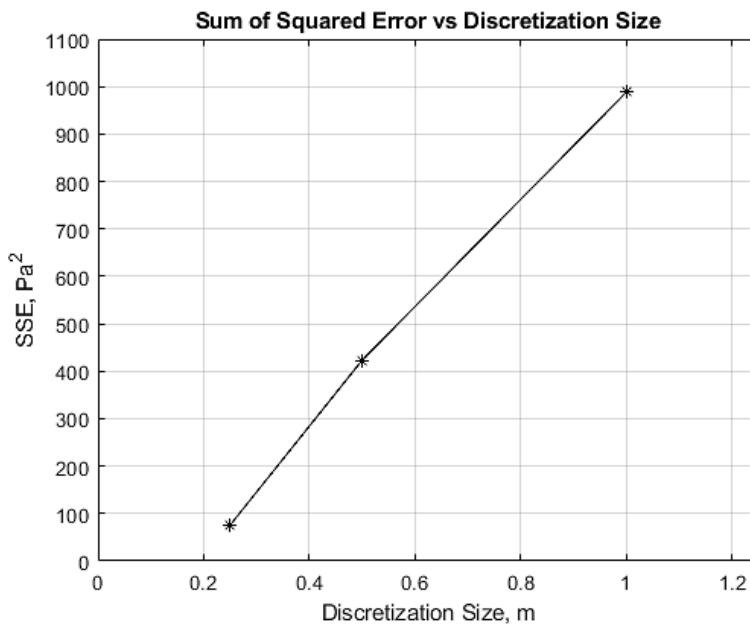
Figure 3.8. Sum of Squared Error of 3DEC results for different discretization sizes

Table 3.1. Fluid flow characteristic parameters for various hydraulic apertures

Fracture Length (m)	Hydraulic Aperture (m)	Hydraulic Diffusivity (m²/s)	Reynolds No.	Characteristic Time (s)	3DEC Timestep (s)
10	2.00E-03	6.67E+05	1.00E+01	1.50E-04	5.30E-08
10	1.00E-03	1.67E+05	1.25E+00	6.00E-04	2.10E-07
10	1.00E-04	1.67E+03	1.25E-03	6.00E-02	2.10E-04
10	1.00E-05	1.67E+01	1.25E-06	6.00E+00	1.76E-02
10	1.00E-06	1.67E-01	1.25E-09	6.00E+02	1.71E+00
10	5.00E-07	4.17E-02	1.56E-10	2.40E+03	8.43E-01

Figure 3.9 also shows the magnitude of SSE against various hydraulic diffusivities that shows a general trend in decrease of SSE against decrease of hydraulic diffusivity.
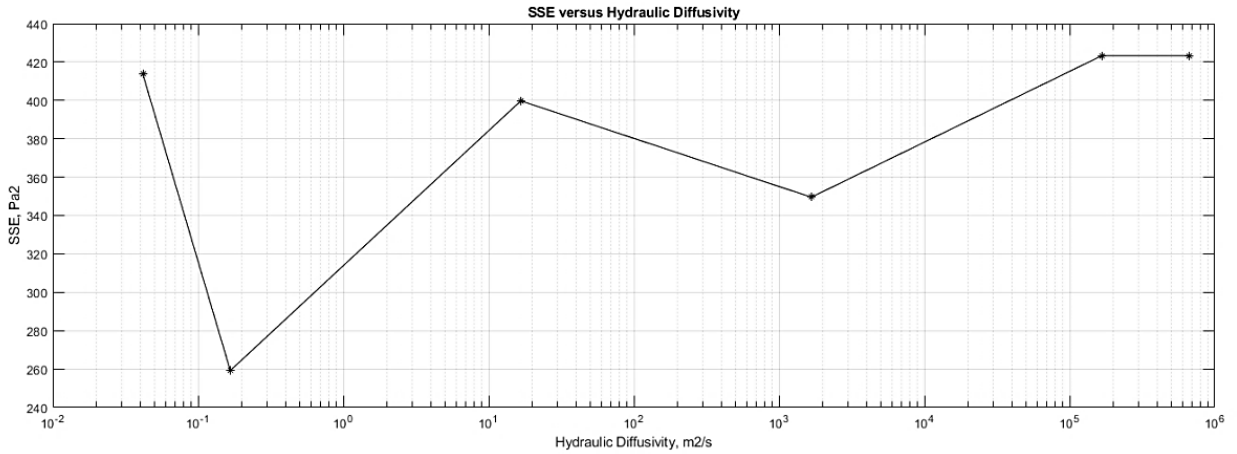
Figure 3.9. Sum of Squared Error for 3DEC model against hydraulic diffusivity of the fracture

3.2   Effects of normal stress on fluid flow through parallel plate fractures

In section 3.1, the fluid flow occurred through a parallel plate fracture dividing a rigid block into upper and lower halves in the z-direction in which, there was no imposed stress boundary condition. In other words, there was not any hydro-mechanical coupling in the fluid flow process throughout the fracture. In this section, the block was first loaded by a normal, uniform, compressive stress on top side of the block, while there was no displacement in remaining five sides (figure 3.10). This loading was compensated with some displacement in the rock matrix and fracture until reaching an equilibrium state. After that, a fluid pressure gradient was imposed into two ends of the fracture in X-direction to assess the interaction of the applied normal load and fluid pressure on each other or hydro-mechanical coupling in the other word.
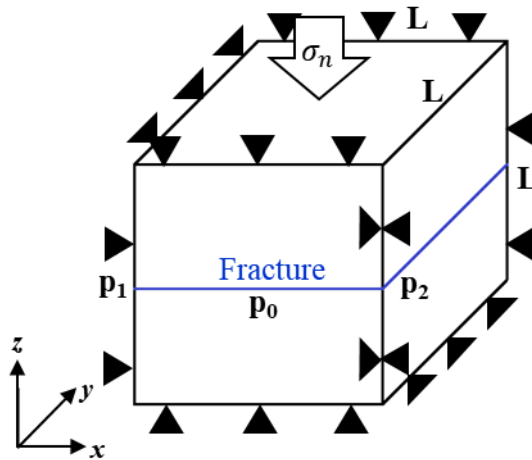
Figure 3.10. Schematic view of boundary conditions imposed to the fractured block

3.2.1   Dry Fracture Condition

If the abovementioned block was loaded perpendicular to the fracture wall (σ_n), a displacement between top and bottom of the block will occur. It will contain two contributions: the deformation of the intact rock (dH_r) and deformation of the fracture (joint closure, $d\delta$) (Goodman, 1976). The magnitudes of these two deformations not

45

only depends on Young's modulus of the intact rock (E_r) and normal stiffness of the fracture (K_n), but also on the magnitude of the normal stress (σ_n). Therefore, the total deformation between top and bottom of a block with height of H, (dH), will be (Jaeger et al., 2007)

$$dH = dH_r + d\delta = -\frac{H}{E_r}d\sigma_n - \frac{1}{K_n}d\sigma_n \quad (3.71)$$

From the right side of equation (3.71), the deformation of the intact rock, dH_r, is explained in detail in the second chapter through three scenarios of uniaxial stress, uniaxial strain, and triaxial stresses. For the current set up of the model, which is uniaxial strain, dH_r can be determined numerically and analytically using equations (2.4) and (2.29) of the aforementioned chapter, respectively. These equations, with some revision, for numerical case is

$$dH_r^n = dH_r^i n_i \quad (3.72)$$

where dH_r^i is increment of relative displacement at the sub-contacts for both rigid and deformable blocks, dH_r^n is normal component of dH_r^i, and n_i is unit normal vector in sub-contact; and for analytical case is

$$dH_r = -\int_0^H \left[\frac{\sigma_n}{E} - \frac{2\vartheta}{E}\sigma_l\right] dh \quad (3.73)$$

in which dh is incremental length of the block height, ϑ is Poisson's ratio and σ_l is the lateral stress which can be determined as (Cornet, 2015)

$$\sigma_l = \frac{\vartheta}{1-\vartheta}\sigma_n \quad (3.74)$$

Deformation of fracture or joint closure, $d\delta$, which depends on magnitude of normal stiffness of the fracture will be explained in the following.

In 3DEC, normal stiffness of a fracture is constant value defined by the user (Itasca, 2016); meaning the existence of a linear relation between normal stress and joint displacement (Hart, 1993) as

$$\sigma_n = K_n d\delta \quad (3.75)$$

It has been experimentally proved that the relation between normal stress and displacement in fractures is not linear, but nonlinear. Various measurements of joint closure as a function of normal stress on dry samples in which a fracture was artificially created were done by Goodman (1976). These measurements were carried out first on intact sample and then on the same sample after inducing of an artificial fracture. Joint closure measurement was performed on both mated (intact fracture surface) and unmated (the two surfaces of the fracture are displaced relative to each other) joints. Joint closure in unmated fractures were greater than that in mated fractures due to the fact that the pore space in the former is more than that in the latter (Cornet, 2015), showing lower joint stiffness for unmated fractures (Goodman, 1976). Figure 11 illustrates measurements of Goodman performed on joint closure which reveals that the joint closure is highly nonlinear function of stress and levels off to some asymptotic value at high magnitudes of the confining stress (Jaeger et al., 2007).
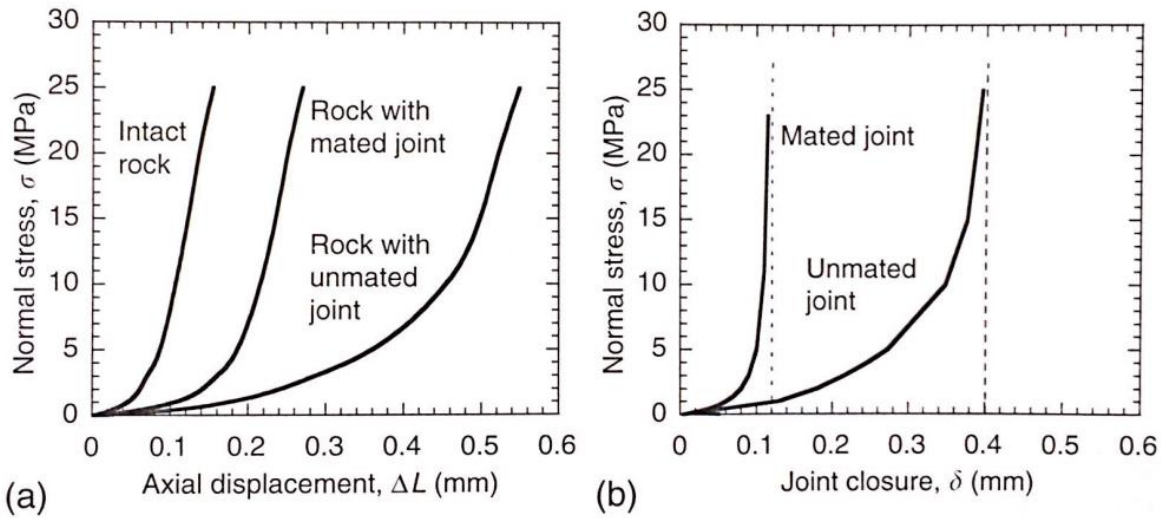
Figure 3.11: measurements made by Goodman (1976) of joint closure on a granodiorite specimen: (a) axial displacement of intact rock, sample with mated joint, and sample with unmated joint; (b) joint closure, determined from subtracting displacement of intact core from displacement of jointed specimen (Jaeger et al., 2007)

In present benchmarking test, to evaluate the accuracy of the 3DEC results compared to the analytical values, it was assumed that the relation between normal stress and normal displacement of the fracture in analytical solution is linear and governed by equation (3.75).

Assuming the block side size of 10 m, fracture's initial aperture of 1 mm, Young's modulus and Poisson's ratio for rock matrix of respectively 25 GPa and 0.3, and finally normal stiffness of the fracture equal to 10 GPa/m, we can analytically use equation (3.73) for calculating displacement of the rock matrix (lower and upper halves of the block) and equation (3.75) for determination of fracture normal displacement. So that, vertical displacement profile through the block height caused by a normal uniform stress of 1 MPa can be determined by summation of results of equations (3.73) and (3.75) using equation (3.71) and can be shown in figure 3.12 which compares displacement profiles of both numerical and analytical solutions. As it is obvious in the middle of the block height (h=5 m) in figure 3.12, the plateau section from about -1.5e-4 m to about -2.5e-4 m indicates closure of the fracture equal to -1e-4 m determined from equation (3.75) when substituting values of normal stress and normal stiffness of the fracture (minus sign serves for displacement in negative directions of system of coordinates).
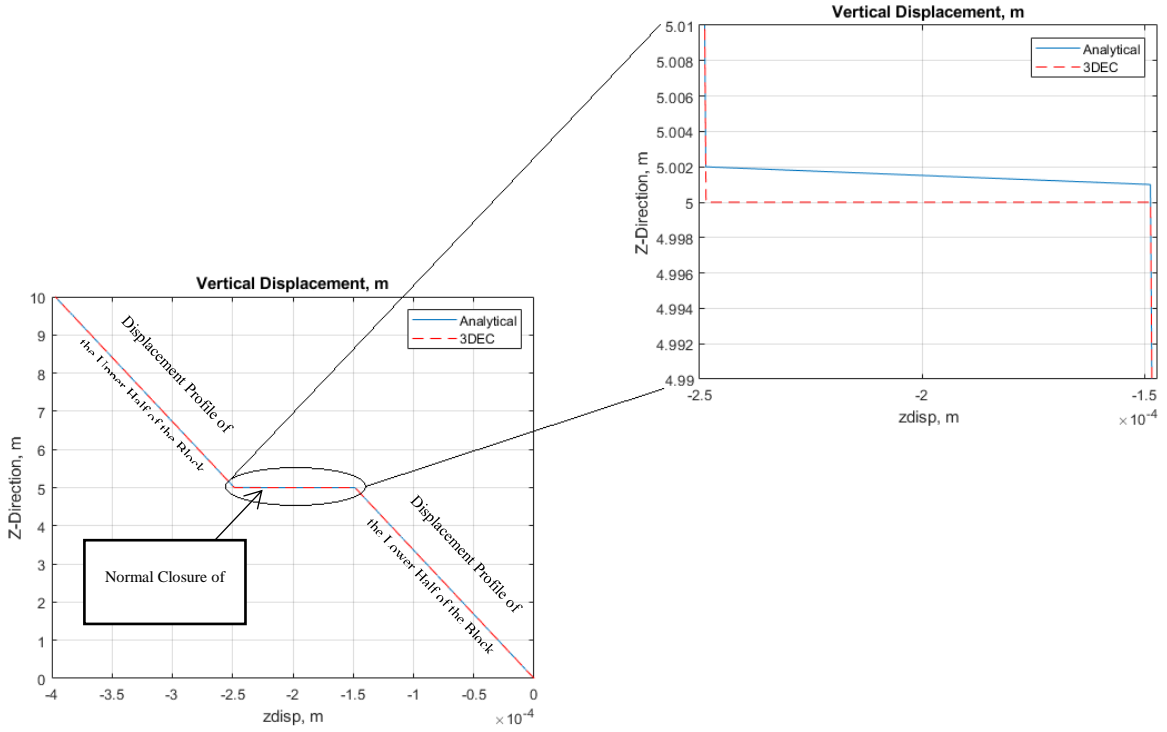
Figure 3.12. Numerical and analytical vertical displacement profile in the block; Zoomed section illustrates vertical displacement in the fracture determined numerically and analytically

3.2.2 Special Cases

To have some more investigations on influence of normal stiffness of the fracture on displacement, it was desired to calculate such values of normal stiffness of the fracture in order, first, the effect of fracture closure was eliminated on total displacement values in the block and second, the closure of the fracture is 1000 times of the first case. To realize the first case, the normal stiffness of the fracture must be equal to stiffness of the rock sample under current boundary conditions. The normal stiffness of the fracture is K_n. Normal stiffness of the rock in present boundary conditions can be obtained as

$$K_r = \frac{\sigma_n}{u_z} \quad (3.76)$$

From equations (3.73) we have

$$u_z = \frac{\sigma_n}{E} - \frac{2\vartheta}{E}\sigma_l h \quad (3.77)$$

where u_z is vertical displacement and h is height. Considering that $\sigma_l = \frac{\vartheta}{1-\vartheta}\sigma_n$ from equation (3.74) and substituting it in (3.74) and doing some simplification and manipulation, magnitude of rock stiffness will be

$$K_r = \frac{1}{E}\left(1 - \frac{2\vartheta^2}{1-\vartheta}\right)h \quad (3.78)$$

Hence the normal stiffness of the fracture must be equal with equation (3.78) in order to eliminate its effect on overall displacement of the block. Substituting values of E (25 GPa) and ϑ (0.3) of rock matrix at l=0.001 m length

48

(initial aperture of the fracture in zero stress condition is 0.001 m) yielded to 33.654e12 MPa/m of normal stiffness for fracture. Now, using equation (3.72), displacement of a fracture with above stiffness under normal stress of 1e6 Pa will be 2.9714e-8 m which is equal with deformation of a length of 0.001 m (l=0.001 m) using equation (3.77) (2.9714e-8 m). Figure 3.13 shows the comparison of vertical displacement in the block for both fractured and intact rock. Looking at figure 3.13 reveals that increasing fracture's normal stiffness to that of rock matrix produces approximately the same displacement magnitudes as the intact block.
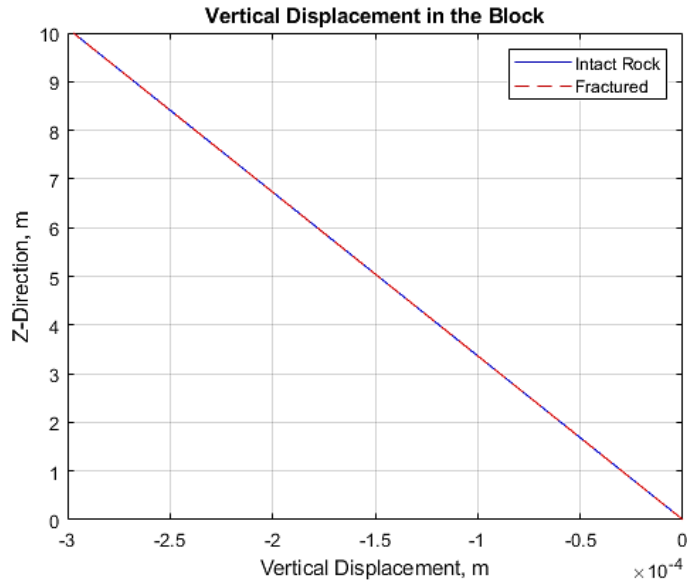
Figure 3.13. 3DEC vertical displacement in some point of the block height for both fractured and not-fractured block; it can be seen that embedding a fracture with stiffness equal to the stiffness of the rock matrix in the block can approximately equalize the magnitudes of the displacement to those of not-fractured block

Comparing displacement profile shown in the figures 3.12 and 3.13 reveals the impact of the normal stiffness of the fracture on the elastic behavior of the model. A block with a fracture as stiff as surrounding rock matrix has no effect on the cumulative displacement of the block while a less stiff fracture will influence the overall as equal as closure of itself as can be seen in figure 3.12.

To have a fracture stiffness so as to obtain a normal displacement in the fracture as large as 1000 times of first case, utilizing equation (3.75) resulted in 3.365e10 MPa/m. Applying this value on fracture embedded in the rock matrix of the model in 3DEC yielded to 9.7028e-4 m of hydraulic aperture or, in other words, normal closure of 0.2972e-4 m for the fracture. Analytical solution (equation 3.75) generated 0.29717e-4 m for normal closure of the fracture.

3.2.3 Imposing Fracture Fluid Pressure

The effect of changes in the fluid pressure of the fracture or in the applied stress has led to the use of the concept of effective stress, which provided a convenient means for treating the many different combinations of pore pressure and confining stress (Walsh, 1981). This type of problem is actually a hydromechanical coupling problem, where the pore pressure change affects the mechanical deformation, and the mechanical deformation affects the pore pressure (Itasca, 2016). When the fracture is filled with the fluid, depending on the fluid pressure and applied

normal stress, the fracture's normal deformation will be influenced. According to Walsh (1981), the effect of pore pressure and applied normal stress on normal deformation can be expressed as

$$\sigma_n' = \sigma_n - sp_p \quad (3.79)$$

in which p_p is pore pressure and s is effective stress coefficient or Biot coefficient. Based on measurements of flow through simulated fractures carried out by Kranz et al. (1979), s can vary between 0.5 and 1.0 for tensile fractures with rough surfaces and fractures with smooth surfaces, respectively. For smooth fracture surfaces of current study, s was considered to be unity, so that, Biot's effective stress becomes equivalent to Terzaghi's effective stress (Cornet, 2015).

For a slightly compressible fluid in a deformable rock fracture with uniform aperture, the continuity equation has the form of (Itasca, 2016)

$$q_{i,i} = -\frac{\delta h}{\delta t} - c_f h \frac{\delta p}{\delta t} \quad (3.80)$$

Combining equation (3.61) and (3.80), we can obtain

$$\frac{\delta p}{\delta t} = \frac{h^2}{12\mu_d c_f} p_{i,i} - \frac{1}{c_f h} \frac{\delta h}{\delta t} \quad (3.81)$$

Equation (3.81) is the diffusion equation for the pressure inside the fracture (Itasca, 2016). Generally, the fracture aperture not only varies with local fracture stiffness and fluid pressure, but it is also a function of the mechanical response of rock mass. Hence, the second term in the right-hand side of the equation (3.81) is determined by coupling between fluid flow and mechanical deformation of the rock mass. In the other words, this term is external or a "source" which, for undrained condition, indicates the pressure change in the fluid trapped within the fracture because of rock mass and rock fracture deformation (Itasca, 2016).

In 3DEC, the relation between hydraulic aperture and effective stress is a bilinear curve shown in figure 3.14. The hydraulic aperture is obtained, in general, (Itasca, 2016) as

$$h_H = h_{H0} + d\delta \quad (3.82)$$

where h_{H0} is the joint aperture at zero normal stress which is defined by the user. In addition to h_{H0}, residual (h_{Hres}) and maximum (h_{Hmax}) hydraulic apertures should also be defined by the user. Below residual hydraulic aperture and above maximum hydraulic aperture the mechanical aperture (h_m) will not have any effect on contact permeability. Therefore, in 3DEC, the hydraulic aperture is always equal with mechanical aperture except when the mechanical aperture exceeds h_{Hmax} or h_{Hres} (Itasca, 2016).
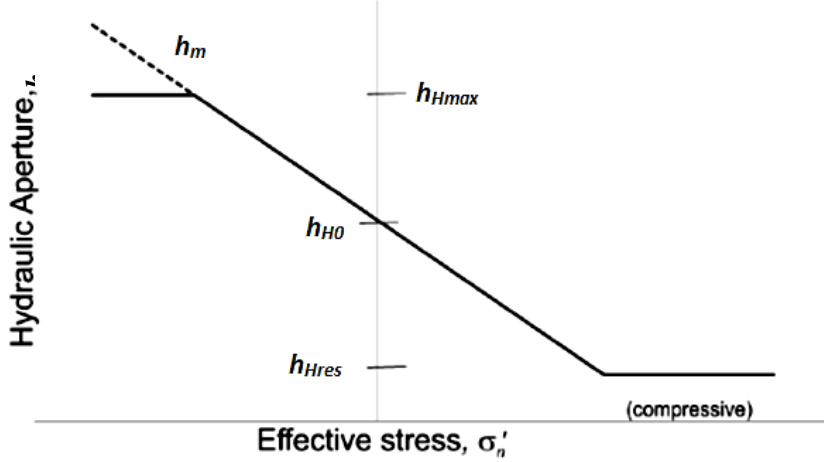
Figure 3.14. Idealized relation between hydraulic aperture and effective normal stress for a rock joint (Itasca, 2016)

Equation (3.79) reveals that when the fracture is dry ($p_p = 0$ Pa), the effective normal stress acting on the rock matrix and fracture is equal with applied normal stress, but existence of fluid pressure in fracture generated by fluid flow through the fracture results in decrease of effective normal stress compared to dry situation. This fluid pressure and consequent decrease of effective normal stress (according to equation 3.79) increases mechanical aperture of the fracture (Trimmer et al., 1980). Figure 3.15 illustrates 3DEC results of hydraulic aperture due to imposing fluid pressure of 1.1 MPa to one side of fracture in x-direction ($p_1 = 1.1$ MPa and $p_2 = 0$ Pa). The h_{Hmax} and h_{Hres} values are assigned 2e-3 and 1e-4 meters, respectively. The results shown in figure 3.15 are related to steady-state fluid flow. It can be seen in figure 3.15 that hydraulic aperture values along the fracture length are showing larger magnitudes in comparison to 0.9 mm obtained in section 2.1.
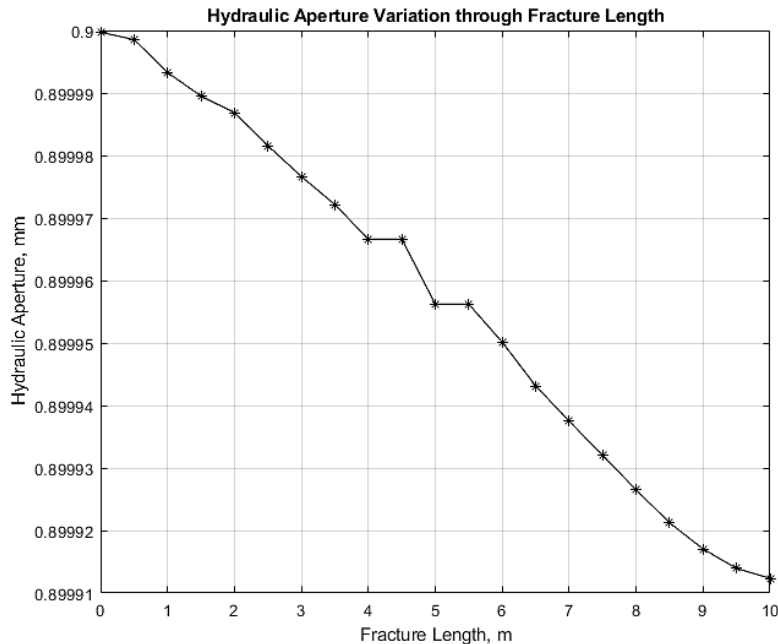
Figure 3.15. 3DEC hydraulic aperture along fracture length for inlet fluid pressure of 1.1 MPa

Figure 3.16 and 3.17 illustrate numerical magnitudes of respectively hydraulic aperture of the fracture and effective normal stress for various values of inlet fluid pressure ranging from 1.1 MPa to 1.4 MPa.
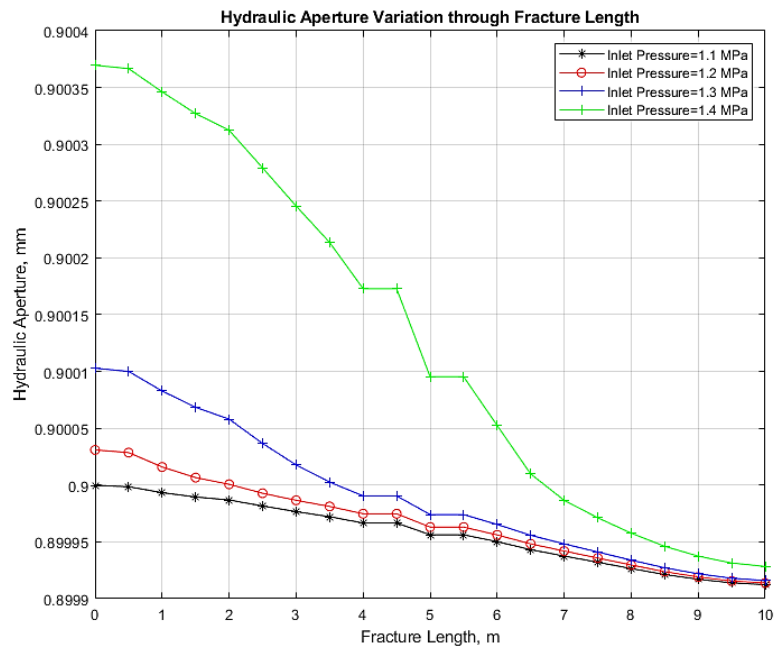
Figure 3.16. Numerical hydraulic aperture of the fracture for various magnitudes of inlet fluid pressure
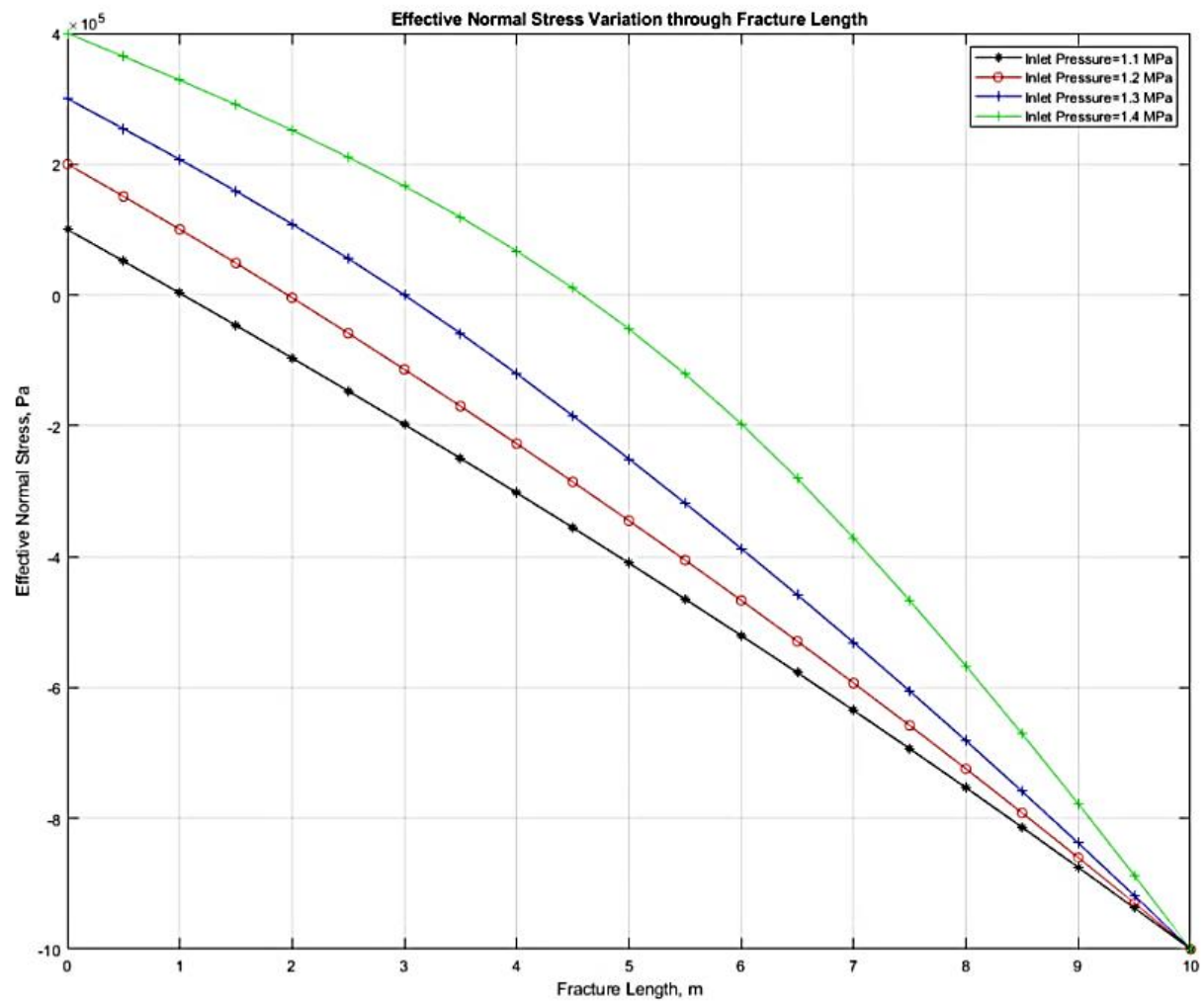
Figure 3.17. Numerical effective normal stress profile throughout the fracture length for various inlet fluid pressures

Chapter 4

4   3DEC Modeling of Large-Scale Fluid Injection into a Kilometer-Scale Fault

4.1   Introduction

This section aims to simulate the year 2000 stimulation of well GPK2 at Soultz-sous-Forêts geothermal reservoir. It was a 6-day operation of 23,400 m^3 water injection into open-hole section of the well at depth of 4400 to 5050 meters (Weidler et al., 2002). This injection, as shown in figure 4.1a, was performed in three steps starting from 30 ls^{-1} injection rate for 24 hours, continuing by 27 hours of injection with flow rate of 40 ls^{-1} and finally ceasing after 90 hours of fluid injection with 50 ls^{-1} of injection rate (Weidler et al., 2002). It can be seen on figure 4.1a that the well-head pressure (WHP) after a sudden rise to approximately 10 MPa at the beginning of the operation followed almost an identical pattern at first and second steps of stimulation, a fairly quick build-up to about 12 MPa and then gradual decrease to 11 MPa, but at the third step, the pressure first quickly increased to 12.2 MPa and its increase gradually continued to a maximum pressure of 13 MPa at the end of stimulation (Weidler et al., 2002). After shut-in, the WHP dramatically dropped by 4 MPa and then gradually and continuously declined in the next days but did not reach to a constant pressure magnitude after one week, implying a less permeable far-field medium where the enhanced fluid pressure could not be released in short periods (Weidler et al., 2002).
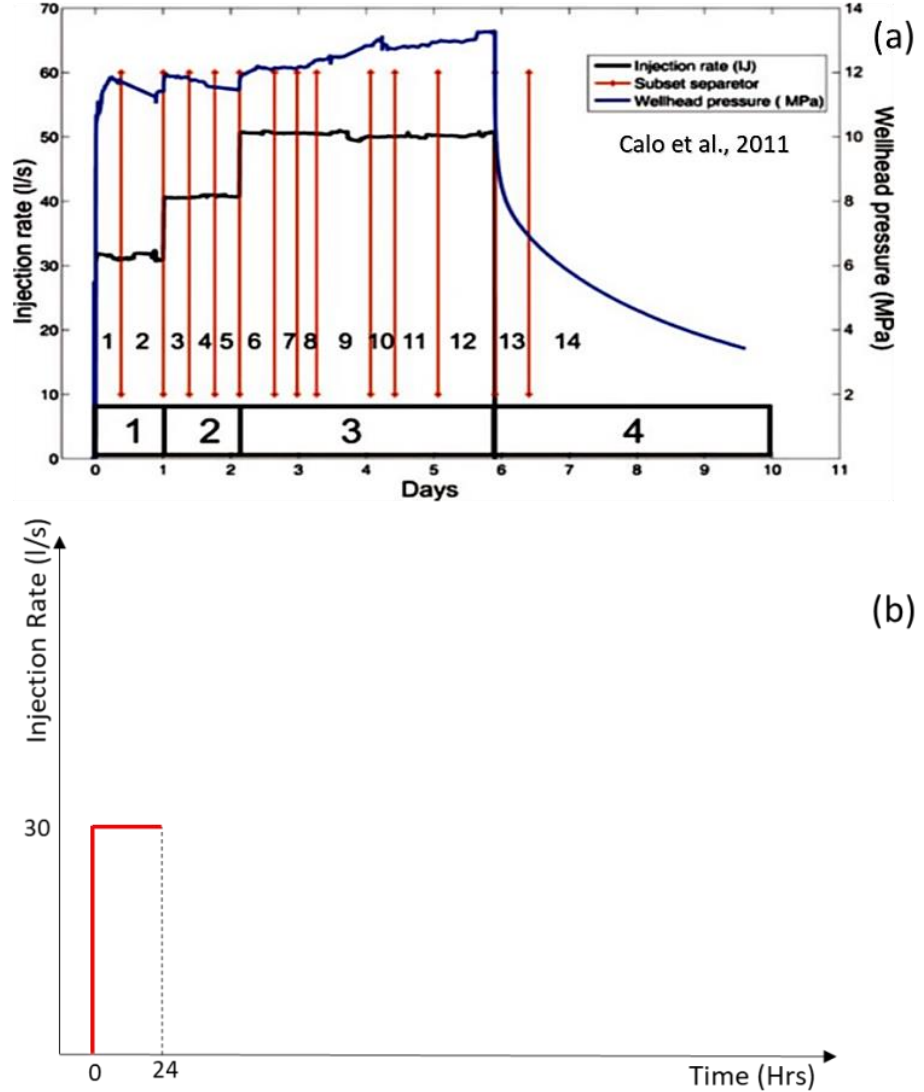
Figure 4.1. The year 2000 GPK2 stimulation Procedure (a) (Calo et al., 2011); Injection procedure numerically modeled at this study (b)

Based on the results achieved from flow logs, Weidler et al., 2002, expressed that the main flows exit during the first injection step, were localized at 4440 m (at the casing shoe), at 4760 m, at 4890 m and below 4950 m (all logging depths). They mention that the last flow loss zone (below 4950 m) was not detected by cutting analyses, but it was remarkable on temperature log, while Dezayes et al., 2010, stated that this zone could correspond to a fracture zone at 5060 m, based on cutting observations. Sausse et al., 2010, also made the same observations as Weidler et al., 2002, stating that at the open hole section of well GPK2 there are three main fractures of GPK2-FZ4760, GPK2-FZ4890, and GPK2-FZ5060 derived from flow tests. They assume that these three fractures have the same dip and dip direction of, respectively, 65° and 250°, intersecting the GPK2 well at 4760, 4890, and 5060 meters of measured depth (MD), or equivalently and respectively, 4712.73, 4836.26, and 5001 meters of true vertical depth (TVD).

On the other hand, Dorbath et al., 2009, analyzed seismic events induced during and after the stimulation of the GPK2 well in 2000 and detected a 2.6 magnitude seismic event 10 days after the stimulation was stopped at a

55

depth of about 4400 m. Even though, they were confident about the epicenter of the seismic event, its depth was not determined precisely due to absence of surface seismic networks when event occurred. Since this approximate depth was not matched with any of fracture zones mentioned in previous paragraph, there is a doubt that another discontinuity may exist and intersects the GPK2 well at its open-hole section. Therefore, it may be worthwhile to consider another option than the three fractures mentioned above.

There is a well-known fracture at Soultz-sous-Forêts reservoir which intersects three wells constructing the EGS pilot plant (GPK2, GPK3, and GPK4). This fracture is called GPK3-FZ4770 by Sausse et al., 2010; the biggest discontinuity among 39 derived by Sausse et al., 2010, from well logs, micro-seismic activities, and vertical seismic profile data available for whole the wells drilled at Soultz-sous-Forêts geothermal reservoir. This fracture had a dip direction and dip of 234° and 71° (64° in Dezayes et al., 2010) (Sausse et al., 2010), respectively. According to Weidler et al., 2002, this fracture intersects the GPK2 well at a depth of 4700 m TVD. However, Sausse et al., 2010, confirms that the GPK3-FZ4770 intersects the well GPK2 at a depth of 3900 m. This expression is compatible with occurrence of a huge cave at 3880 mTVD of GPK2 well according to Genter et al., 1999, Dorbath et al., 2009, Dezayes et al., 2010, and Sausse et al., 2010. Figure 4.2 exhibits abovementioned four discontinuities intersecting well GPK2 at lower granite formation.
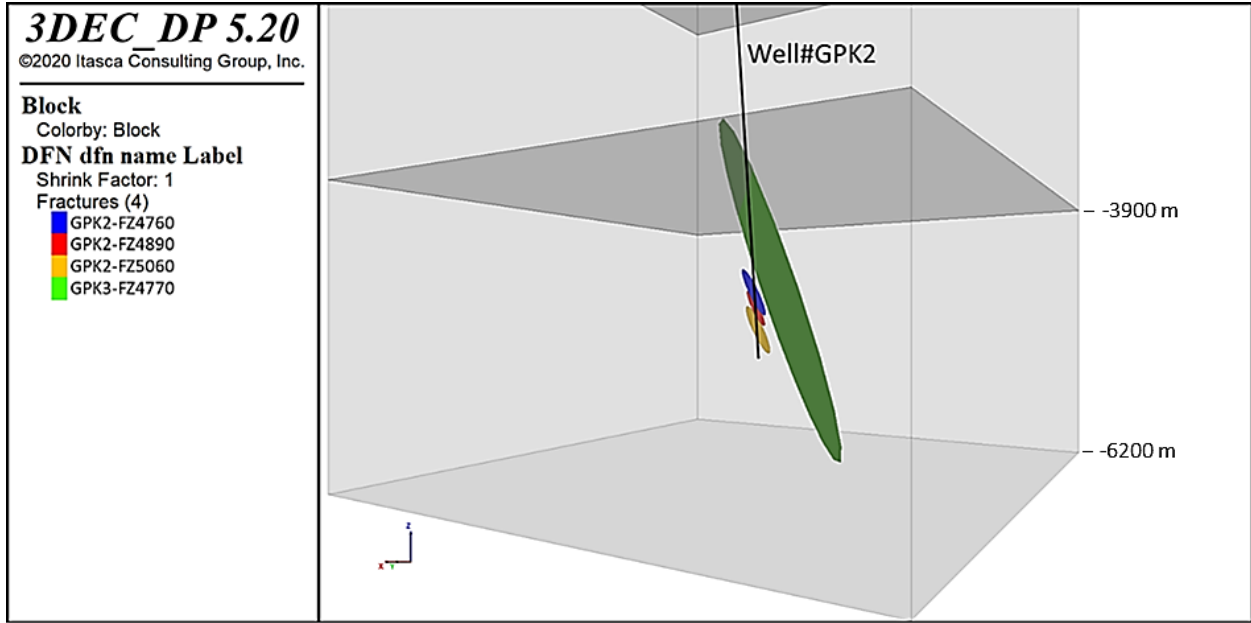
Figure 4.2. The fractures intersecting open-hole section of the well GPK2; the light gray figure represents the cubic model of the reservoir and the dark gray separates the upper granite from the lower one

4.2 In-situ Stress State and Fault Selection

According to the comprehensive study carried out by Valley and Evans, 2007, and Cornet et al, 2007, on the stress state of Soultz-sous-Forêts reservoir using the data acquired from breakouts and drilling induced tensile fractures (DITFs) in the former study and hydraulic stimulation of the year 1993 of GPK1 in the later one, the in-situ stresses can be expressed as:

Table 4.1. In-situ stress state at Soultz-sous-Forêts geothermal reservoir; Z is depth in "km" for Valley and Evans equations and in "m" for Cornet et al., equations; all stresses are in MPa

Valley and Evans, 2007	Cornet et al., 2007
$S_V = -1.3 + 25.5Z$	$S_V = 33.8 + 0.0255(Z - 1377)$
$S_{hmin} = -1.78 + 14.06Z$	$S_{hmin}/S_V = 0.54$
$-1.17 + 22.95Z \leq S_{Hmax} \leq -1.37 + 26.87Z$	$0.95 < S_{hmax}/S_V < 1.1$
$P_p = 0.9 + 9.8Z$	$P_p = 0.9 + 0.0098Z$

In table 4.1 the S_V, S_{hmin}, and S_{Hmax} are respectively vertical, minimum horizontal, and maximum horizontal in-situ stresses in MPa; P_p is pore pressure (MPa) and Z is depth in "km" for Valley and Evans equations and in "m" for Cornet et al., equations. According to Cornet et al., 2007, the maximum horizontal stress has a direction of N170°E±10° (169°±14° based on Klee and Rummel, 1993, and Valley and Evans, 2007). The relation between the vertical stress and the maximum horizontal stress in table 4.1 indicates that the stress regime in the Soultz-sous-Forêts is Normal to Strike-Slip in which the vertical stress is, respectively, the maximum and intermediate principal stresses. Cornet et al., 2007, found that the fault regime is normal down to depth of 3200 m and is strike-slip below.

In current study, 3D Mohr diagrams are used to carry out stability analysis on the GPK3-FZ4770, GPK2-FZ4760, GPK2-FZ4890, and GPK2-FZ5060 fractures, assuming that the fractures intersect the GPK2 at TVD of about 4700, 4712.73, 4836.26, and 5001 meters, respectively. For GPK3-FZ4770 fracture, using equations of table 4.1 at TVD of 4700 m yielded to the stress values listed in table 4.2.

It can be seen that the magnitudes of the pore pressure, vertical and minimum horizontal stresses at the depth of interest are approximately identical, but the range of maximum horizontal stress differs for two sets of equations. While this range is between 0.9 and 1.05 times of vertical stress in Valley and Evans, 2007, it is between 0.95 and 1.1 times of vertical stress at Cornet et al., 2007; indicating an isotropic stress condition in S_v-S_{Hmax} plane while it is not the case on other two planes of S_v-S_{hmin} and S_{Hmax}-S_{hmin} since S_{hmin} is almost half of the S_v and S_{Hmax}; indicating a strong differential stress in these two planes.

Table 4.2. In-situ stress magnitudes at TVD of 4.7 km based on equation introduced in table 4.1

Valley and Evans, 2007	Cornet et al., 2007
S_V= 118.62 MPa	S_V= 118.53 MPa
S_{hmin}= 64.34 MPa	S_{hmin}= 64 MPa
$106.76 < S_{Hmax} < 125$ MPa	$112.61 < S_{Hmax} < 130.39$ MPa
P_p=47 MPa	P_p=47 MPa

To do stability analysis, first, Mohr circles for pore pressure and principal stress magnitudes derived from Cornet et al., 2007, were drawn under two different faulting regimes of normal and strike-slip. Then the Byerlee's law or Coulomb friction law was plotted on the Mohr diagram based on cohesive strength and friction coefficient of the fracture introduced by Cornet et al., 2007. Finally, GPK3-FZ4770 fracture was localized on the resulted Mohr

diagram utilizing values of the shear and effective normal stresses on fracture's plane to see if it slips or not; and if not, how much overpressure is required to destabilize it. All planar features can be represented by a point based on the shear and normal stress in the plane (black dots in figure 4.3, left).

The simplest method to determine the magnitudes of the shear and effective normal stress on an arbitrary oriented plane is to graphically determine the position of the plane on 3-D Mohr diagram by employing two angles of β_1 and β_3 that define the angle between the normal to the fracture plane and the S_1 and S_3 axes, respectively, as shown in figure 4.3b. One can utilize the angles $2\beta_1$ and $2\beta_3$ to find points on the two small circles, and by constructing arcs drawn from the center of the other Mohr circle, P is determined as the intersection of the two arcs (figure 4.3a) (Zoback, 2007).
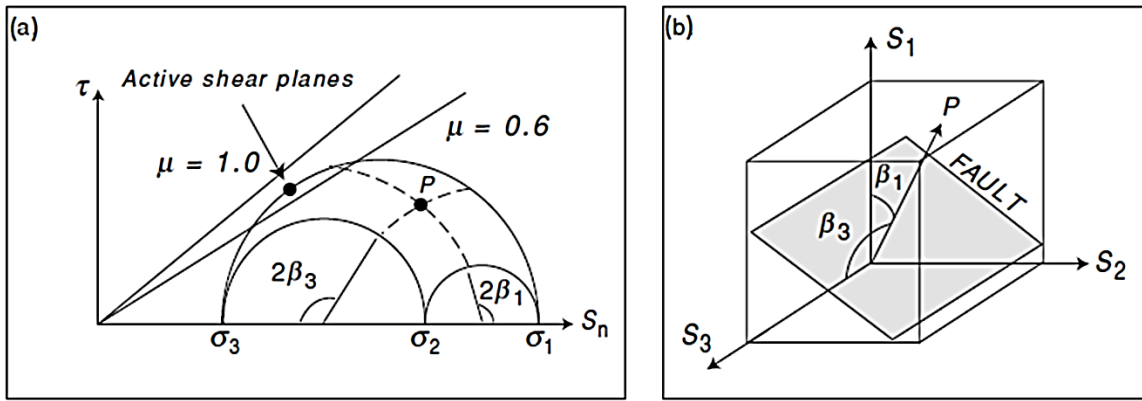
Figure 4.3. Representation of the Mohr circles, Byerlee's law with friction coefficients of 0.6 and 1.0, and arbitrary oriented fracture planes (two black points) on Mohr diagram (a) where the point P is inactive plane while the other one is active shear plane as shown on figure. The two angles of β_1 and β_3 are shown in (b). (Zoback, 2007)

Although the exact position of the fracture plane (point P on figure 4.3a) can be determined with angles β_1 and β_3 measured between the fault normal and S_1 and S_3 directions (figure 4.3b) utilizing the graphical reconstruction explained, mathematical calculation of this and utilization of the three-dimensional Mohr diagram for representation of the data is common as well. The magnitudes of the shear and effective normal stress on an arbitrary oriented plane can be determined using Cauchy tetrahedron. The "Cauchy Tetrahedron", as shown in figure 4.4 (Cornet, 2014), is utilized for determination of stress vector components (t_i) acting on a surface (such as the fault plane in current study) from stress tensor components (σ_{ij}).

In figure 4.4 the vector $\boldsymbol{n}$ is normal of the ABC surface which can be characterized by its three direction cosines of n_1, n_2, and n_3 as

$$n_1 = \cos\alpha \quad (4.1)$$

$$n_2 = \cos\beta \quad (4.2)$$

$$n_3 = \cos\gamma \quad (4.3)$$

where α, β, and γ are the angles between $\boldsymbol{n}$ and $\hat{I}_1$, $\hat{I}_2$, and $\hat{I}_3$.
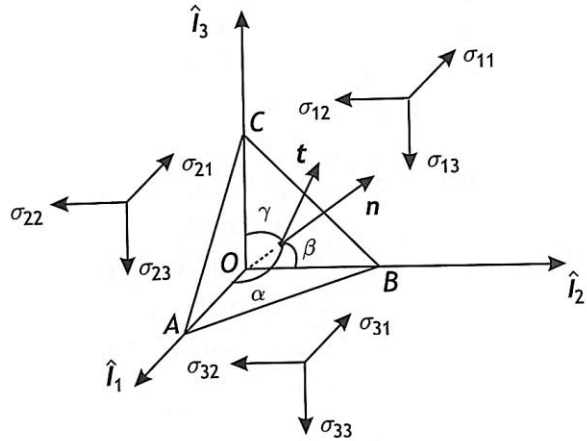
Figure 4.4. Cauchy tetrahedron used to determine stress vector components on a surface element with orientation of $\boldsymbol{n}$ based on stress tensor components (Cornet, 2015)

According to Cornet, 2015, the three components of the stress vector will be

$$t_1 = \sigma_{11}n_1 + \sigma_{21}n_2 + \sigma_{31}n_3 \quad (4.4)$$

$$t_2 = \sigma_{12}n_1 + \sigma_{22}n_2 + \sigma_{32}n_3 \quad (4.5)$$

$$t_3 = \sigma_{13}n_1 + \sigma_{23}n_2 + \sigma_{33}n_3 \quad (4.6)$$

or

$$t_i = \sigma_{ij}n_j, \quad i,j = 1,2,3 \quad (4.7)$$

Or in vector form of

$$\boldsymbol{t} = \tilde{\sigma}\boldsymbol{n} \quad (4.8)$$

where $\boldsymbol{t}$ is called stress vector. Projection of stress vector onto the normal $\boldsymbol{n}$ and onto the fault plane will respectively result in normal component and shear components of the stress vector as

$$\sigma_n \equiv \boldsymbol{t}.\boldsymbol{n} = \tilde{\sigma}\boldsymbol{n}.\boldsymbol{n} = \sigma_{11}n_1^2 + \sigma_{22}n_2^2 + \sigma_{33}n_3^2 + 2\sigma_{12}n_1n_2 + 2\sigma_{13}n_1n_3 + 2\sigma_{23}n_2n_3 \quad (4.9)$$

$$\boldsymbol{\tau} = \boldsymbol{t} - \sigma_n\boldsymbol{n} = \tilde{\sigma}\boldsymbol{n} - (\tilde{\sigma}\boldsymbol{n}.\boldsymbol{n})\boldsymbol{n} \quad (4.10)$$

σ_n is the normal stress acting on the fault which is a scalar and vector $\boldsymbol{\tau}$ is shear component of $\boldsymbol{t}$. The norm of the shear stress vector will give us the shear stress magnitude acting on the fault plane.

$$\tau = \|\boldsymbol{\tau}\| \quad (4.11)$$

Knowing the magnitude of shear stress acting on the fault plane and the orientation of the fault plane and assuming that the slip direction is parallel with the direction of shear stress vector, the slip direction can be determined as

$$rake = \arctan\left(\frac{\tau_d}{\tau_s}\right) \quad (4.12)$$

59

In which τ_d and τ_s are respectively projection of shear stress vector onto dip and strike direction of the fault plane on the basis of n_s and n_d which are normal vectors towards strike and dip of the fault plane.

$$\tau_d \equiv t.n_d \quad (4.13)$$

$$\tau_s \equiv t.n_s \quad (4.14)$$

These two accompanied with n, make the frame of reference on the fault plane. Components of n_s and n_d are determined as

$$n_s = (cos(str), sin(str), 0) \quad (4.15)$$

$$n_d = (-\sin(str)cos(dip), \cos(str)\cos(dip), sin(dip)) \quad (4.16)$$

The n can also be determined as

$$n = (-\sin(str)sin(dip), \cos(str)\sin(dip), -cos(dip)) \quad (4.17)$$

The rake angle describes the direction of fault movement with respect to the strike and is measured anticlockwise from the horizontal where up is positive (Davis and Reynolds, 1996). According to Cornet, 2015 (pp. 268), the peak shear strength (τ_p) of a fracture plane is characterized by a linear relationship between the normal stress (S_n) and the cohesion as

$$\tau_p = \mu S_n + C \quad (4.18)$$

in which μ is fracture's friction coefficient and C is fracture's cohesion strength. Equation (4.18) is called Byerlee's law or Coulomb friction law. However, in Byerlee's law when the normal stress acting on the fracture plane is between 5 and 200 MPa (such as our case in this study), the effect of cohesion is negligible (Byerlee, 1978). It is also worth to distinguish the difference between equation (4.18) and Mohr-Coulomb failure criterion, which is used for rock, samples with an internal friction coefficient (Jaeger et al., 2007).

When there is fluid pressure in the fracture (P_p), the normal stress at equation (4.18) must be replaced by the effective normal stress as

$$\tau_p = \mu(S_n - P_p) + C = \mu\sigma_n + C \quad (4.19)$$

Equation (4.19) can be drawn on Mohr diagram as a line with slope of μ which intersects the shear stress axis at C. From this equation it could be concluded that raising the fracture's fluid pressure (e.g. through fluid injection) will facilitate fracture slide by reducing the effective normal stress (Hubbert and Rubey, 1959) or increasing the ratio of the shear to normal stress on any pre-existing fracture (Zoback, 2007). In other words, when the shear stress on the fault plane (equation 4.11) exceeds the peak shear strength of the fracture (equation 4.19) the fracture slide will occur.

In current study, four different cases of in-situ stress and faulting regime were applied to carry out the stability analysis of GPK3-FZ4770 fracture at a depth of 4703 m as following:

Case 1: Strike-slip faulting regime (S_{Hmax}=1.1 S_v) and in-situ stress equations introduced by Cornet et al., 2007 represented in table 4.1

Case 2: Normal faulting regime (S_{Hmax}=0.95 S_v) and in-situ stress equation introduced by Cornet et al., 2007 represented in table 4.1

Case 3: Strike-slip faulting regime (S_{Hmax}=1.05 S_v) and in-situ stress equation introduced by Valley and Evans, 2007 represented in table 4.1

Case 4: Normal faulting regime (S_{Hmax}=0.9 S_v) and in-situ stress equation introduced by Valley and Evans, 2007 represented in table 4.1

In the case 1, we assume that the faulting regime at the depth of 4703 m is strike-slip with $S_1 = S_{Hmax}$=1.1 S_v =130.39 MPa, $S_2 = S_v$=118.53 MPa, and $S_3 = S_{hmin}$=0.54 S_v = 64 MPa. Then the principal stress tensor or effective principal stress tensor will be

$$\tilde{S} = \begin{bmatrix} -130.39 & 0 & 0 \\ 0 & -118.53 & 0 \\ 0 & 0 & -64 \end{bmatrix} \text{ or } \tilde{\sigma} = \begin{bmatrix} -83.39 & 0 & 0 \\ 0 & -71.53 & 0 \\ 0 & 0 & -17 \end{bmatrix}$$

Here the minus sign represents the compressive stress. For this case, given the direction of principal stresses (right-hand rule where the vertical stress is downward and the maximum horizontal stress has a direction of N170°E) and the orientation of the fault (with dip and strike of 71° and 144°, respectively), first it is required to transform principal stresses to stress tensor at geographical frame of reference and then calculate the n_1, n_2, and n_3. The rotation matrix to transform the principal stress tensor to stress tensor at geographical coordinate system is (Zoback, 2007)

$$R_g = \begin{bmatrix} \cos a \cos b & \sin a \cos b & -\sin b \\ \cos a \sin b \sin c - \sin a \cos c & \sin a \sin b \sin c + \cos a \cos c & \cos b \sin c \\ \cos a \sin b \cos c + \sin a \sin c & \sin a \sin b \cos c - \cos a \sin c & \cos b \cos c \end{bmatrix} \quad (4.20)$$

where the Euler (rotation) angles that define the stress coordinate system in terms of geographic coordinates, are as follows:

$$\begin{cases} a = \text{ trend of } S_1 \\ b = -\text{plunge of } S_1 \\ c = \text{rake } S_2 \end{cases} \quad (4.21)$$

However for cases in which vertical stress is a principal stress, a, b, and c can be defined as table 4.3 (https://dnicolasespinoza.github.io/node38.html).

Table 4.3. Summary of possible values of a, b, and c for cases in which the vertical stress is a principal stress

	Normal Faulting	**Strike-Slip Faulting**	**Reverse Faulting**
a	Azimuth of S_{hmin}	Azimuth of S_{Hmax}	Azimuth of S_{Hmax}
b	90°	0°	0°
c	0°	90°	0°

Then, the stress tensor at geographical coordinate system can be determined (Zoback, 2007) as

$$S_g = R_g^T S R_g \quad (4.22)$$

For case 1, the a, b, and c will be respectively 170°, 0°, and 90° according to the table 4.3. Then, the R_g will give

$$R_g = \begin{bmatrix} -0.985 & 0.174 & 0 \\ -0.174 & 0 & 1 \\ 0.174 & 0.985 & 0 \end{bmatrix}$$

and

$$R_g^T = \begin{bmatrix} -0.985 & -0.174 & 0.174 \\ 0.174 & 0 & 0.985 \\ 0 & 1 & 0 \end{bmatrix}$$

Now, utilizing equation (4.22) will determine S_g as

$$\widetilde{S_g} = \begin{bmatrix} -0.985 & -0.174 & 0.174 \\ 0.174 & 0 & 0.985 \\ 0 & 1 & 0 \end{bmatrix} \begin{bmatrix} -130.39 & 0 & 0 \\ 0 & -118.53 & 0 \\ 0 & 0 & -64 \end{bmatrix} \begin{bmatrix} -0.985 & 0.174 & 0 \\ -0.174 & 0 & 1 \\ 0.174 & 0.985 & 0 \end{bmatrix}$$

$$= \begin{bmatrix} -131.96 & 11.35 & 20.58 \\ 11.35 & -66 & 0 \\ 20.58 & 0 & -118.53 \end{bmatrix}$$

The n_1, n_2, and n_3 in a frame of reference in which n_1, n_2, and n_3 are aligned respectively positive northward, positive eastward and positive downward will be

$$n_1 = n_x = \cos(19) \times \cos(126) = \sin(71) \times (-\sin(144)) = -0.556$$

$$n_2 = n_y = \cos(19) \times \cos(144) = \sin(71) \times \cos(144) = -0.765$$

$$n_3 = n_z = -\cos(71) = -0.326$$

Application of equations (4.9) - (4.11) will yield

$$\sigma_n = 34.18 \text{ MPa}$$

$$\tau = (17.55, -17.92, 12.16)$$

$$\tau = 27.88 \text{ MPa}$$

Figure 4.5 demonstrates the Mohr diagram for this case before (left) and after (right) injection. As shown in figure 4.5 left, the pre-injection values of the three effective principal stresses are used to draw three Mohr circles. For the first case, effective in-situ stresses are $\sigma_1 = S_1 - P_p = 130.39 - 47 = 83.39 \text{ MPa}$, $\sigma_2 = S_2 - P_p = 118.53 - 47 = 71.53 \text{ MPa}$, and $\sigma_3 = S_3 - P_p = 64 - 47 = 17 \text{ MPa}$. The fracture is localized on the Mohr diagram as a red point utilizing τ and σ_n already calculated. The failure criterion is also drawn on the Mohr diagram knowing that the fracture's cohesion and friction coefficient are respectively 6.5 MPa and 0.81 (as stated in table 4.6).

Peak shear strength of the fracture at the depth of interest is determined by equation (4.19) as

$$\tau_p = 0.81 \times 34.18 + 6.5 = 34.18 \text{ MPa}$$

The difference between shear stress acting on the fracture plane (determined by equations 10 and 11) and the peak shear strength of the fracture (determined using equation 4.18) is, in fact, the distance to failure of the fracture, which is called Coulomb Stress (CS) and is defined as (King et al., 1994)

$$CS = |\tau| - \mu(S_n - P_P) - C = |\tau| - (\mu\sigma_n + C) \quad (4.23)$$

where positive CS indicates unstable fracture (since $|\tau|$ is greater than τ_p) and negative shows stable one. By substituting of 27.88 MPa for τ, 0.81 and 6.5 MPa respectively for μ and C, and finally 34.18 for σ_n at the right-hand side of equation (4.25), the CS will be -6.3 MPa.

As it can be seen in figure 4.5 left, the fracture is stable at the in-situ stress state; consistent with the sign of above CS calculations. Figure 4.5 right demonstrates the fracture location on the Mohr diagram when the pore pressure is increased for 8 MPa (e.g. by fluid injection). It can be seen that the red point superimposes on the fracture failure criterion. This 8 MPa of overpressure to de-stabilize fracture, can analytically be determined using below definition.

To determine the minimum required overpressure to de-stabilize the GPK3-FZ4770 fracture at the depth of 4703 meter and under aforementioned in-situ stress state and strike-slip faulting regime, we need to note that at the onset of slippage, the shear stress is equal to shear strength of the fracture (Jaeger et al, 2007) or, in other words, the CS is equal to zero. In fact, the injected fluid will decrease the inherent shear strength of the fracture (equation 4.18) by decreasing the magnitude of effective normal stress acting on the fracture plane (equation 4.31). Then, if we consider σ_{ns} as effective normal stress acting on the fracture plane once slip occurs, we will have

$$\tau = \mu\sigma_{ns} + C \quad (4.24)$$

Doing some manipulation on equation (4.24) reads

$$\sigma_{ns} = \frac{\tau - C}{\mu} \quad (4.25)$$

Difference between effective normal stress at initial state (determined by equation 4.9) and that once slip occurs (determined using equation 4.25) is the required overpressure (ΔP) to de-stabilize the fracture which can be expressed as

$$\Delta P = \sigma_n - \sigma_{ns} = \sigma_n - \frac{\tau - C}{\mu} \quad (4.26)$$

By substituting of 27.88 MPa for τ, 0.81 and 6.5 MPa respectively for μ and C, and finally 34.18 for σ_n at the right-hand side of equation (4.26), the ΔP will be 7.8 MPa; consistent with the required overpressure estimated by Mohr plots. Practically, this 7.8 MPa of overpressure will generate 6.3 MPa of CS if it is multiplied by friction coefficient of 0.81, according to equation (4.23).
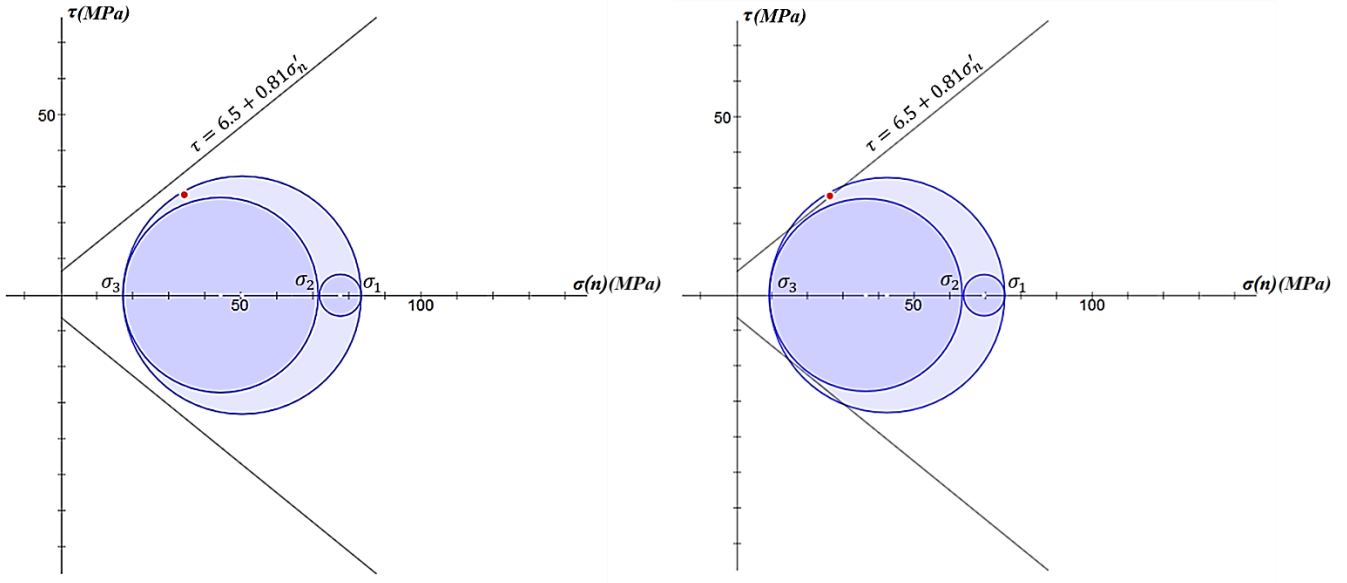
Figure 4.5. Mohr diagram at strike-slip faulting regime (S_{Hmax}=1.1 S_v, case 1) for in-situ stress and pore pressure values introduced by Cornet et al., 2007; the GPK3-FZ4770 fracture is also localized on the diagrams by a red point. The left-side diagram illustrates Mohr circles and fracture plane at hydrostatic pore pressure condition while the right-side one shows them after imposing 8 MPa of overpressure (Mohr diagrams are drawn by "MohrPlotter" software introduced by Richard W. Allmendinger)

The slip direction can also be calculated using equations (4.12)-(4.16) as

$$\boldsymbol{n_d} = (-0.191, -0.263, 0.945)$$

$$\boldsymbol{n_s} = (-0.81, 0.59, 0)$$

$$\tau_d = \boldsymbol{t.n_d} = 12.86 \text{ MPa}$$

$$\tau_s = \boldsymbol{t.n_s} = -24.73 \text{ MPa}$$

$$rake = \arctan\left(\frac{12.86}{-24.73}\right) \cong -27.47°$$

The case 2 assumes the normal faulting regime at the depth of interest with $S_1= S_v$=118.53 MPa, $S_2= S_{Hmax}$= 0.95 S_v = 112.61 MPa, and $S_3=S_{hmin}$= 0.54 S_v = 64 MPa. Performing as same steps as those carried out for the case 1 will yield to shear and effective normal stresses of, respectively, 22.83 MPa and 31.13 MPa acting on the fracture plane before fluid injection. The peak shear strength of the fracture for this case is equal to 31.72 MPa using equation (4.19); indicating a minimum of about 11 MPa of overpressure required for fracture slippage to take place based on equation (4.18). Equation (4.12) results in rake angle of -37.53° for this case.

Figure 4.6 right shows that the GPK3-FZ4770 fracture slips for about 11 MPa of overpressure which is more like the field observation of WHP.
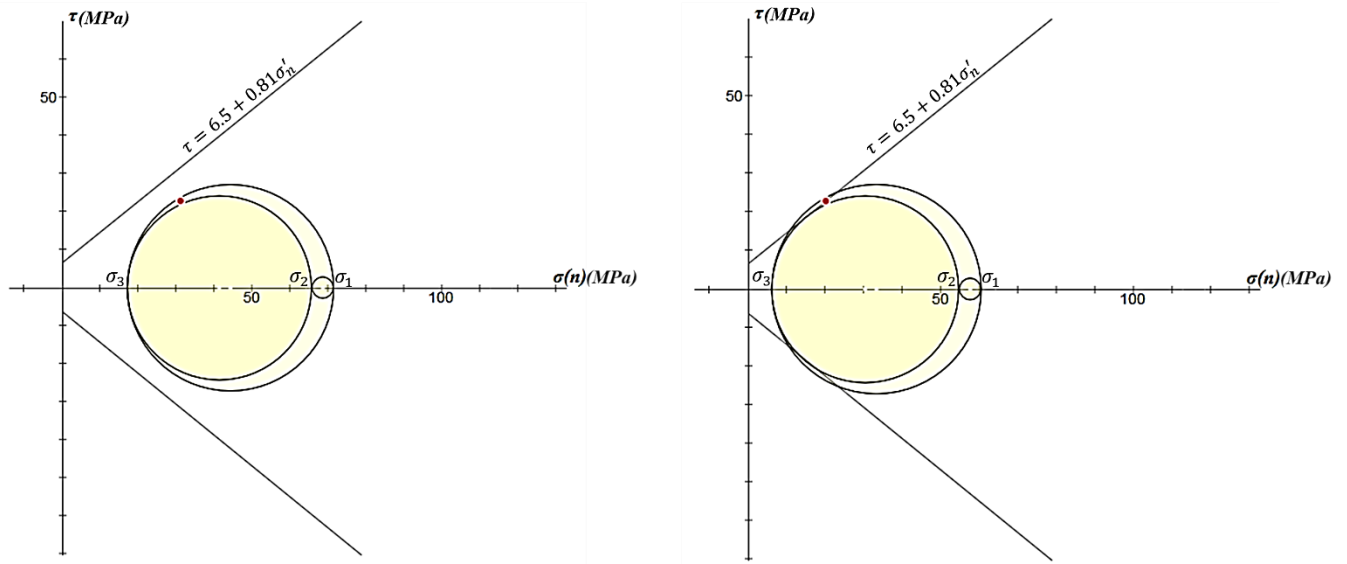
Figure 4.6. Mohr diagram at normal faulting regime (S_{Hmax}=0.95 S_v, case 2) for in-situ stress and pore pressure values introduced by Cornet et al., 2007; the GPK3-FZ4770 fracture is also localized on the diagrams by a red point; left-side diagram illustrates Mohr circles and fracture plane at hydrostatic pore pressure condition while the right-side shows them after 11 MPa of overpressure (Mohr diagrams are drawn by "MohrPlotter" software introduced by Richard W. Allmendinger)

Then, above assessments were carried out for case 3 and case 4 using equations of Valley and Evans, 2007. The components of shear and normal stresses acting on the fracture plane for these two cases as well as peak shear strength and required overpressure to de-stabilize the fracture are summarized in table 4.3.

Table 4.4. The shear and normal stress components acting on the fracture plane, the Fracture's inherent shear strength, the Coulomb Stress and required overpressure to de-stabilize the fracture, and finally Rake angle for case 1 to case 4

Case	S_{Hmax}/S_v	τ (MPa)	σ'_n (MPa)	τ_p (MPa)	CS (MPa)	ΔP (MPa)	Rake (°)
1	1.1	27.9	34.2	34.2	-6.3	7.8	-27.5
2	0.95	22.8	31.1	31.7	-8.9	10.9	-37.5
3	1.05	26.1	33.5	33.6	-7.5	9.3	-30.1
4	0.9	21.2	30.4	31.1	-9.9	12.2	-41.9

To have some more assessment on this issue, abovementioned calculations performed for various ratios of S_{Hmax}/S_V and the required overpressure in order for GPK3-FZ4770 fracture to slip were determined. The results were summarized in table 4.5 for both sets of equations introduced by Cornet et al., 2007, and Valley and Evans, 2007, revealing the fact that it might be reasonable to constrain the upper limit of the S_{Hmax} on 0.95 since the overpressure at this ratio (approximately 11 MPa in both sets of the in-situ stress equations) is close to the field WHP (11-12 MPa).

It seems that in the above results achieved from both sets of equations, at normal faulting regime higher values of overpressure are required for destabilizing GPK3-FZ4770 fracture than strike-slip faulting regime; indicating that

the strike-slip condition is more unstable. This is also mentioned in Dorbath et al., 2010, where the authors inverted focal mechanism of the main events during stimulation of GPK2 at 2000 and found that normal faulting is dominant among the focal mechanism solutions (figure 4.7); which means that seismic initiation in normal faulting regime requires higher fluid overpressures than strike-slip regime. Figure 4.7 illustrates the focal plane mechanisms of micro-earthquakes induced by the year 2000 stimulation of GPK2 well in which the light gray spheres indicates the hypocenters of M>1 events and black spheres shows the hypocenters of events that Dorbath et al, 2010, used in their performed inversion. The shown beachballs in figure 4.7 reveal the dominancy of the normal faulting regime at the area of study among the events Dorbath et al, 2010, used to carry out the stress tensor inversion.

Table 4.5. The shear and normal stress components acting on the fracture plane, the Fracture's inherent shear strength, the Coulomb Stress and required overpressure to de-stabilize the fracture, and finally Rake angle for various ratios of maximum horizontal stress to vertical stress (the yellow color indicates normal faulting regime and blue is used for strike-slip faulting regime)

S_{Hmax}/S_V	Cornet et al., 2007						Valley and Evans, 2007					
	τ (MPa)	σ'_n (MPa)	τ_p (MPa)	CS (MPa)	ΔP (MPa)	Rake (°)	τ (MPa)	σ'_n (MPa)	τ_p (MPa)	CS (MPa)	ΔP (MPa)	Rake (°)
0.90	N/A	N/A	N/A	N/A	N/A	N/A	21.2	30.4	31.1	-9.9	12.2	-41.9
0.92	N/A	N/A	N/A	N/A	N/A	N/A	21.8	30.8	31.4	-9.6	11.9	-40.1
0.95	22.8	31.1	31.7	-8.9	10.9	-37.5	22.7	31.4	31.9	-9.2	11.4	-37.5
0.97	23.5	31.5	32.0	-8.5	10.6	-35.9	23.3	31.8	32.3	-9.0	11.0	-36.0
1	24.4	32.1	32.5	-8.1	10.0	-33.7	24.3	32.4	32.8	-8.5	10.4	-33.7
1.02	25.1	32.6	32.9	-7.8	9.6	-32.3	25.0	32.8	33.1	-8.1	10.0	-32.3
1.03	25.4	32.8	33.0	-7.6	9.4	-31.7	25.3	33.0	33.3	-8.0	9.8	-31.6
1.04	25.8	33.0	33.2	-7.4	9.2	-31.0	25.6	33.2	33.4	-7.8	9.6	-31.0
1.05	26.1	33.1	33.3	-7.2	9.0	-30.4	26.1	33.5	33.6	-7.5	9.3	-30.1
1.08	27.2	33.8	33.9	-6.7	8.3	-28.6	N/A	N/A	N/A	N/A	N/A	N/A
1.1	27.9	34.2	34.2	-6.3	7.8	-27.5	N/A	N/A	N/A	N/A	N/A	N/A
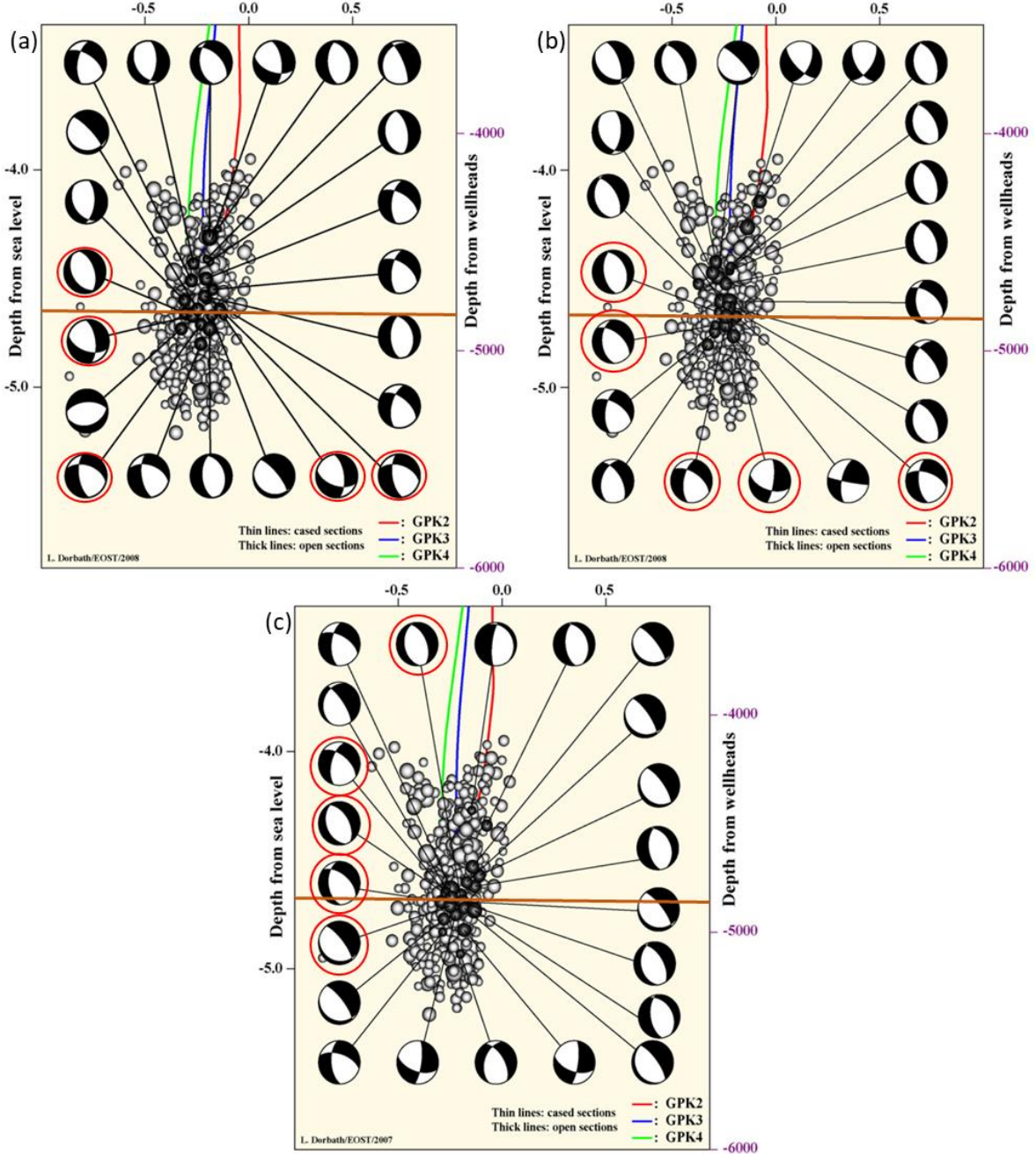
Figure 4.7. Focal plane mechanisms represented on the lower hemisphere and used by Dorbath et al., 2010, for inversion of stress tensor at Soultz-sous-Forêts. The light gray spheres indicate the hypocenters of the M>1 induced seismic events and the black spheres shows the micro-earthquakes used for inversion by Dorbath et al, 2010. Assuming an approximate depth of 4.7 km shown by the brown line in (a), (b), and (c), the beachballs indicated by a red circle are corresponding to the events induced around the brown line. As it can be seen they mainly exhibits a strike-slip-normal faulting regime (oblique), however generally the normal faulting regime is dominant among whole the focal plane mechanisms shown here

Looking at rake angles in table 4.5, ranging from about -27 to -42 degrees, reveals that the faulting regime at the study area is strike-slip to normal (oblique) as mentioned in Cornet et al., 2007. This point is also obvious at figure 4.7 by assuming the depth of about 4.7 km shown by brown lines in figure 4.7(a), (b), and (c) and looking at the

focal plane mechanisms indicated by red circle where it can be seen that the stress regime in the depth of 4700 meters is oblique with rake of approximately -40 to -90 degrees.

In the current study, we assumed that the stress regime at the depth of interest is normal with S_{Hmax} equal to 0.95 times of S_v using equations introduced by Cornet et al., 2007.

It is also worth to assess the slip tendency of the other three fractures which intersect the open-hole section of the GPK2 well as introduced in section 1. Among those three of GPK2-FZ4760, GPK2-FZ4890, and GPK2-FZ5060, the first one intersects the well at TVD of about 4712.73 m while the other two intersected at, respectively, 4836.26 and 5001 m. In mud window design for drilling of hydrocarbon or geothermal wells the upper limit of mud weight is defined based on fracture gradient concept which is the result of dividing of fracture pressure (the required pressure to make a fracture in the formation or stimulate the pre-existing fractures) by TVD (Zhang and Yin, 2017). Since, according to the equations introduced by Cornet et al., 2007, the pore pressure and stress gradients at Soultz-sous-Forêts are hydrostatic and lithostatic (as shown in figure 4.8), it can be stated that the effective normal stress and the shear stress acting on the fracture plane (which are a function of i) in-situ stresses, ii) pore pressure, and iii) fracture attitude with respect to the maximum principal stress, as defined by equations (4.9) and (4.10)) will rise with depth (as shown in figure 4.9) where Coulomb stress is negative (i.e., fracture is stable) and increases with depth just like the required overpressure to de-stabilize the fracture; indicating that any overpressure imposed to the open-hole section of wells will first stimulate the shallower fracture. Therefore, generalizing this fact to GPK2-FZ4760, GPK2-FZ4890, and GPK2-FZ5060 (with dip, dip direction, friction coefficient, and cohesion of respectively 65°, 250°, 0.81, and 6.5 MPa, respectively), during pressure build-up phase of stimulation, the GPK2-FZ4760 fracture will be triggered earlier in time (and consequently in lower fluid overpressure value) than GPK2-FZ4890 and GPK2-FZ5060. So that, it will be reasonable to compare the slip tendency of GPK2-FZ4760 and GPK3-FZ4770 to know which one will first slide at a given overpressure. For that, the Mohr diagram is drawn once again for normal stress regime at depth of 4.7 km and Byerlee's law as well as fracture planes are also plotted on the diagram as shown in figure 4.10 left, the shear and effective normal stresses on GPK2-FZ4760 fracture are respectively 21.7 MPa and 28 MPa (calculated by equations (4.9) and (4.11)). The peak shear strength of the fracture then will be 29.1 MPa. Therefore, the CS of GPK2-FZ4760 fracture is -7.4 MPa, according to equation (4.23). The figure 4.10 right illustrates the over-pressured situation where it can be seen that at 9 MPa of overpressure the GPK2-FZ4760 will slip earlier than GPK3-FZ4770 (remember that the CS of GPK3-FZ4770 fracture is -6.3 MPa, table 4.5). This provisional assessment implies that it may be reasonable to carry out extra research on attitude of fractures intersecting the open-hole section of GPK2 well to utilize appropriate fracture for investigations; however, current research is continued by using GPK3-FZ4770 fracture.

Moreover, it can be seen from Mohr diagrams shown in figures 5, 6, and 10 that by increase of pore pressure, the $\sigma_1 - \sigma_3$ Mohr circle contacts the Coulomb friction criterion at a point which exhibits attitude different from that of GPK3-FZ4770 but similar to attitude of GPK2-FZ4760. Doing some back analysis on the effect of dip and strike of fracture on slip tendency revealed that the first contact-point of the Mohr circle and Coulomb friction law is a plane with dip and strike of 65° and 165°, respectively, which will slip with 9 MPa of overpressure at normal faulting regime (shear and effective normal stresses on the plane are respectively 21.1 and 27 MPa, using 0.81 and 6.5 MPa for friction coefficient and cohesion yields to CS of -7.3 MPa).
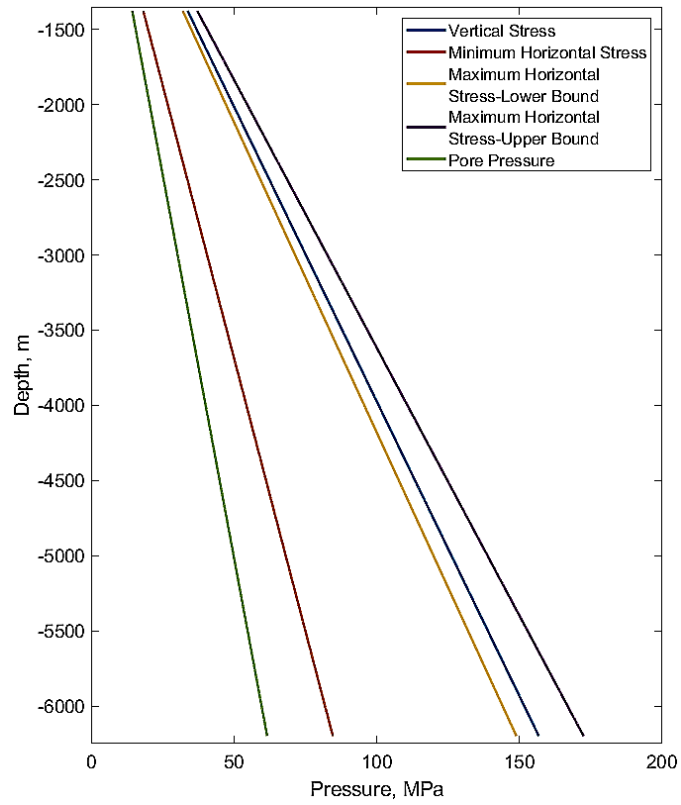
Figure 4.8. In-situ stress state and pore pressure at Soultz-sous-Forêts based on Cornet et al., 2007, equations for the depth starting from the below of sediments (-1377 meters) down to a depth of -6200 meters (bottom of the 3DEC model in current study)
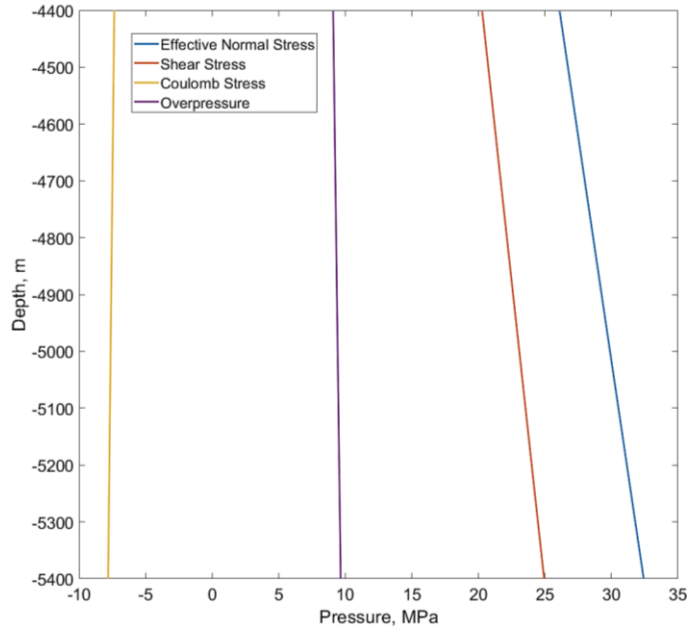
Figure 4.9. Evolution in depth of effective normal stress, shear stress, Coulomb Stress, and required overpressure to de-stabilize a fracture plane with dip and dip direction of respectively 65° and 250° (as equal as attitude of GPK2-FZ4760, GPK2-FZ4890, and GPK2-FZ5060)
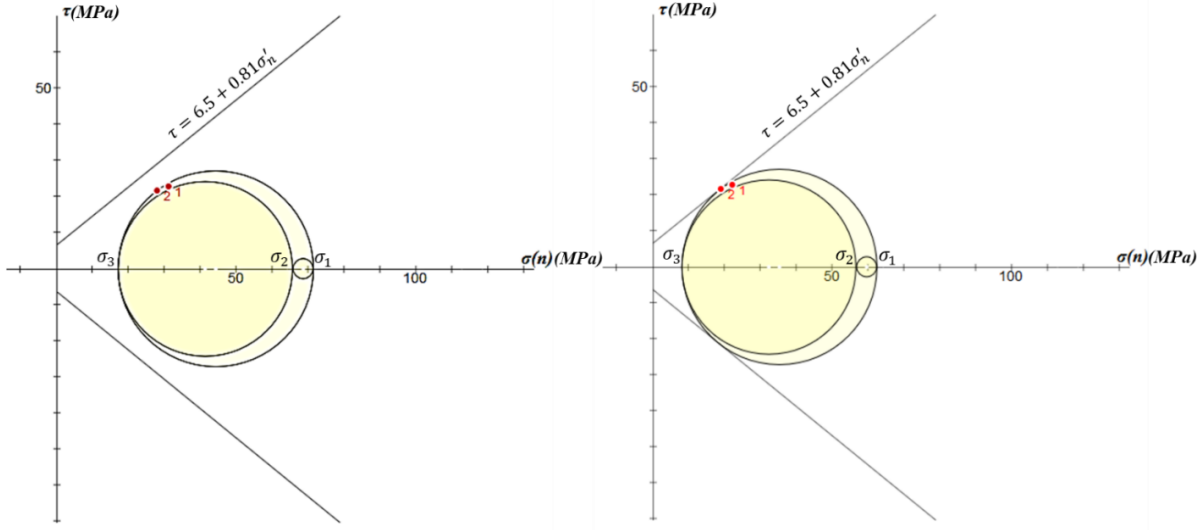
Figure 4.10. Mohr diagram at normal faulting regime for in-situ stress and pore pressure values introduced by Cornet et al., 2007; the GPK3-FZ4770 (red point number 1) and GPK2-FZ4760 (red point number 2) fractures are also localized on the diagrams by a red point; left-hand side diagram illustrates Mohr circles and fracture planes at hydrostatic pore pressure condition while the right-hand side shows them after 7.5 MPa of overpressure in which GPK2-FZ4760 slides but GPK3-FZ4770 does not (Mohr diagrams are drawn by "MohrPlotter" software introduced by Richard W. Allmendinger)

4.3   Methodology

Here, we used 3DEC software to analyze this large-scale fluid injection operation by developing a large-scale numerical model of the Soultz-sous-Forêts reservoir (approximately 5000x5000x5000 m^3; figure 4.11) containing the largest fault of the reservoir defined by Sausse et al., 2010. The objective is to characterize the large-scale hydro-mechanical behavior of the fault against fluid injection.

At the first step of modelling, it was aimed to merely consider one fault and simulate the first stage of the year 2000 stimulation (figure 4.1b, as a 24 hour injection of water (density 1000 kg/m^3, viscosity 1 centipoise) with constant flow rate of 30 ls^{-1} into a fault/fracture located at the open-hole section of the GPK2 well), it was decided to investigate hydromechanical response of GPK3-FZ4770 fracture against hydraulic stimulation as a first proxy.

The numerical model included a block of granite rock matrix containing a 3000 m diameter circular fracture called GPK3-FZ4770. Physical and mechanical properties of the rock matrix at open-hole section of the well and the fracture's properties were derived from existing literature and summarized in table 4.6.

For the elastic moduli of the formations drilled in the Soultz-sous-Forêts reservoir, Vallier et al. (2019) performed an extensive inversion of the observed temperature and stress-depth profiles using a THM model to obtain the possible values of Poisson's ratio and Young's modulus within a wide range reported in the literature. They concluded that 25 GPa is more realistic value for Young's modulus at large scale (100 m) of the lower granite where the open-hole section of GPK2 is located. The density of the lower granite was also chosen to be 2680 kg/m^3, according to Gentier et al. 2005. Gentier et al., 2005, carried out a numerical study using 3DEC on hydraulic stimulation of wells at Soultz-sous-Forêts to reproduce observed behavior in terms of pressure-flow curves and location of the stimulated fractures and found a good agreement between obtained numerical fluid flow results and

the data achieved from in-situ hydraulic tests. At current work, we aim to use 3DEC to better understand P-wave velocity variations by reproducing hydro-mechanical response of the faults located at Soultz-sous-Forêts.

For that, the magnitudes of Poisson's ratio, fracture's normal and shear stiffnesses, initial, residual, and maximum apertures of the fracture which Gentier et al., 2005, used in their models are applied in current study. To have an appropriate value of fracture's cohesion and friction angle among those reported in the literature, we used the data provided by Cornet et al., 2007, in which the authors extensively discussed two hypotheses about shear failure of the pre-existing fractures and initiation of fresh fracture surfaces at Soultz-sous-Forêts reservoir. They stated that for pre-existing fractures to be just in equilibrium at the present stress state, or in other words to be stimulated with a slight increase in in-situ pore pressure, the cohesion and friction angle of fractures should be, respectively, equal to 6.5 MPa and 39° (friction coefficient of 0.81).

The block is constrained to move in the bottom and at the sides of the block a boundary stress condition equal to the in-situ stress state of the previous section is applied, first to prevent the block from moving laterally and second to quickly reach the initial equilibrium condition. The block is also discretized with tetrahedrons of side-size 200 meters. In the 3DEC numerical approach, the flow domain is fully saturated (Itasca, 2016) and discretized into tetrahedral zones defined by four nodes as same discretizing method as mechanical and thermal calculations (Itasca, 2016). This flow domain is indicated by flow plane which is major geometrical element of the flow model and always is a plane extended to the boundaries of the block (Itasca, 2016). The flow plane is a two dimensional surface in which flow is occurring through its thickness. Therefore, flow planes are planar polygons and are connected along the edges (Itasca, 2016). The circular edge of the fracture as well as the boundaries of the model are impermeable.

In 3DEC, the numerical scheme for fluid flow analysis relies on a finite difference nodal formulation of the continuity equation and the resulting ordinary differential equations will be solved using an explicit mode of discretization in time (Itasca, 2016).

Fluid flow through fractures in 3DEC, is governed by simplified Navier-Stokes equation; which is Reynolds lubrication equation for incompressible fluid through two parallel and impermeable surfaces (Itasca, 2016) as

$$\left(\frac{h^3}{12\mu_d}p_{,x}\right)_{,x} = 0 \quad (4.27)$$

This equation is valid only for laminar flow. From equation (4.27), fluid flow rate per unit width of the fracture may be determined (Itasca, 2016) as

$$q = -\frac{h^3}{12\mu_d}p_{,x} \quad (4.28)$$

which is well-known cubic law. Note that in fractures introduced by two parallel plates, aperture of fracture is equal with hydraulic aperture.

The rate of pressure propagation in a saturated medium (in 3DEC the joints and rock matrix are assumed to be fully saturated) is dictated by the fluid diffusivity (3DEC manual, 2016)

$$c = \frac{k_H}{S_t} \quad (4.29)$$

Table 4.6. Physical and mechanical properties of rock matrix and fracture mentioned in literature; the * indicates the values used in the current modelling

Element	Property	Symbol	Value	Unit	Remark
Rock Matrix	Young's Modulus	E	25* - 47	GPa	Rummel, 1992
			52		Gentier et al., 2005
			25*		Sausse, 2002, Vallier et al., 2019
	Poisson's Ratio	υ	0.29*	-	Gentier et al., 2003&2005
			0.1		Sausse, 2002
			0.38		Rummel, 1992
			0.20		Vallier et al., 2019
	Bulk Density	ρ	2680*	Kg/m3	Gentier et al., 2005
			2650 - 2800		Haenel, 1983
Fracture	Shear Stiffness	K_s	20*	GPa/m	Gentier et al., 2005
			80 -180		Gentier et al., 2003
	Normal Stiffness	K_n	80*	GPa/m	Gentier et al., 2005
			80 -180		Gentier et al., 2003
	Friction Angle	φ	39*	°	Cornet et al., 2007
			45		Evans, 2005
			48		Gentier et al., 2005
	Cohesion	S_0	4-8	MPa	Cornet et al., 2007
			6.5*		Evans, 2005
			0		Gentier et al., 2005
	Initial Aperture	h_0	14e-05*	m	Gentier et al., 2005
			6e-07		Gentier et al., 2003
	Residual Aperture	h_{res}	7e-05*	m	Gentier et al., 2005
			1e-08		Gentier et al., 2003
	Maximum Aperture	h_{max}	12e-03*	m	Gentier et al., 2005
			1e-03		Gentier et al., 2003

in which k_H is hydraulic conductivity defined as $\rho g h_H^3 \big/ 12\mu_d$, and S_t is the storage which may be obtained (Itasca, 2016) as

$$S_t = \rho g \left(\frac{c_f h_H}{s} + \frac{1}{K+4/3G} \right) \quad (4.30)$$

where s is spacing between fractures, G and K are shear and bulk moduli of the surrounding rock. If the rock is assumed to be rigid, then the second term in the parenthesis will be equal to zero (Itasca, 2016).

Pressures are calculated and stored in a data structure called flow-knot and are updated subsequent to flow rate calculations, considering the net flow into the flow-knot. Then, the new flow-knot pressure will be (Itasca, 2016)

$$p = p_0 + \frac{Q}{c_f}\frac{\Delta t}{V} - \frac{1}{c_f}\frac{\Delta V}{V_m} \quad (4.31)$$

where p_0 is the flow-knot pressure in the preceding time-step, Q is the sum of flow rates into the flow-knot from all surrounding contacts, Δt is time-step, V is flow-knot volume, c_f is fluid compressibility, $\Delta V = V - V_0$ and $V_m = (V + V_0)/2$, where V and V_0 are the new and old flow-knot volumes, respectively. If the new pressure calculated from equation (4.31) is negative, then the pressure will be set to zero; meaning that the negative pore pressure cannot exist (Itasca, 2016).

In fully coupled hydromechanical analysis where the fluid pressure affects the mechanical deformation and mechanical deformation affects the pressures, the rock and fluid counteraction will be in three aspects as (Itasca, 2016):

→ The effect of pore pressure on deformation and strength of fractured rock masses;
→ The effect of mechanical deformation on permeability which arises as a result of the change in the aperture of the fracture; and
→ The effect of mechanical deformation on pore pressure.

When the fracture is filled with the fluid, depending on the fluid pressure and applied normal stress, the fracture's normal deformation will be influenced. According to Walsh (1981), the effect of pore pressure and applied normal stress on normal deformation can be expressed as

$$\sigma'_n = \sigma_n - \alpha p_p \quad (4.32)$$

in which p_p is pore pressure and α is effective stress coefficient or Biot coefficient. Based on measurements of flow through simulated fractures carried out by Kranz et al. (1979), α can vary between 0.5 and 1.0 for tensile fractures with rough surfaces and fractures with smooth surfaces, respectively. Furthermore, since both tensile and shear failure conditions of the rock fractures are described in terms of the effective, not total, stress, hence the pore pressure can affect the strength of the rock fracture through the effective stress principle.

Mechanical aperture which may be considered as the average distance between two planes of a fracture, is a function of the mechanical deformation. On the other hand, the hydraulic aperture is trivially related to the mechanical aperture and in most of the cases the authors equate the mechanical and hydraulic aperture and directly use them in cubic law for calculation of fluid flow. However, comparison of the measured flow rates in a fracture with those predicted by the cubic law (equation 4.28) using the hydraulic aperture assumed to be equal to the mechanical aperture very often show significant disagreement; a summary of which has been given by Alvarez et al., 1995 (Itasca, 2016). Witherspoon (1980) introduced the following form of the cubic law:

$$q = -\frac{h_m^3}{12\mu_d F}p_{,x} \quad (4.33)$$

where F is a correction factor. Comparing equations (4.28) and (4.33) gives

$$h_H = fh_m \quad (4.34)$$

in which

$$f = \frac{1}{F^{1/3}} \quad (4.35)$$

The parameter f is a representative for the effect of the fracture's plane roughness on the tortuosity of the flow. For smooth or interlocked joint planes, f is approximated by unity while for mismatched joints with a small ratio of span to roughness height, f has values less than 1 (Itasca, 2016).

For a slightly compressible fluid in a deformable rock fracture with uniform aperture, the continuity equation has the form of (Itasca, 2016)

$$q_{i,i} = -\frac{\delta h}{\delta t} - c_f h \frac{\delta p}{\delta t} \quad (4.36)$$

Combining equation (4.28) and (4.36), we can obtain

$$\frac{\delta p}{\delta t} = \frac{h^2}{12\mu_d c_f} p_{i,i} - \frac{1}{c_f h} \frac{\delta h}{\delta t} \quad (4.37)$$

Equation (4.37) is the diffusion equation for the pressure inside the fracture (Itasca, 2016). Generally, the fracture aperture not only varies with local fracture stiffness and fluid pressure, but it is also a function of the mechanical response of rock mass. Hence, the second term in the right-hand side of the equation (4.37) is determined by coupling between fluid flow and mechanical deformation of the rock mass. In other words, this term is external or a "source" which, for undrained condition, indicates the pressure change in the fluid trapped within the fracture because of rock mass and, in particular, rock fracture deformation (Itasca, 2016).

In explicit time integration techniques, it is essential that the timestep size does not exceed the critical timestep. So that, in present explicit analysis of fluid flow it is required to limit the fluid timestep to

$$\Delta t_f = min \left[\frac{c_f V}{\sum_i k_i} \right] \quad (4.38)$$

In which the summation of the permeability factors, k_i, is extended to all contacts surrounding the flow-knot. With this regard, the minimum value of Δt_f over all flow-knots is the critical timestep in the analysis (Itasca, 2016).

As can be concluded from equation (4.38), the fluid timestep is inversely proportional to the fluid bulk modulus and joint transmissivity, which is proportional to aperture cubed, according to the cubic law. For typical joint apertures in practical problem settings, the fluid timesteps on the order of milliseconds are obtained. Furthermore, the first fraction of the second term in the right-hand side of equation (4.37) implies that the fluid trapped inside a fracture will increase the apparent joint stiffness by $1/c_f h$, thus possibly requiring a reduction in the mechanical timestep. Hence, these two together, will make the numerical analysis very time-consuming or impractical; meaning that this algorithm can only be applied in short duration simulations (Itasca, 2016).

In 3DEC, some tips are introduced to increase the timestep in practical analysis such as our case study. One of main tips is called "fast flow" which speeds up the coupled calculations by assuming incompressible fluid which might be a reasonable assumption when the rock is not so stiff relative to the fluid or when the aperture is so small (recalling aforementioned apparent joint stiffness). In this option it is required to define an apparent fluid bulk

modulus as equal to the material bulk modulus divided by the cube of the zone size (i.e., K/edge[3]; using the maximum value of each parameter for models with variable material properties and zone size) (Itasca, 2016). This option, as stated before, increases the fluid timestep in order to decrease the required time of calculations. For example, in our reference case, the fluid timestep was automatically set to a very high magnitude (over 24 hours), however it was manually limited to 60 seconds by the authors, results of which can be found in appendix section where it can be seen that some results such as the value of the fluid pressure at the end of stimulation is as equal as the normal flow calculations, but its evolution during stimulation period shows an oscillation behavior which its characteristics are strongly dependent upon the chosen fluid timestep by the user (figure A2.4). The authors, spent over six months on characterizing the oscillating behavior of the fluid pressure during stimulation period and when it was tried to define a criterion to pick-up appropriate onset time of pressure build-up at measuring point, the effect of the fluid timestep was identified. Then, the reference model was ran in normal flow mode and found that the waveform evolution in fluid pressure was a numerical effect rather than a physical process. The authors highly recommend future users of the 3DEC, to first do a simple simulation using "fast flow" option by setting various values of maximum fluid timestep limit and then to compare the results to the simulation in normal flow mode for checking the consistency with great cares taken into account. In the present work, the normal flow mode is then used.

Figure 4.11 illustrates the block and embedded fracture as well as the injection point at approximately the center of the fracture at depth of 4.7 km. The fracture cuts the block in two parts of light blue and light green. These two parts have the identical properties and are elastic, isotropic, and homogeneous. The reason behind this is that in 3DEC blocks cannot be partially cut, so all the 3DEC joints are necessarily bigger than the corresponding fractures in the DFN (Itasca, 2016). We can deal with this issue by assigning different joint properties to areas lying inside of the circular fractures and areas outside of the circular fractures. It means that, the areas of the fracture plane located outside of the finite-size circular fracture should not have any effect on the fracture's hydromechanical behavior, even though the 3DEC will recognize that district as fracture. For that, it is important to assign appropriate material properties to that district of the fracture plane in such a way to achieve as same hydromechanical behavior as surrounding rock matrix. Therefore, the fracture's shear and normal stiffness must be defined as equal as the stiffness of rock matrix as is explained. For that, the normal stiffness of the fracture located in the area outside of circular fault with initial aperture of 14e-05 m must be identical with the normal stiffness of a cubic element of surrounding rock matrix with side size of 14e-05 m.

Considering an infinitesimal isotropic cubic specimen of surrounding rock matrix with side size of A_0 (initial aperture of the fracture) located on the fracture plane, as shown in figure 4.12, its normal stiffness in the direction of the fault normal (K_n) can be obtained as

$$K_n = \frac{\sigma_{nn}}{u_{nn}} \quad (4.39)$$

where σ_{nn} and u_{nn} are normal stress and normal displacement.
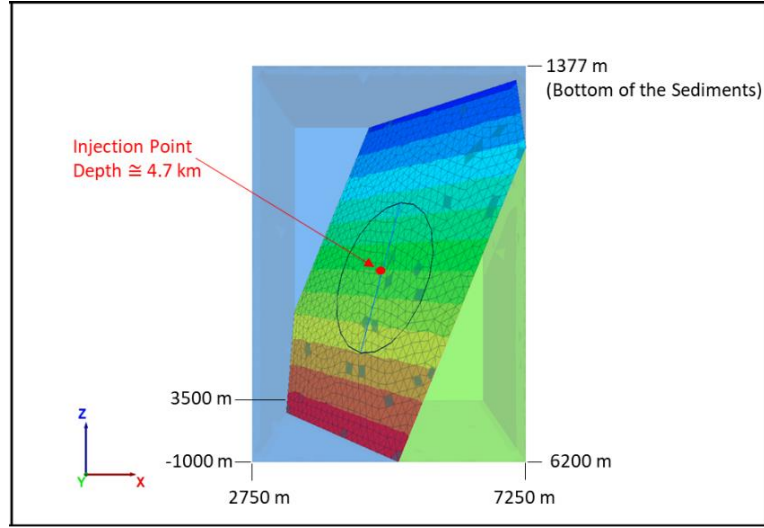
Figure 4.11. 3DEC model of the block, embedded fracture and injection point at approximately 4.7 km; the height of the modelled block starts from the bottom of the sedimentary layers and stops at 6.2 km as it can be seen from the figure.
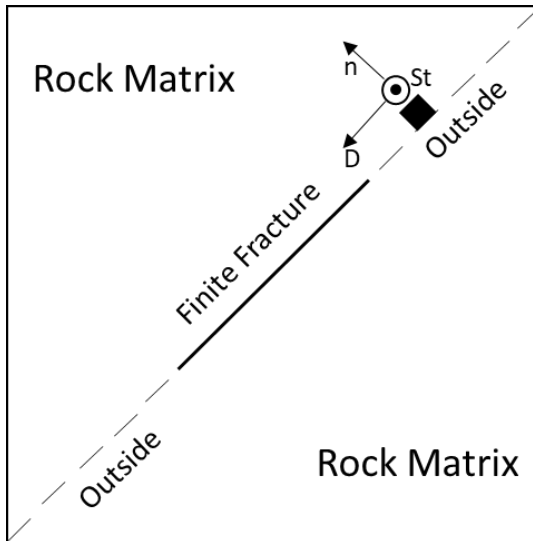
Figure 4.12. Schematic vertical intersection of a block with an embedded finite fracture; the outside areas of the fracture are shown by dashed lines and a black cube with side size of A_0 is located outside of the fracture. A frame of reference can also be assumed as n-D-St with axis respectively parallel to normal, dip direction, and strike of the fracture as represented in the figure

Stress tensor with respect to the $\boldsymbol{n}$, $\boldsymbol{D}$, $\boldsymbol{St}$ frame of reference, respectively, for axis parallel to normal, dip direction, and strike of the fault, as shown in figure 4.12, will be

$$\begin{bmatrix} \sigma_{nn} & \sigma_{nD} & \sigma_{nSt} \\ \sigma_{Dn} & \sigma_{DD} & \sigma_{DSt} \\ \sigma_{Stn} & \sigma_{StD} & \sigma_{StSt} \end{bmatrix} \quad (4.40)$$

For such a cube, the inverse of the Hooke's law is as (Jaeger et al., 2007)

$$
\begin{bmatrix} \varepsilon_{nn} \\ \varepsilon_{DD} \\ \varepsilon_{StSt} \\ 2\varepsilon_{StD} \\ 2\varepsilon_{nSt} \\ 2\varepsilon_{nD} \end{bmatrix} = \frac{1}{E} \begin{bmatrix} 1 & -\vartheta & -\vartheta & 0 & 0 & 0 \\ -\vartheta & 1 & -\vartheta & 0 & 0 & 0 \\ -\vartheta & -\vartheta & 1 & 0 & 0 & 0 \\ 0 & 0 & 0 & 2+2\vartheta & 0 & 0 \\ 0 & 0 & 0 & 0 & 2+2\vartheta & 0 \\ 0 & 0 & 0 & 0 & 0 & 2+2\vartheta \end{bmatrix} \begin{bmatrix} \sigma_{nn} \\ \sigma_{DD} \\ \sigma_{StSt} \\ \sigma_{StD} \\ \sigma_{nSt} \\ \sigma_{nD} \end{bmatrix} \qquad (4.41)
$$

where ε is components of strain tensors at fracture plane. The strain at direction of the fracture normal can then can be determined as

$$
\varepsilon_{nn} = \frac{1}{E}(\sigma_{nn} - \vartheta\sigma_{DD} - \vartheta\sigma_{StSt}) \qquad (4.42)
$$

To have the stress tensor represented by (4.40), stress transformation can be utilized to transfer principal stress tensor to first stress tensor at geographical coordinate system and then to stress tensor acting on the fracture plane coordinate system. The effective principal stress tensor for normal faulting regime of current study is as

$$
\tilde{\sigma} = \begin{bmatrix} -71.53 & 0 & 0 \\ 0 & -65.61 & 0 \\ 0 & 0 & -17 \end{bmatrix}
$$

The transformation matrix of (4.20) is used to have stress tensor with respect to the geographical frame of reference. The a, b, and c angles (Euler angles) for this case are respectively $80°$ (azimuth of S_{hmin}), $90°$, and $0°$, according to table 4.3. Then, using equation (4.22) will read

$$
\widetilde{\sigma_g} = \begin{bmatrix} -64.14 & 8.31 & 0 \\ 8.31 & -18.47 & 0 \\ 0 & 0 & -71.53 \end{bmatrix}
$$

The transformation matrix in order to transform the stress tensor at geographical coordinate system onto fracture's frame of reference is (Zoback, 2007)

$$
R_2 = \begin{bmatrix} \cos(\text{str}) & \sin(\text{str}) & 0 \\ -\sin(\text{str})\cos(\text{dip}) & \cos(\text{str})\cos(\text{dip}) & \sin(\text{dip}) \\ -\sin(\text{str})\sin(\text{dip}) & \cos(\text{str})\sin(\text{dip}) & -\cos(\text{dip}) \end{bmatrix} \qquad (4.43)
$$

where "str" is the fault strike and "dip" is the fault dip (positive dip if fault dips to the right when the fault is viewed in the direction of the strike). To calculate the stress tensor in a fault plane coordinate system, $\widetilde{\sigma_f}$, we once again use the principles of tensor transformation such that (Zoback, 2007)

$$
\widetilde{\sigma_f} = R_2 \widetilde{\sigma_g} R_2^T \qquad (4.44)
$$

Then the $\widetilde{\sigma_f}$ will be

$$
\widetilde{\sigma_f} = \begin{bmatrix} -56.27 & -6.24 & -18.11 \\ -6.24 & -66.74 & 13.91 \\ -18.11 & 13.91 & -31.13 \end{bmatrix}^*
$$

Which is in fact stress tensor represented in equation (4.40).

ε_{nn} by definition is the fractional shortening of an infinitesimal line element that is initially oriented along the n-axis and since the diagonal components of the strain tensor do not contain rotation components (Jaeger et al., 2007) then ε_{nn} will be

$$\varepsilon_{nn} = \frac{u_{nn}}{A_0} \quad (4.45)$$

Substituting strain as equation 45 into equation 42 and solving it against displacement will lead to

$$u_{nn} = \frac{1}{E}(\sigma_{nn} - \vartheta\sigma_{DD} - \vartheta\sigma_{StSt})A_0 \quad (4.46)$$

where σ_{DD} is stress in the direction of fault dip, and σ_{StSt} is stress in the direction of fault strike. Substituting equation (4.46) in equation (4.39) and doing some simplification and manipulation, magnitude of rock normal stiffness will be

$$K_n = \sigma_{nn}E/[\sigma_{nn} - \vartheta(\sigma_{DD} + \sigma_{StSt})]A_0 \quad (4.47)$$

Hence, the normal stiffness of the fracture must be equal with equation (4.47) in order to equalize its normal displacement with displacement of the surrounding rock matrix parallel with normal of the fracture. Substituting values of E (25 GPa) and ϑ (0.29) of rock matrix and h_0=14e-05 m height (initial aperture of the fracture in zero stress condition is 14e-05 m), 56.27, 66.74, and 31.13 MPa, respectively, for σ_{nn}, σ_{DD}, and σ_{StSt} (determined from matrix with superscript of asterisks at page 27) yielded to 3.6e14 Pa/m of normal stiffness for the areas of outside of the fracture. If we assume that the hanging wall of the fault slides along the slip direction obtained in previous section, then it can be considered that the shear stiffness or shear modulus of the area outside of the circular fault will be, using the inverse of the Hooke's law in equation (4.41), equal to

$$G = \frac{\sigma_{DSt}}{2\varepsilon_{DSt}} = \frac{\sigma_{DSt}}{2\left(\frac{1+\vartheta}{E}\right)\sigma_{DSt}} = \frac{E}{2(1+\vartheta)} \quad (4.48)$$

By substituting values of E (25 GPa) and ϑ (0.29) of rock matrix the G will be 9.69 GPa; its cohesion and friction angle were also defined to a high range to prevent any slip to take place at the areas outside of the fracture. The apertures could be any small magnitudes greater than zero. Hence, we just defined them identical with the initial hydraulic aperture of the circular finite fracture. These properties are summarized in table 4.7.

Table 4.7. Physical and mechanical properties assigned to the outside of the circular fracture

Outside of the Circular Fracture
K_n = 3.6e14 Pa/m
K_s= 9.69 GPa/m
φ= 45°
S_0= 1e40 Pa
A_0= A_{res}= A_{max}= 14e-05 m

4.4   Simulation Results

4.4.1   Fluid Pressure Evolution

By simulating the injection procedure illustrated in figure 4.1b, we observed that the fluid pressure at injection point rises sharply to a well-head pressure (WHP) of approximately 13 MPa (WHP is calculated by subtracting hydrostatic pressure at injection point from downhole pressure, DHP) and then continuously increases to a maximum value of over 20 MPa at the end of 24 hour injection which is somehow larger than observed field WHP during the first step of stimulation of GPK2 at the year 2000 (11-12 MPa), even though the sharp rise of WHP is initially similar to that of field observation. Figure 4.13 is WHP variation during injection period at injection point; however, this value is dependent on the magnitude of initial hydraulic aperture of fracture as shown in figure 4.13.
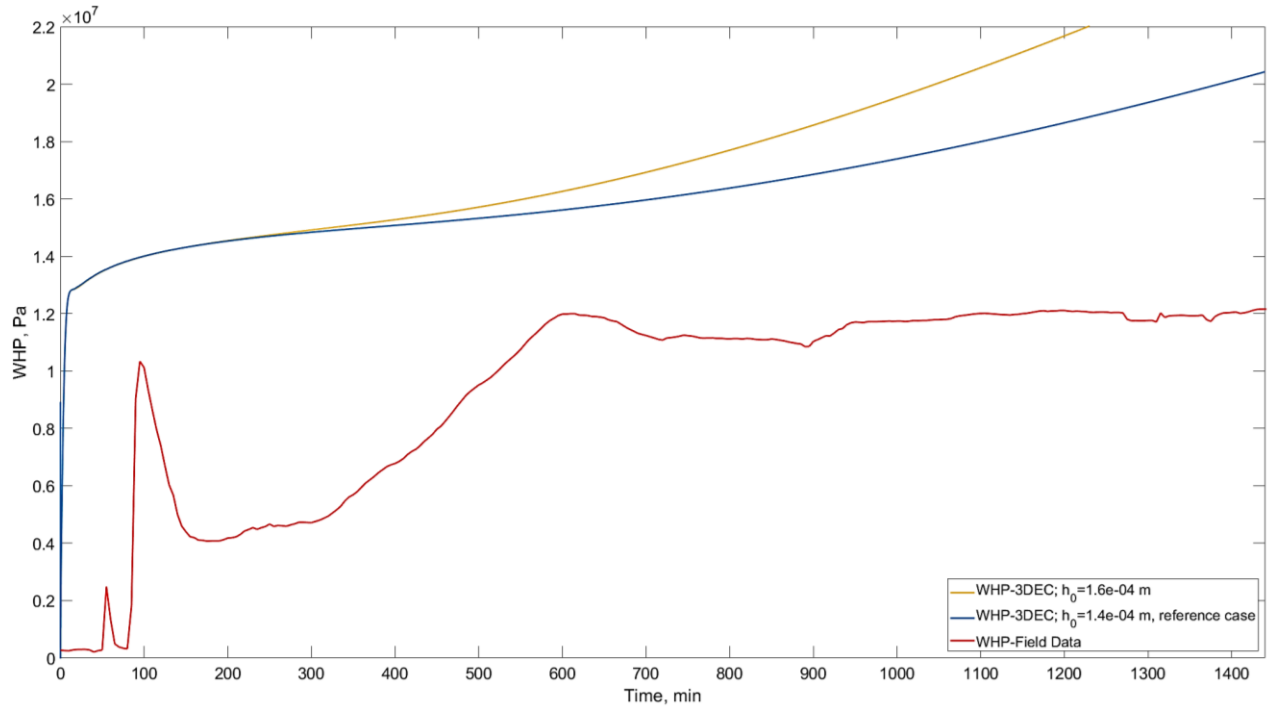
Figure 4.13. Numerical WHP evolution in time at injection point located at approximately 4.7 km depth for fractures with different initial hydraulic apertures in comparison with WHP observed in the field; the numerical WHP (blue curve) suddenly rises to a value of approximately 13 MPa and then continuously increases to over 20 MPa at the end of 24 hours of injection which is higher than field observation of WHP, being approximately stable at 12 MPa (red curve)

To investigate the pressure front migration through the fracture, the onset time of pressure build-up at some measuring points shown in figure 4.14 are determined. These measuring points are the nearest possible flow-knots to the fictitious straight lines connecting point 8, to pints 1 and 15. Using this nearest neighbor interpolation to relate distance from injection point to onset time of pressure build-up is rather a crude approximation especially when the mesh size is large and the pressure propagation is not perfectly circular, but in current study this effect is disregarded to avoid time-consuming discretization with finer mesh sizes. This onset time is considered when the WHP at a measuring point exceeds 1 MPa, as described in figure 4.15. The superimpose of pressure evolution in time for a period starting from pressure build-up onset time (subtracting the time period behind the onset time from 24 hours of injection duration) up to the end of injection period for all 15 measuring points are shown in figure 4.16. Figure 4.17 is a plot of depth versus onset time on the left-hand side and distance versus onset time on the

right-hand side. The red curves in the left-hand side graph represent the pressure curves of figure 4.16. Furthermore, it can be seen on the right-hand side graphs of figure 4.17 that the upward and downward velocities of pressure propagation are approximately the same and obey a power-law function with exponent of 0.5 or better to say $\sqrt{t}$ propagation process.
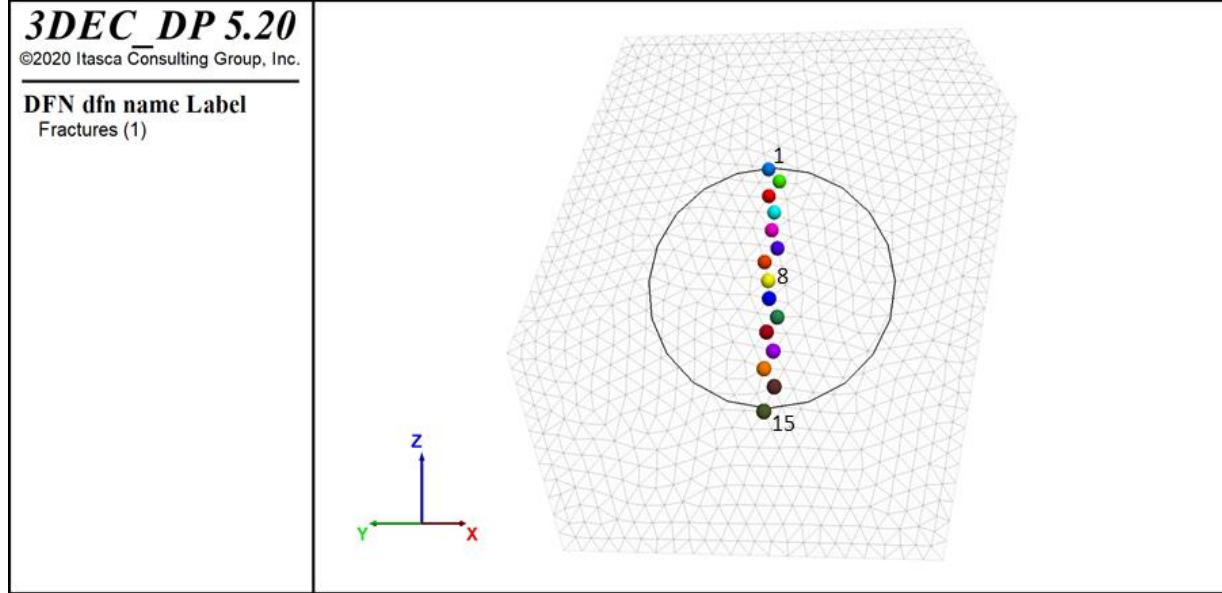
Figure 4.14. Locations of the measuring points on the fracture indicated by colored spheres; the discretized polygon is the fracture plane containing the finite size circular fracture (black circle); the yellow sphere (sphere number 8) is the injection point
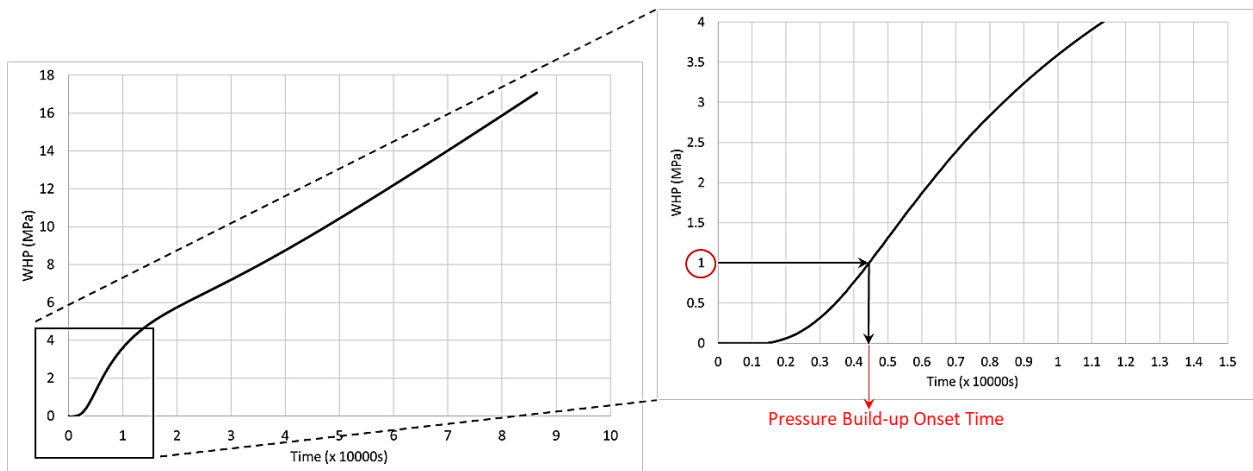
Figure 4.15. Illustration of pressure build-up onset point selection at a measuring point; the left-hand side graph shows the WHP evolution at measuring point during the injection period while the right-hand side graph is the zoomed exhibition of the black square of the left-hand side graph. As it can be seen from RHS graph, the time-point when the WHP is 1 MPa, is opted as the onset time of pressure build-up at corresponding measuring point.
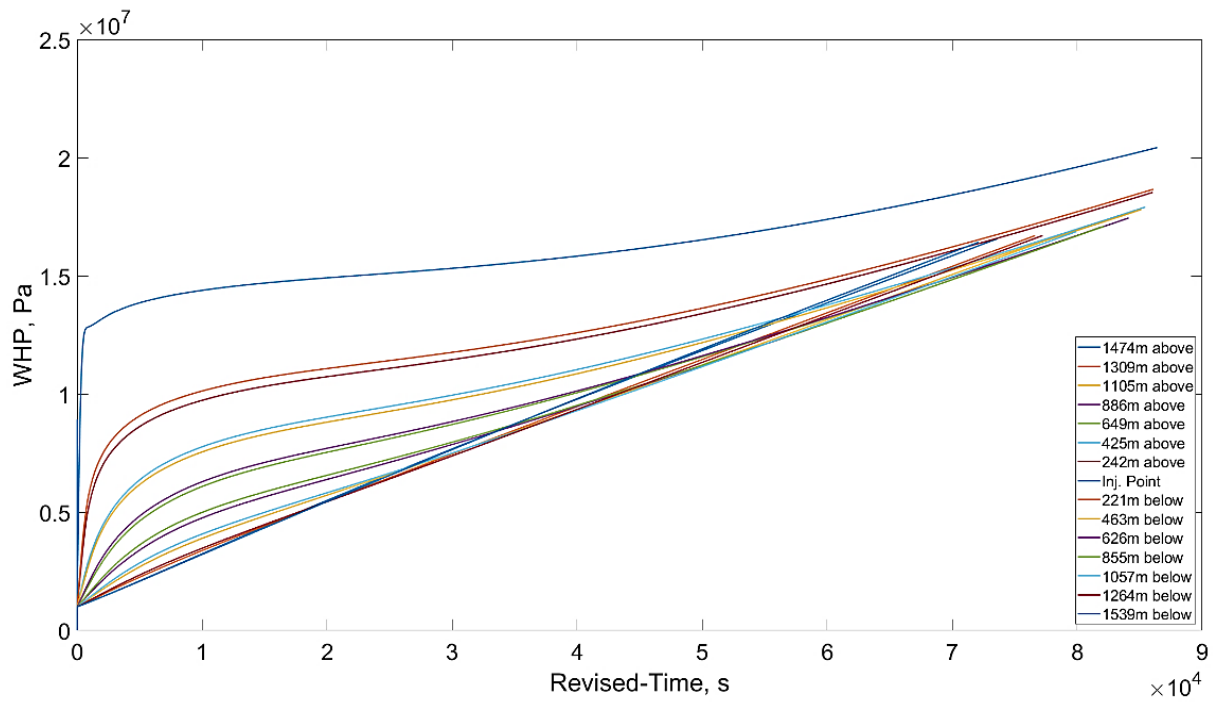
Figure 4.16. Superimpose of WHP curves as a function of time for measuring points. The time period starts from the onset time of pressure build-up at measuring points which is determined using the process described in figure 4.13, so that, all the pressure curves start from 1 MPa except at injection point where the flow-knot volume at this point encountered a sudden increase due to high rate of fluid injection and had some fluctuation at initial seconds and then stabilized
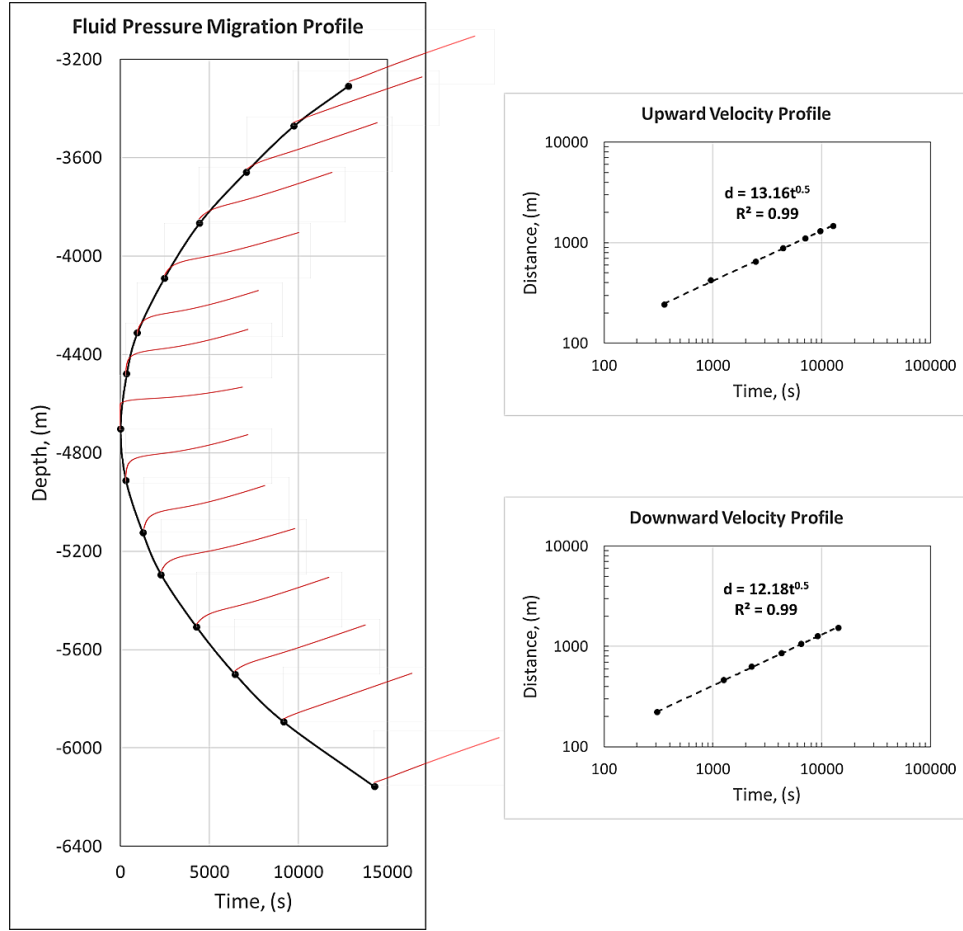
Figure 4.17. Pressure front migration from injection point at depth of about 4.7 km to the top and bottom frontiers of the fracture shown for measuring points; the velocity of fluid pressure migration along the fracture, as it can be seen in the figure, obeys a power-law function with exponent of 0.5

4.4.2 Effective Hydraulic Diffusivity

Shapiro et al., 1997, evaluated spatio-temporal distribution of approximately over 400 microseismic events induced during hydraulic fracturing experiment of KTB borehole in Germany in order to estimate permeability. At this study, fluid injection in KTB was approximated by a point source fluid injection into an infinite homogeneous, isotropic, poroelastic, and saturated medium for which the pore pressure diffusion can be considered as the mechanics of poroelastic media.

The Biot (1962) equations describe the poroelastic deformation's linear dynamics. These equations predict the existence of two compressional waves and one shear wave in the system in the general case, while neglecting the shear wave in the fluid. The first shear and compression waves are typical seismic P and S waves moving across the medium. For frequencies below the crucial Biot frequency (which, for the medium under consideration, is often of the order of several MHz), the second type of compressional wave is a diffusional wave. It is analogous to the pore-pressure diffusion mechanism which is as below in the extremely low-frequency range

$$\frac{\partial p}{\partial t} = D\nabla^2 p \quad (4.49)$$

82

that is the diffusion equation for the pore pressure perturbation in the rock mass. Shapiro and associates, by ignoring all non-mechanical (e.g. chemical and electro-chemical) solid –fluid interactions, solved pore pressure diffusion equation for their simulated model assuming a boundary condition as an initial pore pressure perturbation being supplied as a function of time, $p_0(t)$, on a tiny spherical surface of radius a, with the injection point as its center. In the case of a time-harmonic perturbation, $p_0(t) = p_0 exp(-iwt)$, the solution of equation (4.49) fulfilling aforementioned boundary condition is as follows:

$$p(r,t) = p_0 e^{-i\omega t} \frac{a}{r} exp\left[(i-1)(r-a)\sqrt{\frac{\omega}{2D}}\right] \quad (4.50)$$

where ω is angular frequency and r is the distance from the injection point. It can be seen from equation (4.50) that the solution is an increasingly attenuating spherical wave. This is the Biot theory's second compressional wave, with an attenuation coefficient equal to $\sqrt{\omega/2D}$, the reciprocal diffusion length, and a slowness equal to $1/\sqrt{\omega 2D}$, the reciprocal velocity of relaxation.

Now, the following reasoning may be used to estimate the diffusivity D. The step function is approximated by the injection signal: $p_0(t) = 0$ if $t < 0$ and $p_0(t) = 1$ if $t > 0$. However, the rectangular pulse $p_0(t) = 0$ if $t < 0$, $t > t_0$, and $p_0(t) = 1$ if $0 \leq t \leq t_0$ (since the development of the injection after the event's triggering is irrelevant to this event) is what causes a seismic event to be triggered at a time t_0. The range of this signal's prominent frequencies is from 0 to $\omega_0 = 2\pi/t_0$. The pore pressure perturbation's relaxation periods are thus of the order of $r_0\sqrt{t_0/(4\pi D)}$ and greater if the event happened at a distance of r_0. However, it is anticipated that the initial triggerings may take place prior to a major relaxation (i.e., a significant drop in pore pressure). Consequently, for the very first occurrences

$$t_0 \leq r_0\sqrt{t_0/(4\pi D)} \quad (4.51)$$

This disparity leads to the following

$$D \leq \frac{r_0^2}{4\pi t_0} \quad (4.52)$$

Using above arguments on about 9000 seismic events induced during hydraulic stimulation of GPK1 well of Soultz-sous-Forêts at 1993, Shapiro et al., 2002, estimated an effective hydraulic diffusivity of 0.05 m²/s. The diffusion distance of pore pressure perturbation from injection point can be obtained by reordering of equation (4.52) as

$$r = \sqrt{4\pi D t} \quad (4.53)$$

Comparison of which with equations of fitted lines shown in right sub-figures of figure 4.17 leads to an average effective hydraulic diffusivity of ~13 m²/s. This value is approximately consistent with the results of Calo et al., 2011, where rapid migration of more than 1000 m in 3 h was observed. Substituting these observations into equation (4.53) as $r \approx 1000$ m and $t \approx 10500$ s gives $D \approx 8$ m²/s. This discrepancy may be due to the fact that in the present numerical simulation, the surrounding rock matrix is impermeable and thus there is no leakage in the fracture, unlike in the in-situ reservoir.

4.4.3   Hydraulic Aperture Evolution

In 3DEC, normal and shear joint stiffness are represented by linearly elastic springs. The normal stiffness of a fracture (K_n) in 3DEC is constant value defined by the user (3DEC manual, 2016); meaning the existence of a linear relation between effective normal stress (σ'_n) and joint displacement ($d\delta$) (Hart, 1993) as defined by equation (4.39) or

$$\sigma'_n = K_n d\delta \quad (4.54)$$

In 3DEC, the relation between hydraulic aperture and effective normal stress is a bilinear curve shown in figure 4.18. The hydraulic aperture (h_H) is obtained, in general, (3DEC manual, 2016) as

$$h_H = h_{H0} + d\delta \quad (4.55)$$

where h_{H0} is the joint aperture at zero normal stress or initial hydraulic aperture which is defined by the user. In addition to h_{H0}, residual (h_{Hres}) and maximum (h_{Hmax}) hydraulic apertures should also be defined by the user. Below residual hydraulic aperture and above maximum hydraulic aperture the mechanical aperture (h_m) will not have any effect on joint permeability. Therefore, in 3DEC, the hydraulic aperture is always equal with the mechanical aperture except when the mechanical aperture exceeds h_{Hmax} or h_{Hres} (3DEC manual, 2016) (figure 4.18). It can also be understood from the fact that in 3DEC the fractures are simulated as two parallel plates, so that any change in the mechanical aperture will consequently change the hydraulic aperture; however, to mimic the non-zero residual hydraulic aperture found in the field or laboratory despite a near-zero mechanical aperture, in 3DEC the hydraulic aperture is not equal to the mechanical aperture when it falls below h_{Hres}. The maximum hydraulic aperture is also defined by the user to improve explicit calculations (3DEC manual, 2016).

Comparing equations (4.54) and (4.55) reveals that in 3DEC, the relation between effective normal stress ($\sigma'_n = S_n - P_p$) and hydraulic aperture of the fracture will be linear, dependent on the magnitude of the fracture normal stiffness. One may also state that the relation between fluid pressure and fracture aperture are linear owing to constant fracture stiffness in 3DEC.
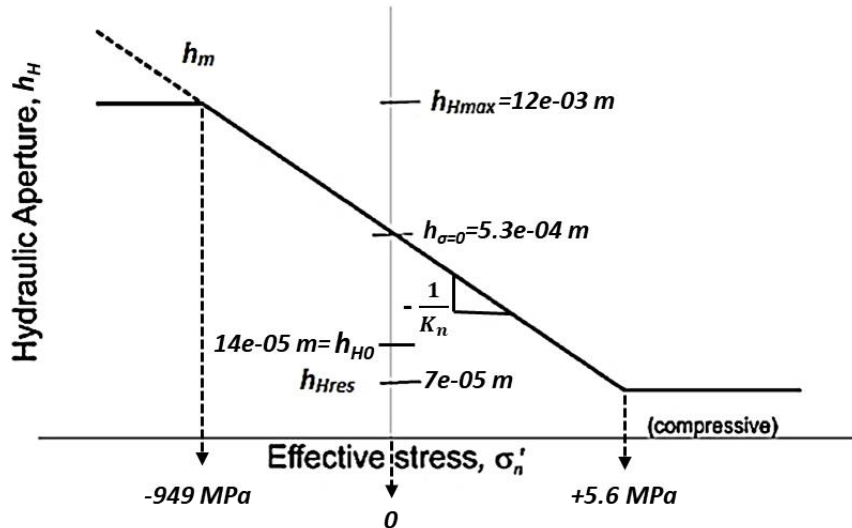
Figure 4.18. Idealized relation between hydraulic aperture and effective normal stress for a rock joint (reproduced from 3DEC manual, 2016)

If the variation of the hydraulic aperture as a function of the effective normal stress acting on the fracture plane is plotted as shown in figure 4.19 for the injection point, the linear relationship between hydraulic aperture and effective stress can be seen, as shown in figure 4.18, where the slope of the fitted line on the curve is the negative inverse of the effective normal stiffness of the fracture (-1/-1.255e-11 = 79.7 GPa); approximately equal to 80 GPa/m assigned to the model.
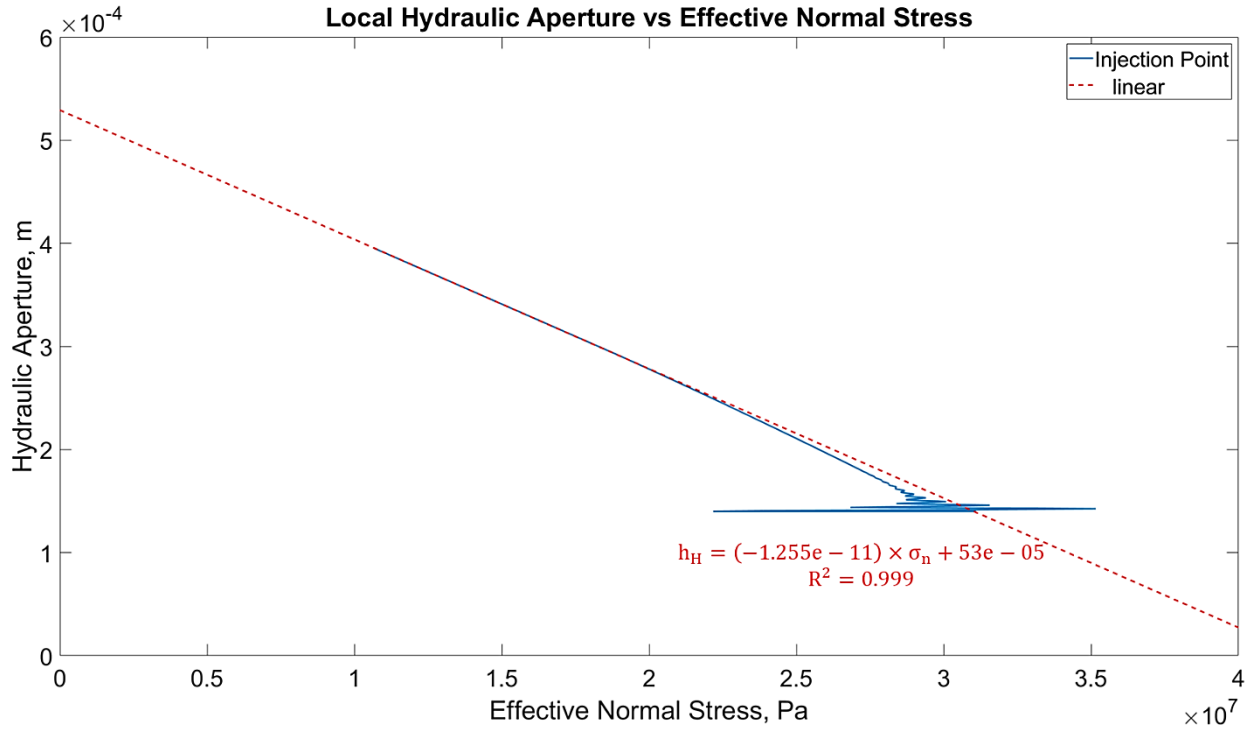
Figure 4.19. Local hydraulic aperture variation versus effective normal stress values at injection point where compressive stress is positive; as it can be seen the numerical relation between effective normal stress acting on the fracture plane and the hydraulic aperture at injection point is linear in which the slope of the fitted line is approximately negative inverse of the normal stiffness of the fracture (-1/-1.255e-11 = 79.7 GPa/m); furthermore, the y-intercept of the graph is the hydraulic aperture at zero effective normal stress ($h_{\sigma=0}$) or h_{Hmax}

Figure 4.21 illustrates fracture opening migration velocity along the fracture towards upper and lower edges of the fracture along its diameter. The onset of aperture increase considered when the change of aperture exceeded the 5% of initial hydraulic aperture. Here, knowing the initial hydraulic aperture of 14e-05 meters, the onset time will be when the hydraulic aperture exceeds 14.7e-05 meters which is equal to the sum of initial hydraulic aperture and 0.05 times of that. This process is demonstrated in figure 4.20. The red curves in figure 4.21 are derived using the process explained in figure 4.20. To avoid any boundary condition effect on hydraulic aperture variation at the edges of the fracture, the data of two last measuring points in either side of the fracture diameter are not considered for evaluations of hydraulic aperture variation in time. As it can be seen in the figure 4.21 (sub-figures at the right-hand side), the velocity obeys a power-law function with exponent of 0.49 just as pressure propagation.
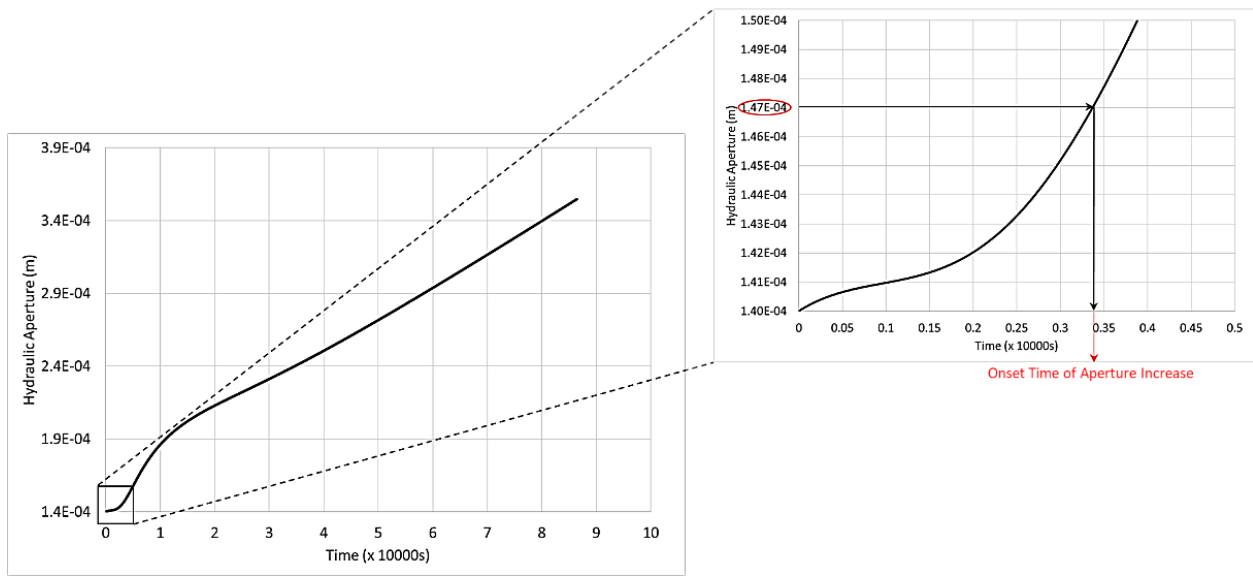
Figure 4.20. Illustration of onset point selection for aperture increase at a measuring point; the left-hand side graph shows the hydraulic aperture evolution at measuring point during the injection period while the right-hand side graph is the zoomed exhibition of the black square of the left-hand side graph. As it can be seen from right-hand side graph, the time-point when the hydraulic aperture is 1.47e-04 meters, is opted as the onset time of aperture increase at corresponding measuring point
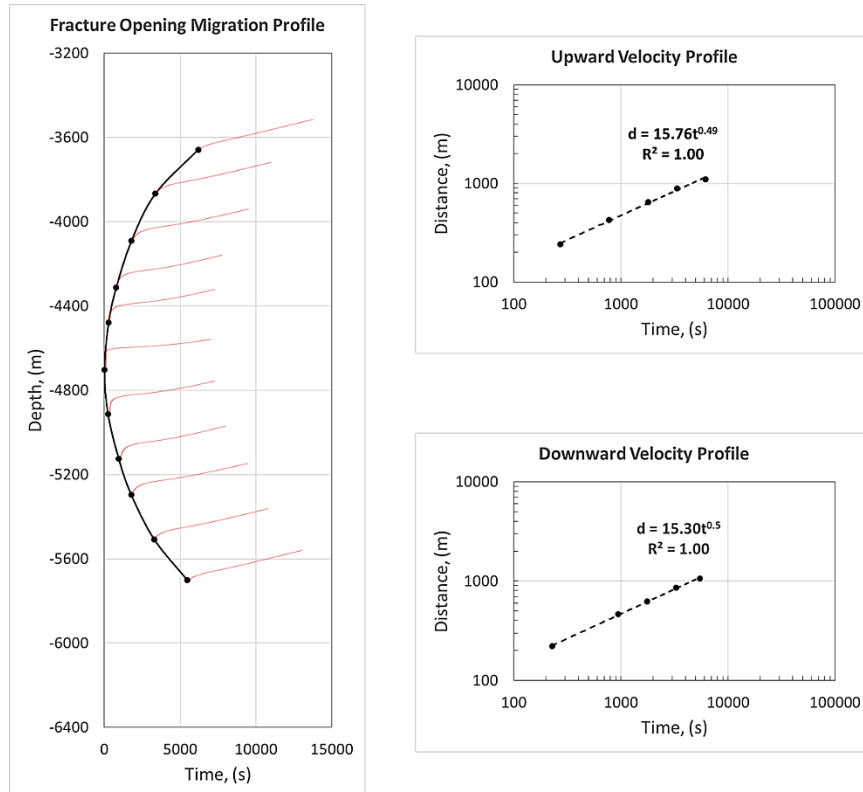
Figure 4.21. Increase of hydraulic aperture from injection point at about 4.7 km to the top and bottom frontiers of the fracture shown for measuring points located at fracture's diameter; the velocity of fracture opening along the fracture, as shown in the figure, also obeys power-law a function with exponent of about 0.5

86

Furthermore, looking at local hydraulic aperture variation in time at injection point in figure 4.19 clearly reveals the fact that the propagation of hydraulic aperture and fluid pressure along the fracture are exhibiting the same behavior; implying that the variation of hydraulic aperture and fluid pressure during injection period are linearly related to each other depending on the magnitude of fracture normal stiffness, consistent with figure 4.18.

To better understand the $\sqrt{t}$ behavior of the pressure front migration, we explore the impact of the injection rate. As a first attempt, a variable flow rate of injection, $Q(t) = 0.00001 \times t$ in which $Q(t)$ is variable flow rate and t is time, is applied to the injection point and the velocity profiles were plotted. In this case the flow rate increased by 0.00001 m³/s at each second contrary to the fixed flow rate of 0.03 m³/s of reference case. By applying such variable flow rate with time to the model, it was expected to have a linear velocity profile in both upward and downward migration. A fluid volume $(V(t) = \int_0^t Q(t)dt = Qt = 0.03 \times 86400 = 2592 \ m^3)$ as equal as reference case was injected to the fracture for 22768 seconds $(V = \int_0^t Q(t)dt = \int_0^t (0.00001 \times t)dt = \frac{1}{2} \times 0.00001 \times t^2)$ and the pressure propagation profile and velocity profiles were plotted as figure 4.22 in which a linear relation between pressure propagation distance and time is obvious.
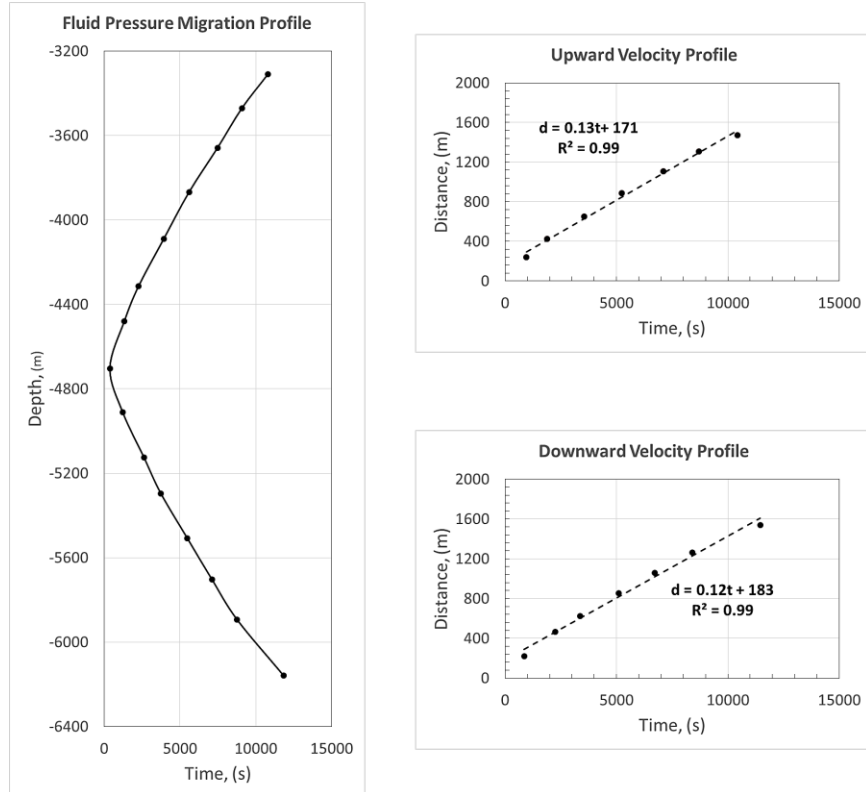
Figure 4.22. Pressure front migration from injection point at about 4.7 km to the top and bottom frontiers of the fracture shown for measuring points for variable flow rate case; the velocity of fluid pressure migration along the fracture, as it can be seen in the figure, obeys a linear function

4.4.4   A simple Liftoff Model

Lengliné et al., 2017, proposed a simple hypothesis for the migration of the seismic activity occurring during hydraulic stimulations. It is in fact a statement of a pressure front migration radius, *r(t)*, and a constant aperture, *h*, behind it, using the injected fluid volume, *V(t)*, during stimulation time *(t)* assuming incompressibility of the

injected fluid and that the seismicity expands over a disk of radius r. There is also an implicit assumption that once the pressure exists in the fracture, the aperture jumps from zero to h without any stiffness effect. This relationship is expressed as

$$r(t) = \sqrt{\frac{\int_0^t Q(t')dt'}{\pi h}} \quad (4.56)$$

where

$$V(t) = \int_0^t Q(t')dt' \quad (4.57)$$

is injected volume at different flow rates of $Q(t')$ at different time-steps of dt'. Supposing that the injected fluid migrates over a disk of radius r, then injected volume can be calculated as

$$V(t) = \pi h r^2 \quad (4.58)$$

Replacing equation (4.58) in equation (4.57) and doing some manipulation and reordering will yield to equation (4.56). Equation (4.56) predicts the radius of pressure propagation by assuming a constant aperture throughout the fracture in which the fluid flows.

For our cases of study, it is attempted to implement the equation introduced by Lengliné et al., 2017, in 3DEC in order to have a prediction of pressure propagation using this equation for problems in which the fracture aperture is variable with pressure. For that, the average hydraulic aperture throughout the fracture at each time-step of numerical modeling is used, as a crude approximation of aperture in position and time, to determine the radius of pressurized zone. Figures 23 and 24 show hydraulic aperture profile versus distance from the injection point for both constant and variable flow rate cases at 14284 and 11382 seconds, respectively.

Additionally, average hydraulic aperture in figure 4.23 is approximately 1.9e-04 meters. Using definition of hydraulic diffusivity as equation (4.60) and assuming 1e-03 Pa.s and 5e-10 1/Pa respectively for dynamic viscosity and compressibility of the water, the effective hydraulic diffusivity will be 6000 m^2/s. Worth to keep in mind that this value is for a rigid fracture (or a low fluid pressure) in which solid part does not deform.

Shapiro et al, 1997, by taking the assumption of correspondence of seismicity front to the pressure front, introduced an equation to calculate diffusivity employing distance of seismic activity from well and time of seismic activities as

$$r = \sqrt{4\pi D t} \quad (4.59)$$

Where r is distance from well, D is hydraulic diffusivity and t is time of seismic activity. Doing some manipulation on equation (4.59) and comparing it to the equation of fitted lines to variation of distance with time shown in right sub-figures of figure 4.17 yields to upward and downward hydraulic diffusivity of 13.8 and 11.8 m^2/s, respectively. These values are for deformable fractures simulated by 3DEC in reference case of current study compared to the hydraulic diffusivity of heterogeneous crystalline reservoir of Soultz-sous-Forêts (from depth of 2500 to 3500 meters) equal to 0.05 m^2/s estimated by Shapiro et al., 2002.
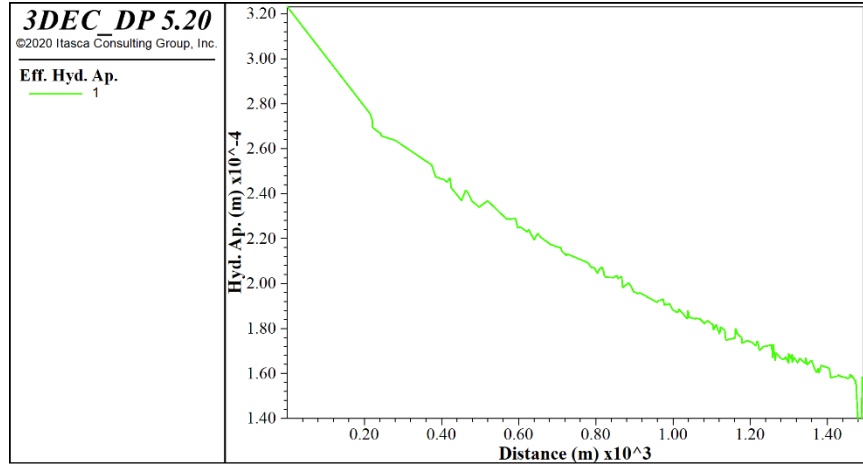
Figure 4.23. Hydraulic aperture profile along the fracture in terms of distance from injection point at 14284 seconds after start of injection used to predict the radius of pressure propagation for constant flow rate case based on Lengliné et al., 2017, hypothesis; this profile is progressively updated at each time-step of numerical modeling to generate the curves plotted in figure 4.25
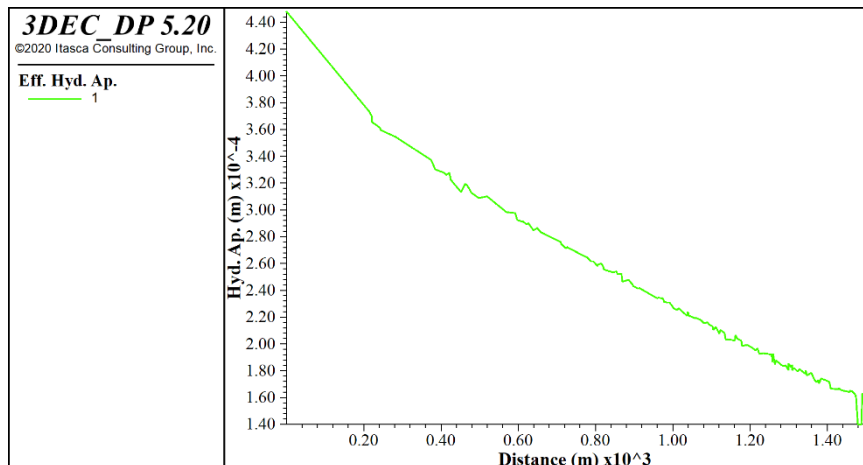
Figure 4.24. Hydraulic aperture profile along the fracture in terms of distance from injection point at 11382 seconds after start of injection used to predict the radius of pressure propagation for variable flow rate case based on Lengliné et al., 2017, hypothesis; this profile is progressively updated at each time-step of numerical modeling to generate the curves plotted in figure 4.26

The results of generalizing Lengliné et al., 2017, hypothesis for the reference cases of current report with both constant and variable flow rates are shown in figures 25 and 26, respectively. The comparison is done for the time period when the overpressure arrives the furthest measuring point on the fracture plane. These time periods are 14284 and 11832 seconds for respectively constant and variable flow rate cases. As it can be seen, in both cases, the predicted radius by Lengliné et al., 2017 hypothesis (about 1370 meters and 1627 meters, respectively) has a good agreement with the radius of overpressure at numerical method (about 1539 meters).
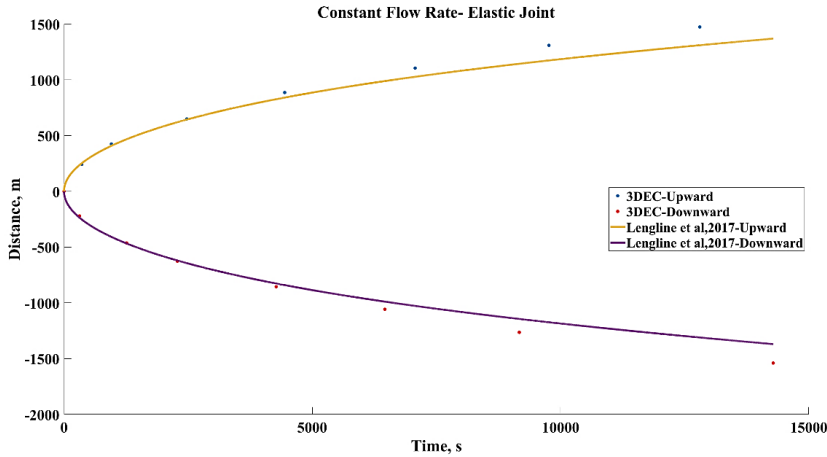
Figure 4.25. Pressure front position (with respect to the injection point) as a function of time for constant flow rate case based on Lengliné et al., 2017, hypothesis (solid lines) and 3DEC (blue and red points)
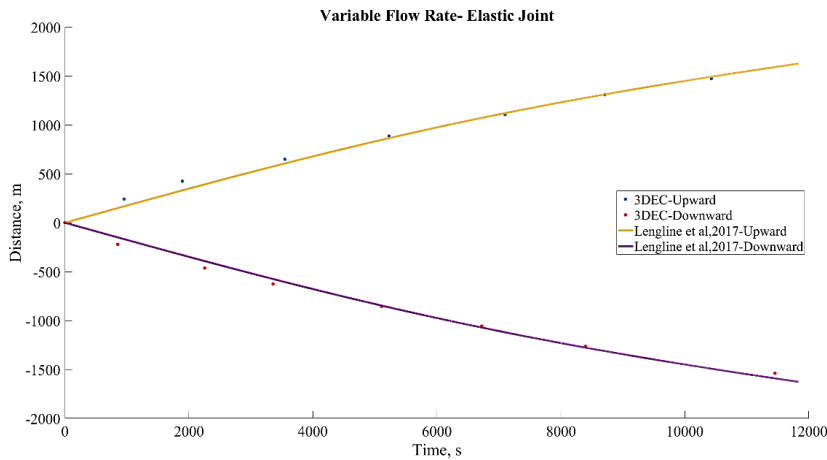
Figure 4.26. Pressure front position (with respect to the injection point) as a function of time for variable flow rate case based on Lengliné et al., 2017, hypothesis (solid lines) and 3DEC (blue and red points)

4.4.5 An Advanced Model

The Lengliné et al., 2017, argument is a simple advective model (assuming a constant aperture along the open part of the crack and a sharp front between open and close part of the crack with no diffusion equation), so it is rather a geometrical dispersion.

Here, we discuss Murphy et al., 2004, approach which is more advanced 1D model, in particular to explain the origin of the front. It is, in fact, a comprehensive study which converts linear fluid dynamic equation in terms of aperture rather than pressure. So that, Pressure and other flow parameters can be obtained from the aperture solution through joint compressibility relationships. Assuming a Darcy flow in the fracture and no flow between the surrounding rock and the open space of the fracture, mass conservation can be formulated as:

$$\frac{\partial}{\partial x}\left(\frac{\rho h^3}{12\mu_d}\frac{\partial P}{\partial x}\right) = \left(\rho \frac{\partial h}{\partial P} + h \frac{\partial \rho}{\partial P}\right)\frac{\partial P}{\partial t} \quad (4.60)$$

90

in which ρ and μ_d are respectively fluid density and fluid's dynamic viscosity. Taking into account the assumption of constant μ_d and ρ for the fluid will read

$$\frac{1}{12\mu_d h}\frac{\partial}{\partial x}\left(h^3\frac{\partial P}{\partial x}\right) = C\frac{\partial P}{\partial t} \quad (4.61)$$

where $C = c_j + c_f$; in which c_j and c_f are respectively compressibility of the joint and the fluid and defined as

$$c_j = \frac{1}{h}\frac{\partial h}{\partial P} \quad (4.62)$$

$$c_f = \frac{1}{\rho}\frac{\partial \rho}{\partial P} = \frac{1}{K_f} \quad (4.63)$$

Murphy et al., divided fluid flow along the fractures to two categories of linear diffusion and non-linear diffusion. In the cases, which the joint deformation due to pressure change, is small and can be considered negligible, in equation (4.61), h^3 can be taken out of the derivative and c_j will be zero. Then, equation (4.61) is represented as

$$D\frac{\partial^2 P}{\partial x^2} = \frac{\partial P}{\partial t} \quad (4.64)$$

where the hydraulic diffusivity for fractures, D, is

$$D = \frac{h^2}{12\mu_d c_f} \quad (4.65)$$

According to Murphy et al., 2004, the linear diffusion equation is valid so long as h^3 is reasonably constant or so long as

$$\frac{dh^3}{h^3} \ll 1 \quad (4.66)$$

or

$$\frac{1}{h^3}\frac{\partial h^3}{\partial P}dP \ll 1 \quad (4.67)$$

implying that there is not a pressure or aperture propagation front. Using definition of joint compressibility, c_j, as equation (4.62) and replacing in (4.67) will read

$$3c_j dP \ll 1 \quad (4.68)$$

For the cases in which the fluid pressure significantly changes the aperture of fracture (called joints in contact and lifted-off joints, according to Murphy et al., 2004) and consequently the equation (4.62) is not met, the diffusion of pressure turns into nonlinear diffusion (Murphy et al., 2004).

By doing some manipulation on equation (4.62) we will have

$$\frac{\partial P}{\partial x} = \frac{1}{c_j h}\frac{\partial h}{\partial x} \quad (4.69)$$

Substituting (4.69) in (4.60) and doing some manipulation and simplification will read

$$\frac{1}{12\mu_d}\frac{\partial}{\partial x}\left(\frac{h^2}{c_j}\frac{\partial h}{\partial x}\right) = \frac{\partial h}{\partial t} \quad (4.70)$$

For a joint in contact (meaning that the liftoff in joint surfaces has not occurred yet, even though the fluid pressure inside the fracture is high enough to reduce the effective stress acting on the fracture plane and closing it, hence the aperture will increase), c_j is

$$c_j = bh/h_0 \quad (4.71)$$

where b is determined (Murphy et al., 2004) as

$$\frac{1}{b} = \sigma_n\left(\frac{h_{\sigma=0}-h_{min}}{h_{\sigma=0}-h} - 1\right) \quad (4.72)$$

So that, the solution of equation of flow represented by (4.69) is

$$\frac{h_{\sigma=0}}{12\mu_d b}\frac{\partial}{\partial x}\left(h\frac{\partial h}{\partial x}\right) = \frac{\partial h}{\partial t} \quad (4.73)$$

For lifted-off joint (means that the fluid pressure inside the fracture exceeds the earth stress holding the joint surfaces together and they are parted) the c_j is

$$c_j = L/(h\bar{E}) \quad (4.74)$$

in which L is spacing between joints and $\bar{E}$ is reduced elastic modulus that can be defined as

$$\bar{E} = \frac{E(1-\vartheta)}{(1-\vartheta-2\vartheta^2)} \quad (4.75)$$

Hence

$$\frac{\bar{E}}{12\mu_d L}\frac{\partial}{\partial x}\left(h^3\frac{\partial h}{\partial x}\right) = \frac{\partial h}{\partial t} \quad (4.76)$$

For the case where h varies only slightly with respect to x, or when fluid pressure inside the fracture is not high enough to increase the aperture (linear diffusion case), the high-order, small-term $(\partial h/\partial x)^2$ (Murphy et al., 2004) can be ignored, and then the equation of linear diffusion of pressure represented by equation (4.73) will be recast to

$$\frac{\bar{h}h_{\sigma=0}}{12\mu_d b}\frac{\partial^2 h}{\partial x^2} = \frac{\partial h}{\partial t} \quad (4.77)$$

where $\bar{h}$ is an average over the fracture at initial stage. Equation (4.77) is similar to equation (4.64) only now in terms of aperture, not pressure. Murphy et al., 2004, summarized equations (4.73), (4.76), and (4.77) as

$$a\frac{\partial}{\partial x}\left(h^n\frac{\partial h}{\partial x}\right) = \frac{\partial h}{\partial t} \quad (4.78)$$

$$a = \begin{cases} \dfrac{\bar{h}h_{\sigma=0}}{12\mu_d b} & \text{for } n = 0 \\[2mm] \dfrac{h_{\sigma=0}}{12\mu_d b} & \text{for } n = 1 \\[2mm] \dfrac{\bar{E}}{12\mu_d L} & \text{for } n = 3 \end{cases}$$

In which a represents the grouping of the coefficients; and $n=0$, 1, and 3 represents whether the fracture has almost constant aperture, surfaces are in contact, or lifted off, respectively. Equation (4.78) is valid for fluid flow along a set of parallel plate fractures located on spacing of L from each other. This equation for a single joint embedded in a rock block of kilometer scale, such as our case, where there is not any spacing of L, which is in fact characteristic dimension, can be derived as below. By analogy of pre-existing fracture opening propagation distance with hydraulic fracturing propagation distance introduced by Perkins and Kern (1961) and Nordgern (1972) and benefiting from St. Venant principle, which states that stresses diminish with distance in any direction once that distance exceeds the minimum of the fracture plane dimension, Murphy et al. found that the characteristic length for such fracture is time-varying propagation distance, δ, and equation (4.78) can be replaced by (4.79) as (the details can be found in Murphy et al., 2004),

$$\frac{a'}{\delta}\frac{\partial}{\partial x}\left(h^n \frac{\partial h}{\partial x}\right) = \frac{\partial h}{\partial t} \quad (4.79)$$

$$a' = \begin{cases} \dfrac{\bar{h}h_{\sigma=0}}{12\mu_d b} & \text{for } n = 0 \\[2mm] \dfrac{h_{\sigma=0}}{12\mu_d b} & \text{for } n = 1 \\[2mm] \dfrac{\bar{E}}{12\mu_d} & \text{for } n = 3 \end{cases}$$

which is aperture propagation through a single fracture for every condition likely to be encountered. Here a' is the same as the a in equation (4.79) except that now L has been deleted. Assuming that the fluid diffusion in our circular fracture is uniformly across a disc of radius r, same as the assumption taken by Lengliné et al., 2017, reduces the problem to a 1D propagation study with following initial and boundary conditions

$$\text{Initial Condition: } h(x,0) = h_0$$

$$\text{Boundary Conditions: } \begin{cases} h(0,t) = h \\ h(L,t) = h_0 \end{cases}$$

and the entry flow rate of q at injection point as

$$q = -a'\left(h^n \frac{\partial h}{\partial x}\right)_{x=0} \quad (4.80)$$

Benefiting from similarity transformation for the constant flow rate case introduced by Murphy et al., 2004, as

$$\theta = \frac{h}{(q^3 t^2/a')^{\frac{1}{n+3}}} \quad (4.81)$$

93

$$\zeta = \frac{x}{(a' q^n t^{n+1})^{\frac{1}{n+3}}} \quad (4.82)$$

where θ and ζ are respectively dimensionless aperture and distance, yields

$$\frac{d}{d\zeta}\left(\theta^n \frac{d\theta}{d\omega}\right) + \frac{n+1}{n+3}\zeta\frac{d\theta}{d\omega} - \frac{2\theta}{n+3} = 0 \quad (4.83)$$

With boundary conditions of

$$\begin{cases} \theta^n(0)\dfrac{d\theta}{d\zeta} = -1 \\ \quad \theta(L) = h_0 \end{cases}$$

The results of equation (4.83) are represented in figure 4.27 in which the three cases of linear diffusion, joint in contact, and lifted-off joint can be seen. It can be noted the shock-like behavior of the joint aperture for cases of $n=1$ and 3 where there is not aperture disturbance beyond ζ of slightly greater than 1 and 1.5 respectively, while for $n=0$ the diffusion behavior is linear in which θ slowly approaches zero, but, in fact, never attains it except at infinite ζ.
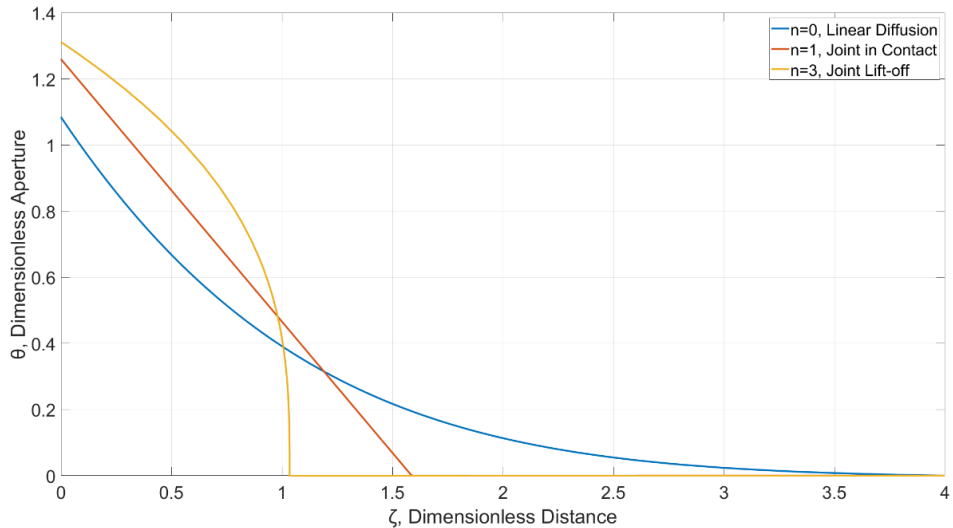
Figure 4.27. Dimensionless aperture profile of fracture versus distance from injection point for constant flow rate cases where n=0, 1, and 3 represent respectively linear diffusion, joint in contact, and lifted-off joint

Benefiting from the same dimensionless aperture and distance represented in equations (4.81) and (4.82) to plot the average aperture along the fracture during injection time (such as those shown in figure 4.23 and 4.24) yields to graphs illustrated in figure 4.28 for different time spans and different values of n equal to 0, 1, and 3 as defined by Murphy et al., 2003. To utilize equations (4.81) and (4.82) it is required to have a' calculated using its definition for each case in equation (4.79) where $\bar{h}$, $h_{\sigma=0}$, μ_d, b, and $\bar{E}$ are required to be determined. $\bar{h}$ can be considered as h_0, because the fracture at current case is modeled as a parallel plate and therefore the average hydraulic aperture of that at initial state will be uniform and equal to the initial hydraulic aperture of 14e-05 meters. $h_{\sigma=0}$ is already determined as 53e-05 meters shown in figure 4.19. μ_d for water can be considered as 0.001 Pa.s. $\bar{E}$ is defined in equation (4.75) where we can substitute 25 GPa and 0.29 for E and υ to get 32.76 GPa. According to Murphy et

94

al., 2004, b can be determined as $b = 9/\sigma_{0.9}$ in which $\sigma_{0.9}$ is the effective stress required to attain a joint closure, $h_{\sigma=0} - h$, equal to 0.9 times of the maximum closure, $h_{\sigma=0} - h_{min}$. Knowing the $h_{min} = 7e - 0.5$ meters from table 4.6 and substituting the other parameters will give us the b equal to 2.44e-07 Pa⁻¹. Now, the a' can be calculated by substituting the above parameters in the equation definition in (4.79). Doing so, a' are 25.34, 1.81e05, and 2.73e12 respectively for $n=0$, 1, and 3. After that, the values of dimensionless aperture and distance can be determined by substituting of above a', $q=0.03$ m³/s, and t in equations (4.81) and (4.82), results of which are shown in figure 4.28 for different t values. Comparing the plots of figure 4.28 with figure 4.27 reveals the fact that current numerical simulation might be of the cases in joint is in contact (or $n=1$).
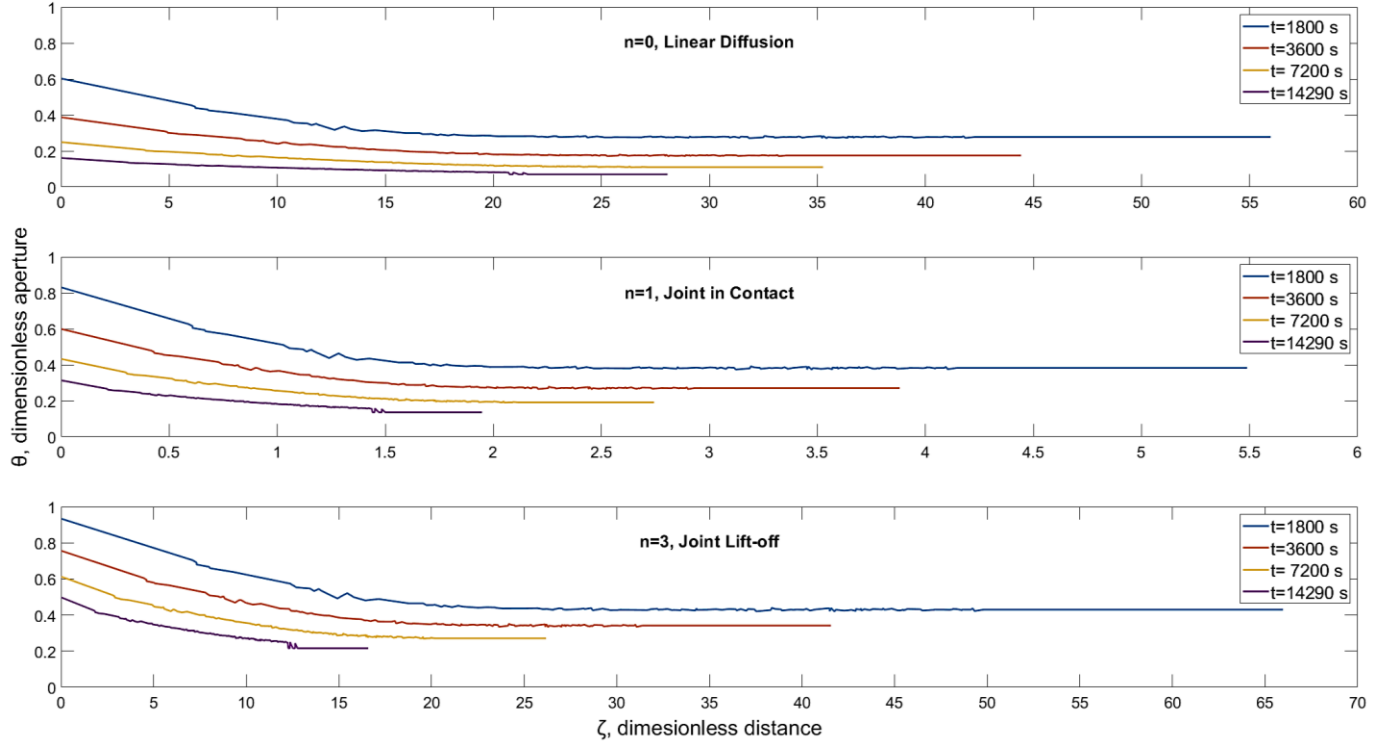
Figure 4.28. Dimensionless aperture profile versus dimensionless distance from injection point for numerical results derived from 3DEC for constant flow rate case; the graphs are drawn for all three cases of $n = 0$, 1, and 3 at different times to clearly observe the opening migration along the fracture. Comparison of these plots with figure 4.27 reveals the similarity of propagation distance between 3DEC results (1.5 to 2 in all time spans) at middle graphs (n=1, Joint in Contact) with that of $n = 1$ case of Murphy et al., 2004, shown in figure 4.27 where the dimensionless distance is just over 1.5

4.4.6   Discussion

In last subsections we tried to monitor the fluid pressure and aperture opening propagation along the fracture during hydraulic stimulation simulated using 3DEC numerical modeling tool. First, a constant volume flow rate of 0.03 m³/s was applied to a point on the fracture approximately located at a depth of 4.7 km for 24 hours (total injected volume of 2592 m³). The pressure build-up at injection point as well as at few measuring points located on the fracture diameter was considered the time when the WHP at corresponding point exceeded 1 MPa. The plot of these onset-times versus the distance of corresponding measuring points from injection point (figure 4.16) showed a power-law relation with exponent of 0.5 (a $\sqrt{t}$ behavior). This behavior further investigated by applying a time-variable volume flow rate of 0.00001t m³/s in second for 22768 seconds (total injected volume of 2592 m³) and

the results of onset-time versus distance from injection point once again plotted (figure 4.21) and showed a linear relationship; proofing a $\sqrt{t}$ behavior of fluid pressure migration. It is also found that the migration of the fracture aperture opening has the same behavior as fluid pressure migration along the fracture. This was understood by investigation of the aperture opening onset time versus distance of measuring points from injection point (the same process as fluid pressure migration assessments in figure 4.14) (figure 4.20). Additionally, it was found that the fluid pressure and the fracture aperture has a linear relationship depending on the magnitude of fracture normal stiffness (figure 4.18).

Shapiro et al., 1997, proposed a model for the diffusion of pore pressure in a homogeneous permeable rock mass when a pressure point source is varied instantaneously and then remains constant. This sudden pressure variation occurs at distance r from the source according to the diffusion equation: $r = \sqrt{4\pi Dt}$, where D is the hydraulic diffusivity in the rock and t is time. Hydraulic diffusivity at Soultz-sous-Forêts reservoir during 1993 hydraulic stimulation was measured by Shapiro as equal to 0.05 m^2/s, as (Shapiro et al., 2002). Comparing the equations shown in right hand side sub-figures of figure 4.17 (no-slip condition) with abovementioned Shapiro equation yields effective hydraulic diffusivity of 12-14 m^2/s with average on 13 m^2/s. This value is compatible with observations of Calo et al., 2011 where P-wave velocity anomaly occurred within 1000 m distance in about 3 hours, but is two order of magnitude larger than that deduced from seismicity migration by Shapiro et al., 2002 (i.e., 0.05 m^2/s).

Then, the findings of both aforementioned injection scenarios were compared to the model introduced by Lengliné et al., 2017 (figures 24 and 25). This model is in fact a simple advective model (obeying $\sqrt{t}$ behavior) assuming a constant aperture along the open part of the crack and a sharp front between open and closed part of the crack with no diffusion equation, however we tried to generalize the model to our numerical results by using time and space varying fracture aperture derived from 3DEC during injection period. The comparison revealed the fact that in the first injection scenario the fluid pressure propagated a little faster than Lengliné et al., 2017 prediction which might be due to the fact that in their model the fracture is initially assumed to be closed and it is opened to its maximum aperture once fluid flow reaches it (binary behavior), but the fracture in our model has an initial non-zero aperture.

Finally, a more advanced model of diffusion, introduced by Murphy et al., 2003, was used to evaluate the numerical aperture propagation data which were obtained from the first stimulation scenario. They divided whole the cases which a fracture might be encountered during fluid injection into two cases of linear and non-linear diffusion. The linear diffusion take place when the pressure evolution is not large enough to generate aperture opening. In this case the fluid flows in the space between two planes forming the fracture (a $\sqrt{t}$ behavior). The non-linear diffusion is divided into two cases of "joint in contact" and "joint lift-off" at which the fracture opening due to fluid injection happens, but in the latter the whole normal stress which keeps the fracture planes together is overcome by the fluid pressure and the whole hanging wall moves up. Murphy et al. distinguished these three case and corresponding equations by assigning a variable of n which is respectively 0, 1, and 3 for linear diffusion, joint in contact, and joint lift-off cases.

Here, the dimensionless parameters introduced in Murphy et al. paper was utilized to plot the aperture variation along the distance from injection point in different time periods. These periods were actually the time passed from beginning of the hydraulic stimulation. This time partitioning was chosen to better investigate the existence of the propagation front along the fracture during injection period and started from 1800 s, continued to 3600 s, 7200 s and finally 14290 s (which was approximately the time when the WHP at the furthest measuring point exceeded of 1 MPa). These plots were shown in figure 4.27. Comparison of figure 4.26 (which is a plot dimensionless

aperture versus dimensionless distance from injection point achieved from semi-analytical equations of Murphy et al., 2003) reveals the fact that, in our simulation, the aperture propagation along the fracture most probably obeys the case of "joint in contact" (n=1). It is also consistent with the achievement of aforementioned comparison of numerical results with Lengliné et al.'s model where the numerical propagation was shown to be a bit faster than $\sqrt{t}$ behavior represented by Lengliné et al.

Moreover, according to Murphy et al., 2004, the propagation distance, d, of aperture is denominator of equation (4.82) as

$$d = (a'q^n t^{n+1})^{\frac{1}{n+3}} \quad (4.84)$$

Substituting 0, 1, and 3 for n in equation (4.84) reveals that d varies with t to power of 0.33, 0.5, and 0.67, respectively for $n = 0$, 1, and 3. Comparison of the numerical results shown in figures 20 (right sub-figures) with aforementioned values from Murphy et al., 2004, demonstrates the similarity of n=1 case with the aperture propagation behavior in no-slip fracture where the exponent of 0.49 can be seen in the right sub figures of figure 4.20, again consistent with previous conclusions.

Worth to note that, and contrary to above observations, Murphy et al., 2004, introduce the joint compressibility in equation (4.62) as

$$c_j = \frac{1}{h}\frac{\partial h}{\partial P}$$

In 3DEC, for the situation in which the hydraulic aperture is between residual and maximum hydraulic aperture as shown in figure 4.18, $\frac{\partial h}{\partial P}$ is equal to $-\frac{1}{K_n}$. Substituting this in above equation reads

$$c_j = \frac{1}{h}\left(-\frac{1}{K_n}\right) \quad (4.85)$$

Knowing that in 3DEC, K_n is constant, then c_j will be an inverse function of aperture. For three cases introduced by Murphy et al, 2004, meaning $n = 0$, 1, and 3, c_j is respectively zero, bh/h_0 (equation (4.70)), and $L/(h\bar{E})$ (equation (4.74)); comparison of which with equation (4.85) reveals the similarity of 3DEC joint compressibility with n=3 case of Murphy et al., 2004, where, in both of them, c_j is an inverse function of aperture. For the two end sections in figure 4.18 where the hydraulic aperture is constant and equal to maximum hydraulic aperture or residual hydraulic aperture, $\frac{\partial h}{\partial P}$ is zero; yielding a joint compressibility of zero and indicating a linear diffusion case of Murphy et al., 2004, in which c_j is zero.

4.4.7   Simulation of the whole stimulation

As mentioned above, Calo et al, 2011 reported a P-wave velocity evolution over a distance of more than 1000 m in a period of about 3 hours during the hydraulic stimulation of the GPK well in 2000. This is also shown by our numerical model results in the right subfigures of Figures 4.17 and 4.21 in which both the propagation of fluid pressure and fracture opening fronts reached to a distance of over 1000 m at time of about 11000 s (i.e., 3 hours). These results were obtained by simulating the first phase of fluid injection in the undrained boundary condition, where there was no leakage from the fracture wall and the edge into the surrounding rock matrix. A series of complementary tests were performed to simulate the full fluid injection process (shown in Figure 4.29) to assess

the performance of the numerical models to cover the observed wellhead pressure evolution during the injection phases and shut-in phase. This was done by first changing the undrained boundary condition to the drained condition, where the fluid was allowed to flow through the outer plane up to the boundaries of the block, through which a discharge equal to the injected flow rate was set to complete the drained condition in the model. The parameters controlling the response of the fracture to the injected fluid were then adjusted to mimic the observed pressure evolution in the field. Figure 4.30 shows the wellhead pressure evolution obtained from the numerical simulation compared to the field observation. The numerical curve is obtained from the model where the normal stiffness of the fracture is set to 40 and 80 GPa/m inside and outside, respectively. In addition, the hydraulic aperture values on the outside of the fracture were the same as those on the inside of the fracture.

As can be seen from Figure 4.30, the numerical wellhead pressure generally follows the field observations, with an approximate 1 MPa sharp increase when the injection rate is increased by 10 ls^{-1}, a continuous and gradual increase in the third stimulation stage, and finally a 4 MPa sudden pressure drop in the shut-in phase and then a gradual decline to a pressure of 5-6 MPa. However, the slope of the pressure drop in the shut-in phase is smaller in the field observation than in the numerical simulation, suggesting a long-term pressure decline in the field observation, which is addressed by Weidler et al. (2002) as a result of the lower rock mass permeability of the deeper reservoir compared to the upper reservoir of Soultz-sous-Forêts. In addition, and among many others, the more complex geometry of the fracture network compared to a single fracture may be another reason for the observed difference between the shut-in phase pressure drop in the field observation and the numerical simulation. Furthermore, during the first and second stimulation stages of the field observation, a well-head pressure of more than 12 MPa was observed which was dropped for about 1 MPa (as can be seen in Figures 4.29 and 4.30), but was not apparent in the numerical results, although the pressure curve rose sharply. This could be due to the fact that the fault behavior in the numerical simulation was elastic, while the filed observation, as could be inferred from the recorded induced seismic events, occurred in the elastic-plastic regime. In fact, as explained by Weidler et al. (2002) about the field observation, in the first and second stages, after reaching the peak break-down pressure of about 12 MPa, the fluid flows along a more permeable medium and thus the pressure decreases continuously, while in the third stage the fluid pressure front has reached an impermeable outer boundary through which the fluid pressure rises from 12 MPa to 14 MPa.
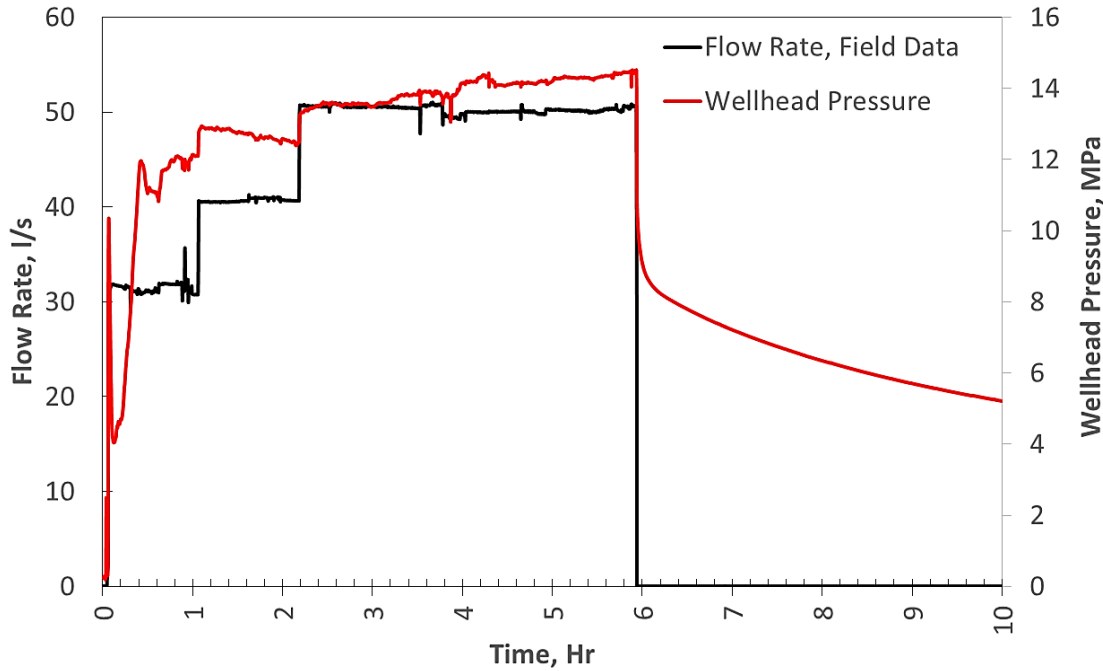
Figure 4.29. Injection rate and pressure measured at GPK2 wellhead
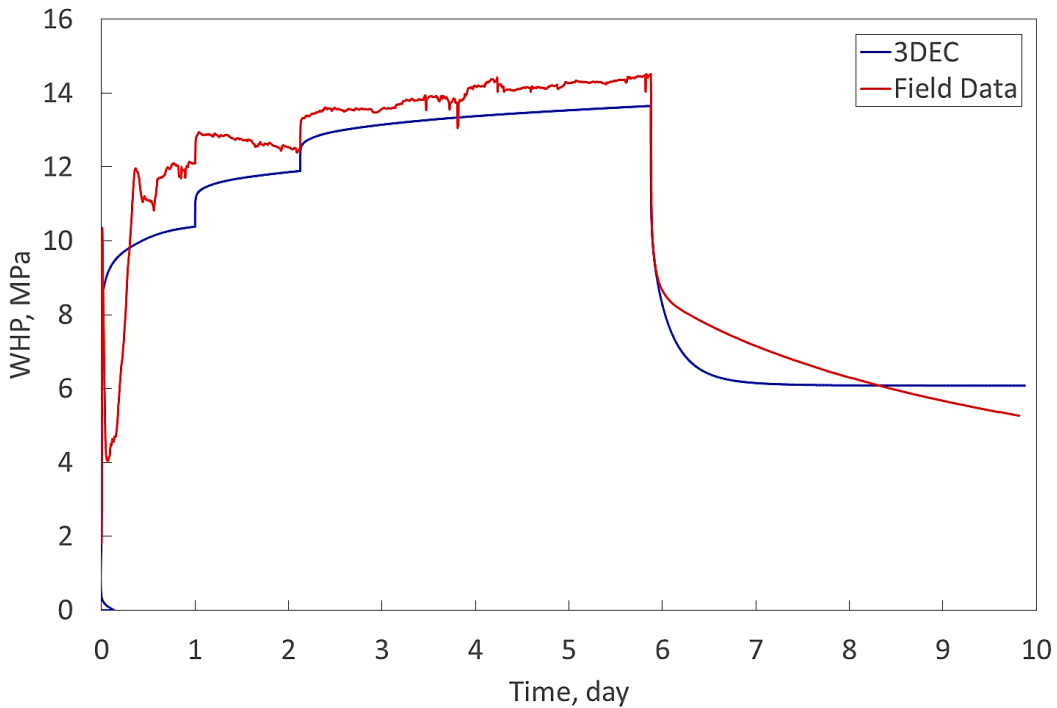
Figure 4.30. Numerical WHP evolution over time at the injection point compared to that measured at the wellhead of the GPK2 well

As mentioned above, the 2000 stimulation operation of GPK2 was accompanied by more than 24000 microseismic events detected by surface and borehole receiver networks, of which 7200 were selected by Calo et al. (2011) for 4D P-wave tomography. The entire injection operation was divided into 14 sets based on the changes in flow rate

and fluid pressure that occurred (Figure 4.31), and 4D P-wave tomography was performed on the events that occurred in each set. Figure 4.32 shows 6 sets out of these 14 where a variation in P-wave velocity can be observed at a distance of over 1000 m over a period of approximately 3 hours. A measurement point close to the injection source has been selected on the subplots of Figure 4.32(A), where an approximation of the P-wave velocity evolution has been plotted against the change in set and flow rate, as shown in Figure 4.32(B). It can be seen that an increase in P-wave velocity occurs as the flow rate is increased from 30 to 40 and from 40 to 50 ls^{-1} when moving from set 2 to 3 and set 5 to 6, respectively. This behavior is inverse to the fact that any increase in pore/fluid pressure will decrease the P-wave velocity (Mavko and Vanorio, 2010; Darot and Reuchle, 2000; Todd and Simmons, 1972). Considering the low permeability medium addressed by Weidler et al. (2002), in addition to the existence of a fluid pressure/fracture opening front that propagates along the fracture faster than fluid diffusion in the fractured surrounding medium which was demonstrated in this study, one can state that the overpressure generated by the injected fluid in the fracture acts as an additive component to the confining pressure of the rock mass, instead of playing the role of pore pressure enhancement. In this situation, and according to the literature already mentioned, especially Todd and Simmons (1972), any increase in confining pressure can cause an increase in P-wave velocity. In our case, an overpressure of 1 MPa acting normal to the fracture plane with a dip and azimuth of 71° and 144°, respectively, can be translated into a confining pressure component of about 0.6 MPa on average in all three Cartesian directions, which, based on the results of Todd and Simmons, can produce a 2% increase in P-wave velocity, assuming an average confining pressure of 90 MPa and a pore pressure of about 50 MPa. This increase in P-wave velocity is comparable to the 10% and 2% increases seen in the field observations after the first and second injection rate increases, respectively, as can be roughly calculated from Figure 4.32(B).
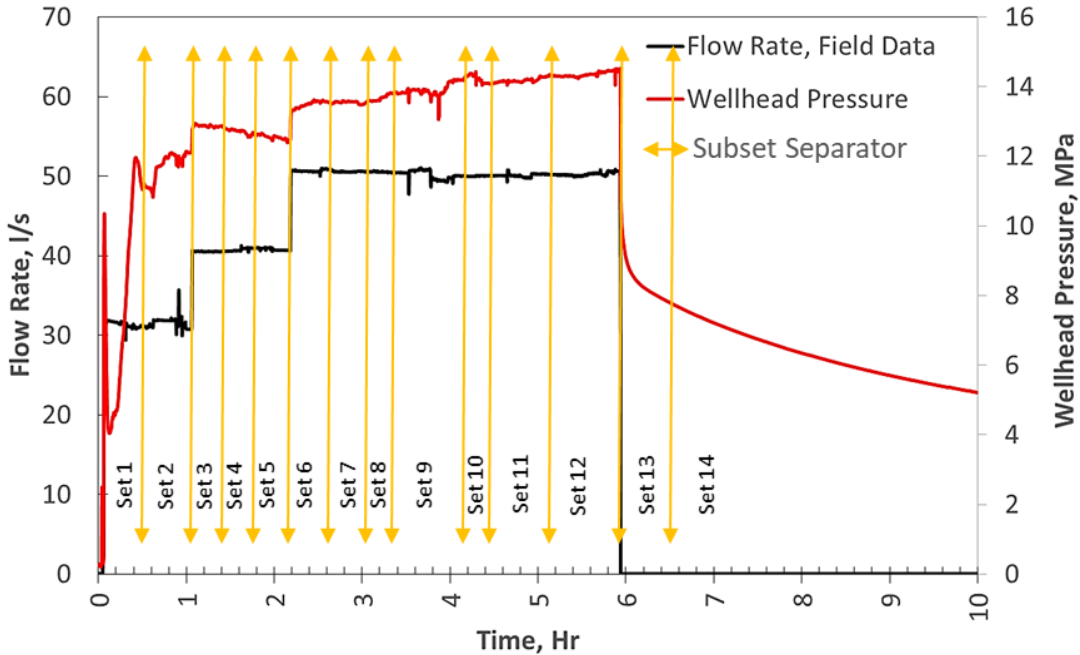
Figure 4.31. Numerical WHP evolution over time at the injection point compared to that measured at the wellhead of the GPK2 well (reproduced after Calo et al. (2010))
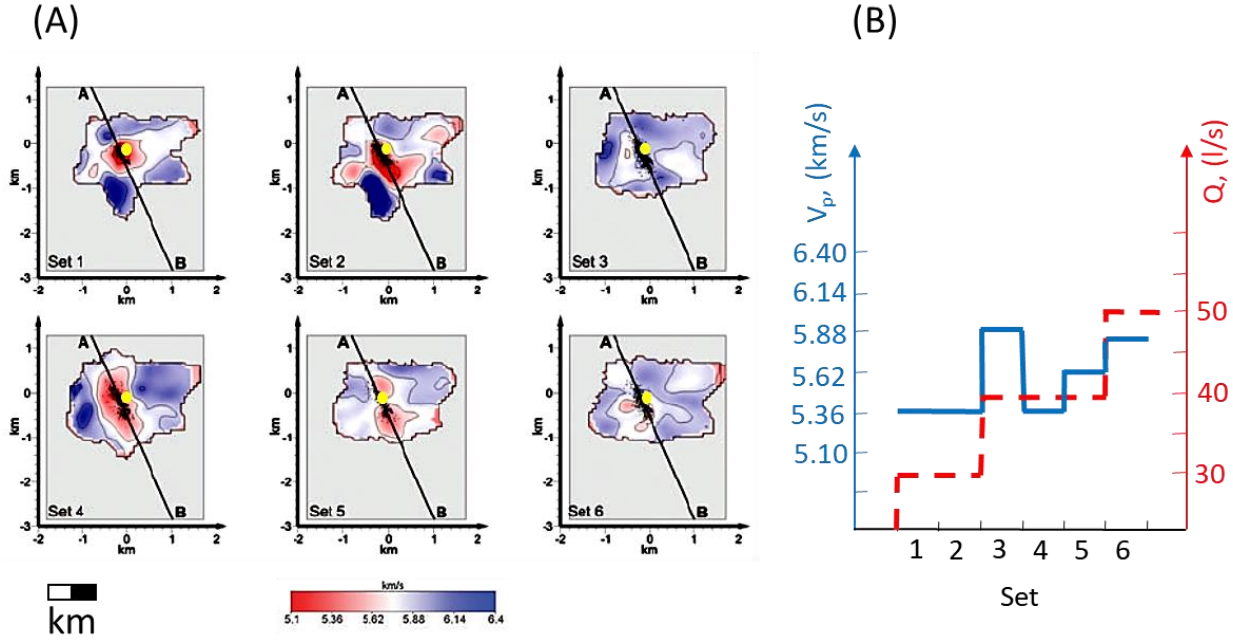
Figure 4.32. (A) Evolution of the P-wave seismic velocity at 4.6 km depth during the 2000 stimulation test (after Calo et al., 2011) on which the V_p measuring point is shown by a yellow circle; (B) Approximate P-wave velocity changes at the yellow point shown in (A) versus set and flow rate

4.5   Sensitivity Analysis

In this section, it is aimed to investigate the effect of the fracture's shear and normal stiffness, size, and in-situ stress orientation on the velocity of observed pressure front migration and magnitude of maximum pressure. Let us assume that in all investigated cases the overpressure propagates as a circular disk and the time when the overpressure reaches the furthest measuring point is a proxy of pressure propagation velocity. The maximum reachable overpressure is also measured at injection point as another parameter to be investigated against many other parameters which were changed during sensitivity analysis.

4.5.1   Fracture Stiffness Effect

First, the sensitivity of the fracture response to fluid injection with respect to normal and shear stiffnesses of the fracture are analyzed. The analysis carried out by first maintaining the normal stiffness on initial value of 80 GPa/m and changing the shear stiffness to values lower and higher than its initial magnitude of 20 GPa/m. Then the same procedure was performed by keeping the shear stiffness on initial value and changing the normal stiffness. These variable values were 10 GPa/m, 30 GPa/m, 50 GPa/m, 80 GPa/m, 150 GPa/m, 180 GPa/m, and finally 300 GPa/m. Onset time of pressure build up at furthest measuring point at a distance of 1539 meters as a function of fracture normal stiffness are illustrated in figure 4.33.

In the graphs of figure 4.33, the pressure build-up time decreases by increase of the fracture normal stiffness (figure 4.33, left), while the maximum WHP at the injection point increases by increase of the normal stiffness (figure 4.33, right). In addition, in figure 4.33, right, shows that the normal stiffness of 10-30 GPa/m produces a WHP closer to the field observations of about 10-12 MPa.
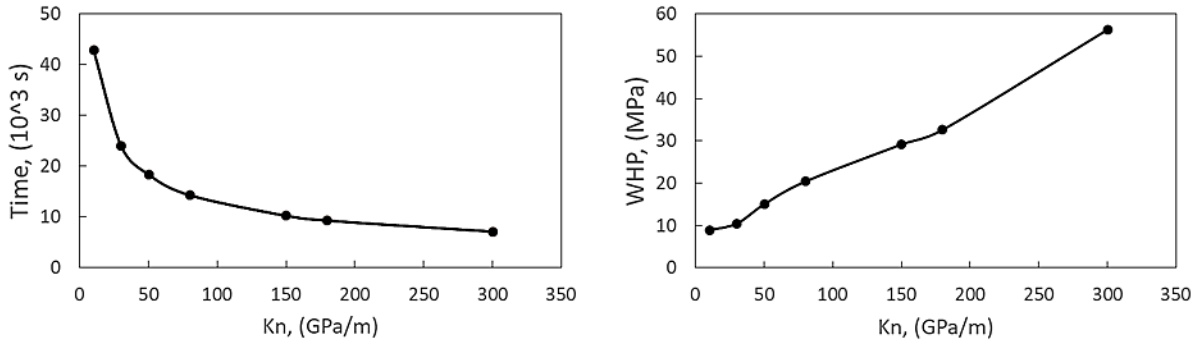
Figure 4.33. Effect of normal stiffness of the fracture on the overpressure onset time at the furthest measuring point located at a distance of 1539 meters related to the injection point (left), and the maximum overpressure (or WHP) at injection point reached during injection period (right); it can be seen in the figures that the onset time decreases by increase of normal stiffness from 10 to 300 GPa/m following a power law function, contrary to the maximum well-head pressure showing a linear increase by increase of the normal stiffness.

Figure 4.34 illustrates the same graphs of figure 4.33 for the cases in which the fracture's normal stiffness maintained constant on the reference value (80 GPa/m) and the shear stiffness are changed from 10 to 300 GPa/m to assess its influence on the elastic response of the fracture. As it can be seen in the figure 4.34, left and right it seems that the fracture's shear stiffness does not have a meaningful effect on the pressure build-up time at the furthest measuring point as well as on the maximum WHP at injection point.
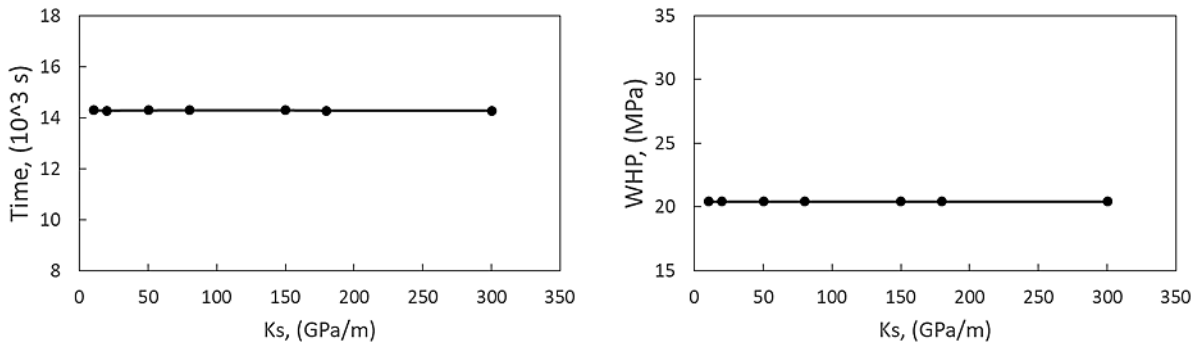
Figure 4.34. Effect of shear stiffness of the fracture on the overpressure onset time at the furthest measuring point located at a distance of 1539 meters related to the injection point (left), and the maximum overpressure (or WHP) at injection point reached during injection period (right); it can be seen in the figures that the shear stiffness of the fracture does not have any meaningful effect on the pressure build-up time or the maximum well-head pressure.

4.5.2   Fracture Strike Effect

The sensitivity analysis continued with assessment of the effect of the fracture's orientation with respect to the direction of the maximum horizontal stress (or in other words the orientation of the in-situ principal stresses) in geographical frame of reference on hydromechanical response of the fracture against hydraulic stimulation. Here, this angle is called ζ (figure 4.35). The ζ plays an important role on mechanical behavior of the fractures by controlling the magnitudes of shear and normal stresses resolved on the fracture's plane. The initial ζ was $26°\pm10°$ (considering the S_{Hmax} orientation of N170°E±10°, Cornet et al., 2007) and $25°\pm14°$ (considering the S_{Hmax} orientation of N169°E±14°, Valley and Evans, 2007), so we investigated the effect of change of this angle on

fracture's hydro-mechanical elastic behavior by assigning 0°, 11° (which is 25°-14°), 16° (which is 26°-10°), 36° (which is 26°+10°) approximately the same as 39° (which is 25°+14°), 60°, and 90° to ζ. Since any change in the ζ angle has changed the coordinate of the furthest measuring point, merely considering the pressure build-up time at that point was not a reliable parameter. Hence, at each case the distance of the furthest measuring point to the injection point is divided by the pressure build-up time to have the velocity in which the overpressure propagated to the furthest point and this velocity is used as a proxy to analyze the effect of the fracture strike on the its elastic response. For each case aforementioned velocity was derived and plotted as figure 4.36. The results reveal that the angle between the maximum horizontal stress and the fracture strike does not have a significant effect on the pressure propagation rate (with one exception at the 26° angle) and on the maximum WHP at the injection point.
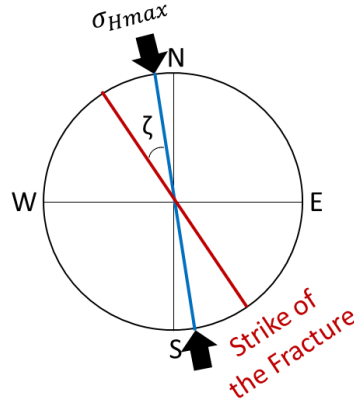
Figure 4.35. Schematic view indicating the angle between the maximum horizontal stress and fracture strike
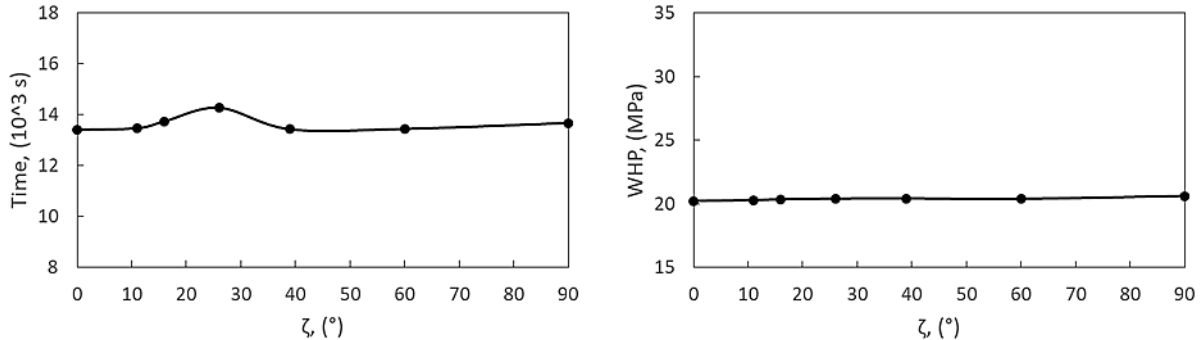
Figure 4.36. Fracture's strike effect on the overpressure arrival time to a given measuring point (left), and on the maximum WHP at injection point (right); it seems that the fracture's strike does not effectively change the behavior of the fracture in terms of the pressure propagation and the maximum WHP at injection point

4.5.3   Fracture Dip Effect

Then, the sensitivity analysis continued by assessing the influence of fracture dip on pressure propagation through the fracture. Fracture dip varied from 30° to 90° including 71° and 64° which are stated as dip of GPK3-FZ4770 in the literature such as Sausse et al., 2010, and Dezayes et al., 2010, respectively. Figure 4.37, left, shows the variation of the pressure propagation velocity for different fracture dips, where it can be seen that an increase in the fracture dip is accompanied by an increase in the pressure propagation velocity. The variation of the WHP at the injection point is also plotted in Figure 4.37, right; it shows that the behavior of the WHP variation is not influenced by the evolution of the fracture dip.

103
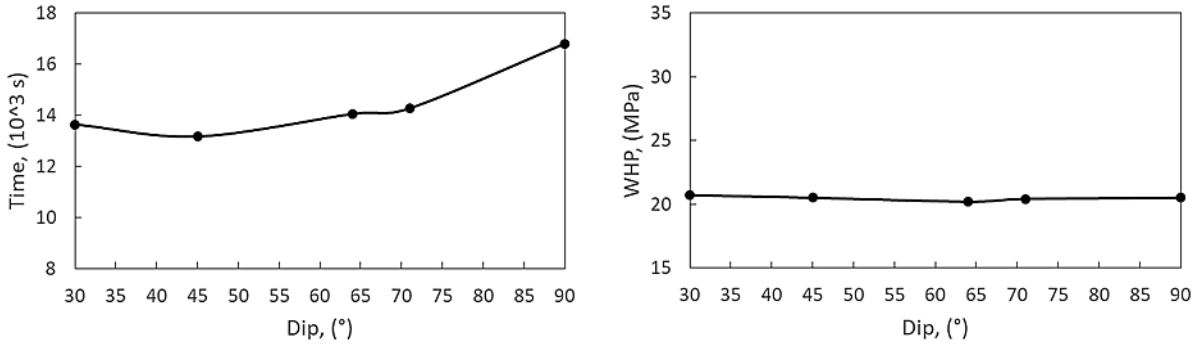
Figure 4.37. Fracture's dip effect on the overpressure arrival time to a given measuring point (left), and on the maximum WHP at injection point (right); it might be reasonable to state that the fracture's dip does not affect the elastic behavior of the fracture in terms of both the pressure propagation and the maximum WHP at injection point

4.5.4   Fracture Size Effect

Then, the size of the fracture is changed to analyze the sensitivity of the fracture's response to fluid injection with respect to the fracture size. The diameter of the fracture is changed from initial value of 3000 m to 4000, 5000, and then 2000 m and the corresponding velocity of fluid pressure build-up at the furthest measuring point for each case are plotted. Figure 4.38 illustrates the corresponding results for each fracture size. It can be seen from figure 4.38, left, that increase in fracture diameter decreases the onset time of pressure build-up as well as the maximum WHP at injection point as it can be seen in figure 4.38, right. It is caused by the increase in fracture volume as the fracture diameter increases from 2 km to 5 km. Therefore, a given volume of injected fluid will be compressed more in a small fracture than in a large fracture, and consequently will generate more pressure than the latter.
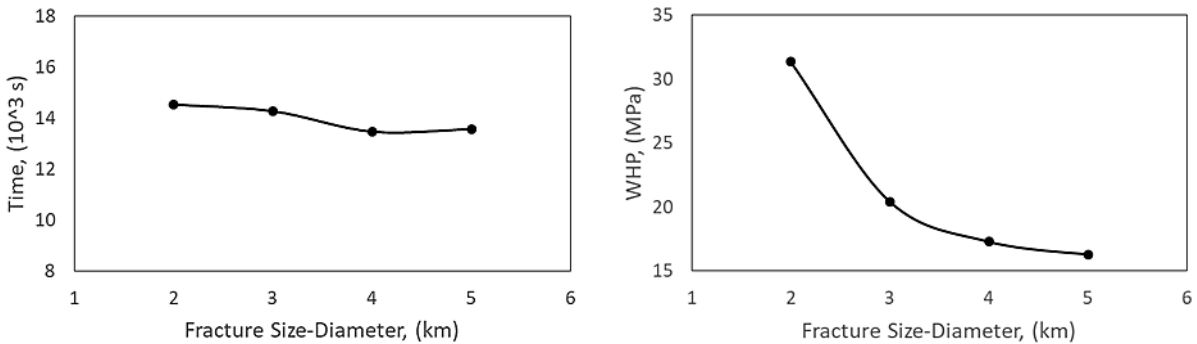
Figure 4.38. The effect of fracture size variation on overpressure arrival time to a given measuring point (left), and on the maximum WHP at injection point (right); it seems that the increase in the fracture size decreases both the overpressure arrival time and the maximum WHP at injection point

4.5.5   Initial Hydraulic Aperture Effect

Finally, initial hydraulic aperture of the fracture is changed to analyze the sensitivity of the fracture's response to fluid injection with respect to the initial aperture. The initial aperture of the fracture is changed from initial value of 1.4e-04 m at reference model to 0.5e-04, 1e-04, and then 1.6e-04 m and the corresponding onset time of fluid pressure build-up at the furthest measuring point and the maximum WHP at injection point for each case are plotted. Figure 4.39 illustrates the corresponding results for each aperture size. It can be seen from figure 4.39, left and right, that increasing the fracture aperture does not meaningfully affect the pressure front arrival time or the

104

maximum WHP at the injection point. Referring to Figure 4.40, it can be seen that the numerical WHPs are completely superimposed on each other up to a time of about 250 minutes (15000 seconds), which is approximately the time required for the overpressure to reach the farthest measuring point at 1539 meters from the injection point.
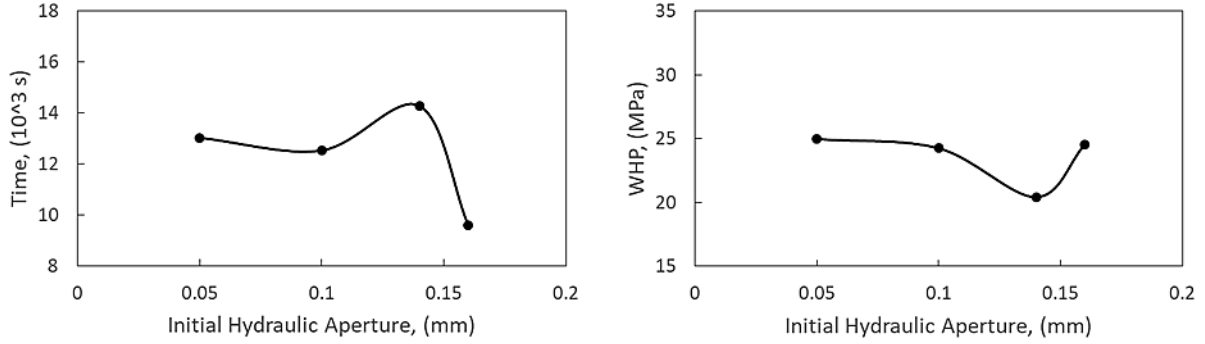
Figure 4.39. The effect of fracture aperture variation on overpressure arrival time to a given measuring point (left), and on the maximum WHP at injection point (right); it seems that the increase in the fracture's initial aperture does not affect the arrival time of overpressure and maximum WHP
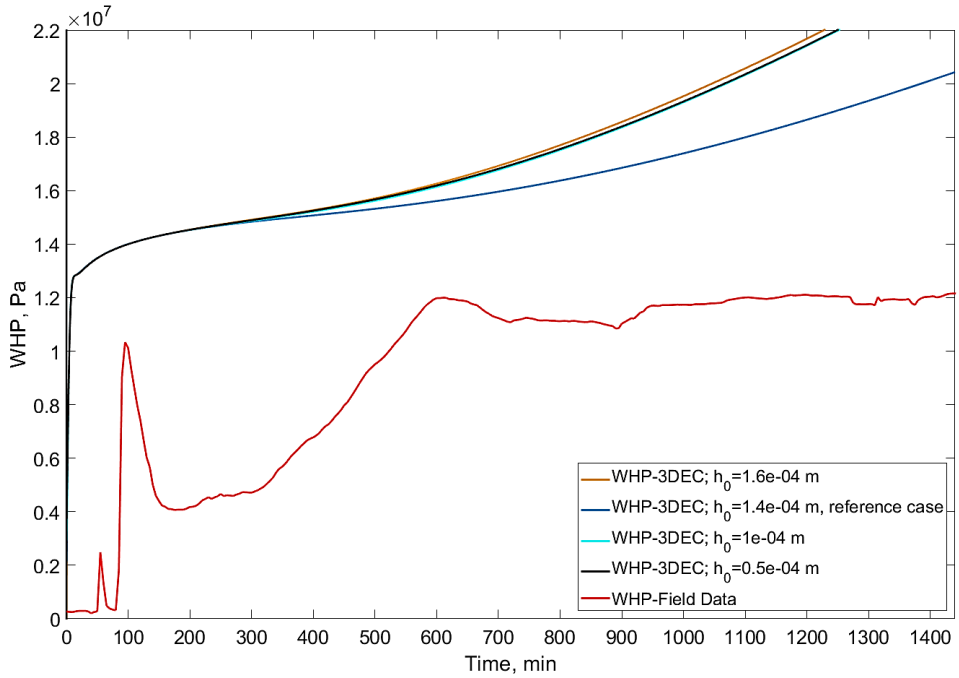
Figure 4.40. WHP evolution in time for apertures with different values of initial hydraulic aperture

4.6   Fracture Slip Effect on the Results

So far, in this report the investigations were focused on the elastic response of the fracture to fluid injection; meaning that the permanent shear displacement along the fracture when reaching the failure criterion (Coulomb friction law) were not taken into account. In this section, it is aimed to assess characteristics of pressure propagation through the fracture when fracture slip is allowed to take place once the Coulomb failure criterion is met, following an approach similar to first studied no-slip case. To do so, in 3DEC, the Coulomb slip law with weakening is

applied to the fracture instead of previously used elastic constitutive law. So that, the fracture will behave based on pre-defined parameters of the Coulomb slip law (cohesion and friction coefficient), but the cohesion strength of the fault will be set to zero once the slip occurs (Itasca, 2016) (equation 4.82). This instantaneous loss of strength approximates the "displacement-weakening" behavior of joint (3DEC manual, 2016).

$$\begin{cases} \tau = \mu\sigma_n + C & \text{before slip occurs} \\ \tau = \mu_d\sigma_n & \text{after slip occurs} \end{cases} \quad (4.82)$$

where μ_d is dynamic friction coefficient which is, by default, equal to the static friction coefficient. It is also possible to define dilation angle of the fracture surface asperities to take into account the normal displacement caused by fracture dilation during slip, however it is assumed to be zero at this step.

The comparison of WHP evolution at injection point during stimulation for slip fracture and no-slip fracture and field observation are shown in figure 4.41. It can be seen that the pressure evolution for slip fracture is almost identical with the no-slip fracture except that there are some irregular section along the curve which might be due the stress drop event once slip occurs.
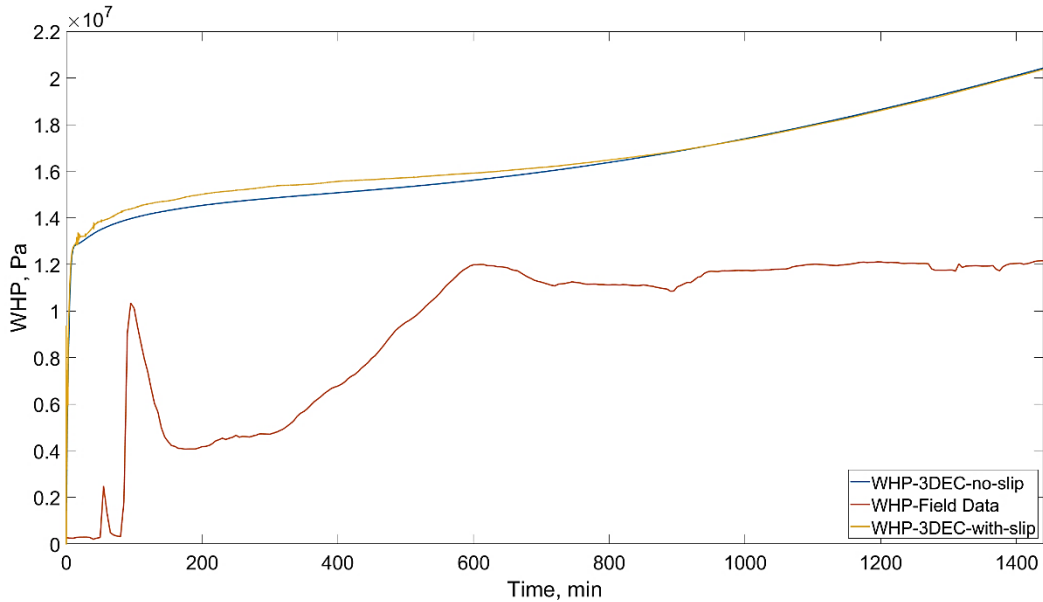
Figure 4.41. WHP evolution at injection during hydraulic stimulation for slip fracture compared to the field WHP and WHP for no-slip fracture

The pressure front migration along the fracture diameter can also be found in figure 4.42 (left sub-figure) in which it can be seen that the pressure build-up arrives to the furthest measuring point at the top frontier of the fracture earlier than that for the bottom, so that the fluid upward migration is faster than that of downward. It might be because the stress state of the model as shown in figure 4.8, increases with depth and consequently there exist less confining stress at shallower depth compared to deeper parts of the fracture. It seems that the propagation process is more or less identical between no-slip and slip fractures; however, the slip affects the velocity of migration (less velocity in slip fracture compared to the no-slip one). It seems to be mostly related to the difference between constitutive models of the cases. In no-slip fracture, the mechanical behavior of the fracture merely is controlled by the normal stiffness of the fracture, as concluded from sensitivity analysis section. But, for the slip case, the

mechanical behavior is also controlled by the shear and effective normal stresses acting on the fracture plane as well as the intrinsic shear strength of the fracture (which is itself a function of the effective normal stress acting on the fracture plane). So that, any overpressure will increase the fracture aperture (and simultaneously will decrease the effective normal stress) as long as the intrinsic shear strength of the aperture falls below shear stress acting on the fracture plane. After that, a stress drop will occur which may influence the fluid pressure evolution in time (the fluctuation spots, or the irregular sections, on the pressure curves of figure 4.38). By assuming as same proxy for pressure propagation velocity as elastic behavior cases (section 4.4), the required time for pressure propagation can be determined as equal as 13446 and 33858 seconds respectively for upward and downward propagations (compared to 12805 and 14284 seconds for the no-slip case of section 4.4). In figure 4.39 it can be seen that the upward pressure propagation profile for both cases of no-slip fracture and slip fracture are almost matched, which is not the case downward profiles. Moreover, application of Shapiro et al., 1997 pressure diffusion equation to the data deduced from figure 4.38 yields, respectively, upward and downward effective hydraulic diffusivity of approximately 11 and 6 m^2/s in comparison with 7 m^2/s obtained by Calo et al., 2011; indicating the effect of fracture shear slip on evolution of hydraulic diffusivity when it is compared to 13 m^2/s on average computed for no-slip condition at 4.4.5.
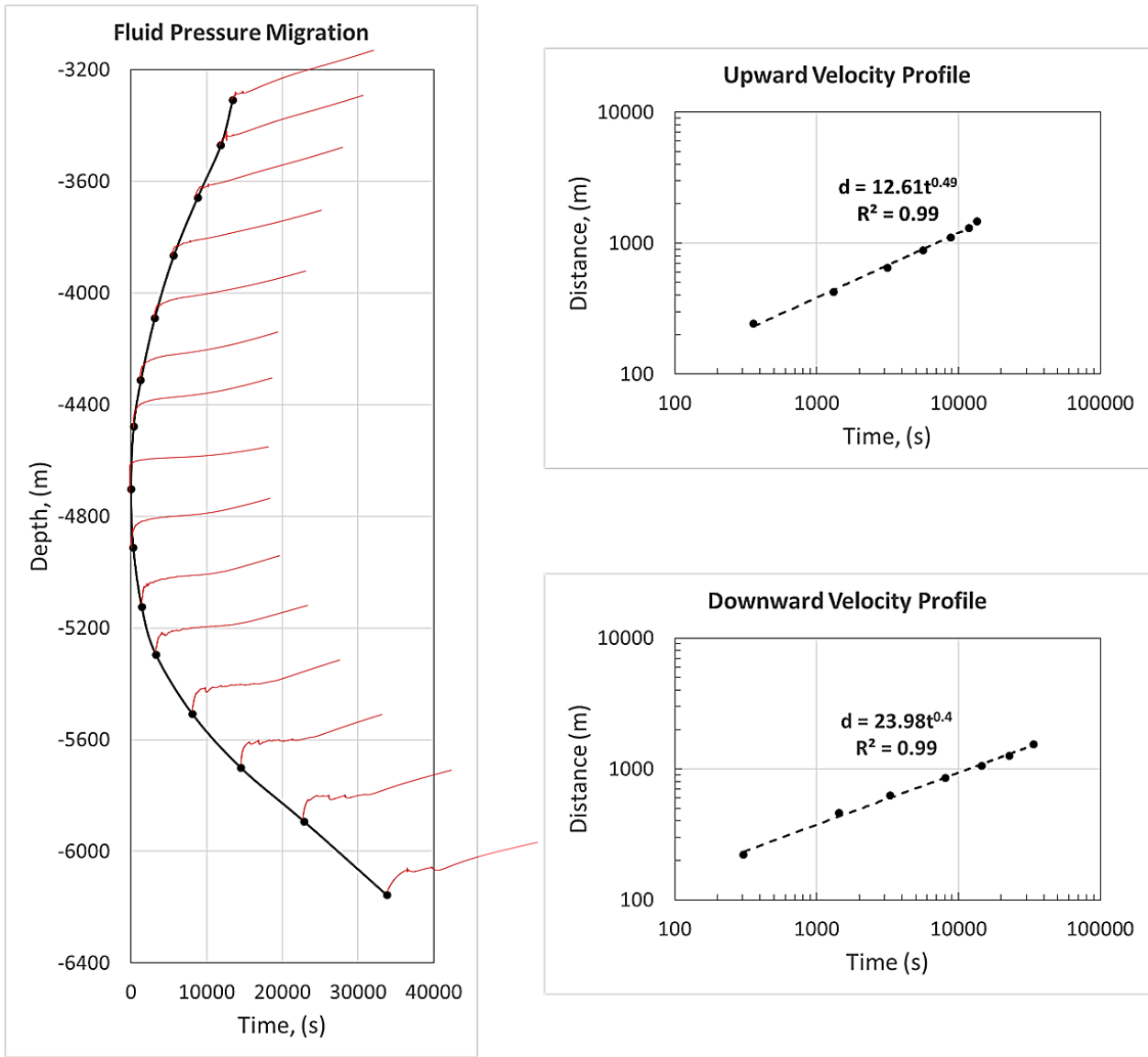
Figure 4.42. Pressure front migration from injection point at about 4.7 km to the top and bottom of the fracture for the fracture with shear slip; the left-hand side figure is plot of WHP build-up onset time versus depth of measuring points on which the red curves are WHP variation in time determined using the process explained in figure 4.14. The right-hand side sub-figures are illustration of upward and downward velocity functions along the fracture where the both profiles obey a power-law function, but the exponent of downward function is 0.4 compared to 0.5 of upward one
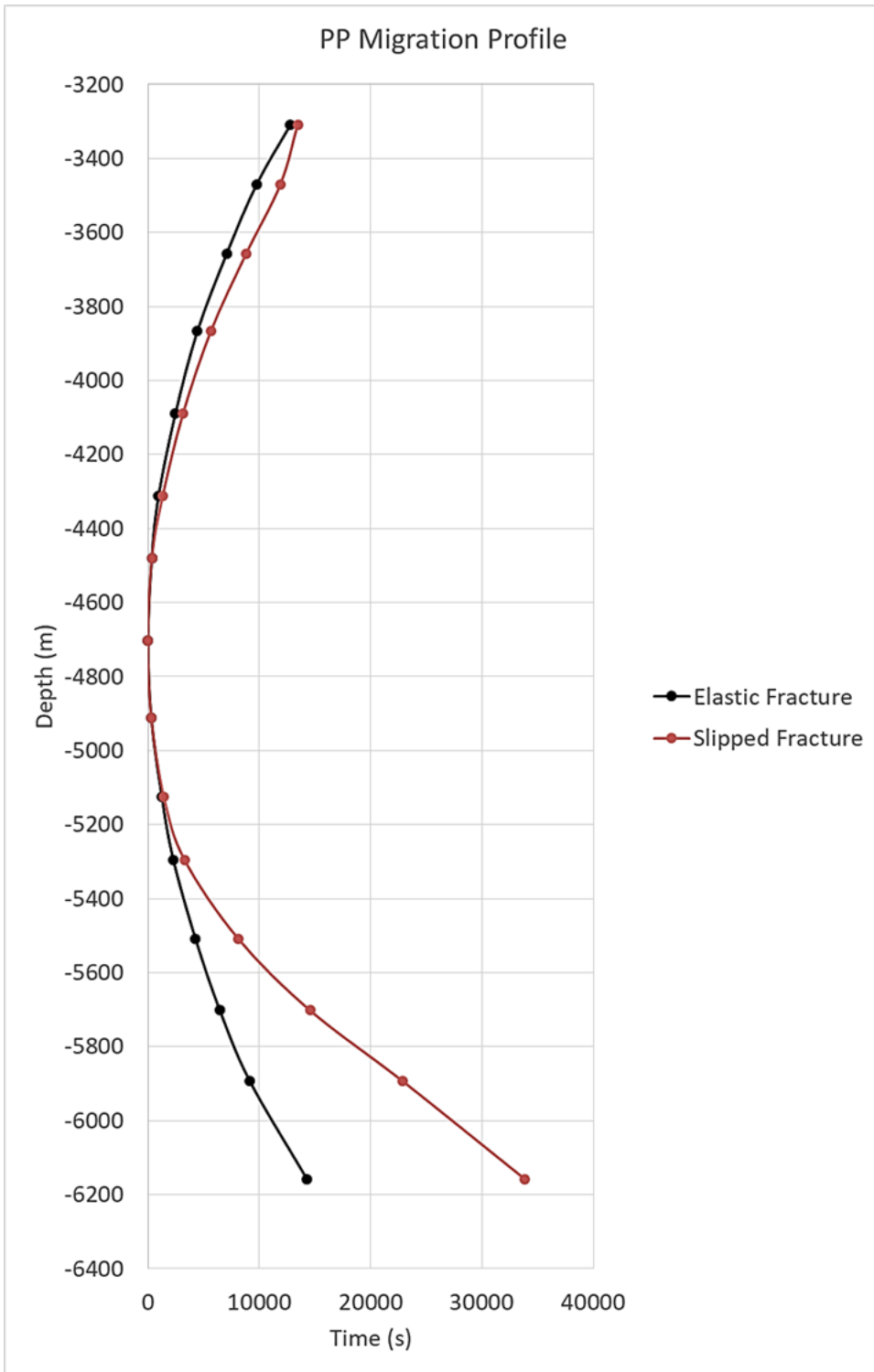
Figure 4.43. The comparison of fluid pressure propagation profile for two cases of no-slip fracture (black curve) and slip fracture (red curve); while the upward propagation are almost identical in both fractures, the downward propagation velocity might be of double in no-slip case compared to the slip one

Fracture's local aperture opening migration for slip fracture, as shown in figure 4.44, exhibits the same power-law behavior as for no-slip fracture. It is the same behavior observed in figure 4.42 for fluid pressure evolution in

109

time at injection point. Furthermore, migration of the local aperture opening, shown in the right-hand side sub-figures of 4.44, obeys a power law with exponents respectively 0.47 and 0.38 for upward and downward velocities, approximately as equal as those observed for pressure propagation in figure 4.42. Worth to note that, for the no-slip fracture case, these exponents are approximately identical (and equal to 0.5) for both fluid pressure and local aperture opening migrations (see figures 4.17 and 4.21).
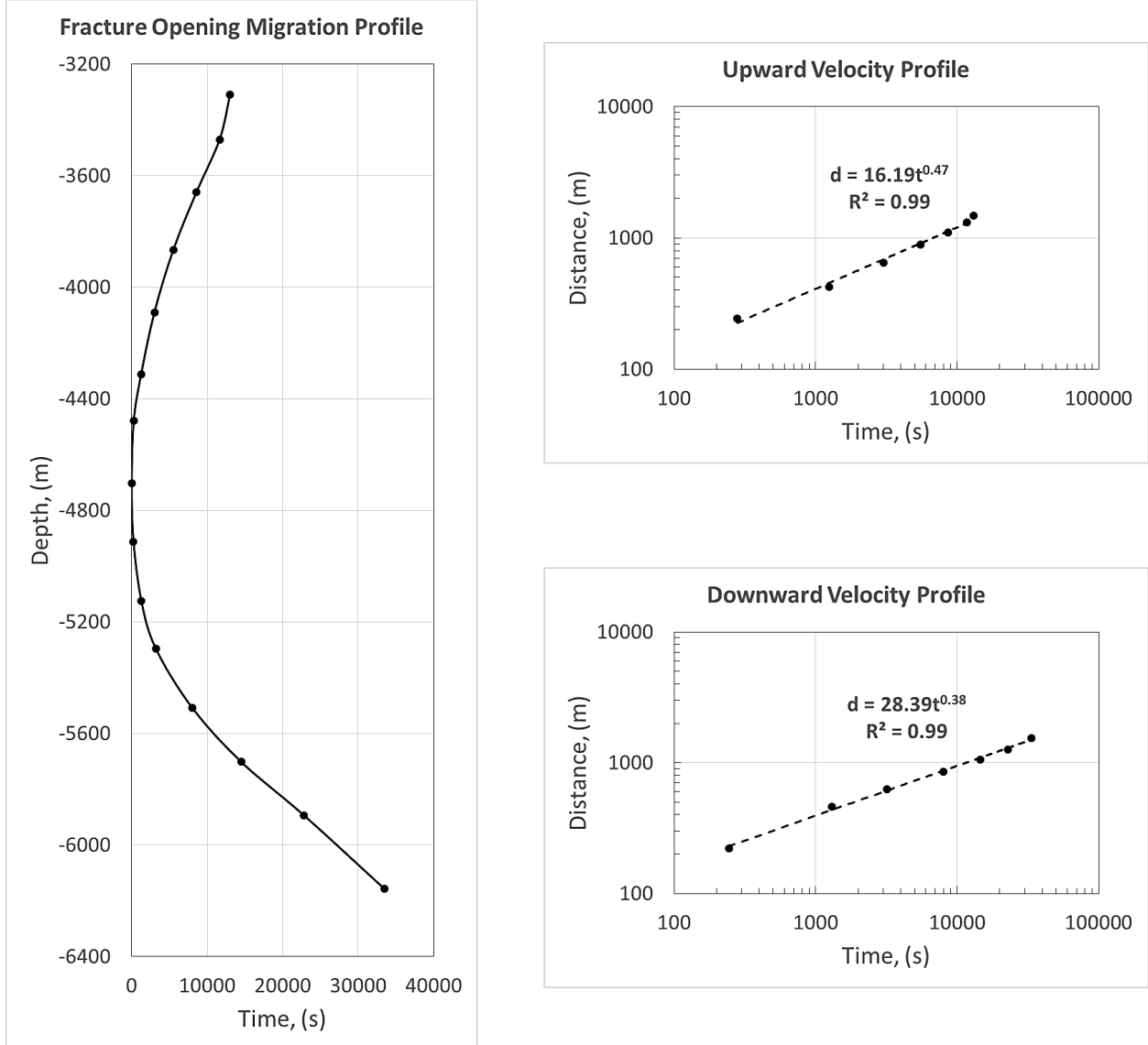
Figure 4.44. Migration of the fracture's local aperture opening to the top and bottom of the fracture for the fracture with shear slip; the left-hand side figure is plot of local aperture opening onset time versus depth of measuring points. The right-hand side sub-figures are illustration of upward and downward velocity functions along the fracture where the both profiles obey a power-law function, but the exponent of downward function is 0.38 compared to 0.47 of upward one

Further assessment between pressure increase and local aperture opening is done by plotting one versus the other (as done in figure 4.19 for no-slip fracture) to evaluate influence of shear displacement on effective normal stiffness of the fracture. The result can be found in figure 4.45 in which the effective normal stiffness is again negative inverse of the slope of the graph and equal to approximately 79.43 GPa/m (note that the applied normal stiffness to the fracture is 80 GPa/m). However, the relation between the effective normal

110

stress and the local fracture opening are more or less identical for both no-slip and slip fractures, but as shown in figure 4.46 the migration of the local aperture opening along the no-slip fracture is faster than that of slip one, just like pore pressure migration velocities compared in figure 4.43.
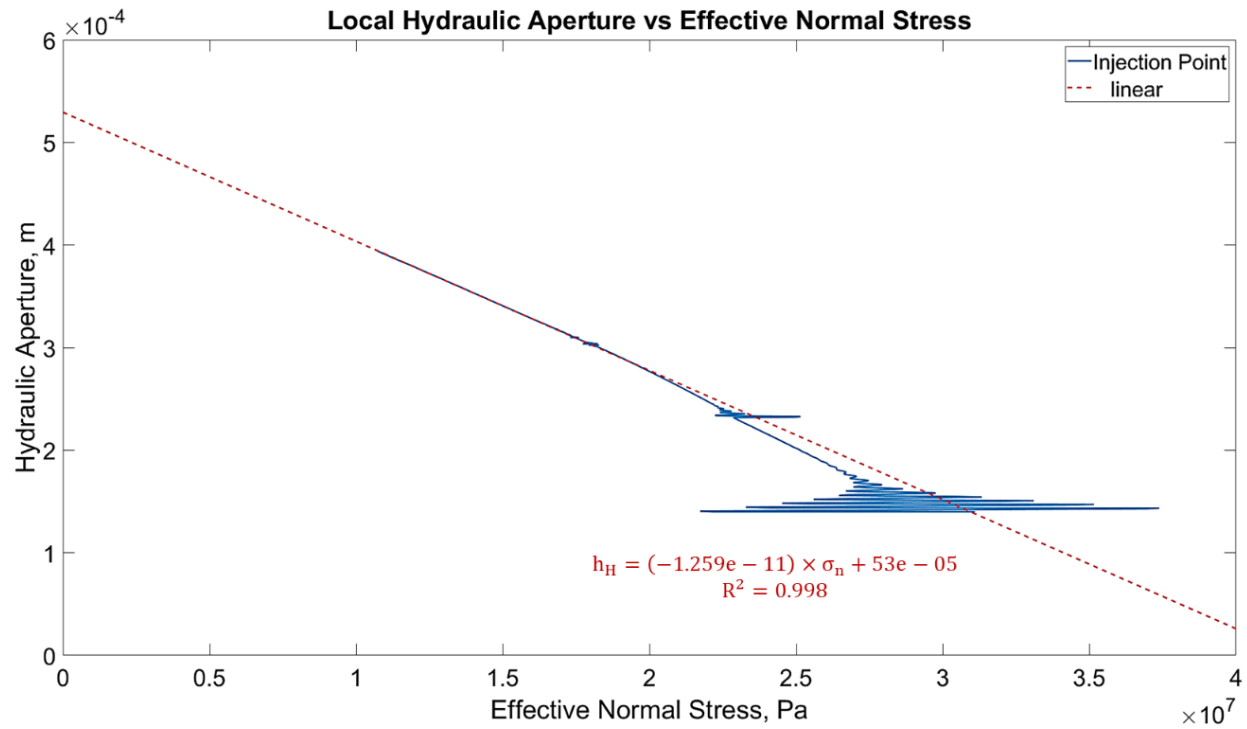
Figure 4.45. Local hydraulic aperture variation versus fluid pressure values at injection point; as it can be seen the numerical relation between effective normal stress acting on the fracture plane and the local hydraulic aperture at injection point is linear in which the slope of the fitted line is approximately negative inverse of the normal stiffness of the fracture (-1/-1.259e-11 = 79.43 GPa/m)
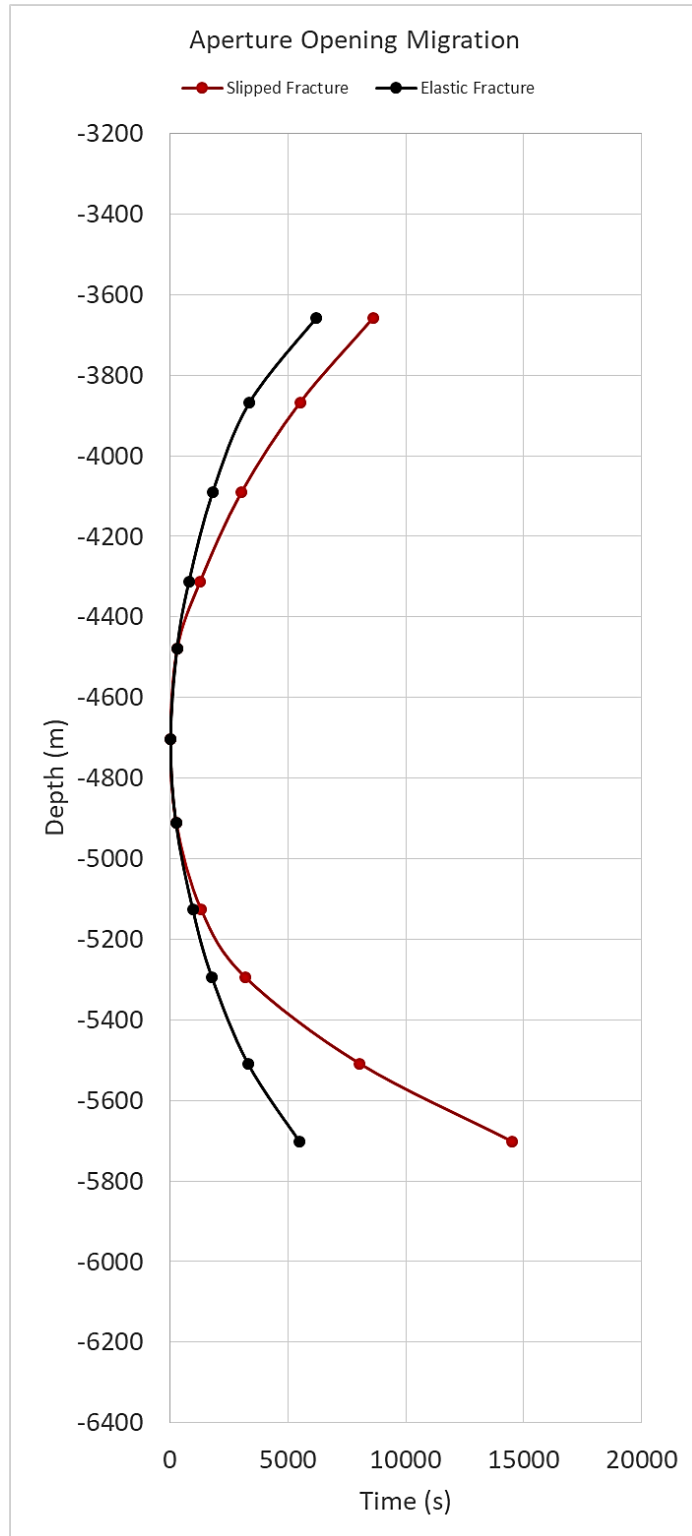
Figure 4.46. The comparison of local fracture opening propagation profile for two cases of no-slip fracture (black curve) and slip fracture (red curve); it can be seen that the fracture opening migration in no-slip fracture is a bit faster than that of slipped fracture.

4.6.1   Comparison with Seismicity Evolution

Figure 4.47 illustrates depth of seismic events versus of time for seismic activities recorded during hydraulic stimulation of the year 1993 of GPK1 well of Soultz-sous-Forêts at depth of about 3 km. It can be seen in the figure 4.47 that the upward and downward velocity of seismicity migration are respectively about 0.3 and 1.1 mm/s. If we assume that the seismic events are induced by fluid overpressure and the seismic wave velocities are independent of magnitude of fluid injection flow rate (Alghannam & Juanes, 2020), then it might be reasonable to compare the seismicity migration velocity observed in 1993 GPK1 stimulation (with flow rate of 3 l/s) to pressure propagation velocity observed in our simulation (with flow rate of 30 l/s). This comparison is made because no other data are available for seismic propagation during the 2000 hydraulic stimulation of the GPK2 well. Referring back to figure 4.46, one can see that the furthest measuring points are located at a distance of approximately 1100 and 1050 meters, respectively, above and below the injection point. Moreover, the aperture opening propagation requires 8600 and 14500 seconds to reach these measuring points, according to figure 4.45. Assuming the same seismicity velocity, shown in figure 4.47, to be valid in the depth of current study, the arrival time of seismicity to abovementioned points will be 3.68e6 and 0.9e6 seconds, respectively upward and downward. One possible reason for this significant difference, among many of others such as various possible values for initial aperture, fracture roughness, friction law, aseismic slip, temperature effects, etc., might be due to the fact that, at our simulation the effect of fluid leak-off to the surrounding rock matrix was not taken into account by defining an impervious rock matrix. The leak-off causes decrease in the volume of the fluid trapped in the fracture which, in turn, compensates the fluid pressure propagation velocity. The same role might be played by background fracture networks where a considerable volume of injected fluid can flow through an extended network of interconnected discontinuities. This factor might be crucial to be precisely analyzed especially when the medium of study is crystalline rock such as granite of Soultz-sous-Forêts.
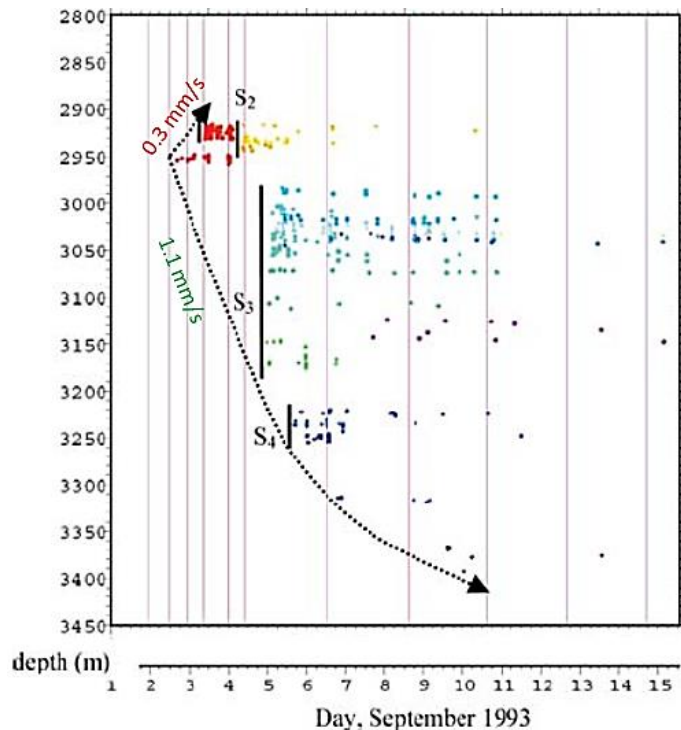
Figure 4.47. Depths of seismic events versus time recorded during hydraulic stimulation of well GPK1 at 1993 (reproduced after Bourouis and Bernard, 2007)

113

Worth to note that, the variation of slip front along the fracture for time periods of 6 hours from beginning of injection is shown in figure 4.48. It can be seen that, the slip front migrates upward faster than downward, just like the pressure front migration behavior shown in figure 4.42.

Figure 4.49 also illustrates the slip direction of the fracture in the model. Knowing that the X direction is strike of the fault and –Z direction is dip direction, then the growth of the slip area, as can be seen from sequence of figures in 4.48, is approximately in the direction of shear stress (yellow arrow); consistent with analytical results of table 4.5 for normal faulting regime with maximum horizontal stress of 0.95 times of vertical stress.

Evolution of shear displacement (in meter) and shear stress (in Pa) at injection point during stimulation period can also be found in figures 4.50 and 4.51. It can be seen from figures 4.51 and 4.52 that the initial shear stress at injection point located at depth of 4703 meter is about 24.5 MPa which is almost consistent with analytical value of 22.8 MPa calculated in section 3, tables 4 and 5. Figure 4.52 also demonstrates shear stress as a function of shear displacement for a measuring point located at a distance of 1105 m from injection point. The average shear stress as a function of average shear displacement of whole fault is plotted in figure 4.53. Another interesting plot might be average shear stress in terms of average effective normal stress acting on the fracture as shown in figure 4.54. The slop of this curve shows friction coefficient of the fracture as equal as 0.81.
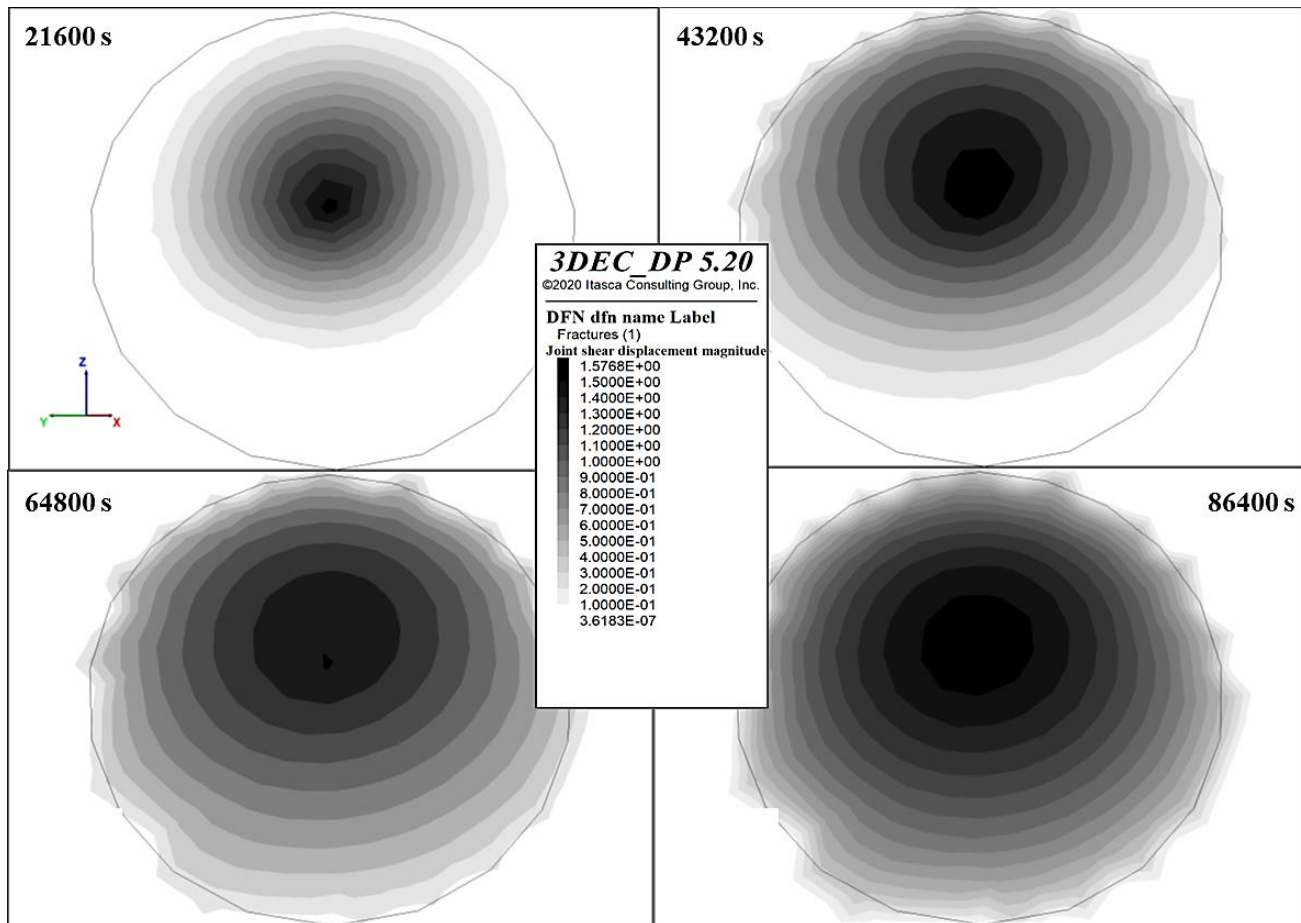
Figure 4.48. Propagation of fracture slip front throughout the fracture plotted every 6 hours after start of injection; the finite-size fracture is represented by black circle and the slip front is shown by gray scale. Shear displacements are in terms of meters.

114
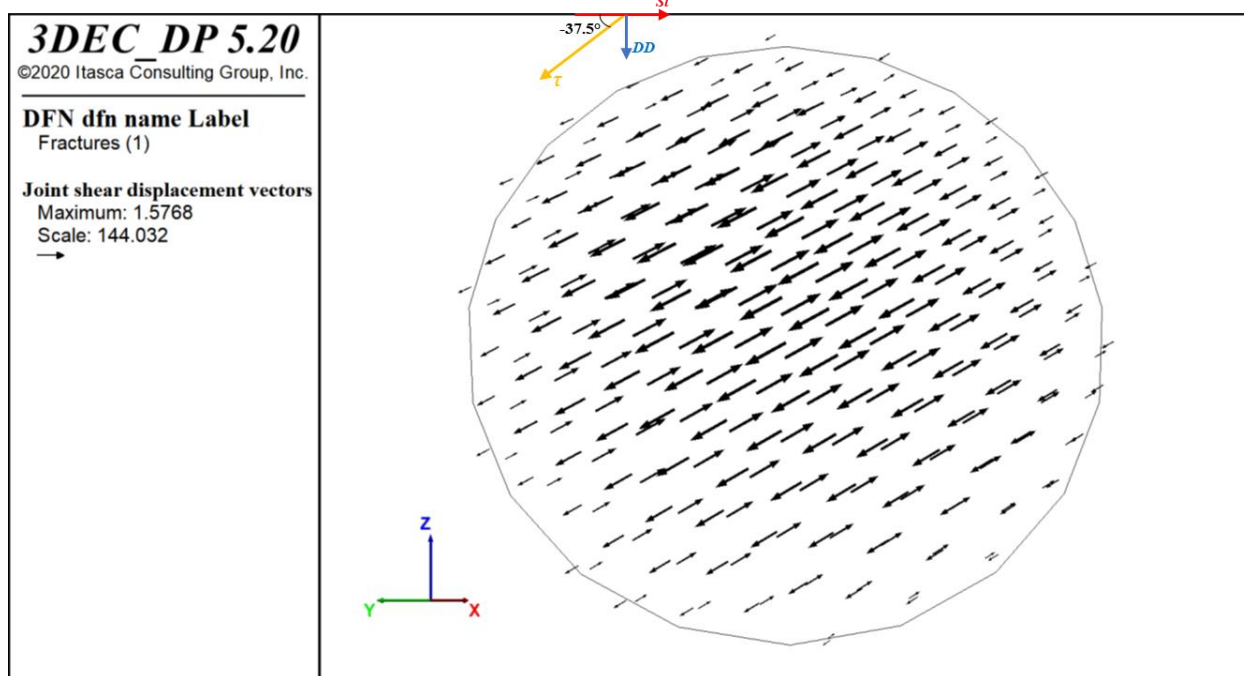
Figure 4.49. Direction of shear displacement (slip) of the simulated fracture
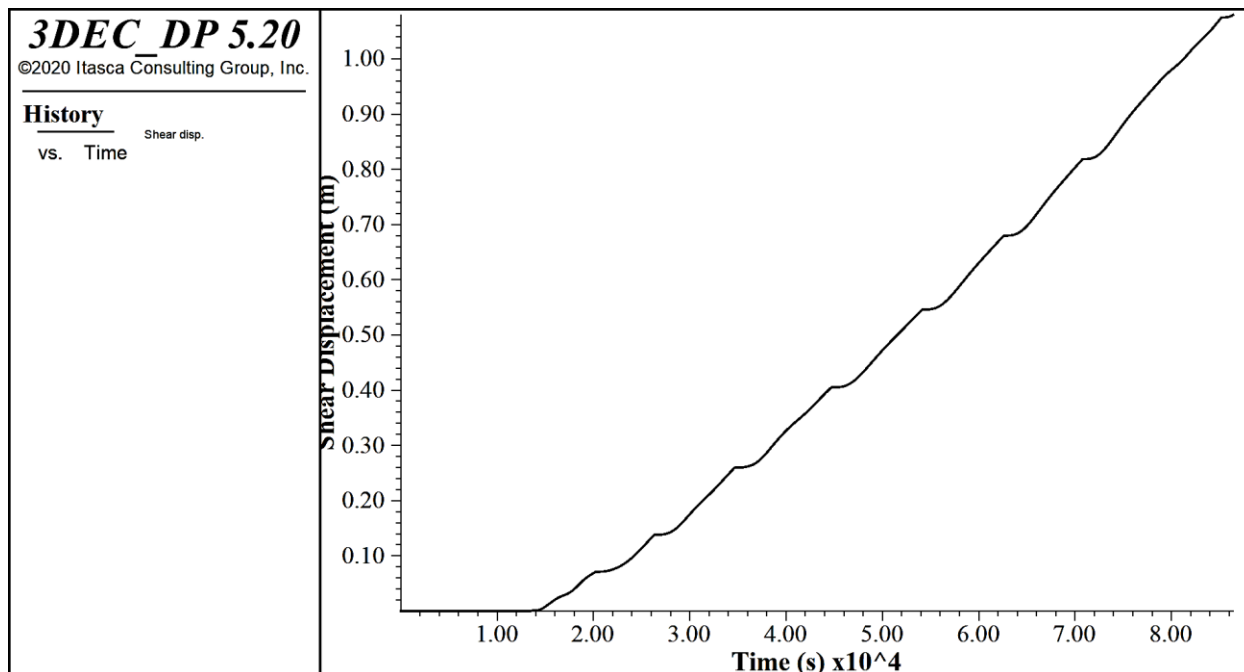
Figure 4.50. Evolution of shear slip in time at a measuring point located at a distance of 1105 m from injection point
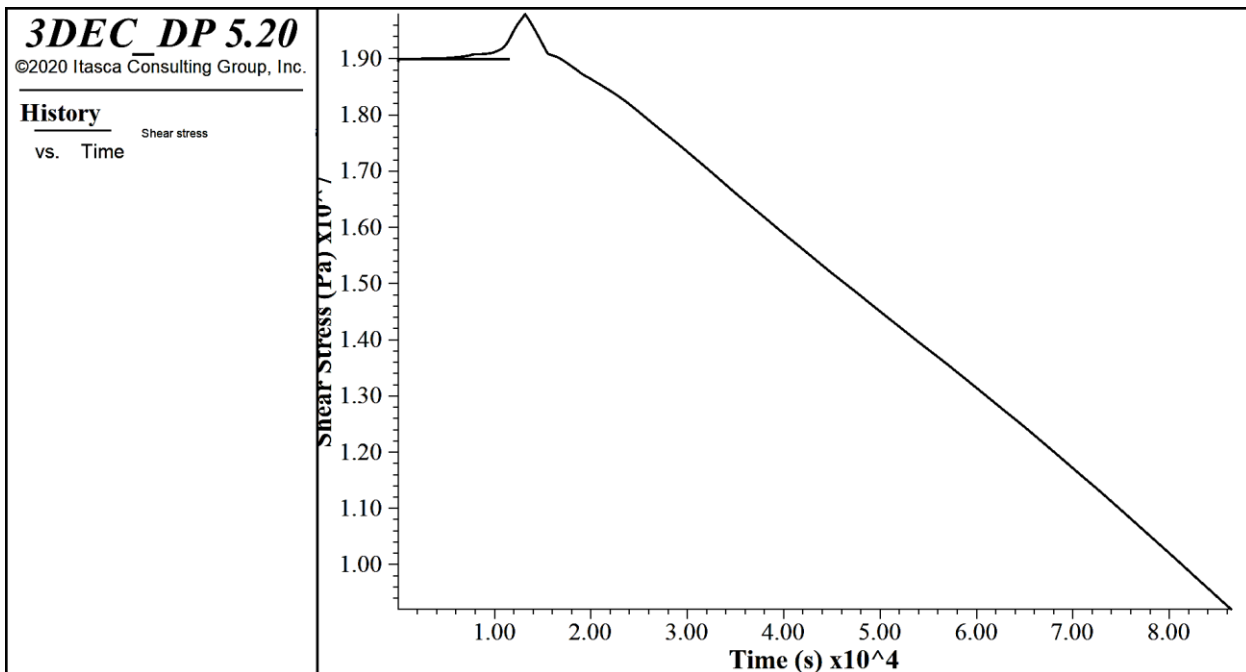
Figure 4.51. Evolution of shear stress in time at a measuring point located at a distance of 1105 m from injection point
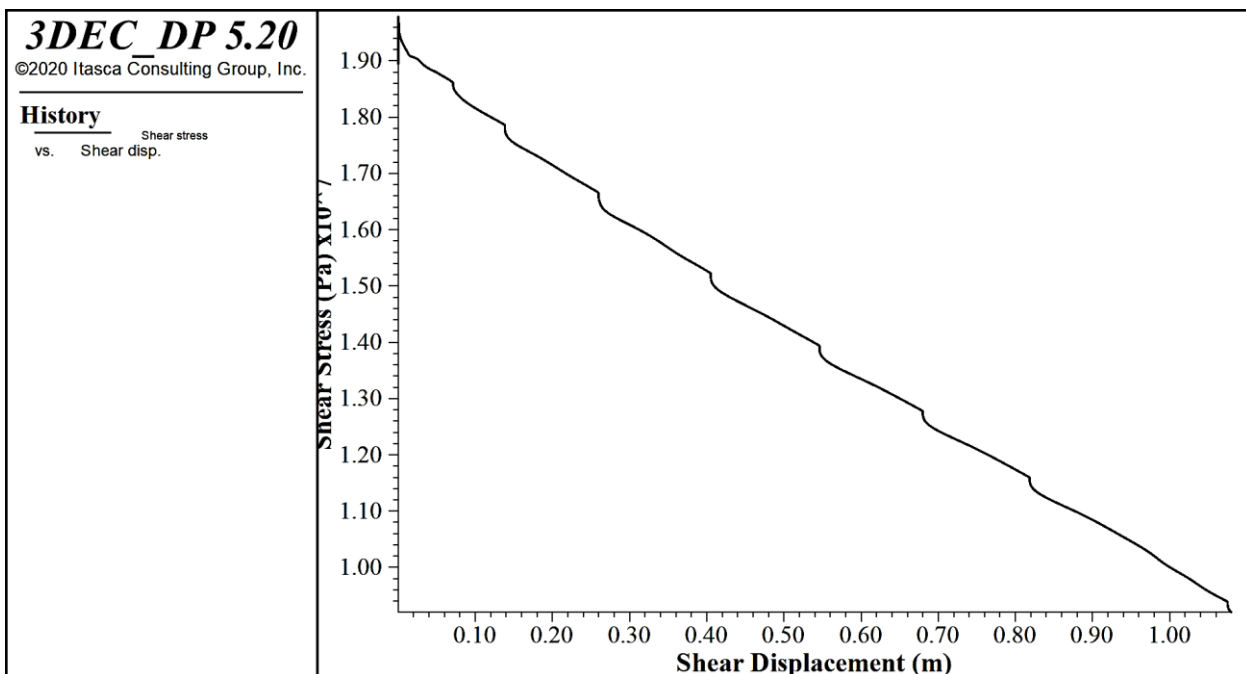
Figure 4.52. Shear stress as a function of shear displacement at a measuring point located at a distance of 1105 m from injection point
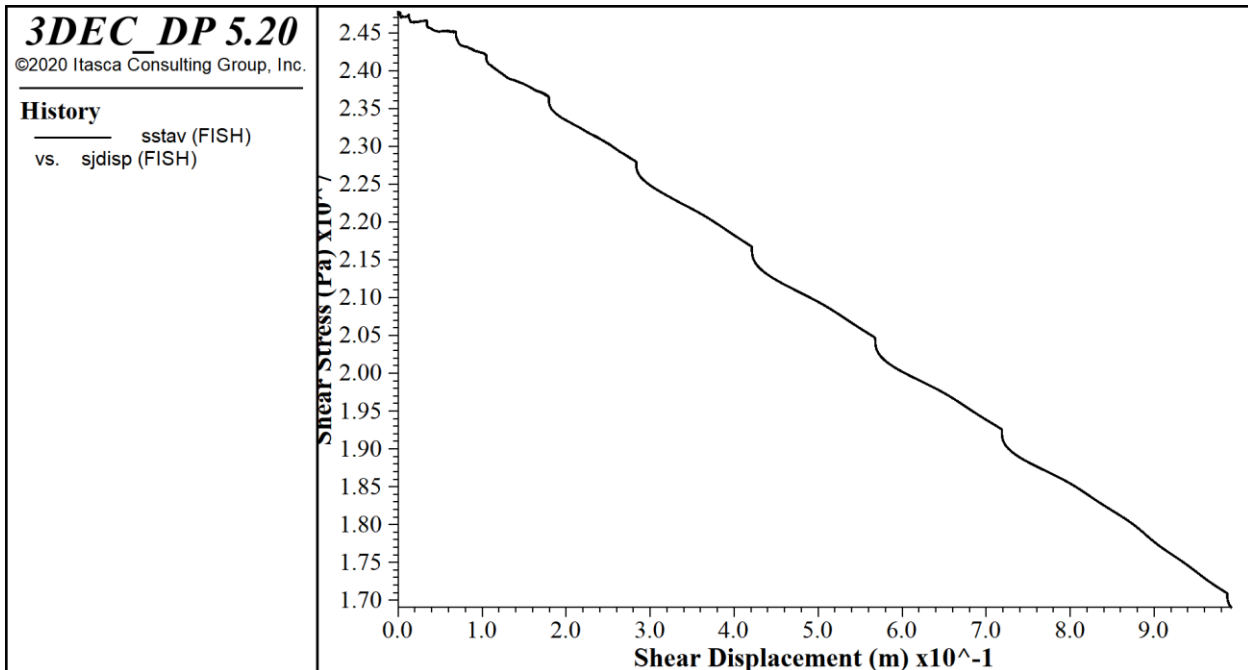
Figure 4.53. Average shear stress acting on the fracture as a function of average shear displacement along the fracture
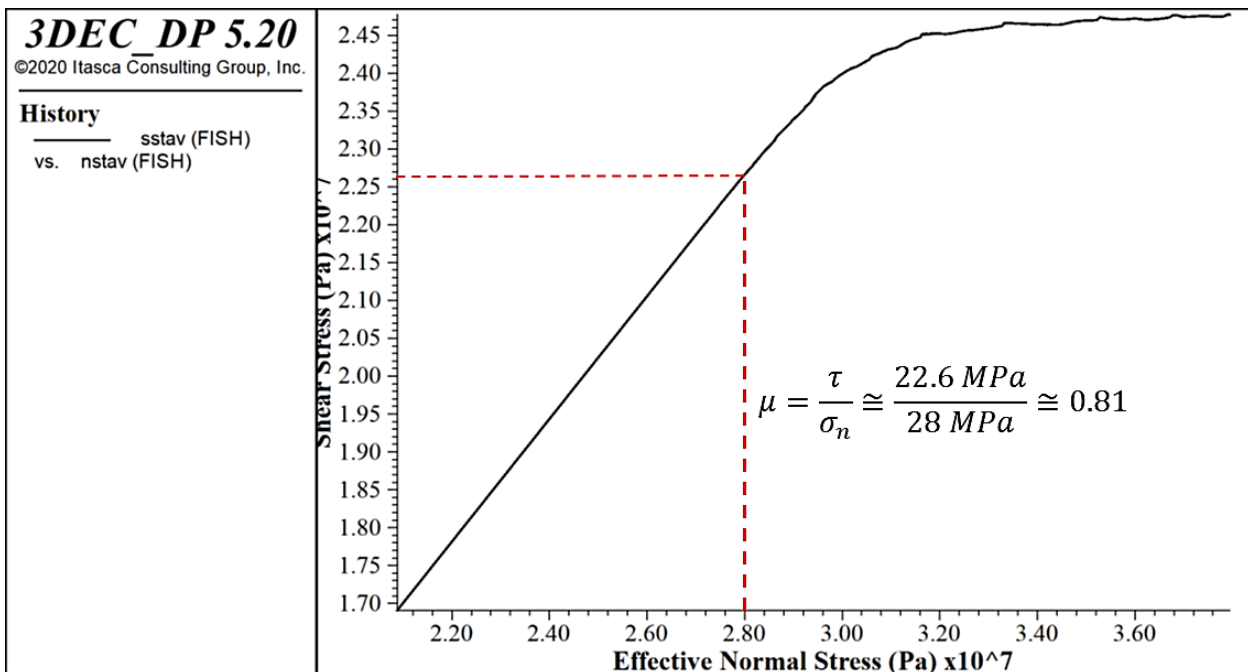
Figure 4.54. Average shear stress as a function of average effective normal stress acting on the fracture plane

It is worth to note that, the magnitudes of the shear slip shown in above figures seems to be far from reality. The authors are aware of this issue and will tackle it during future steps.

4.7 Conclusion

At present work it was aimed to numerically simulate the large-scale hydraulic stimulation of well GPK2 of Soultz-sous-Forêts performed in the year 2000 to better characterize both elastic behavior and slip of the fault against hydraulic stimulation. The 3DEC distinct element method (DEM) of ITASCA was used to stimulate GPK3-FZ4770 fracture introduced by Sausse et al., 2010 and Dezayes et al., 2010 embedded in an elastic, homogeneous, isotropic, and impermeable block of granite by injection of water for 24 hours at a constant flow rate. The results indicated that a fluid pressure front exists and migrates as a function of $\sqrt{t}$; leading to an average effective hydraulic diffusivity of 13 m²/s compared to 7 m²/s obtainable from Calo et al., 2011, where over 1000 m of V_p variation is observed in about 3 h. Then, a complementary simulation with variable flow rate was performed and found that the fluid pressure propagated as a function of t. These behaviors were also seen in the fracture's local hydraulic aperture owing to linear relation between effective normal stress and fracture aperture due to the fact that the fracture stiffness is considered constant in 3DEC calculations.

Then, the findings of both aforementioned injection scenarios were compared to the model introduced by Lengliné et al., 2017. This model is in fact a simple advective model (obeying $\sqrt{t}$ behavior) assuming a constant aperture along the open part of the crack and a sharp front between open and close part of the crack with no diffusion equation, however we tried to generalize the model to our numerical results by using time and space varying fracture aperture derived from 3DEC during injection period. The comparison revealed the fact that in the first injection scenario the fluid pressure propagated a little faster than Lengliné et al., 2017 prediction which might be due to the fact that in their model the fracture is initially assumed to be closed and it is opened to its maximum aperture once fluid flow reaches it (binary behavior), but the fracture in our model has an initial non-zero aperture.

Finally, a more advanced model of diffusion, introduced by Murphy et al., 2003, was used to evaluate the numerical aperture propagation data which were obtained from the first stimulation scenario. They divided whole the cases which a fracture might be encountered during fluid injection into two cases of linear and non-linear diffusion. The linear diffusion take place when the pressure evolution is not large enough to generate aperture opening. In this case the fluid flows in the space between two planes forming the fracture (a $\sqrt{t}$ behavior). The non-linear diffusion is divided into two cases of "joint in contact" and "joint lift-off" at which the fracture opening due to fluid injection happens, but in the latter the whole normal stress which keeps the fracture planes together is overcome by the fluid pressure and the whole hanging wall moves up. Murphy et al. distinguished these three case and corresponding equations by assigning a variable of n which is respectively 0, 1, and 3 for linear diffusion, joint in contact, and joint lift-off cases.

Here, the dimensionless parameters introduced in Murphy et al. paper was utilized to plot the aperture variation along the distance from injection point in different time periods. These periods were actually the time passed from beginning of the hydraulic stimulation. This time partitioning was chosen to better investigate the existence of the propagation front along the fracture during injection period and started from 1800 s, continued to 3600 s, 7200 s and finally 14290 s (which was approximately the time when the WHP at the furthest measuring point exceeded of 1 MPa). These plots were shown in figure 4.28. Comparison of figure 4.27 (which is a plot dimensionless aperture versus dimensionless distance from injection point achieved from semi-analytical equations of Murphy et al., 2003) reveals the fact that, in our simulation, the aperture propagation along the fracture most probably obeys the case of "joint in contact" (n=1). It is also consistent with the achievement of aforementioned comparison of numerical results with Lengliné et al. model where the numerical propagation was shown to be a bit faster than $\sqrt{t}$ behavior represented by Lengliné et al., 2017.

Moreover, according to Murphy et al., 2004, the propagation distance, d, varies with t to power of 0.33, 0.5, and 0.67, respectively for $n = 0$, 1, and 3. Comparison of the numerical results of present study with aforementioned values from Murphy et al., 2004, demonstrated the similarity of $n=1$ case with the aperture propagation behavior in no-slip fracture where the exponent of 0.49 can be seen in the right sub figures of figure 4.21, again consistent with previous conclusions.

Contrary to above observations, analytical comparison between joint compressibility introduced by Murphy et al., 2004, with that of 3DEC demonstrated similarity of 3DEC joint compressibility with $n=3$ case of Murphy et al., 2004, where in both cases the c_j was an inverse function of aperture. However, for the two end sections of aperture evolution with respect to effective stress, where the hydraulic aperture is constant and equal to maximum hydraulic aperture or residual hydraulic aperture, $\frac{\partial h}{\partial P}$ is zero; yielding a joint compressibility of zero and indicating a linear diffusion case of Murphy et al., 2004, in which c_j is zero.

Numerical simulation of the entire hydraulic stimulation procedure, in which, compared to the initial numerical simulation of the first stage of fluid injection, the boundary condition was changed from the undrained state to the drained one, and some modifications were also made to the normal stiffness of the fracture both inside and outside the fracture. In addition, the hydraulic aperture values on the outside of the fracture were the same as those on the inside of the fracture. It is found that the numerical wellhead pressure generally follows the field observations, with a sharp increase of about 1 MPa when the injection rate is increased by 10 ls^{-1}, a continuous and gradual increase in the third stimulation stage, and finally a sudden pressure drop of 4 MPa in the shut-in phase and then a gradual decline to a pressure of 5-6 MPa. However, the slope of the pressure drop in the shut-in phase is smaller in the field observation than in the numerical simulation, suggesting a long-term pressure decline in the field observation, which is addressed by Weidler et al. (2002) as a result of the lower rock mass permeability of the deeper reservoir compared to the upper reservoir of Soultz-sous-Forêts.

To fully characterize the observed behavior of fluid pressure/fracture aperture against fluid injection, a series of sensitivity analysis carried out on various parameters such as normal and shear stiffness of the fracture, relative orientation of the fracture plane and in-situ stresses, the dip of the fracture, and finally the size of the fracture. Among these parameters, it was found that the elastic behavior of the fracture (here as rate of fluid pressure propagation and maximum WHP at the injection point) was significantly affected by normal stiffness, fracture size, and fracture opening, while the changes were not significant against variation of other parameters. In addition, holding all evaluated parameters constant during the sensitivity analyses, it can be seen that the normal stiffness of 10-30 GPa/m produces a WHP closer to the field observations of about 10-12 MPa.

In addition, taking into account the effect of shear slip of the fracture based on Coulomb slip law with weakening showed a decrease in pressure propagation velocity compared to the no-slip fracture; however, these velocities (by taking the disturbance arrival time to a specific point as a proxy of the wave velocity) were higher than that observed at the shallower depths during stimulation of GPK1 well at 1993 reported by Bourouis and Bernard, 2007. One possible reason for his difference, among many of them such as various possible values for initial aperture, fracture roughness, friction law, aseismic slip, temperature effects, etc.), might be due to the fact that, at our simulation the effect of fluid leak-off to the surrounding rock matrix was not taken into account by defining an impervious rock matrix. The leak-off causes decrease in the volume of the fluid trapped in the fracture which, in turn, compensates the fluid pressure propagation velocity. The same rule might be played by background fracture networks where a considerable volume of injected fluid can flow through a huge network of interconnected discontinuities.

Chapter 5

5   Estimation of Effective Elastic Properties of Fractured Rock Mass

5.1   Introduction

Rock mass is composed of discontinuities at all scales, intact rock surrounding these discontinuities and the fluid which flows through the discontinuities. These discontinuities are of engineering importance due to their effects on the mechanical and hydraulic behavior of rock masses (Singh, 1973; Bieniawski, 1973, 1978; Barton et al, 1974; Amadei & Goodman, 1981; Hoek, 1994; Hoek et al, 1995; Hoek & Diederichs, 2006). There are usually four types of discontinuities in the engineering classification composed of bedding surfaces, slip surfaces, tension fractures, and shear fractures (Cai and Horii, 1992). A discontinuity can be characterized with its position or density, orientation (dip and dip direction), size, and thickness or hydraulic aperture. They may be defined in a stochastic and/or deterministic approach. In the deterministic version, each fracture and fault is presented as a plane with specific characteristics of dip, dip direction, size, position, and hydraulic aperture. In stochastic type, fractures and faults are presented statistically as a set of planes in which their characteristics are related to a distribution model such as log normal, gamma law, or power law.

The influence of fractures in altering the effective elastic moduli of intact rock was first noted by Simmons and Brace (1965) and Walsh (1965). Compared to intact rocks, jointed rock masses are weaker and more deformable, and are highly anisotropic and heterogeneous (Cai and Horii, 1993). Constitutive modeling of jointed rock masses has long been a subject of interest, and numerous models have been developed in attempts to simulate their mechanical responses, which are divided into two groups of models: discrete models and continuum models. The discrete models, in which the joints are implicitly modeled, often leads to very large and complex problems in the cases with pervasive and closely spaced joints. In continuum models, the joint rock mass is treated as a continuum material with equivalent material properties which reflects the influence of the joints (Cai and Horii, 1993). The latter model is easier to handle in the cases where the dimension of the underground structures are great enough compared to the heterogeneity size (Pouya & Ghoreychi, 2001) and many authors (Budianski & O'Connell, 1976; Hashin, 1983; Oda, 1988; Huet, 1990; Cai & Horii, 1992, 1993; Kachanov, 1980; Le Ravalec & Gueguen, 1996) have published their investigations in this area.

Here, it is aimed to numerically determine the effective mechanical properties (Young's modulus and Poisson ratio) of a 100x100x100 m^3 fractured rock block in which the fractures' normal and shear stiffnesses are defined based on non-linear stress-dependent equations introduced by Bandis et al., 1983. For that, the 3DEC of Itasca is used to first do a few benchmarking tests on the intact rock samples. Then, a set of

verification tests carried out on the implemented non-linear fracture behavior. This phase was composed of a rock block of 1x1x2 m^3 containing a 0.5 m diameter circular finite fracture with dip and dip direction of 45° and 90°, respectively. The resulting numerical normal Stress-displacement (for both interlocked and mismatched joints as described by Bandis et al., 1983) and shear stress-displacement curves were then compared to the analytical curves to verify the behavior of the developed model. This model was then generalized to a block of 100x100x100 m^3 hosting a discrete fracture network (DFN) located under in-situ stress state of Soultz-sous-Forêts geothermal reservoir at a depth of approximately 4.7 km to evaluate effective elastic moduli of the fractured rock mass.

5.2   Methodology

Mechanical behavior of a rock mass not only depends on properties of intact rock, but also, and to a high extent, is a function of mechanical and physical characteristics of the existing fractures. In Soultz-sous-Forêts, it is found that the macro-fractures decrease the strength of the rock mass (Villeneuve et al., 2018). Therefore, to effectively evaluate effective elastic moduli of the rock mass located in the field of interest, it is necessary to take into account the role of discontinuities on mechanical behavior of the rock. In the current project, 3DEC distinct element modeling tool of Itasca was utilized to evaluate effective elastic moduli of granitic basement in the Soultz-sous-Forêts geothermal reservoir. For that, stochastic DFN previously characterized by some researchers such as Valley, 2007, Massart et al., 2010, and Afshari Moein et al., 2019 and 2021, were embedded in a cubic block made of granitic intact rock basement of Soultz-sous-Forêts and the resulting rock mass block underwent some true triaxial compressive stress tests. Measured values of average axial and lateral stress and strain components in X-, Y-, and Z-directions were then used to evaluate effective elastic moduli of the fractured rock block.

5.2.1   Discrete Fracture Network (DFN)

A DFN can be characterized with fracture position or density, fracture orientation (dip and dip direction), fracture size, and fracture thickness or hydraulic aperture. DFNs may be defined in a stochastic and/or deterministic approach. In the deterministic version, each fracture and fault are presented as a plane with specific characteristics of dip, dip direction, size, position, and hydraulic aperture. Stochastic scaling of fracture system has widely become an active research field in the last 50 years where, fractures and faults are presented statistically as a set of planes in which their characteristics, e.g. size distribution, are scaled by a distribution model such as log normal , exponential law, gamma law, and power law. Bonnet et al., 2001, has provided a description of use of these models where it can be found that lognormal distribution is well-suited for fracture length distribution (Priest and Hudson, 1981; Rouleau and Gale, 1985), Exponential law has been widely used to describe the size of discontinuities (Cruden, 1977; Hudson and Priest, 1979, 1983; Priest and Hudson, 1981; Nur, 1982; Carbotte and Mc Donald, 1994; Cowie et al., 1993b) and gamma law is common to use in fault and earthquake statistics and seismic hazard assessment (Davy, 1993; Main, 1996; Kagan, 1997; Sornette and Sornette, 1999). Numerous studies are performed at various scales and in different tectonic settings and published results indicate that although some fracture systems are best described by scale-limited laws, i.e. lognormal and exponential, but it is now recognized that power laws and fractal geometries provide more appropriate and applicable descriptions for characterization of fracture networks (Bonnet et al., 2001). The main point of the power law and fractal scaling is the absence of characteristic length scales in the fracture growth process and having upper and lower bounds (Bonnet et al., 2001).

Davy et al., 1990, proposed a first order dual-power-law model that links the fractal spatial patterns of fractures to power-law distributions of fracture length and fracture centers as:

$$n(l, L)dl = \alpha . L^{D_M} . l^{-a} . dl, \quad l \in [l_{min}, l_{max}] \quad (5.1)$$

where $n(l,L)dl$ is the number of fractures having a length between l and $l+dl$ in a box of size L, D_M is the mass dimension of fracture barycenter, a is the exponent of the frequency distribution of fracture lengths, and α is a fracture density term which is not essentially equal to the common fracture density values such as P_{10} or P_{32} but is, in fact, the number of fractures, trances or fracture lengths, or intersections which is required to cover the fractal box or surface or line (Bonnet et al., 2001). In the model, it is assumed that the length distribution of fractures follows a power law, but equation (5.1) is valid regardless of D_M value, even for a non-fractal distribution of elements in a plane ($D_M = 2$), or in a volume ($D_M = 3$) (Bour et al, 2002).

Methods for Computing Size Distribution

Frequency, frequency density, and cumulative frequency distributions are three different types of distribution which might be used to characterize fracture size data (Bonnet et al., 2001). The value of the power law exponent, a in equation (5.1), depends on the type of distribution on which the analysis is based as well as on the bin type if it is linear or logarithmic (Bonnet et al., 2001). Table 5.1 is a comparison between the power law exponent values for different types of binning and distributions.

Table 5.1. Relationship between distributions and bin types with their exponents (Bonnet et al, 2001)

Type of distribution	Logarithmic Binning	Linear Binning
Frequency	$a - 1$	a
Density	a	a
Cumulative	$a - 1$	$a - 1$

For a population of fractures that follows a power-law model, frequency distribution of fracture size can be expressed (Bonnet et al., 2001) as

$$N(L) = \alpha . l^{-a} . dl \quad (5.2)$$

Where $N(L)$ is the number of fractures whose length belong to the range of $[l, l + dl]$ with $dl \ll l$, α is a density constant and a is the power law exponent. Davy, 1993, defined the density distribution as the number of fractures belonging to an interval divided by the bin size as

$$n(l) = \frac{N(L)}{dl} = \alpha . l^{-a} \quad (5.3)$$

As long as dl is small enough, the density distribution is independent of the chosen bin type (Bonnet et al, 2001). For a power-law population exhibited in a log-log plot of $N(L)$ or $n(l)$ in terms of l, the slope of the straight line fitted to the distribution gives the exponent of the power law (Reches, 1986; Scholz and Cowie, 1990). Looking at equations (5.2) and (5.3) reveals that a small change in dl may have a significant effect on the number of fractures appeared in an interval, hence the choice of dl is crucial in the sense that it defines the degree of smoothing of the distribution trend (Bonnet et al., 2001). Davy, 1993, introduced an objective method for determining an optimum dl size at which $n(l)$ shows the lowest fluctuations.

The cumulative distribution is the number of fractures whose length is larger than l and corresponds t the integral of the density distribution (Bonnet et al., 2001) as

$$C(l) = \int_l^{l_{max}} \alpha \, n(l)dl \quad (5.4)$$

where l_{max} is the largest fracture length in the population. Worth to note that if $n(l)$ is a power-law distribution with the exponent of a, then and according to table 5.1., the $C(l)$ will also be a power-law distribution with the exponent of $a - 1$, which is commonly denoted as c (Childs et al., 1990; Walsh et al., 1991; Jackson and Sanderson, 1992; Cowie et al., 1993a; Pickering et al., 1997). The advantage of cumulative distribution compared to the other two distribution types is that it is easily computed and the data binning is not necessary (Bonnet et al., 2001), but on the other hand, its high sensitivity to finite size effects can be considered as a disadvantage for cumulative distribution type.

Moreover, all observed fracture populations suffer from "truncation" and "censoring" effects that alter the appearance of the fracture length distributions. Truncation refers to the fracture lengths that are not spotted in the sampling operation due to the resolution problems and hence are not reported in the distribution. This problem imposes a shallow slope of the distribution trend at the lower end of the scale range (small fracture lengths). Censoring happens when the long fractures' real length are not correctly sampled because they overpass the observation region and in consequence causes an artificial steeping of the distribution trend at the upper end of the scale range (large fracture lengths) (Bonnet et al., 2001).

Methods for Computing Fractal Dimension

The great advantage of the model presented in equation (5.1) is to allow the derivation of the fracture density term, α, which fixes the number of fractures of a given length per unit of ''fractal'' area (Davy et al., 1990). The validated model can then be used for scaling of some other properties of the fracture network, e.g. fracture density and fracture connectivity (Bour and Davy, 1997, 1998; Berkowitz et al., 2000).

Mandelbrot, 1982, described mathematical theory of the fractals and Feder, 1988, Falconer, 1990, and Vicsek, 1992, gave more information regarding that. It is very important to keep in mind that the fractal dimension does not completely define the geometry of the fracture system, and a complete characterization should include various geometrical attributes such as density, length, orientation, etc. (Bonnet et al., 2001).

Depending on the measured parameter, there are different methods of computing fractal dimension. According to the classical definition of the fractal, it is equal to the number of segments, circles, or spheres of dimension d equal to 1, 2, or 3, and of characteristic length scale r, necessary to cover the part of fractal object included in volume R^d. This number should vary as $N(r, R) \approx (\frac{R}{r})^D$, where D is the fractal dimension and $N(r, R) \times r^d$ is an estimate of the length, surface, or volume of the fractal object. Based on this definition, D may be obtained (Bonnet et al., 2001) as

$$D = \lim_{r \to 0} \frac{lnN(r)}{ln(1/r)} \quad (5.5)$$

Meaning the typical box-counting method where the fractal dimension is computed for infinitely small details of the objects, or

$$D = \lim_{R \to \infty} \frac{lnN(R)}{ln(R)} \quad (5.6)$$

Which is obtained by increasing the volume limiting the fractal object.

In the box-counting method, the number of boxes of size r, required to cover the fractal object is counted and should vary as

$$N(r) \approx r^{-D} \quad (5.7)$$

Thus, by log-log plotting of $N(r)$ versus r, the slope of the fitted straight line can be reported as fractal dimension, D, e.g. works performed by Okubo and Aki, 1987; Barton and Larsen, 1985; Barton et al., 1986; Barton and Hsieh, 1989; Barton, 1995a, Chiles, 1988.

Researchers generally benefited from mass method, at which the mass of the object replaces its volume in the definition and scales as

$$M(R) \approx R^{D_M} \quad (5.8)$$

where D_M is called mass dimension and is not essentially equal to D because it refers to different geometrical properties of the object. Davy et al., 1990 and Sornette et al., 1993, have defined the mass of the fracture pattern as the total fracture length included in disks of radius r. By averaging over typically 100 disks centered on the fracture pattern, a function such as

$$L(r) = r^{D_M} \quad (5.9)$$

may be obtained which explains the variation of the $L(r)$ as a function of r. Equivalently, D_M is also called mass dimension. These two methods are illustrated in figure 5.1.
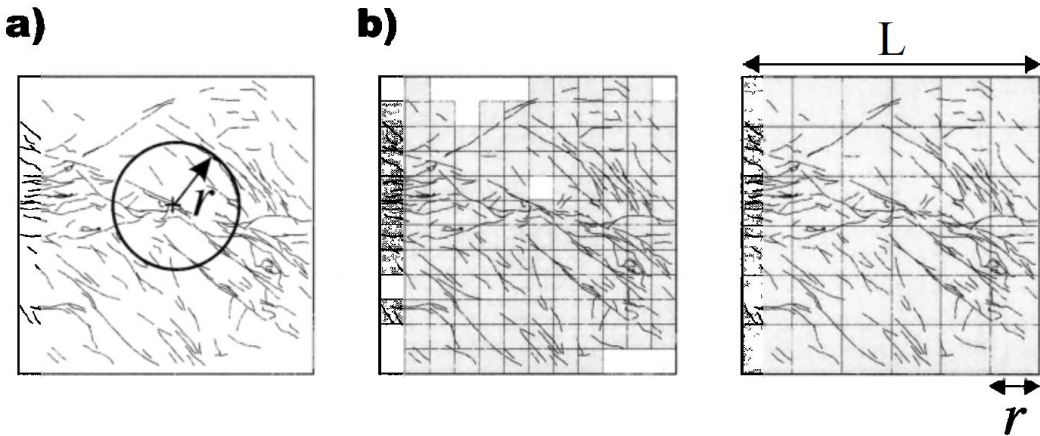
Figure 5.1. (a) Mass dimension method, where the total length of the fracture lying in a disk of radius r is obtained, and (b) the box counting method, for which the system of size L is covered by a regular mesh of size r; showing two different mesh sizes in which the fracture contained boxes are shaded whereas empty boxes are left blanc (reproduced after Bonnet et al., 2001)

Another method which is commonly used for computing the fractal dimension of fracture sets is the two-point correlation function (Hentschel and Procaccia, 1983) which gives the probability that two points belong to the same structure (Bonnet et al., 2001). While the box-counting method suffers from strong

effects of finite size, the two-point correlation function methods is less affected and seems a better method to derive the scaling exponent of the spatial distribution of the fracture centers in 2D outcrops (Afshari Moein et al., 2019; Bonnet et al., 2001; Bour et al., 2002; Vicsek, 1992). This method can be described (Hentschel and Procaccia, 1983) as

$$C_2(r) = \frac{1}{N^2} N_d(r) \quad (5.10)$$

or (Bour et al., 2002; Afshari Moein et al., 2019, 2021) as

$$C_2(r) = \frac{2}{N(N-1)} N_d(r) \quad (5.11)$$

In which N is the total number of points and N_d is the number of pairs of points/fracture barycenter whose distance apart is less than r (Hentschel and Procaccia, 1983). Hence, this definition is based on a cumulative frequency and for a fractal population of the points, it is expected to have

$$C_2(r) \approx r^{D_C} \quad (5.12)$$

Where D_C is the correlation dimension of the system (Bonnet et al., 2001). This technique is used to describe the spatial distribution of the fracture barycenters, which are defined as the midpoints of the fracture traces (Davy et al., 1990; Sornette et al., 1993; Bour and Davy, 1999). According to Hentschel and Procaccia, 1983, the correlation dimension in (5.12) is equivalent to the correlation dimension obtained from the box-counting method. Bour, 1997, verified that the both models lead to similar results. The two-point correlation function therefore gives an accurate estimation of the mass dimension which fixes the scaling of the number of fractures in a box of size L in the model presented in equation (5.1) (Bour et al., 2002). Noteworthy is that the two-point correlation function method is more effective at distinguishing natural fracture patterns from purely random ones compared to the box-counting method (Bour, 1997).

Relation between Spatial Distribution and Topological Dimension of DFN

According to Bonnet et al., 2001, it seems that there is a misunderstanding between the fractal dimension concept of spatial distribution and power-law distribution of the other topological dimensions of the fracture systems such as length, displacement and aperture distribution. It stems from a simple theoretical fragmentation model (generally known as the Apollonian model in physics) originally proposed by King, 1983, and Turcotte, 1986 and 1992, which gives rise to a power-law length distribution, exponent of which was equated to the fractal dimension of the system. Following this, many researchers incorrectly concluded that the system is fractal in a condition that the length distribution is power law (Bonnet et al., 2001). In fact, the fractal dimension term should be only applied for description of the spatial distribution of fractures (Mandelbrot, 1982). A fractal network indicates a spatial correlation and organization between fractures that may be quantified by a fractal dimension that is independent of the distribution of the other fracture parameters such as length. On the other hand, fractures may be nonfractal (i.e. randomly distributed in the space) while other parameters may follow a power law distribution model (Bonnet et al., 2001; Bour and Davy, 1997). Therefore, the dual power-law model represented in (5.1) contains no direct relationship between fractal dimension and power-law exponent and hence it is called first order model (Afshari Moein et al., 2019).

Among a few studies carried out on analysis of spatial and length distribution of the fracture networks (e.g. Davy et al., 1990 and 1992; Sornette et al., 1993), Bour and Davy, 1999, have proposed that the fractal dimension and the length distribution exponent are related through the relation

$$D = (a-1)/x \quad (5.13)$$

where x is the exponent indicating the average distance from a fracture barycenter to its nearest neighbor with larger length. The case of $a = D + 1$ of the fragmentation model introduced by King, 1983, and Turcotte, 1986, corresponds to a particular self-similar case in which x is equal to 1.

Some other works in this regard are performed by Darcel et al., 2003a, to relate the length of the fracture to the mean distance of the fracture center to its nearest neighbor in the Hornelen basin of Norway. Davy et al., 2010, introduced a universal model of fracture scaling based on categorizing the fracture systems to two regimes of dilute and dense ("dilute" regime for the smallest fractures where they can grow independently of each other and "dense" regime for which the density distribution is controlled by the mechanical interactions between fractures) and the inhibiting role that the fractures do not cross the larger one. They found that those two crude rules resulted in a self-similar distribution whose exponents and density term are fully determined by the fractal dimension and a dimensionless parameter γ that contains the information of the fracture orientations and correlations.

Relation Between 1D, 2D, and 3D exponents (Stereological Relations)

Another important point of discussion here is the stereological relations between 1D, 2D, and 3D exponents and fractal dimensions. A detailed explanation of stereological analysis of fractal DFN can be found in Darcel et al., 2003b. It is obvious that the statistical analysis can be carried out in one-dimensional data (gathered from well logs and scan-lines, two-dimensional data (provided by outcrop maps and other images), and three-dimensional data (achieved from seismic surveys and serial sectioning in, for example, quarries (Gervais and Genter, 1991; Gertsch, 1995). When the size distribution of the disks in 3D follows a power law, trace lengths in an outcrop of that as well as the length distribution of them in a scan-line are also power law with exponents of (Marret and Allmendinger,1991; Westway 1994; Marret, 1996; Piggott, 1997; Berkowitz and Adler, 1998)

$$a_{2D} = a_{3D} - 1 \quad (5.14)$$

$$a_{1D} = a_{3D} - 2 \quad (5.15)$$

Similarly, these rules are valid for fractal dimensions (Bonnet et al., 2001) as

$$D_{2D} = D_{3D} - 1 \quad (5.16)$$

$$D_{1D} = D_{3D} - 2 \quad (5.17)$$

However, above equations are established based on assumptions of ideal Euclidean shapes or fractal sets, assuming that all the geometric parameters of the fracture systems are independent and homogeneous (Bonnet et al., 2001). These assumptions may not be valid in some cases, where, for example, there exists a correlation between fracture length and position (Ackerman and Schlisch, 1997; Bour and Davy, 1999).

Extrapolation of power law exponent and fractal dimension results from 1D or 2D datasets to 3D remains one of the major challenges in the study of fracture systems. Borgos et al., 2000, performed a theoretical analysis on reconstructing of 3D exponents from synthetic 1D and 2D data and proposed

$$\xi_{3D} = \xi_{2D} + B \quad (5.18)$$

where ξ is the exponent and $0 \leq B \leq 1$. Comparison of scaling exponents from acoustic emission data (3D) and direct fracture trace data (2D) in laboratory experiments of subcritical tensile crack growth by Hatton et al., 1993, showed that a combination of preferential crack nucleation at the tensile surface and directional fracture anisotropy led to a scaling equation as

$$\xi_{3D} = A \times \xi_{2D} + B \quad (5.19)$$

where the best fitted line to the whole data set yield $A = 1.28 \pm 0.30$ and $B = -0.23 \pm 0.36$ at which the error bounds are one standard deviation.

Darcel et al., 2003b, assessed the stereological rules for fractal fracture networks, which means networks whose fracture-to-fracture correlation is scale-dependent with a non-integer fractal dimension. They introduced some relations between 1D and 2D as well as between 2D and 3D exponents. These relations for 1D and 2D are

$$D_{1D} = 1, \quad a_{2D} \leq 2 \quad and \quad a_{2D} \leq D_{2D} \quad (5.20)$$

$$D_{1D} = D_{2D} - a_{2D} + 1, \quad a_{2D} \leq 2 \quad and \quad a_{2D} \geq D_{2D} \quad (5.21)$$

$$D_{1D} = D_{2D} - 1, \quad a_{2D} \geq 2 \quad (5.22)$$

and for 2D and 3D are

$$D_{2D} = 2, \quad a_{3D} \leq 2 \quad and \quad a_{3D} \leq D_{3D} - 1 \quad (5.23)$$

$$D_{2D} = D_{3D} - a_{3D} + 1, \quad a_{3D} \leq 2 \quad and \quad a_{3D} \geq D_{3D} - 1 \quad (5.24)$$

$$D_{2D} = D_{3D} - 1, \quad a_{3D} \geq 2 \quad (5.25)$$

For 1D and 3D relations, Darcel et al., 2003b, found that it is not possible to constrain 3D exponents from lower-dimension exponents, except when the length exponent is known. Afshari Moein et al., 2019, analyzed stereological relations of exponents for some synthetic DFN and compared the results with those deduced from equations 5.20-25 (Darcel et al., 2003b) and found that even when the fracture systems' length distribution is known, it is not possible to deduce 3D scaling parameters from 1D data.

Therefore, the extrapolation of the exponents from 1D or 2D to 3D are not as simple as the above theoretically suggested models (Bonnet et al., 2001).

DFN at Soultz-sous-Forêts

The DFN at Soultz-sous-Forêts has been characterized in the literature in both probabilistic (Dezayes et al., 2004, 2005, 2010a, 2010b; Valley, 2007; Massart et al., 2010, Afshari Moein et al., 2019 and 2021) and deterministic (Sausse et al., 2010 and Dezayes et al., 2010b) approaches.

Fracture Orientation

Among those working on the probabilistic DFN, Massart et al., 2010, re-interpreted the whole existing Ultrasonic Borehole Image (U.B.I) logs and characterized 1878 fractures through the three deep Soultz well paths (i.e., GPK2, GPK3, and GPK4). These fractures were then labeled from 1 to 9 based on the type of the fractures shown in table 5.2. Among which, the natural open fractures were labeled 1 to 6, damage zones were labeled 7, horizontal and vertical induced drilling fractures were labeled 8 and 9. They also used the main and largest fractures characterized by Sausse et al., 2010, and labeled those 11, 12 and 14. Another classification on the fractures were carried out according to dip direction; based on that the fractures were grouped into two conjugated sets of West and East dipping which demonstrated N-S orientation and a mean dip of 58˚-72˚ and for former set and 69˚-74˚ for the later one (Massart et al., 2010). The Soultz-sous-Forêts basement is also represented by two different granite facies. The first one is located at depth of about 1200 meters down to 4000 meters is a monzogranite facies which consists of porphyritic granite, rich in potassic feldspars appeared in quartz, plagioclase, biotite and amphibolite matrix which also can be strongly altered (Genter, 1989). The second facies, starting from over 4000 meters, is a two micas facies composed of biotite and muscovite in a gray quartz matrix which is more homogeneous and less concerned by the hydraulic alteration than the first facies (Dezayes et al., 2005). Information of all fractures are summarized in table 5.3 A, B, and C.

Table 5.2. Classification of fractures (Massart et al., 2010)

Label	Fracture Type
1	Discontinuous Open
	0-25% of UBI trace
2	Discontinuous Open
	25-50% of UBI trace
3	Discontinuous Open
	50-75% of UBI trace
4	Vuggy Fractures
5	Continuous Open
	Fine aperture, more than 75% of the UBI trace
6	Wide Open
	Big aperture, more than 75% of the UBI trace
7	Damage Zones
	Intense fractures zones
8	Horizontal Induced Fractures
9	Vertical Induced Fractures

Valley, 2007, analyzed borehole image logs of GPK2, GPK3, and GPK4 wells of Soultz-sous-Forêts and clustered them to 7 sets based on their orientation. Figure 5.2 illustrates the results of the clustered fractures where the poles of fractures of all seven sets are plotted on stereonet of lower hemisphere equal area. According to Valley, 2007, the set 1 to 4 fractures are present along the entire borehole length, whereas sets 5 to 7 are observed at some specific locations. Set 5 fractures are sub-horizontal fractures existing at the depths above 2.5 km and between 3.2 and 3.8 km. Set 6 and 7 are E-W striking fracture sets occurring mainly below 4 km depth where set 6 fractures are sub vertical and set 7 fractures are dipping 45°. It can be deduced from the statistics given in figure 5.2 that 95% of fractures belong to sets 1 to 4 with 3876 fractures compared to the 210 fractures clustered in sets 5 to 7.

Table 5.3. Results of statistical analysis of fracture database (Massart et al., 2010)

A

	Label & fracture type	Number of fractures	rate (%)	Number of fractures FACIES 1	Number of fractures FACIES 2	Number of fractures SET W	Number of fractures SET E
1	Discontinuous open traces (25%)	1361	72.47	1170	191	837	524
2	Discontinuous open traces (50%)	85	4.53	83	2	47	38
3	Discontinuous open traces (75%)	30	1.60	21	9	16	14
4	Vuggy Fractures	125	6.84	117	8	86	39
5	Continous open	23	1.22	20	3	17	6
6	Wide open	13	0.69	10	3	8	5
7	Damage zones	82	4.37	80	2	49	33
8	Induced subhorizontal drilling fractures	159	8.47	137	22	88	71
	Total	**1878**	**100**	**1638**	**240**	**1148**	**730**
	Fracture density (Fractures/m)			**1.890**	**0.952**	**0.18**	**0.12**

B

	Label & fracture type	SET W				
		Mean Dip Direction	Fisher coefficient	Mean Dip	Fisher coefficient	Fracture density (Fractures/m)
1	Discontinuous open traces (25%)	263	0.73	68	5.8	0.202
2	Discontinuous open traces (50%)	249	0.92	67	5.65	0.177
3	Discontinuous open traces (75%)	246	1.3	61	3.74	0.003
4	Vuggy Fractures	270	0.6	63	4.77	0.017
5	Continous open	247	1.29	72	8.24	0.006
6	Wide open	241	1.14	58	10.68	0.002
	All fractures	266	0.72	68	5.57	**0.18**

C

	Label & fracture type	SET E				
		Mean Dip Direction	Fisher coefficient	Mean Dip	Fisher coefficient	Fracture density (Fractures/m)
1	Discontinuous open traces (25%)	81	1.1	69	5.57	0.134
2	Discontinuous open traces (50%)	77	1	74	10.07	0.012
3	Discontinuous open traces (75%)	96	1.23	70	6.87	0.004
4	Vuggy Fractures	74	1.17	71	7.32	0.011
5	Continous open	76	3.89	71	10.68	0.002
6	Wide open	117	1	71	2.71	0.002
	All fractures	77	1.06	70	5.65	**0.12**
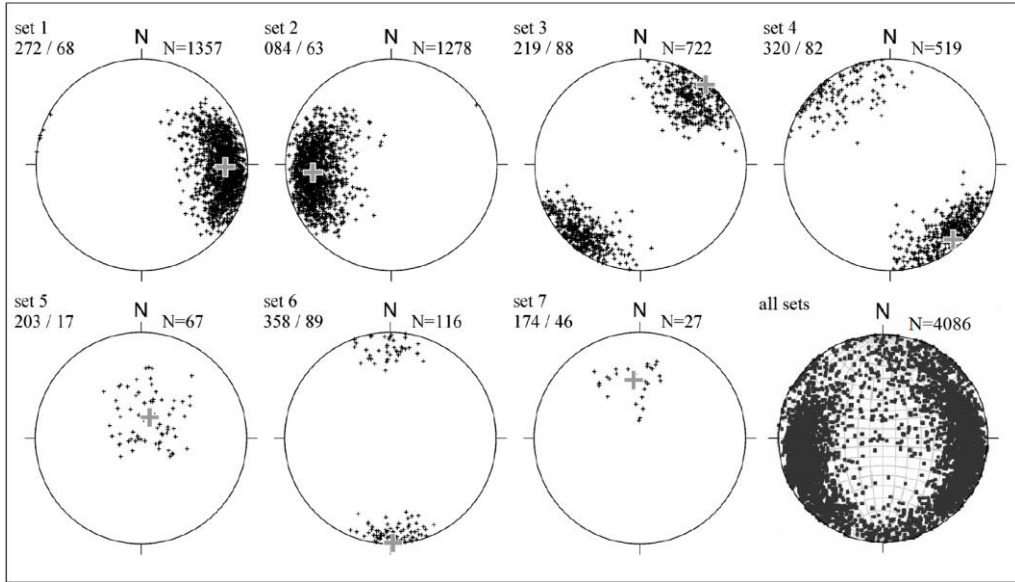
Figure 5.2. Stereographic projection of fractures clustered in 7 sets based on their orientation as well as whole fracture dataset (Valley et al., 2007)

Afshari Moein et al., 2019, computed Fisher coefficient of fracture orientation for four main sets of 1 to 4 which is summarized in table 5.4.

Table 5.4. Fisher coefficient of fracture orientation for fracture sets of 1 to 4 at each well of GPK3 and GPK4

Fracture Set	Fisher Coefficient	
	GPK3 Well	GPK4 Well
Set 1	15.2	15.5
Set 2	14.9	13.9
Set 3	10.4	12.4
Set 4	12.1	12.4

Fractal Dimension Estimation

Massart et al., 2010, determined the fractal dimension of the Soultz-sous-Forêts fractures through following two methods described in Bonnet et al., 2001:

- Distribution frequency of the fracture width

- Spacing interval method of Harris et al. (1991)

For the first approach, the data of table 5.3 were used by Massart et al., 2010. Labels 11, 12, and 14 in table 5.4 were dedicated to the main fractures and faults characterized by Sausse et al. (2010) and Dezayes et al. (2010b). The results of the first approach is illustrated in figure 5.2 in which it can be seen that the fractal

dimension of D is about 1.04. This value is approximately equal to that determined from Harris et al., 1991, method through which they proposed to plot the cumulative number of fractures, N_S, as a function of their mean spacing, S, in a bi-logarithmic diagram, where the N_S is the number of fracture spacing values higher than a specific spacing of S (figure 5.3) and is linked to that as follows

$$N_S \approx S^{-(D+1)} \quad (5.26)$$

S is the mean distance along the well path between i^{th} fracture and fractures i-1 and $i+1$. The fitted line in figure 5.2, is the best fitting line to the database excluding labels 5 and 6 which are removed from considerations due to insufficient numbers to be fitted with general trend. In figure 5.4 also the fitted line is the best fitting line to the whole fracture database spacing. The exponent of this line is -2.0471, comparison of which with equation 5.26 reveals the fractal dimension of about 1.04; just as equal as the fractal dimension determined by comparison of fitted line equation in figure 5.3 with equation 5.26 which yields 1.04 as well.

Genter et al., 1997, analyzed cumulative fracture spacing distribution derived from core of granite of well ESP1 of Soultz-sous-Forêts and found that the distribution generally follows a power-law in which the exponent for spacing less than 3 m was about 1. This is also calculated by Valley et al., 2007, where they did statistical analysis on the segment of spacing distribution of the range 1 to 5 m and found a fractal dimension close to 1.

Recently, Afshari Moein et al., 2019 and 2021, assessed the borehole image logs of GPK3 and GPK4 wells of Soultz-sous-Forêts to scale the fracture patterns. They used a two-point correlation function method of Henteschel and Procaccia, 1983, to determine the fractal dimension of the fracture network at Soultz-sous-Forêts and showed that the 1D fractal dimension in both wells are 0.88 with an error bar of 0.02 and 0.05 for GPK3 and GPK4 wells, respectively. Considering the fact that, according to Vicsek, 1992, the two-point correlation function method is more appropriate for natural data sets, then we chose a fractal dimension of about 0.9 obtained by Afshari Moein et al., 2019 and 2021, using the two-point correlation function method.

Table 5.5. Data used to plot distribution frequency of fractures in terms of their width (Massart et al., 2010)

A	Label & fracture type	Mean widths W (cm)	Number of fractures
1	Discontinuous open traces (25%)		
2	Discontinuous open traces (50%)	3.15	1476
3	Discontinuous open traces (75%)		
4	Vuggy Fractures	10.69	125
5	Continous open fractures	6.32	23
6	Wide open fractures	20.31	13
11	minor faults	150.11	18
12	medium faults	269.83	8
14	major faults	626.53	4
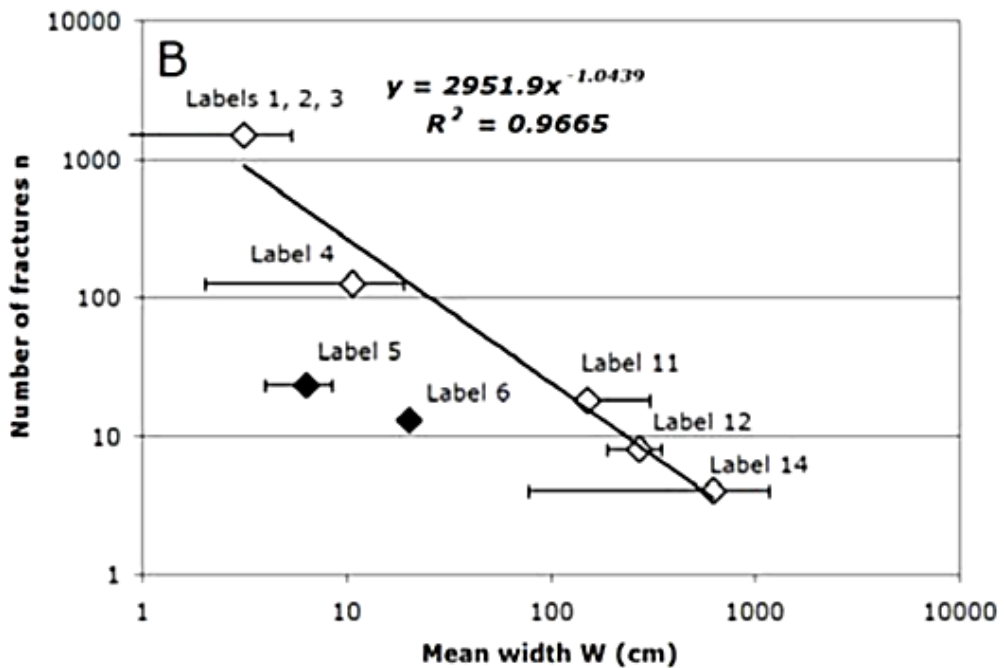
Figure 5.3. Bi-logarithmic diagram representing the number of fractures as a function of width (Massart et al., 2010)
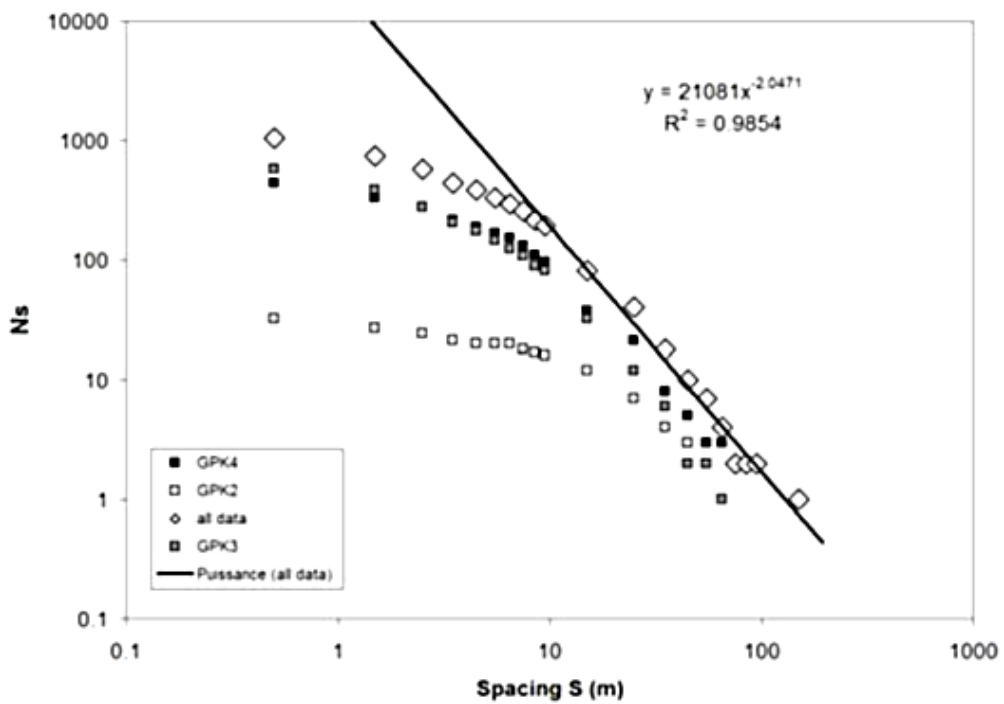
Figure 5.4. Bi-logarithmic diagram of cumulative number of fractures as a function of spacing (Massart et al., 2010)

Fracture Length Distribution Exponent

Massart et al., 2010, were linked fracture's extension/size to its width using Johnston and Mc Caffray (1996) equation as

$$L = k.W^D \quad (5.27)$$

in which L is the extension of the fracture, W is its width, k is a coefficient characteristic of the facies, and D is the fractal dimension of the fracture set. Going back to the equation 5.27, the only parameter which is required to establish the link between size and width of the fractures at Soultz-sous-Forêts is coefficient of k. According to observations carried out on veins of lava flow at reservoir scale by Gudmundsson (2000), k is equal to 400 but with a poor correlation coefficient of $R = 0.81$. Vermilye and Scholz (1995) performed the same observation as Gudmundsson (2000) on fractures of various magmatic and sedimentary facies. In the case of the granodiorite of Florence Lake, quite similar to the monzogranite of Soultz (porphyritic granite), the coefficient k is equal to 526 with a good squared correlation factor of $R^2 = 0.96$. This characteristic coefficient in Johnston and McCaffray (1996) varies from 20 to 2000 for granitic facies, with a wide range of 57 to 1231 in extensional context and mean of 402. Massart et al., 2010, assigned 400 to the characteristic coefficient of k.

Substituting above mentioned D and k in equation 5.27 yields to evaluation of mean extension of the fractures, results of which are summarized in table 5.5. Figure 5.5 demonstrates a bi-logarithmic diagram of frequency of fractures in terms of length in which the fractures carrying labels 5 and 6 are eliminated from consideration, as was the case for width distribution frequency plot of figure 5.3, showing a power-law exponent of 1.0, which is 1D exponent. According to Darcel et al., 2003b, the relation between the length distribution exponent in 2D and 3D is

$$a_{3D} = a_{1D} + 2 \quad (5.28)$$

Then, here, the power-law exponent of length distribution in 3D will be 3.

Shapiro et al., 2013, reinvestigated rupture radius of fluid-induced seismic events resulting from some hydraulic stimulation and fracturing operations and found that it follows a power-law distribution whose slope is related to the Gutenberg-Richter's b-value through following equation

$$a_r = 2b + 1 \quad (5.29)$$

A list of the b-values of microseismicity at Soultz-sous-Forêts during various hydraulic stimulation operations and their corresponding rupture area distribution based on equation 5.29 are shown in table 5.7. It can be seen that a_r is between 2.9 and 4.0.

Table 5.6. Mean fracture extensions by fracture labels (Massart et al., 2010)

	Label & Fracture Type	Mean Width (cm)	Mean Extension (m)	Number of Fractures
1	Discontinuous Open Traces (25%)			
2	Discontinuous Open Traces (50%)	3.15	11	1476
3	Discontinuous Open Traces (75%)			
4	Vuggy Fractures	10.69	39	125
5	Continuous Open Fractures	6.32	23	23

6	Wide Open Fractures	20.31	76	13
11	Minor Faults	150.11	610	18
12	Medium Faults	269.83	1123	8
14	Major Faults	626.53	2697	4
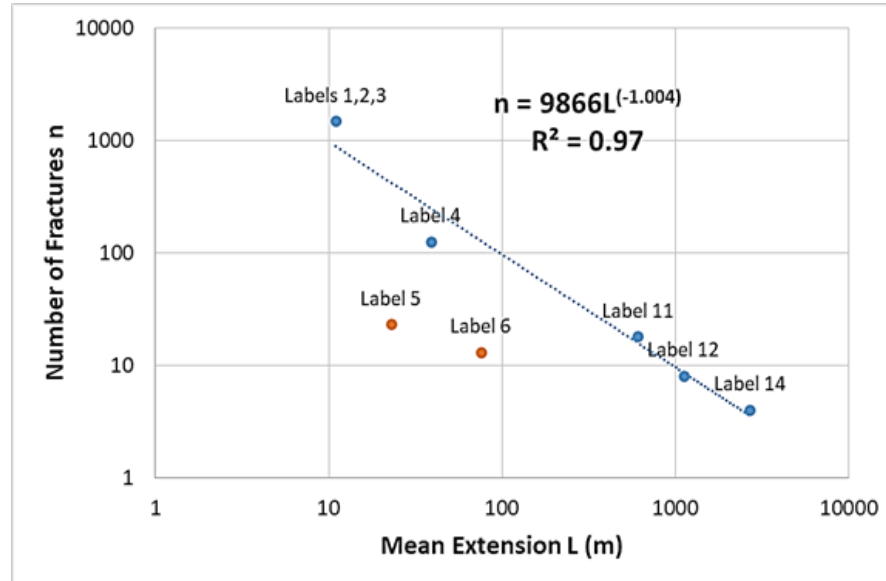
Figure 5.5. Bi-logarithmic diagram representing the number of fractures as a function of extension

Table 5.7. Gutenberg-Richter b-value of seismic events occurred at Soultz-sous-Forêts

b-value	Analyzed Seismic Events	Reference	a_r
1.06	1993 stimulation of GPK1	Shapiro et al., 2013	3.12
1.23	2000 stimulation of GPK2	Dorbath et al., 2009	3.46
0.94	2003 stimulation of GPK3	Dorbath et al., 2009	2.88
1.26	1993 stimulation of GPK1	Cornet et al., 1997	3.52
0.7-2.0	1993 stimulation of GPK1	Cauchie et al., 2020	2.4-5
1.29	2000 stimulation of GPK2	Cuenot et al., 2008	3.58

Fracture Density

As previously mentioned, Valley, 2007, analyzed acoustic televiewer images of GPK2, GPK3 and GPK4 wells of Soultz-sous-Forêts reservoir. They determined 1871 natural fractures along borehole GPK3 and 2215 natural fractures at well GPK4 leading to an average P_{10} (1D fracture density along a scanline/borehole in terms of fracture/m which is also called frequency or linear density) of 0.51 and 0.58 fractures per meter at GPK3 and GPK4, respectively, as shown in figure 2.6. Then, it might be possible to state that the average fracture density at Soultz-sous-Forêts is 0.55 fracture per meter based on the observations of Valley, 2007,

on borehole image logs. However, Genter et al., 1997, compared the number of fractures observed on cores with those on image logs and found that in granite only 17% of the fractures detected on cores were visible on image logs.
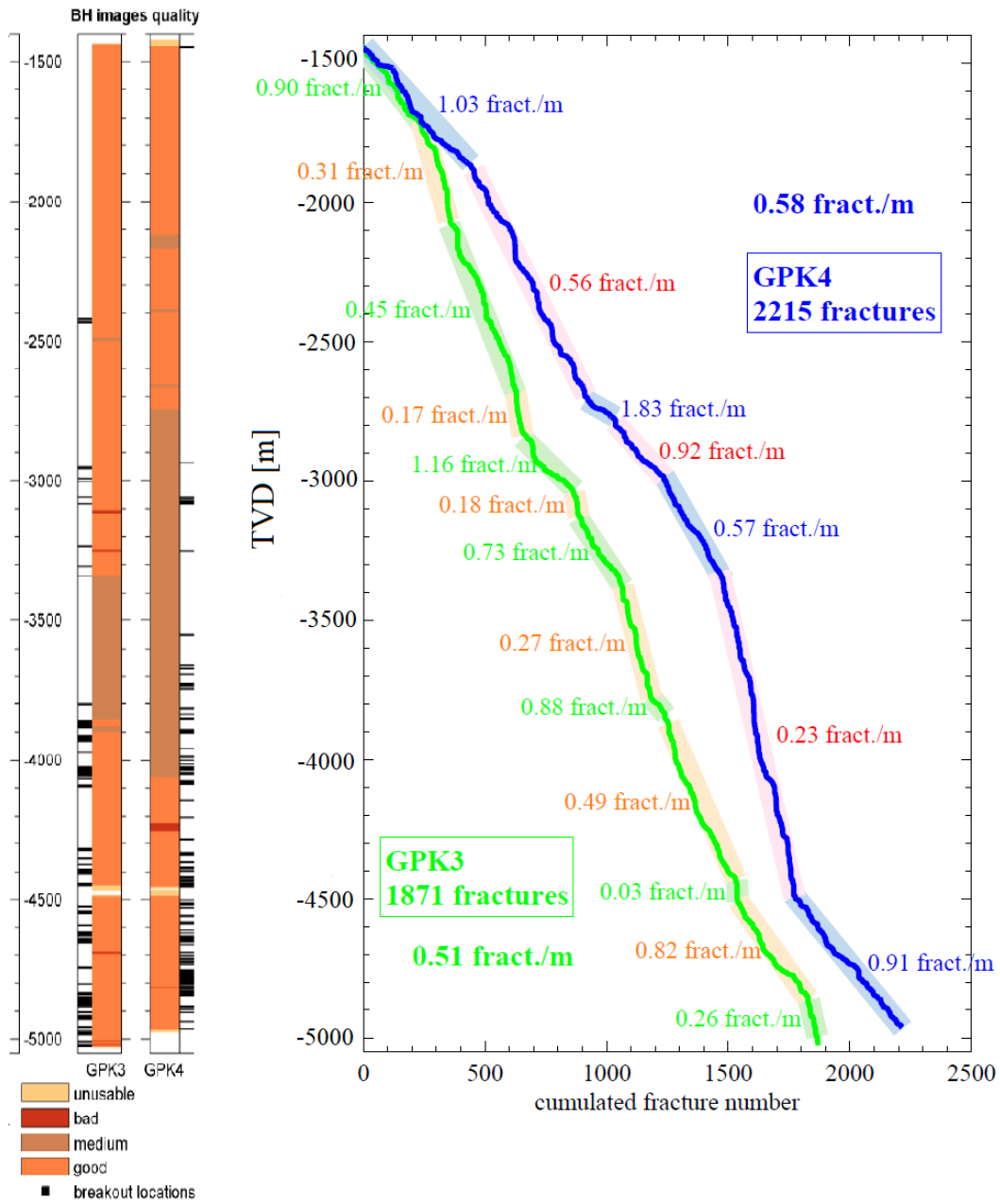
Figure 5.6. Depth-dependent fracture density along GPK3 and GPK4 wells accompanied by logged borehole length on the left-hand side (Valley, 2007)

Volumetric fracture density (P_{30}) is also determined through GPK2, GPK3, and GPK4 wells by Massart et al, 2010 along about, respectively, 500, 3600, and 3500 meters of TVDSS. The most fractured well was found to be GPK3 with 0.0056 fractures/m³, while the least one was GPK2 with 0.0015 fractures per cubic

meter. The fracture density of GPK4 was 0.0052 fractures/m^3. Figure 2.7 illustrates fracture density of all three wells along the true vertical depth of the wells. The point in this figure is that the fracture density of GPK2 well is only measured in an interval of approximately 500 meters from 3250 to 3750 meters, which shows a good agreement with fracture densities of two other wells. Therefore, it might be reasonable to assume that the fracture density of all three wells probably obey a same pattern of distribution and consequently use an interval-weighted average fracture density using the measurement intervals of each well. Doing so, an average fracture density of 0.0051 fractures/m^3 is obtained. But, comparing the total number of fractures measured from image logs of three deep wells at Soultz-sous-Forêts by Valley, 2007, Genter et al., 1997, and Massart et al., 2010, one may find that Massart and associates measured as one third of fractures as Valley, 2007, and Genter et al., 1997, did (1878 fractures on well-logs of three deep wells by Massart et al, 2010, compared to 4086 fractures for GPK3 & GPK4 reported by Valley, 2007, plus 1792 fractures for GPK2 measured by Genter et al., 1997). If this difference is taken into account, then it seems plausible to state that volumetric fracture density is on average about 0.016 fractures/m^3.
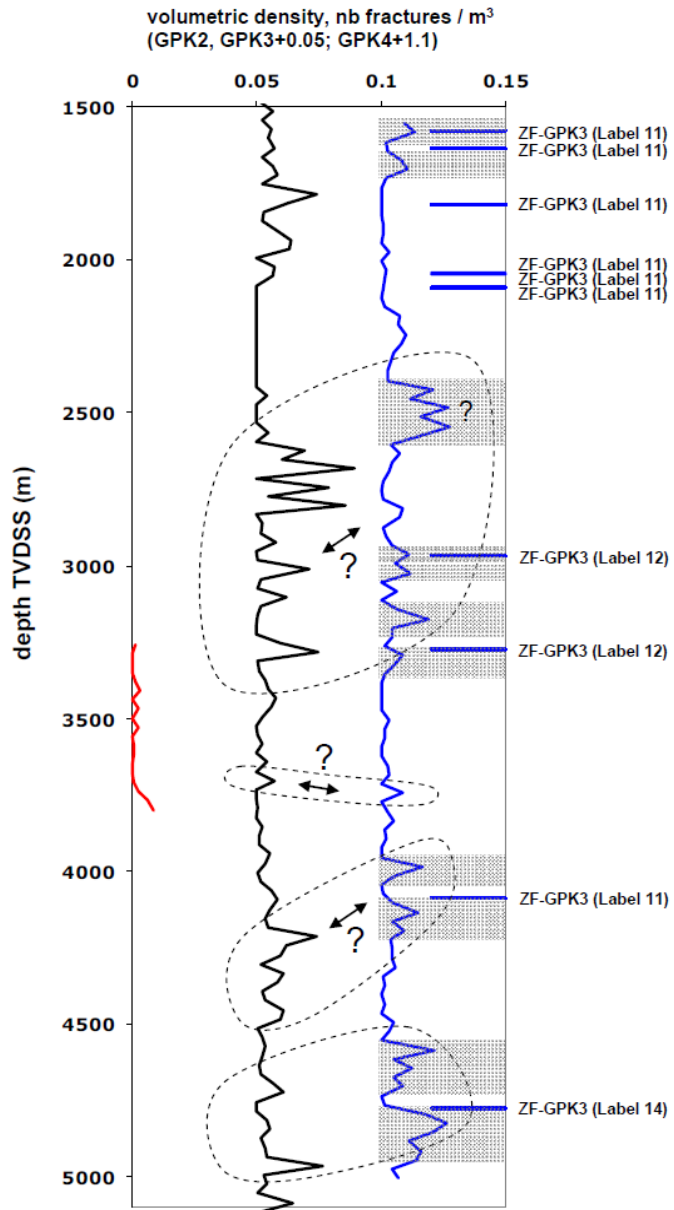
Figure 5.7. Volumetric fracture density at the wells GPK2 (red curve), GPK3 (black curve), and GPK4 (blue curve). The curves corresponding to the wells GPK3 and GPK4 are shifted by addition of 0.05 and 0.1 to the determined densities, respectively (Massart et al., 2010)

5.2.2   DFN Realization by 3DEC

3DEC can generate both stochastic and deterministic DFN. To generate stochastic DFN, a template containing size, position, and orientation distribution of fractures is defined. Size distribution in 3DEC can be uniform, Gauss, power law, bootstrapped, or user-defined distribution using the FISH programming language of 3DEC. Position distribution also can be defined as uniform, Gauss, bootstrapped, or FISH. Orientation of fractures is uniform, Gauss, Fisher, or user-defined FISH bases.

Fractures in 3DEC are generated as circular disks with a defined diameter range of $[l_{min}, l_{max}]$. The number of fractures whose size is in the range of $[l_{min}, l_{max}]$ and are located inside a volume with side size of L is given (Bour et al., 2002) by

$$n(l_{min} \leq l_{max}) = \int_{l_{min}}^{l_{max}} n(l) L^{D_M} \, dl = \alpha \frac{[l_{max}^{-a+1} - l_{min}^{-a+1}]}{-a+1} L^{D_M} \quad (5.30)$$

In equation 5.30, L is domain size, and the other parameters are as same as those in equation 5.1. Equation (5.30) implies that any DFN is, beside orientation of fractures, θ, a function of fracture density, minimum and maximum fracture length, and power-law exponent of fracture length distribution, domain size, and fractal dimension of spatial distribution of fractures and can be explained as:

$$DFN \propto f(\theta, \alpha, a, l_{min}, l_{max}, L, D_M) \quad (5.31)$$

Among those parameters listed in parentheses at the right-hand side of the equation (5.31), θ is extensively analyzed by Valley, 2007; D_M is also obtained by Afshari Moein et al., 2018 and 2021; L is domain size to be considered 100 m in the current study; l_{max} is also assumed to be 3000 m even though, and according to the negative power of that in equation (5.30), it has the least effect on the DFN generation. The remaining parameters of α, a, l_{min} are unknowns which have to be constrained by utilizing observations and measurements carried out on the field data such as P$_{10}$, fracture spacing distribution, number of intersections, and fractal dimension. Figure 5.8, an iterative forward modeling process shows at which a set of unknowns (α, a, l_{min}) are used in combination with known/assumed data $(\theta, l_{max}, L, D_M)$ to generate a synthetic DFN example. Then, a set of measurements, which are called verification data, are calculated to be compared with field observations as a validation step for the generated synthetic DFN. If Π is a parameter that shows the difference between synthetic and real DFNs, the objective is to minimize Π.
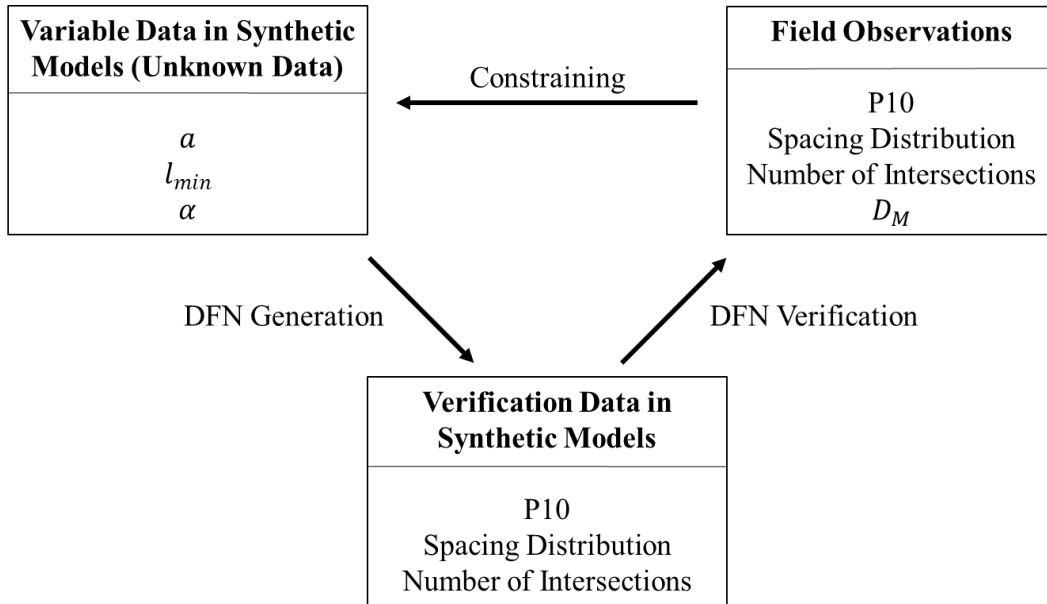
Figure 5.8. Iterative process to constrain unknown DFN parameters of α, a, l_{min}

Field observations were previously explained whereas P$_{10}$ was in the range of 0.51-0.58 fracture/m with average of 0.55 fracture/m and D_M=2.7. Spacing distribution and number of intersections of each fracture

set with each well were also evaluated by Valley, 2007, and summarized in figure 5.9 where the results correspond to approximately 3600 m of image logs at the granite section of GPK3 and GPK4 wells.
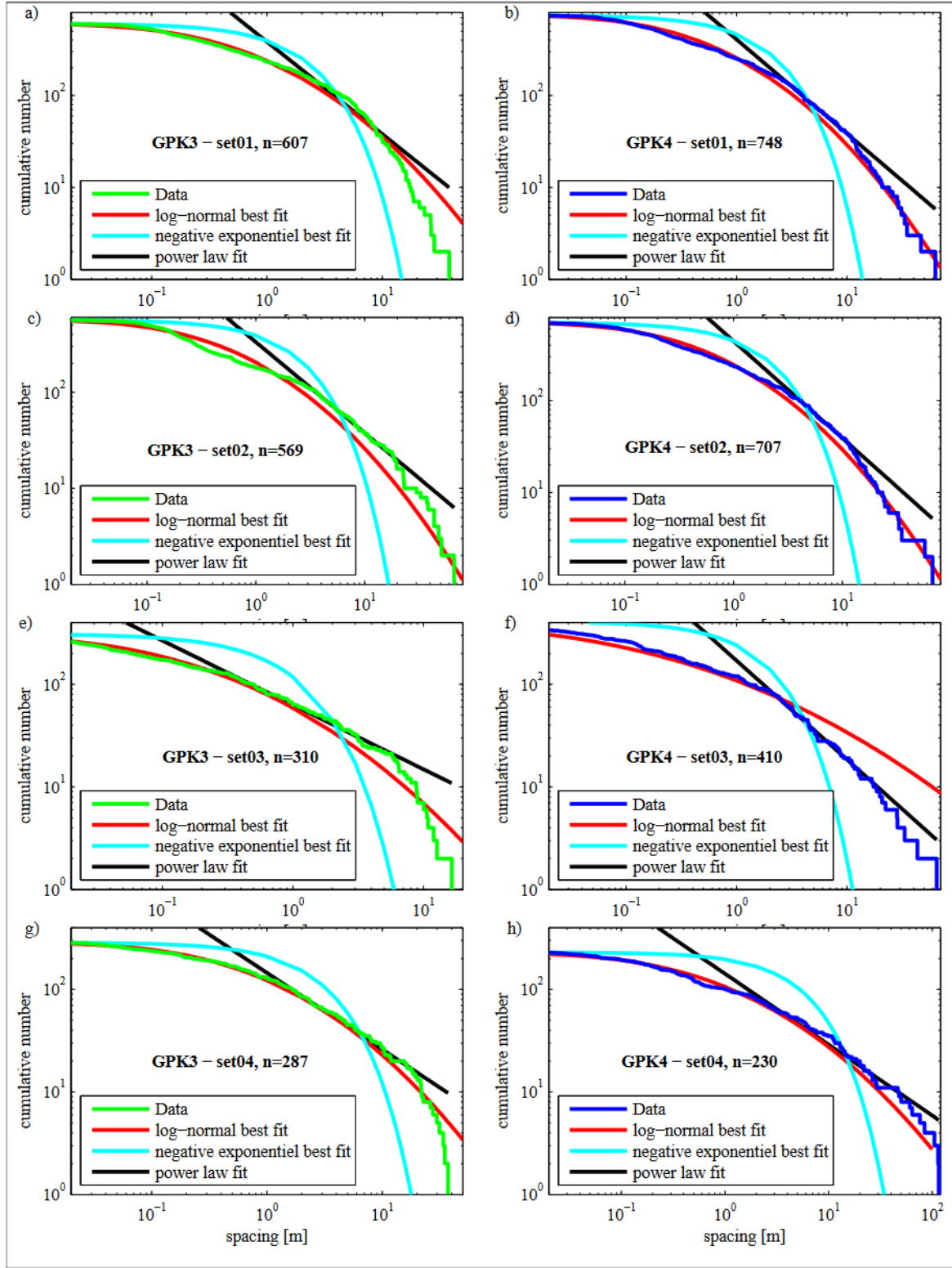
Figure 5.9. Fracture spacing distribution for the four major fracture sets at each well (Valley, 2007)

139

To numerically generate synthetic DFN by 3DEC, four major sets of fractures (sets 1 to 4), encompassing 95% of measured fractures by Valley, 2007, were aimed to be realized. For each fracture set, it was required to define not only the orientation of the fractures but also the a, l_{min}, l_{max}, D_M.

Orientation of these fracture sets, characterized by average dip and dip direction, beside the number of fractures occurring at each set are shown in figure 5.2. Afshari Moein et al., 2019, introduced Fisher coefficients of fracture orientation for each of four main fracture sets at each well of GPK3 and 4. These coefficients for each set at each well and the averages weighted by the number of fractures observed at each well are shown in table 5.8. The average values of Fisher coefficients for each fracture set were used for distribution of fracture orientation in the numerical model.

Table 5.8. Average P_{10} and average Fisher coefficient of fracture orientation distribution for each major fracture sets

Fracture Set	Number of Fractures (and P_{10})		Total Number of Fractures (and ave. P_{10})	Percent of each Set from the Total Number of Fractures (%)	Mean Fisher Coefficient		Average Fisher Coefficient (Weighted)
	GPK3	GPK4			GPK3	GPK4	
1	608 (0.17)	748 (0.21)	1357 (0.19)	35	15.2	15.5	15.4
2	570 (0.16)	708 (0.20)	1278 (0.18)	33	14.9	13.9	14.3
3	311 (0.09)	411 (0.12)	722 (0.10)	19	10.4	12.4	11.5
4	288 (0.08)	231 (0.07)	519 (0.08)	13	12.1	12.4	12.2

In table 5.5 and figure 5.5 it can be determined that the fracture length range is between 11 to 2697 meters. These lengths are not far from the minimum and the maximum fracture size of 8 m and 3000 m reported by Valley et al., 2007, and Sausse et al., 2010, respectively. However, Cauchie et al., 2020, analyzed seismic events of 1993 GPK1 hydraulic stimulation and reported a minimum source radius of about 2 meters. Here, we kept the maximum fracture length at 3000 m and used the minimum fracture length of 2 m as well as 10 m to generate synthetic DFN examples.

Distribution of the fracture position is also opted to be uniform (D_M=3.0; in equation 5.32) in the DFN generator of 3DEC, even though, according to the obtained fractal dimension of 2.7, the position distribution of fractures at Soultz-sous-Forêts are not uniform.

In 3DEC, there are many thresholds, which can be benefited from to stop DFN generation when threshold is met. P_{10} along a borehole/scanline and total number of fractures are two among existing thresholds. Based on the data obtained, we generated a few DFN examples using total number of fractures as threshold:

1) By using P_{10} as a validation parameter, different values of l_{min}, α, and a were replaced in equation 5.30 to obtain the total number of fractures in the domain of 100x100x100 m^3. Assuming that the contribution of each fracture set (set 1 to set 4) to this total fracture number is analogous to the contribution of them to the number of fractures observed on the borehole image logs (summarized in table 5.8), number of fractures belonging to each fracture set and occurring in the defined domain was obtained and set as threshold for DFN generator.

2) By using the resulting P$_{10}$ values of first set of generated DFN examples, values of l_{min}, α, and a in the second set of DFN's were constrained so as to have P$_{10}$ closer to the observations (on average of 0.55 fractures/m).

For the first category, 16 DFN were generated by assigning various values to the l_{min}, α, and a as below:

a) The a exponent was set to 2.5, 3.0, 3.5, and 4.0.

b) The assigned values for l_{min} were 2 and 10 meters.

c) The α density term was initially set to 0.1 and then, according to the resulting P$_{10}$, the second value was also defined to have another DFN example for which the P$_{10}$ approaches the validation value of 0.55 fracture/m.

The resulting DFN are illustrated in figures 5.10 to 5.13 looking at which reveals that:

Based on P$_{10}$ value of 0.55 fracture/m obtained by Valley et al., 2007, for power-law length exponent of 2.5 (figure 5.7), if l_{min} is assumed to be 2 m then the α tend to be between 0.08 and 0.1, whereas for l_{min} equal to 10 m, α can be 0.1 and 0.12. By increase of a from 2.5 to 3.0 (figure 5.8), and for the l_{min} values of 2 and 10 m, the α will be, respectively, about 0.5 and more than 0.5. One may also observe that for a=3.5 (figure 5.9), α can be less than 2 and more than 2 for l_{min} of 2 and 10 m, respectively, whereas it yields over 2 and 5 for a=4.0 (figure 5.13).

On the other hand, and according to some preliminary evaluations based on Massart et al., 2010, and Valley et al., 2007 explained at previous subsection, the total number of fractures occurred in a domain of 100^3 m^3 is about 16000. Looking at the total fracture number of each DFN example in figures 5.10-5.13, it can be seen that when a exponent is larger than 3 and l_{min} is 2 m, the total number of fractures, in the cases with P$_{10}$ close to 0.55, is by far more than 16000 (e.g. second example in both figure 5.14).

Therefore and based on above mentioned observations, the second set of DFN's were created by refining geometrical parameters of some examples from the first synthetic DFN set (illustrated in figures 5.10 to 5.13) at which the P$_{10}$ is close to 0.55 fracture/m. So that, in detail,

a) for a=2.5 and l_{min}=2 m, then $0.08 \leq \alpha \leq 0.1$.

b) for a=2.5 and l_{min}=10 m, then $0.1 \leq \alpha \leq 0.12$.

c) for a=3.0 and l_{min}=2 m, then $\alpha \simeq 0.5$.

d) for a=3.0 and $l_{min} = 10$ m, then $\alpha > 0.5$.

e) for a=3.5 and l_{min}=10 m, then $\alpha > 2.0$.

f) for a=4.0 and l_{min}=10 m, then $\alpha > 5.0$.

Using above details, six more DFN examples were generated which are illustrated in figure 5.14. It is aimed in these six DFN's, to have a P$_{10}$ of approximately 0.55. These six DFN examples were then investigated

to assess the spacing distribution as well as number of intersections along 17 fictitious scanlines/boreholes (figure 5.15) generated vertically in the numerical block of $100^3\ m^3$. The reason behind the number of fictitious wellbores was just to distribute wellbores throughout the block to have uniform sampling and therefore having sufficient data to do a reliable statistical analysis. But, again for the sake of reliability of the analysis, we just then normalized analyses carried out on the spacing distribution and the number of intersections so as to have a comparable result in a length of 100 m. The second set of DFN examples are illustrated in figure 5.14.
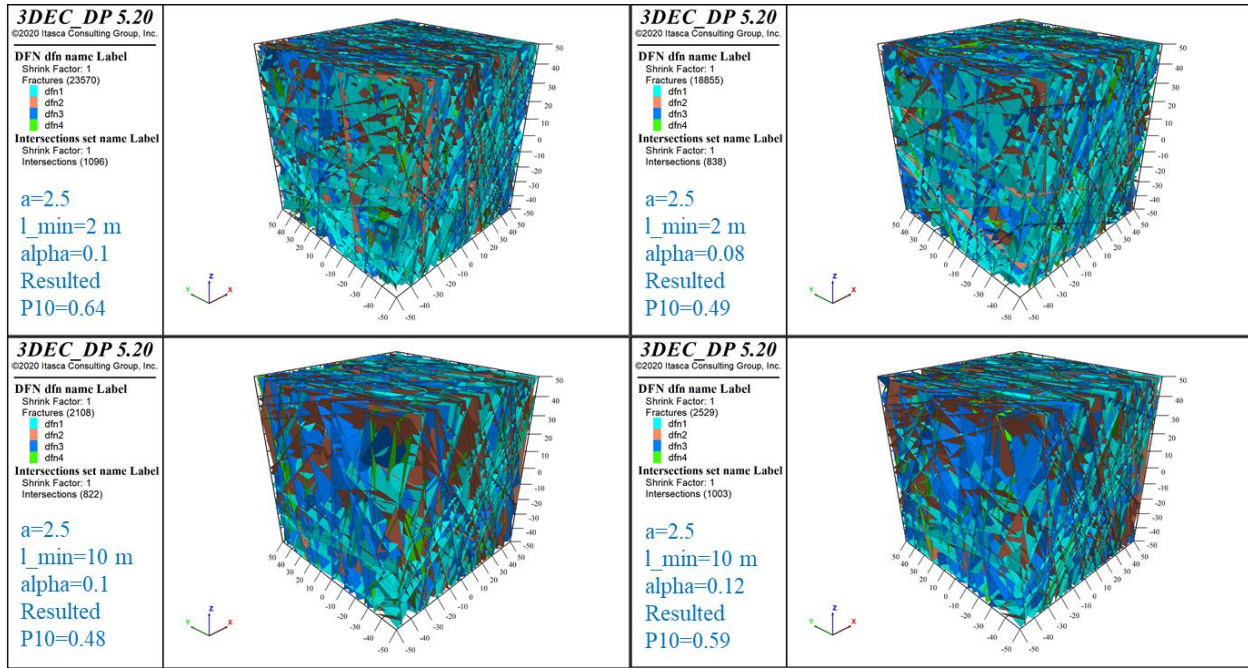
Figure 5.10. DFN examples generated for different values of l_{min} and α where a is kept constant on 2.5; the resulted P$_{10}$ values are also shown in the figures
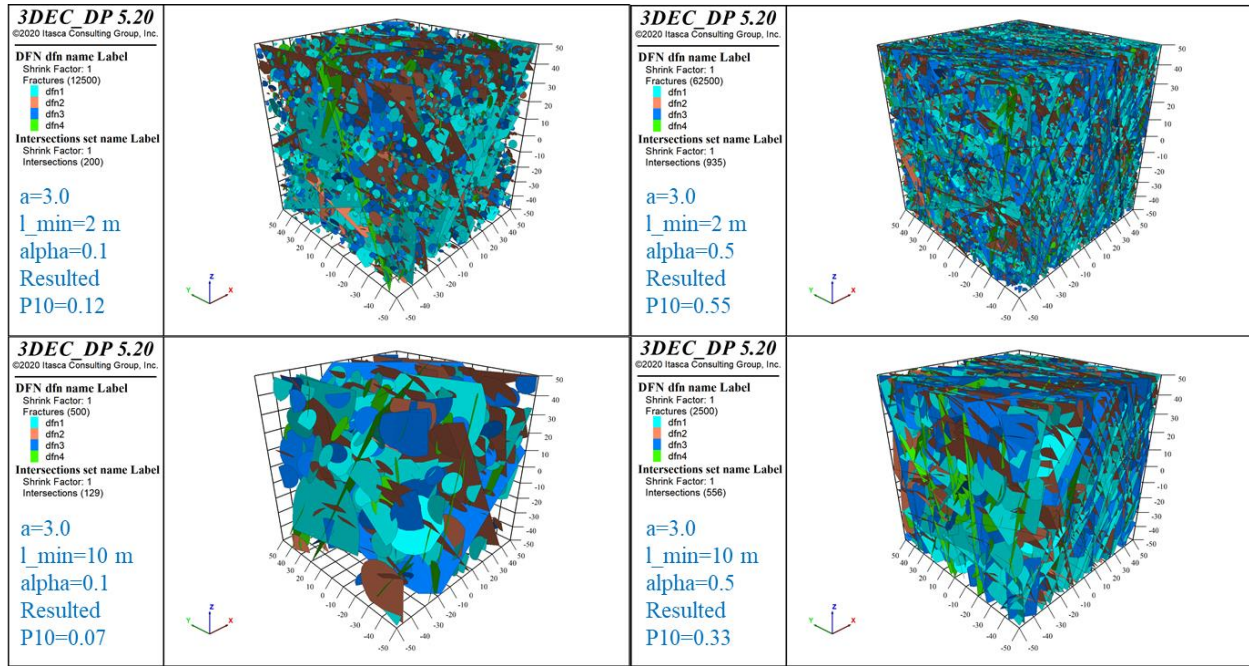
Figure 5.11. DFN examples generated for different values of l_{min} and α where a is kept constant on 3.0; the resulted P_{10} are also shown in the figures
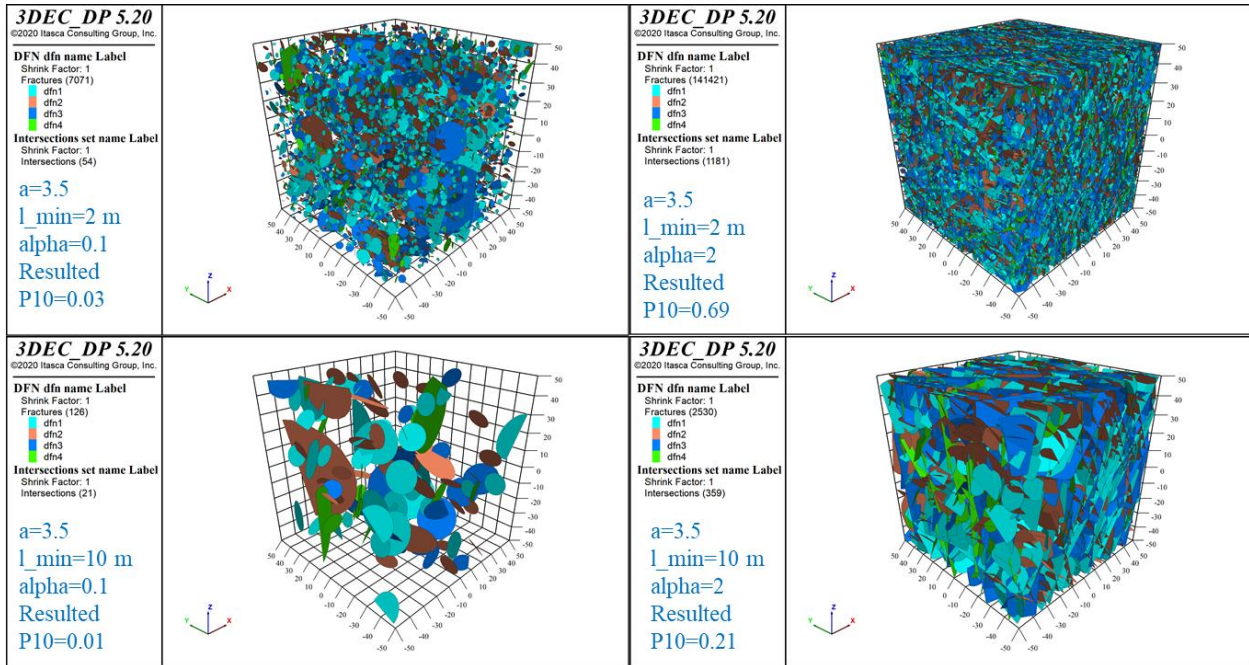
Figure 5.12. DFN examples generated for different values of l_{min} and α where a is kept constant on 3.5; the resulted P_{10} are also shown in the figures
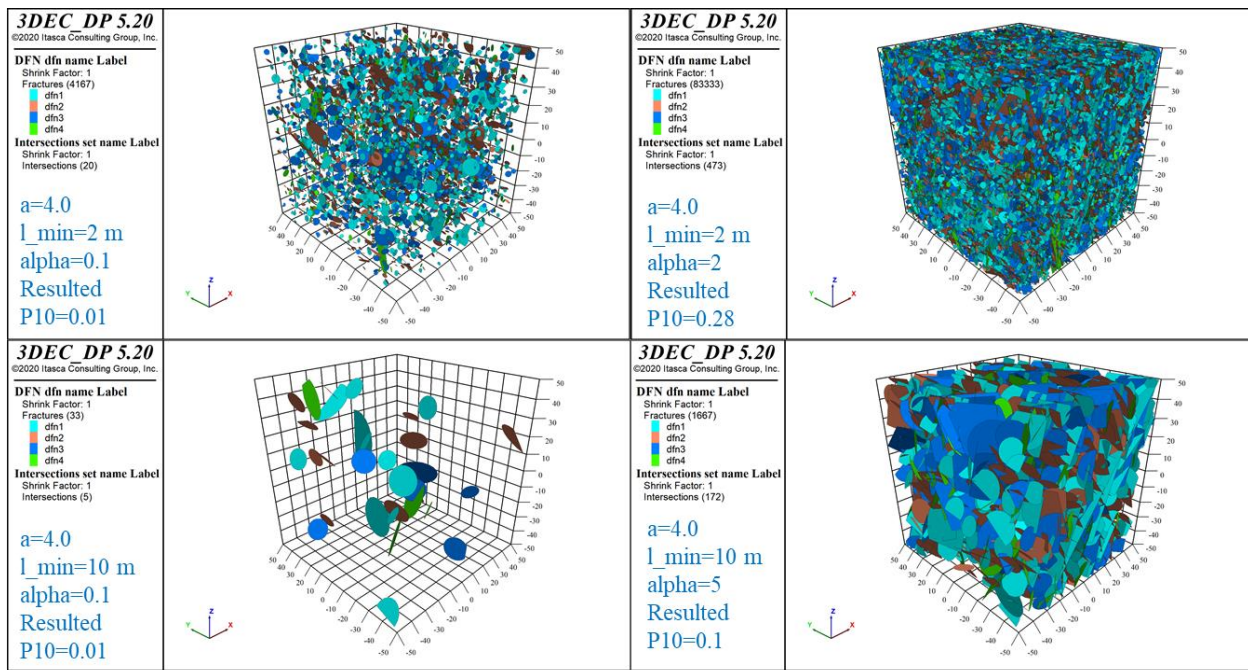
Figure 5.13. DFN examples generated for different values of l_{min} and α where a is kept constant on 4.0; the resulted P₁₀ are also shown in the figures

144
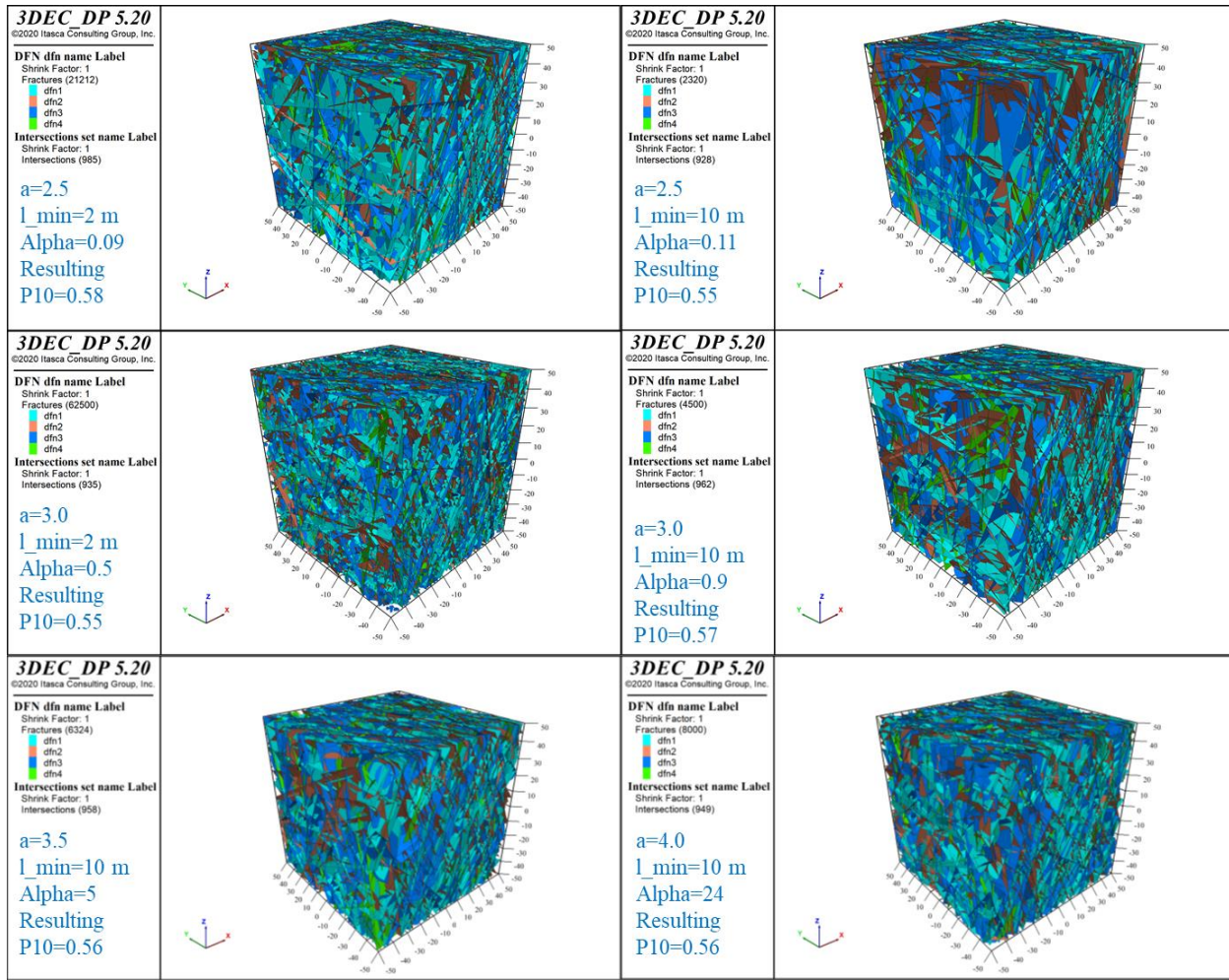
Figure 5.14. DFN examples generated for different values of l_{min} whereas a is 2.5 to 4.0; the resulted alpha is also shown in the figures being around 0.55
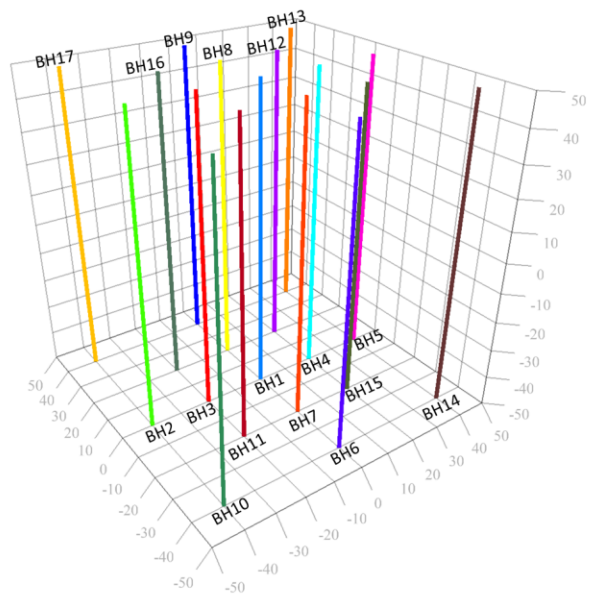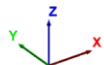
Figure 5.15. Schematic 3-D view of 17 fictitious boreholes distributed in the cubic block of 100x100x100 m^3

Spacing distributions of synthetic DFN examples of the second set (figure 5.14) superimposed on those extracted by Valley, 2007, are shown in figures 5.16 to 5.21 where the Y-axis of the plots are normalized cumulative number of spacing frequency so as to have them in a length of 100 m. For that and assuming a uniform distribution of spacing along the GPK3 and 4 Wells as well as 17 fictitious numerical wells, synthetic cumulative numbers are divided by 17 and the field observations (figure 5.9) are divided by 36, since the study of Valley, 2007, was carried out on about 3600 meters of GPK3 and 4 wells (from 1420 m to 5000 m).
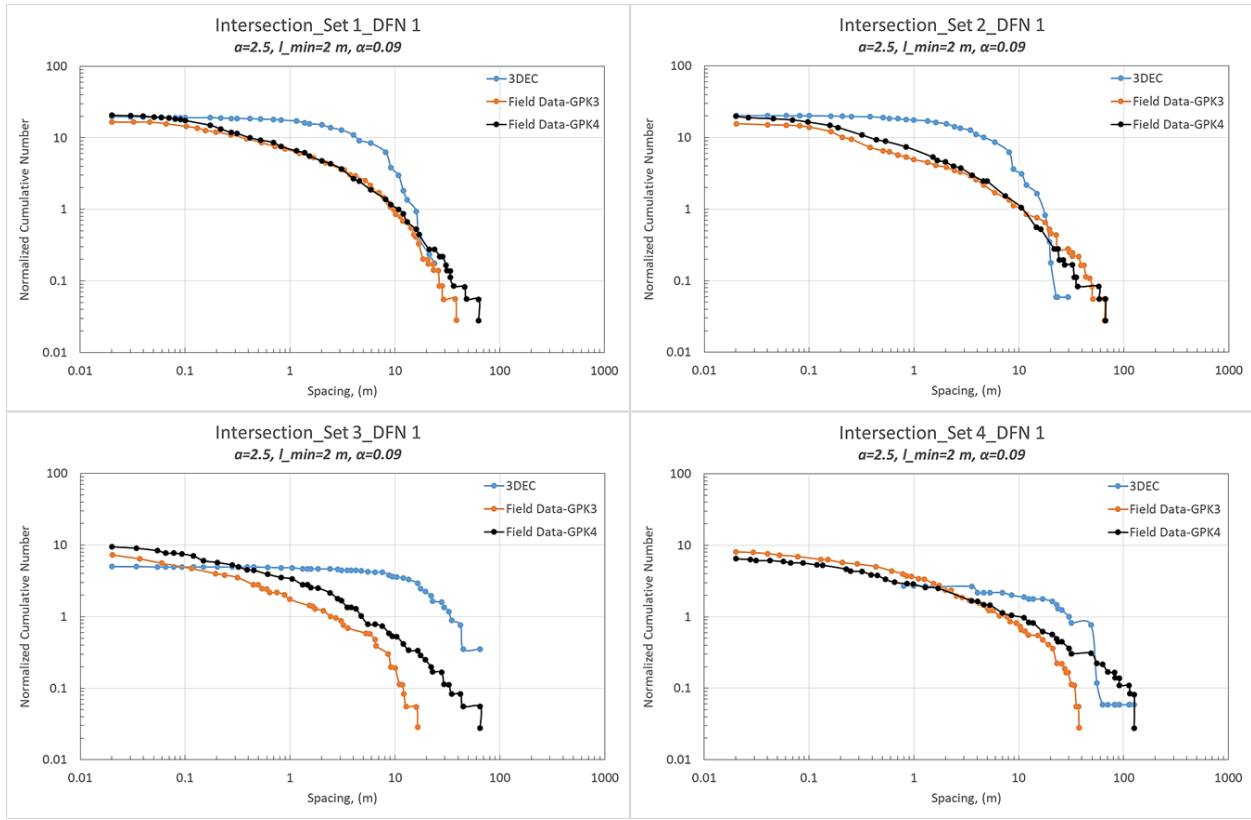
Figure 5.16. Spacing distribution of the first synthetic DFN example (blue curves) superimposed on the observations of Valley, 2007, on image logs of GPK3 and 4 wells (red and black curves, respectively)
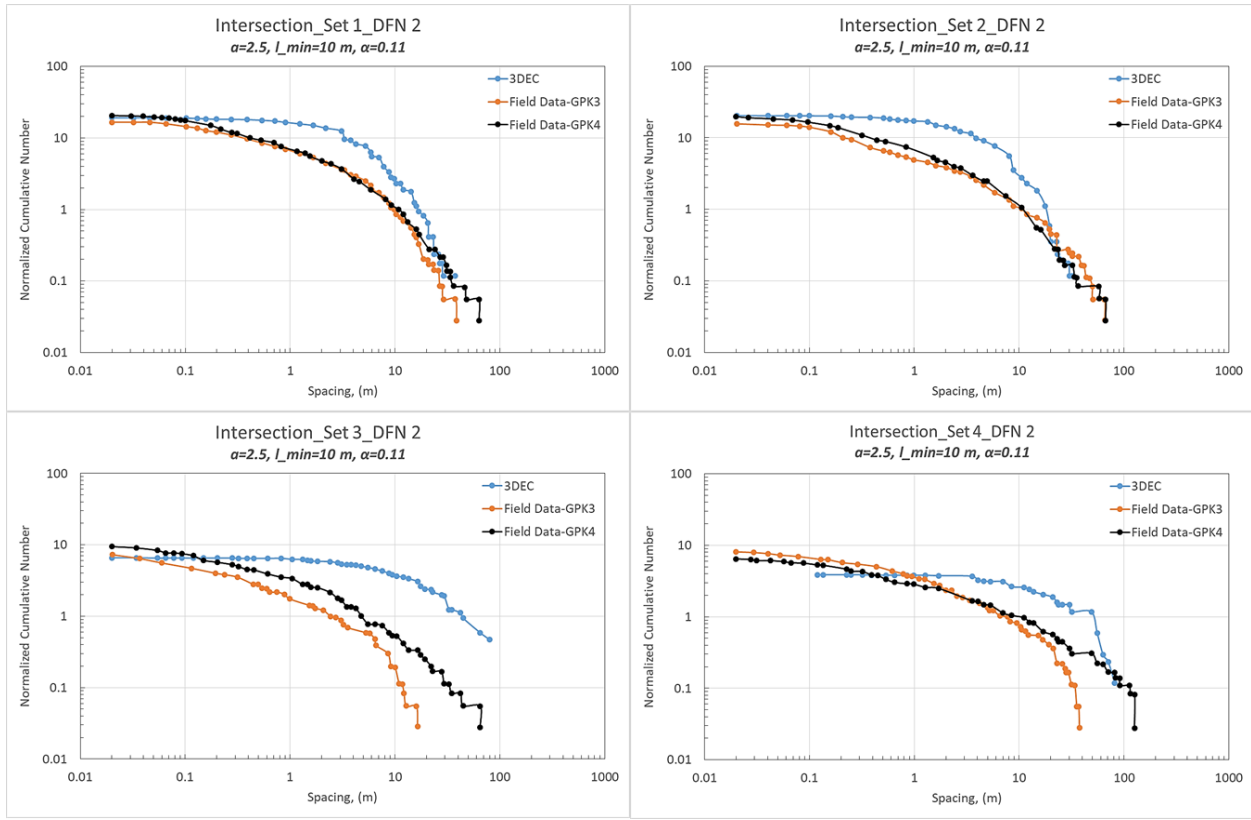
Figure 5.17. Spacing distribution of the second synthetic DFN example (blue curves) superimposed on the observations of Valley, 2007, on image logs of GPK3 and 4 wells (red and black curves, respectively)
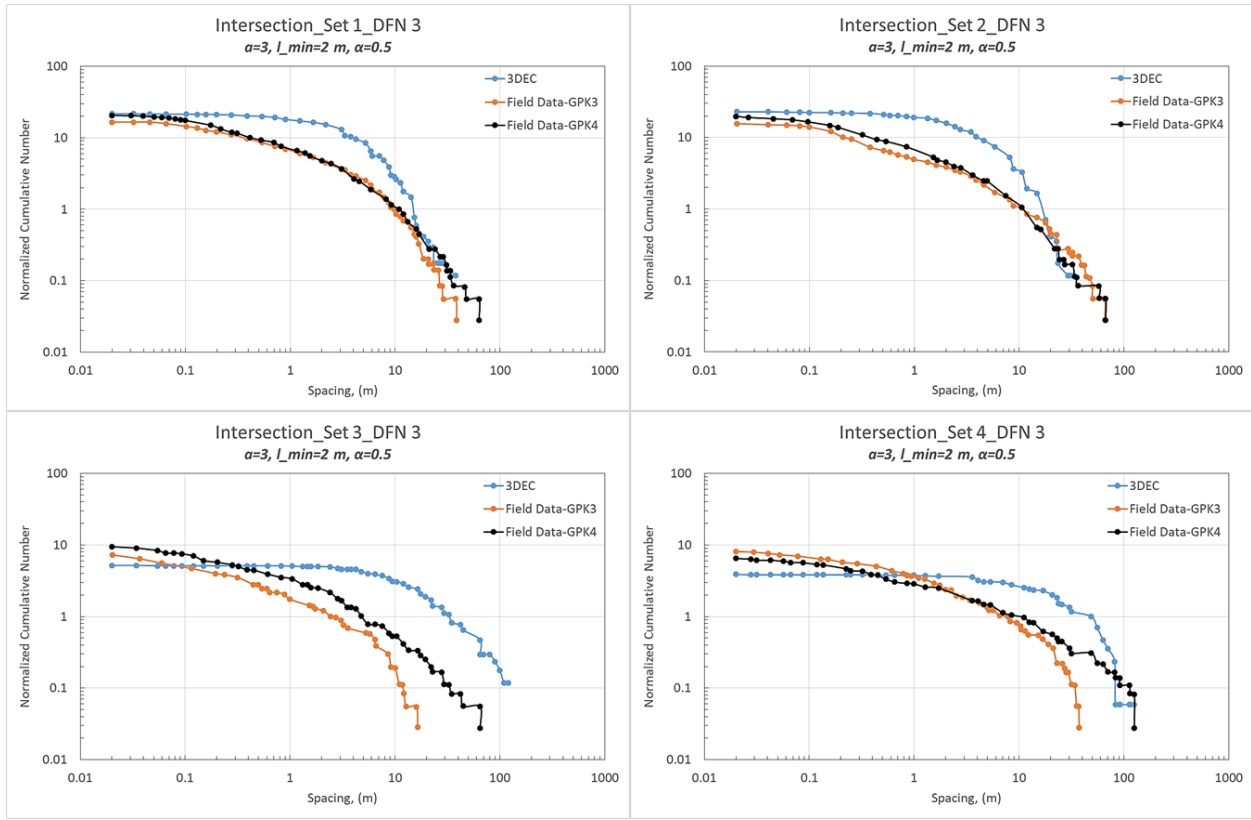
Figure 5.18. Spacing distribution of the third synthetic DFN example (blue curves) superimposed on the observations of Valley, 2007, on image logs of GPK3 and 4 wells (red and black curves, respectively)
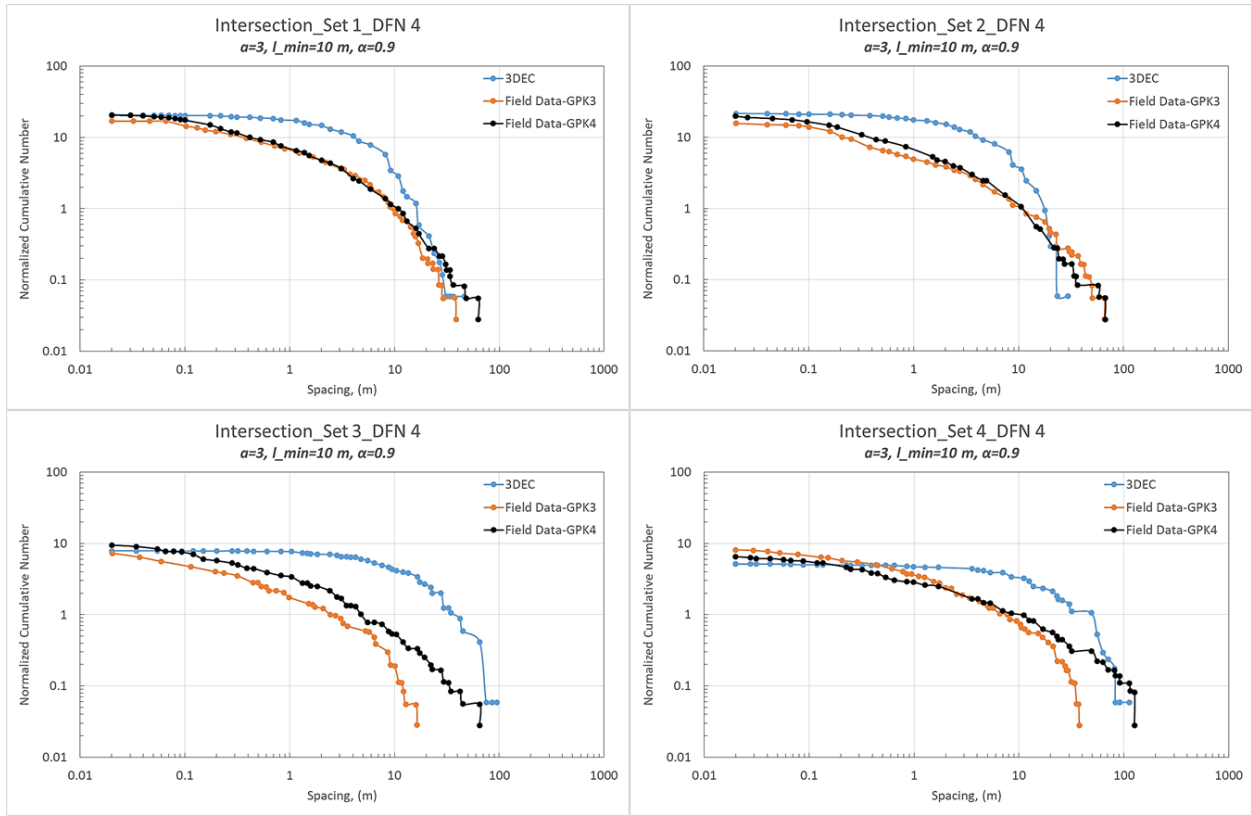
Figure 5.19. Spacing distribution of the fourth synthetic DFN example (blue curves) superimposed on the observations of Valley, 2007, on image logs of GPK3 and 4 wells (red and black curves, respectively)
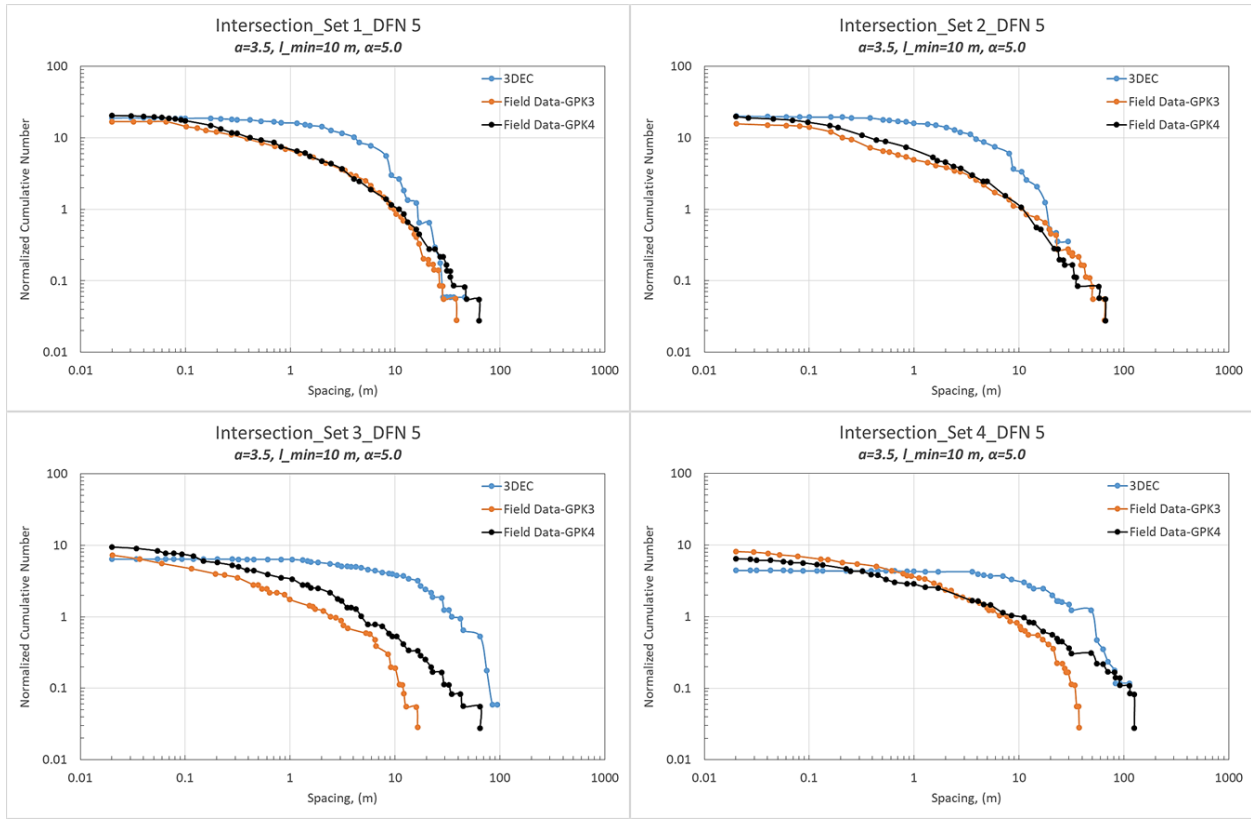
Figure 5.20. Spacing distribution of the fifth synthetic DFN example (blue curves) superimposed on the observations of Valley, 2007, on image logs of GPK3 and 4 wells (red and black curves, respectively)
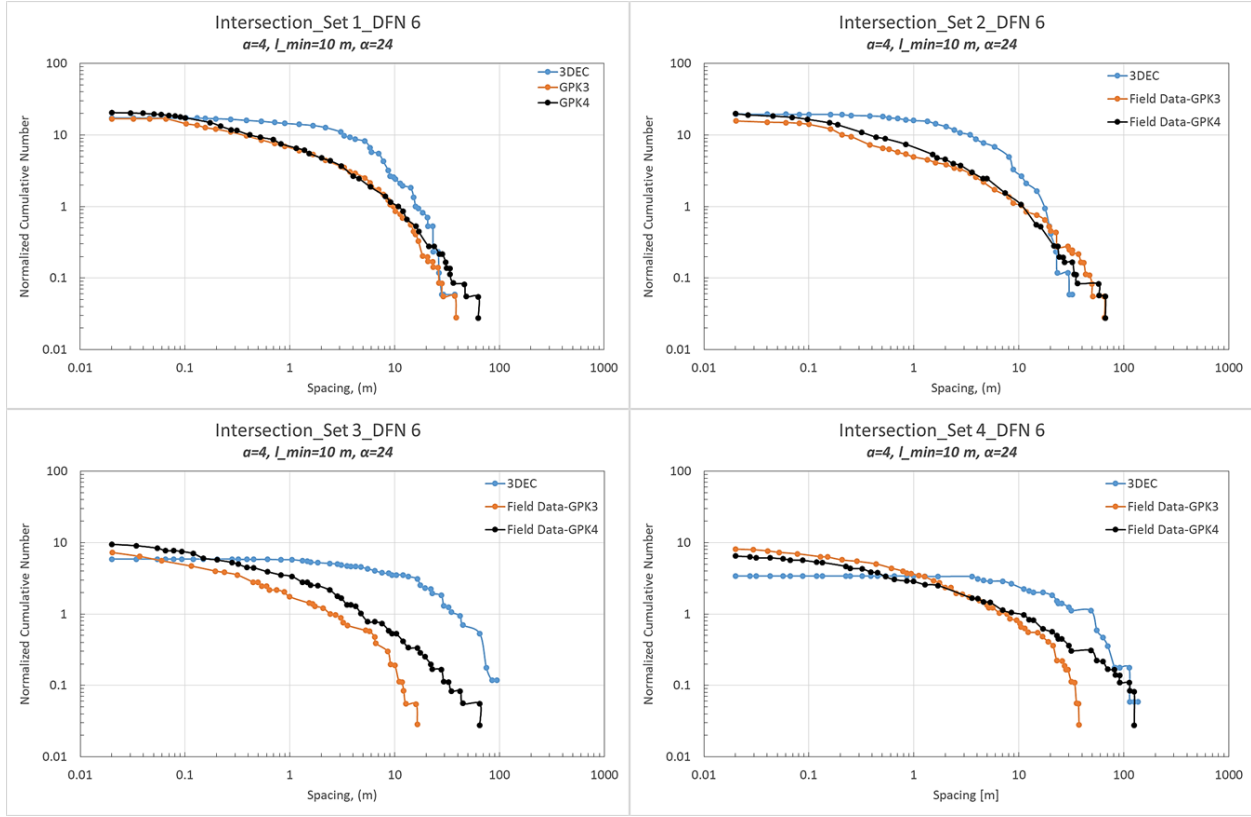
Figure 5.21. Spacing distribution of the sixth synthetic DFN example (blue curves) superimposed on the observations of Valley, 2007, on image logs of GPK3 and 4 wells (red and black curves, respectively)

Looking at figures 5.16 to 5.21 shows that, in most of the cases, at small scale the number of occurrences is reproduced or at least show the same order of magnitude, but at the large scales a poor match between 3DEC results and field data is shown. As previously mentioned, Afshari Moein et al., 2019 and 2021, obtained 1D fractal dimension of 0.9, which indicates that at Soultz-sous-Forêts position distribution of fractures are not uniform at which 1D fractal dimension is 1.0. On the other hand in 3DEC, spatial distribution of fractures can be uniform, Gaussian, bootstrapped, or FISH. Since here we used uniform spatial distribution of fractures, then it imposed some differences to the numerically generated DFN examples compared to the field observations by Valley, 2007, as shown in the figures 5.16 to 5.21. Mean Squared Error (MSE) of the differences between numerical and in-situ spacing distribution frequency at each fracture set, shown as "Normalized Cumulative Number" on the y-axis of figures 5.16-5.21, were computed for all spacing values shown on the x-axis of aforementioned figures. The resulting MSE values for each fracture set then were summed to indicate the total MSE of the numerical DFN example compared to the in-situ observed DFN by Valley, 2007. In table 5.9, set-based MSE and total MSE values for numerical DFN examples are summarized.

Table 5.9 reveals that the numerical example of DFN 3 (a=3.0, l_{min}=2 m) has the most difference with in-situ DFN while the example DFN 6 (a=4.0, l_{min} =10 m) shows the least difference. These significant disagreements between numerically realized DFN examples illustrated in figure 5.14 and in-situ fracture network scaled by Valley, 2007, probably stem from the fact that the position distribution of the fractures at Soultz-sous-Forêts is not uniform.

In current work and in spite of above mentioned disagreement, the fourth example of DFN in figure 5.14 (a=3.0, l_{min} =10.0 m) is opted afterwards to be embedded in the intact rock block for estimation of effective elastic moduli of the fractured rock mass. This example benefited from the DFN characteristics mentioned in the literature.

Table 5.9. MSE values of the difference between numerical and in-situ spacing distribution

DFN Example	Fracture Set	MSE	∑MSE
DFN 1	Set 1	44.5	115.7
	Set 2	61.7	
	Set 3	5.7	
	Set 4	3.8	
DFN 2	Set 1	34.0	99.0
	Set 2	54.9	
	Set 3	7.25	
	Set 4	2.8	
DFN 3	Set 1	53.7	141.4
	Set 2	79.7	
	Set 3	5.3	
	Set 4	2.7	
DFN 4	Set 1	43	128.6
	Set 2	70.5	
	Set 3	12.3	
	Set 4	2.8	
DFN 5	Set 1	32.5	99.5
	Set 2	56.6	
	Set 3	7.6	
	Set 4	2.8	
DFN 6	Set 1	22.9	84
	Set 2	51.9	

	Set 3	6.2	
	Set 4	3.0	

5.3   Estimation of Effective Elastic Moduli

As previously stated, to effectively model the response of geo-material around the injection point as well as the far field during stimulation, it is necessary to take into account the role of discontinuities on mechanical behavior of intact rock. Before that, it is recommended to investigate intact rock's mechanical properties through a set of numerical benchmarking modeling. In subsection 5.3.1, a brief explanation of laboratory tests on the rock specimens are presented. Mechanical behavior of discontinuities are described in subsection 5.3.2. A description regarding the mechanical calculation scheme used in 3DEC is presented in subsection 5.3.3. In subsections 5.3.4 and 5.3.5 a set of benchmarking modeling on both intact rock and a rock mass containing an infinite fracture are designed and carried out using 3DEC. Subsection 5.3.6 is dedicated to describe development of a numerical code that is capable of taking the stress-dependent fracture stiffness into accounts. In subsection 5.3.7, effective elastic moduli of a fractured rock mass, which is a 100x100x100 m^3 granite specimen of Soultz-sous-Forêts being fractured by a fictitious DFN, is evaluated by 3DEC and the results are compared to those obtained using no-interaction, self-consistent, differential schemes as well as the analytical formulation introduced by Davy et al., 2018. Finally and in subsection 5.3.8, P-wave velocity variation through the numerically generated fractured rock mass models are assessed.

5.3.1   Mechanical Behavior of intact rock

Here, it is aimed to explain the methodology of evaluation of elastic moduli of a homogeneous, isotropic, and elastic intact rock block in the laboratory through uniaxial compressive stress, confined uniaxial compressive stress, and true triaxial compressive stresses tests. Noteworthy that the gravitational effect of the rock is not taken into account and that only the elastic domain of the mechanical behavior of the rock block is taken into account.

Uniaxial Compressive Test

This test is usually used to characterize elastic moduli of the rock, its unconfined compressive strength, and its post-elastic behavior (Cornet, 2015). In this test, a right circular cylinder or prism of rock, with height of H and diameter or side length of L, is compressed between two parallel rigid plates (Jaeger et al, 2007). Hence, the stress tensor in such test configuration will be as (Cornet, 2015)

$$\tilde{\sigma} = \begin{bmatrix} \sigma_1 & 0 & 0 \\ 0 & 0 & 0 \\ 0 & 0 & 0 \end{bmatrix} \quad (5.32)$$

In which it is assumed that the X-, Y-, and Z-direction are respectively I_1, I_2, and I_3 principal directions.

Analytically, assuming an ideal test condition in which counteraction between test machine and specimen has negligible effect (an explanation about the effects of loading machine on test results can be found in

Jaeger et al., 2007) on the measurements, the elastic moduli can be determined by doing some measurements of vertical and lateral displacements, respectively dH and dL, as (Jaeger et al., 2007)

$$\varepsilon_1 = -\frac{dH}{H} \quad (5.33)$$

$$E = \frac{\sigma_1}{\varepsilon_1} \quad (5.34)$$

$$\varepsilon_2 = \varepsilon_3 = -\frac{dL}{L} \quad (5.35)$$

$$\vartheta = -\frac{\varepsilon_2}{\varepsilon_1} \quad (5.36)$$

$$\varepsilon_{12} = \varepsilon_{23} = \varepsilon_{13} = 0 \quad (5.37)$$

Confined Uniaxial Compressive Test

This test, according to the author's knowledge, is not a common experiment in the laboratory, but it is numerically performed for benchmarking needs. In this test, all sides of the specimen are prevented from movement in the direction of face-normal except the top side. Hence, the stress tensor in such test configuration will be as

$$\tilde{\sigma} = \begin{bmatrix} \sigma_1 & 0 & 0 \\ 0 & \sigma_2 & 0 \\ 0 & 0 & \sigma_3 \end{bmatrix} \quad (5.38)$$

Analytically, by taking into account the assumptions of uniaxial compressive stress test about interaction between the loading machine and the specimen, since the lateral displacement of the specimen is zero, the strain values in I_2 and I_3 directions will be zero.

$$\varepsilon_2 = \varepsilon_3 = \varepsilon_{23} = \varepsilon_{13} = \varepsilon_{12} = 0 \quad (5.39)$$

In this case, since the lateral sides are prevented from movement, the vertical stress generates some lateral stresses through the block according to Newton's third law. This lateral stress can be analytically expressed as:

$$\sigma_2 = \sigma_3 = \frac{\vartheta}{1-\vartheta}\sigma_1 \quad (5.40)$$

The vertical strain, however, will be affected by the lateral stresses and can be calculated as below (Jaeger et al., 2007)

$$\varepsilon_1 = \frac{1}{E}[\sigma_1 - \vartheta(\sigma_2 + \sigma_3)] \quad (5.41)$$

Triaxial Compressive Test

This test is one of the most widely used rock mechanics tests which offers useful data of mechanical behaviors of rocks. Through this test, the sample, which is in a pressure vessel, undergoes a laterally homogeneous stress, P_c, perpendicular to the axial stress of σ_1. Then the stress tensor for such test will be (Cornet, 2015) as

$$\tilde{\sigma} = \begin{bmatrix} \sigma_1 & 0 & 0 \\ 0 & P_c & 0 \\ 0 & 0 & P_c \end{bmatrix} \quad (5.42)$$

Analytically, the strain values for above-mentioned test can be calculated as below (Jaeger et al., 2007)

$$\varepsilon_1 = \frac{1}{E}[\sigma_1 - \vartheta(\sigma_2 + \sigma_3)] \quad (5.43)$$

$$\varepsilon_2 = \frac{1}{E}[\sigma_2 - \vartheta(\sigma_1 + \sigma_3)] \quad (5.44)$$

$$\varepsilon_3 = \frac{1}{E}[\sigma_3 - \vartheta(\sigma_2 + \sigma_1)] \quad (5.45)$$

$$\varepsilon_{23} = \varepsilon_{13} = \varepsilon_{12} = 0 \quad (5.46)$$

where the lateral confining pressure, P_c, is replaced by σ_2 and σ_3.

5.3.2 Mechanical Behavior of Discontinuities

Mechanical response of discontinuities can be controlled, among other parameters, by their orientation (dip and dip direction), stiffness matrix, and hydraulic conductivity. Orientation of discontinuities can be determined from DFN and may have a significant effect on magnitudes of effective normal stress and shear stress acting on the fracture plane. Stiffness matrix influences fracture's normal and shear displacement in a known regime of stresses (according to equation 5.15). This matrix has two diagonals and two non-diagonals; where the latter components are often assumed to be zero (Cornet, 2015).

$$\begin{pmatrix} \sigma_n \\ \tau \end{pmatrix} = \begin{pmatrix} k_{nn} & k_{ns} \\ k_{sn} & k_{ss} \end{pmatrix} \begin{pmatrix} d_n \\ d_s \end{pmatrix}$$

Bandis et al. (1983) performed a series of experiments on fresh and weathered joints of some samples of five rock types under normal and shear loading conditions. Normal deformability was studied by conducting loading/unloading and repeated load cycling tests and shear deformability was studied by performing direct shear tests under a range of normal stresses. In both normal and shear loading scenarios, as shown in figure 5.22, deformability of samples versus applied stresses showed non-linear behavior irrespective of joint type, indicating non-linearity of normal and shear stiffness of fractures which are, respectively, slope of normal stress versus normal displacement and shear stress versus shear displacement. According to Bandis et al., 1983, normal stiffness curve of the tested interlocked fractures can be described as

$$k_n = k_{ni}\left[1 - \frac{\sigma_n}{V_m k_{ni} + \sigma_n}\right]^{-2} \quad (5.47)$$

where k_{ni} is normal stiffness of the fracture at initial state or under in-situ stress state, and V_m is maximum closure of the joint. For mismatched joints, at which the two faces of the joints were dislocated for 0.5 to 1 mm relative to each other, the normal stiffness can be described as

$$k_n = \frac{q.\sigma_n}{0.4343} \quad (5.48)$$

where q is a constant depending on the rock type. Shear stiffness of the fracture can also be described as

156

$$k_{st} = k_j(\sigma_n)^{n_j} \left[1 - \frac{\tau.R_f}{\tau_P}\right]^{-2} \quad (5.49)$$

which is the tangent shear stiffness of a joint at any level of shear and normal stresses and where k_j is stiffness number, n_j is stiffness exponent, R_f is failure ratio which is defined as τ/τ_{ult}, and τ_P is peak shear strength of the fracture which can be explained as (Cornet, 2015)

$$\tau_P = c + \mu\sigma_n \quad (5.50)$$

at which c is cohesive strength of the fracture, and μ is the friction coefficient of that. τ_{ult} is shear stress associated with horizontal asymptote of t_{ult} to the hyperbolic of $\tau - u_s$.
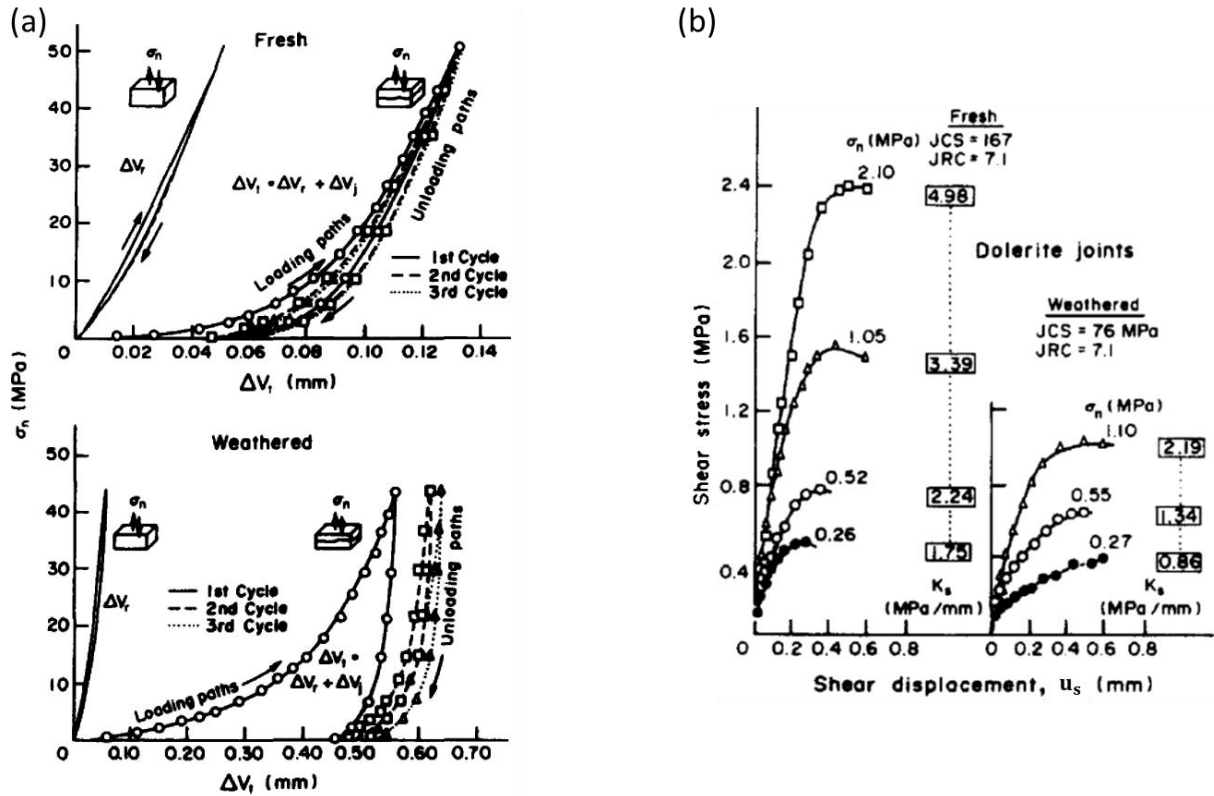
Figure 5.22. (a) Normal stress versus total deformation relations for fresh and weathered joints in dolerite specimens under cyclic loading; loading-unloading curves can also be seen on (a) which were resulted from tests carried out on intact samples of the same size; (b) Shear stress versus shear displacement curves for fresh and weathered joints in dolerite at various normal stress levels; secant peak shear stiffness values are also included in the graphs (Bandis et al., 1983)

Here, we first assumed that the fracture stiffness parameters are constant and carried out some benchmarking modeling and then successfully implemented stiffness values variable with respect to the resulting normal stress acting on the fracture plane to a finite circular fracture. This implementation finally generalized to the fracture network generated in section 2 and the effect of non-linear fracture stiffness on effective elastic moduli of the rock mass was investigated.

157

Deformation of Infinite fractures

Although commonly explained in previous reports prepared for this project, we develop the expression of the contribution of a single infinite fracture on displacement of a boundary of a rock block. Let us consider a rock block divided into two identical parts by a discontinuity as shown in figure 5.23.
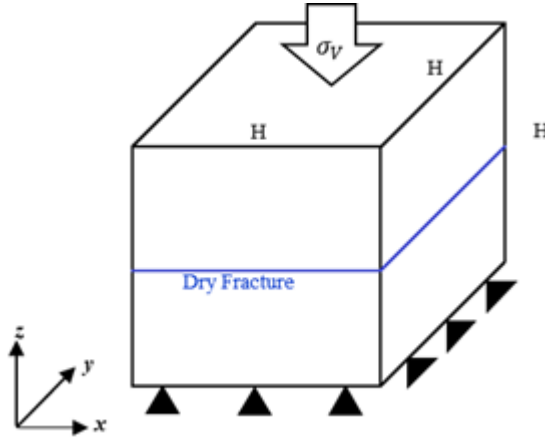
Figure 5.23. Schematic view of a fractured block and imposed stress and displacement boundary conditions

If the above-mentioned block was loaded perpendicular to the fracture wall (σ_V), a displacement between top and bottom of the block will occur. It will have two contributions: (i) the displacement of the intact rock (dH_r) and (ii) the displacement of the fracture (joint closure, $d\delta$) (Goodman, 1976). The magnitudes of these two displacements not only depend on Young's modulus of the intact rock (E_r) and normal stiffness of the fracture (k_n), but also on the magnitude of the applied stress (σ_V). Therefore, the total displacement between top and bottom of the block with height of H, dH, will be (Jaeger et al., 2007)

$$dH = dH_r + d\delta = -\frac{H}{E_r}d\sigma_V - \frac{1}{k_n}d\sigma_n \quad (5.51)$$

From right-hand side of equation (5.51), vertical deformation of intact rock, dH_r, can be analytically determined as

$$dH_r = -\int_0^H \frac{\sigma_V}{E}dh \quad (5.52)$$

in which dh is incremental length of the block height. For rock specimen under in-situ stress condition, where the minimum and maximum horizontal stress are also acting on the rock, the intact rock's deformation can be determined as

$$dH_r = -\int_0^H \left[\frac{\sigma_V}{E} - \frac{\vartheta}{E}(\sigma_h + \sigma_H)\right]dh \quad (5.53)$$

Deformation of fracture or joint closure, $d\delta$, depends on magnitude of normal stiffness of the fracture and effective normal stress acting on the fracture plane. In figure 5.23, the fracture's normal is parallel with the applied stress, and therefore the effective normal stress acting on the fracture plane, σ_n, is equal to the applied vertical stress, σ_V. For fractures oblique to the direction of the applied vertical stress, the effective normal stress can be determined by use of Cauchy tetrahedron. The "Cauchy Tetrahedron", as shown in

158

figure 5.24 (Cornet, 2015), is utilized for determination of stress vector components, t_i, acting on a surface from stress tensor components, σ_{ij}.

In figure 5.3 the vector n is normal of the ABC surface which can be characterized by its three direction cosines of n_1, n_2, and n_3 as

$$n_1 = cos\alpha \quad (5.54)$$

$$n_2 = cos\beta \quad (5.55)$$

$$n_3 = cos\gamma \quad (5.56)$$

where α, β, and γ are the angles between n and $\hat{I}_1$, $\hat{I}_2$, and $\hat{I}_3$.
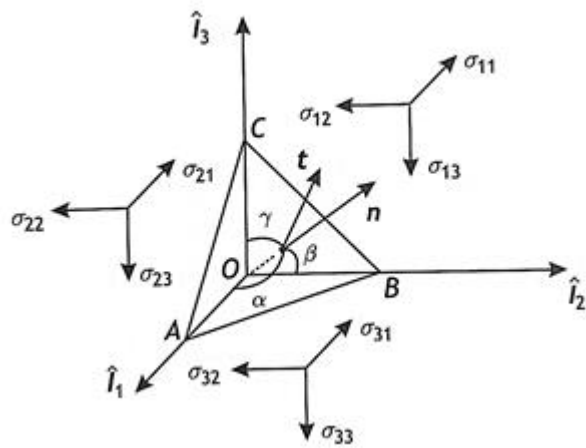
Figure 5.24. Cauchy tetrahedron used to determine stress vector components on a surface element with orientation of n based on stress tensor components (Cornet, 2015)

According to Cornet, 2015, the three components of the stress vector will be

$$t_1 = \sigma_{11}n_1 + \sigma_{12}n_2 + \sigma_{13}n_3 \quad (5.57)$$

$$t_2 = \sigma_{12}n_1 + \sigma_{22}n_2 + \sigma_{23}n_3 \quad (5.58)$$

$$t_3 = \sigma_{13}n_1 + \sigma_{23}n_2 + \sigma_{33}n_3 \quad (5.59)$$

or

$$t_i = \sigma_{ij}n_j \ , \quad i,j = 1,2,3 \quad (5.60)$$

or in vector form of

$$t = \tilde{\sigma}\,n \quad (5.61)$$

where t is called a stress vector. Projection of stress vector onto the normal n and onto the fault plane will respectively result in normal component and shear components of the stress vector as

159

$$\sigma_n \equiv \boldsymbol{t}.\boldsymbol{n} = \tilde{\sigma}\,\boldsymbol{n}.\boldsymbol{n} = \sigma_{11}n_1^2 + \sigma_{22}n_2^2 + \sigma_{33}n_3^2 + 2\sigma_{12}n_1n_2 + 2\sigma_{13}n_1n_3 + 2\sigma_{23}n_2n_3 \quad (5.62)$$

$$\boldsymbol{\tau} = \boldsymbol{t} - \sigma_n\,\boldsymbol{n} = \tilde{\sigma}\,\boldsymbol{n} - (\tilde{\sigma}\,\boldsymbol{n}.\boldsymbol{n})\boldsymbol{n} \quad (5.63)$$

σ_n is the normal stress acting on the fault which is a scalar and vector $\boldsymbol{\tau}$ is the shear component of $\boldsymbol{t}$. The norm of the shear stress vector will give us the shear stress magnitude acting on the fault plane.

$$\tau = \left\| \boldsymbol{\tau} \right\| \quad (5.64)$$

The effective normal stress acting on the fault plane resulting from equation (5.62) can be substituted in the second term in the right-hand side of equation (5.51) to determine the fracture's normal displacement, sum of which with intact rock's vertical displacement will yield the displacement of the fractured rock mass in Z-direction. It is obvious that for an inclined fracture, projection of normal and shear displacement on principal directions will be added to displacement of intact rock in those directions in order to determine elastic moduli.

Finite-size circular shaped fractures

The shear and normal displacement, u_s and u_n, of a disk shaped fracture which is free to slip and embedded in an infinite elastic rock matrix can be expressed (Davy et al., 2018; Kachanov & Sevostianov, 2013; Sneddon & Lowengrub, 1969) as

$$u_s = \frac{4(1-\nu_m^2)}{\pi(1-\frac{\nu_m}{2})}\tau_m\frac{D_f}{E_m}\sqrt{1 - \left(\frac{2d}{D_f}\right)^2} \quad (5.65)$$

$$u_n = \frac{4(1-\nu_m^2)}{\pi}\frac{min(\sigma_m,0)}{E_m}\frac{D_f}{E_m}\sqrt{1 - \left(\frac{2d}{D_f}\right)^2} \quad (5.66)$$

where D_f is diameter of the fracture, E_m and ν_m are intact rock's Young's modulus and Poisson's ratio, and d is distance to the disk center. It has to be noticed that these equations are developed for freely slipping disk-shaped fractures, therefore the shear and normal stresses of τ_m and σ_m are due to deformation of the rock matrix with the convention that normal stress and displacement are positive in compression (Davy et al., 2018).

According to Davy et al., 2018, the average shear displacement, $\overline{u_s}$, calculated by integrating equation (5.65) over fracture plane, is two third of the displacement at the fracture center, which leads to an apparent elastic shear stiffness of the matrix surrounding the fracture, k_m, which will be called the matrix-fracture stiffness thereafter, such as

$$k_m = \frac{\tau_m}{\overline{u_s}} = \frac{3\pi}{8}\frac{(1-\frac{\nu_m}{2})}{(1-\nu_m^2)}\frac{E_m}{D_f} \quad (5.67)$$

Above equation can be simplified as

$$k_m = \frac{E_m^{\,*}}{D_f} \quad (5.68)$$

$$E_m{}^* = \frac{3\pi}{8} \frac{(1-\frac{v_m}{2})}{(1-v_m^2)} E_m \quad (5.69)$$

For the normal displacement, it is worth to note that the normal stiffness of the rock matrix and fracture are barely operating together. In compressional situations and when the fracture's normal stiffness is too high, the fracture walls can hardly interpenetrate and, thus, the deformation of the rock matrix is limited (Davy et al., 2018). Normal displacement of the fracture is perpendicular to the fracture plane and is controlled by magnitude of normal stiffness of the fracture, k_n, as

$$u_n = \frac{\sigma_n}{k_n} \quad (5.70)$$

Since k_n is larger than k_s, the shear displacement is much larger than normal displacement in fractures (Davy et al., 2018). For a fracture plane with normal vector of $\boldsymbol{n}$ located at a medium under stress tensor of $\tilde{\sigma}$, the normal and shear stresses acting on the fracture plane can be expressed by equations (5.62) and (5.63) or according to Davy et al., 2018, as

$$\sigma_n = \boldsymbol{n}^T.\boldsymbol{\sigma}.\boldsymbol{n} \quad (5.71)$$

$$\tau = \boldsymbol{n}^T.\tilde{\sigma}.\boldsymbol{s} \quad (5.72)$$

with the shear direction given by

$$s = \frac{s_g}{\|s_g\|} \quad (5.73)$$

where

$$s_g^T = \boldsymbol{n}^T.\boldsymbol{\sigma}.(\tilde{1} - \boldsymbol{n} \otimes \boldsymbol{n}^T) \quad (5.74)$$

with $\tilde{1}$ as the identity matrix. The previous expressions were calculation of displacements in the fracture plane. To know the contribution of a fracture to the displacement of a specific boundary such as X, the displacement field should be integrated and projected on X with surface and normal vector of s_X and $\boldsymbol{n}_X$, (Davy et al., 2018) such as

$$u_x = (\boldsymbol{n}.\boldsymbol{n}_x)\frac{\int_S t dS}{s_X} \quad (5.75)$$

where S is the plane that includes the fracture and u is the displacement vector field in the plane. Equation (5.75) can be used to determine deformation of a specimen at boundary X and in the, for example, y-direction as below

$$\varepsilon_{xy} = \frac{t_X.n_y}{l_x} \quad (5.76)$$

Where x refers to the surface X and y to a direction vector of n_y. l_x is the dimension of the specimen in the direction perpendicular to X (i.e., in the direction n_x). Knowing that the volume of specimen is $V = S_x * l_x$ and substituting (5.75) in (5.76) will yield to (5.77) as

$$\varepsilon_{xy} = (n.n_x)\frac{\int_S (t.n_y)dS}{V} \quad (5.77)$$

According to Davy et al., 2018, since most of the displacement takes place at the fracture plane, equation (5.77) can be expressed as the average displacement at the fracture disk, $\overline{u_f}$, with the surface of S_f as

$$\varepsilon_{xy} = (n.n_x)\frac{S_f}{V}(\overline{u_f}.n_y) \quad (5.78)$$

Equation (5.77) estimates contribution of a fracture to deformation of a specimen. It can be generalized for contribution of a DFN to specimen's deformation benefiting from effective theories. Generally, most of the effective theories are based on incrementally adding fractures into the medium which is already discretized by previous fractures. Then it can be stated that the total deformation of a specimen is the sum of two following terms (Davy et al., 2018):

- Deformation of the specimen already discretized by i-1 fractures, ε_i, due to the far-field stress tensor, $\tilde{\sigma}$, applied on the equivalent medium constituted of (i-1) fractures with equivalent elastic properties, E_i and v_i;

- Plus deformation generated by the displacement on the additional i^{th} fracture.

Then, equation (5.78) might be written (Davy et al., 2018) as

$$(\varepsilon_{xy})_i = (\varepsilon_{xy})_{i-1} + (n_i.n_x)\frac{S_i}{V}(\overline{t_i}.n_y) \quad (5.79)$$

where S_i is the surface of the ith fracture with normal of n_i, and $\overline{t_i}$ is the displacement of this additional fracture.

As an example, the final deformation for non-critically loaded fractures, obtained by summing the contribution of all fractures can be written as

$$(\varepsilon_{xy})_i = (\varepsilon_{xy})_m + \Sigma_i(\boldsymbol{n_i}.\boldsymbol{n_x})\frac{S_i}{V}\left(\left(\frac{n_i^T.\tilde{\sigma}.s_i}{k_{si}+k_{mi}}\boldsymbol{s_i} + \frac{n_i^T.\tilde{\sigma}.n_i}{k_{ni}}\boldsymbol{n_i}\right).\boldsymbol{n_y}\right) \quad (5.80)$$

By applying equation (5.80) to different boundary planes and directions, the modulus of elasticity and Poisson's ratio can be calculated.

The normal component of $\overline{u_f}$ is assumed to be equal to equation (5.70). The shear component of displacement, $\overline{u_f}$ can be evaluated as described in Davy et al., 2018 in which a simplified elastic-plastic behavior is considered, where the elastic resistance of fracture walls is modeled by constant elastic stiffness coefficients of k_s and k_n, respectively for shear and normal displacements. These coefficients are supposed to be constant over the whole fracture plane. For shear displacement, a plastic limit of τ_p is defined above which the fracture freely slips independent of τ, as shown in figure 5.25 and equation (5.81):

$$\tau_f = min(k_s * u_s, \tau_p) \quad (5.81)$$

It has to be noted that the plastic shear slip which takes place beyond the fracture's shear strength is out of the scope of current work, but only the elastic shear displacement is under investigation.
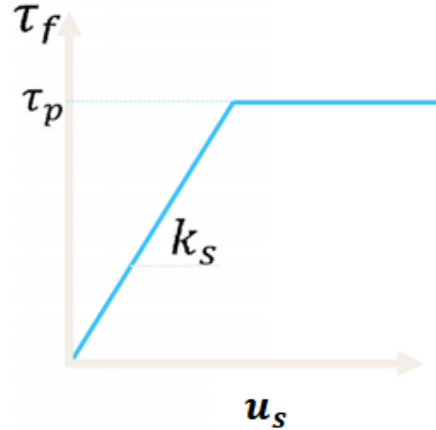
Figure 5.25. Rheological model of fracture slip in terms of shear stress versus shear displacement

In equation (5.80), τ_f is shear stress acting on the fracture plane, k_s is shear stiffness of the fracture, and u_s is shear displacement. The shear stress acting on the fracture plane, τ, has to overcome to two resisting parameters of:

1) The resistance to shear displacement across fracture walls or τ_f, and

2) The elastic stress generated by matrix deformation, $\tau_m = k_s * u_s$.

According to Davy et al., 2018, the shear displacement along the fracture walls, u_s, generated by a shear stress applied to the fracture surface can be expressed as:

$$\frac{\tau}{u_s} = \frac{\frac{2}{3}k_m}{\sqrt{1-\left(\frac{2r}{D_f}\right)^2}} + k_s \quad (5.82)$$

If $\tau_f = \tau_p$, i.e. fracture slips, the above equation must be rewritten as:

$$\frac{\tau-\tau_p}{u_s} = \frac{\frac{2}{3}k_m}{\sqrt{1-\left(\frac{2r}{D_f}\right)^2}} \quad (5.83)$$

The average displacement can be determined by integrating equations (5.82) and (5.83) over the fracture plane as

$$\overline{u_s} = \frac{1}{\pi R^2}\int_\Theta \int_0^R u_s r\, dr d\Theta = \frac{1}{R^2}\int_0^R u_s r\, dr \quad (5.84)$$

In which R is the fracture radius. For slipping fracture the above equation can be

$$\overline{u_s} = \frac{\tau-\tau_p}{k_m} \quad (5.85)$$

163

Nevertheless, for no-slipping fracture the integration result will be

$$\overline{u_s} = \frac{\tau}{k_m} \frac{2}{R^2} \int_0^R \frac{rdr}{\frac{\frac{2}{3}}{\sqrt{1-\left(\frac{r}{R}\right)^2}}+k_s^*} \quad (5.86)$$

where

$$k_s^* = \frac{k_s}{k_m} \quad (5.87)$$

However, Davy et al., 2018, approximated the average displacement of no-slipping fracture (i.e., equation (5.82)) by below equation with maximum difference of less than 4%.

$$\overline{u_s} = \frac{\tau}{k_m+k_s} \quad (5.88)$$

Equations (5.85) and (5.88) quantify the shear stress partitioning between the average resistance of the fracture plane, $\overline{\tau_f}$, and the resistance to deformation of the surrounding matrix, $\underline{\tau_m}$.

$$\tau = \overline{\tau_f} + \overline{\tau_m} = min(k_s u_s , \tau_p) + k_m \overline{u_s} \quad (5.89)$$

The shear component of $\overline{u_l}$ depends on three terms of i) the shear stress, $\tau = \boldsymbol{n}^T.\boldsymbol{\sigma}.\boldsymbol{s_i}$ with s_i the direction of shear, ii) the elastic shear stiffness k_{si} which may depend on each fracture, and iii) the local matrix-fracture stiffness k_{mi}, which is a function of the elastic properties of the medium surrounding the fracture and is the main term in evaluating the $\overline{u_l}$ (Davy et al., 2018). There are different theories to estimate the matrix-fracture stiffness such as follows.

No-interaction Model

This is the simplest model which considers that the surrounding medium in the vicinity of the fracture is not damaged, hence the elastic properties are those of the intact rock matrix (E_m and ϑ_m). It yields to an expression of k_{mi} as

$$k_{mi} = \frac{3\pi}{8} \frac{(1-\frac{\vartheta_m}{2})}{(1-\vartheta_m^2)} \frac{E_m}{D_{fi}} \quad (5.90)$$

where D_{fi} is the length of the ith fracture. The no-interaction model is a good description of a system with a small density of fractures, where fractures are far from each other and any fracture is surrounded by intact rock, meaning that the contribution of each fracture to the specimen's deformation is independent of other fractures. While this model estimates well the Poisson's ratio of the equivalent medium whatever the fracture density is, it just gives a dependable estimate for Young's modulus of medium with low fracture density.

The Effective Medium Theory

The effective medium theories approximate the interaction between fractures utilizing different schemes among which the self-consistent theory of O'Connell and Budianski (1974) and the differential scheme of Hashin (1988) are the most popular theories. A review of effective medium theories can be found in

164

Gueguen and Kachanov (2011), Jaeger et al. (2007) and Kachanov (1987). Davy et al., 2018, developed the differential scheme theory, in which some inconsistencies of this theory at high fracture densities were avoided (Bruner, 1976). It, in fact, considers that the ith fractures is surrounded by the medium which has already damaged by i-1 fractures, but with a homogeneous Young's modulus and Poisson's ratio which are average basically average properties of the medium constituted of i-1 fractures, i.e. E_{i-1} and ϑ_{i-1}. Therefore, the k_{mi} will read

$$k_{mi} = \frac{3\pi}{8} \frac{(1-\frac{\vartheta_{i-1}}{2})}{(1-\vartheta_{i-1}^2)} \frac{E_{i-1}}{D_{fi}} \quad (5.91)$$

The effective medium theory evaluates the Young's modulus less than the no-interaction model since the medium is supposed to be softer than the no-interaction model due to damage of previous fracture imposed to the medium in the effective medium theory.

5.3.3   Mechanical Computations in 3DEC

3DEC is a Discrete Element Method (DEM) for discontinuum environment and can simulate the interaction between blocks. It is best suited to model discontinuous materials that show non-linear behavior. It comprises many built-in constitutive models for blocks and joints and provides an option for user-written models by introducing FISH scripting language. In addition to representing or importing any shape of geometries, it can carry out static and dynamic analysis and considers thermal stress and time-dependent behavior of geomaterial.

To account for the observed non-linear behavior, a description of the fracture network is required which may be achieved by definition of a Discrete Fracture Network (DFN). In addition to assigning a DFN to a numerical model of the target area, it must be built applying mechanical properties of the intact rock and fractures, pore pressure, and in-situ stress field.

In 3DEC, two blocks which are in contact have interacted with each other when some load is applied. For these two blocks, a unit normal vector is defined which indicates the contact plane of blocks. Direction of this unit normal vector continuously changes as the two blocks move relative to one another. A common-plane (c-p) is also determined which bisects the space between the two blocks and each block is separately tested for contact with this c-p (figure 5.26).

If a block face is in contact with the c-p, then it is automatically discretized into sub-contacts which keeps track of the interface forces between blocks, as well as other conditions such as sliding and separation. If the other side of the interface is also a face, then identical conditions apply, sub-contacts are created, and relative displacements, and hence forces, are calculated. When two blocks come together, the forces from both sets are divided by two, so that the overall interface behavior is the average of that of both sets.
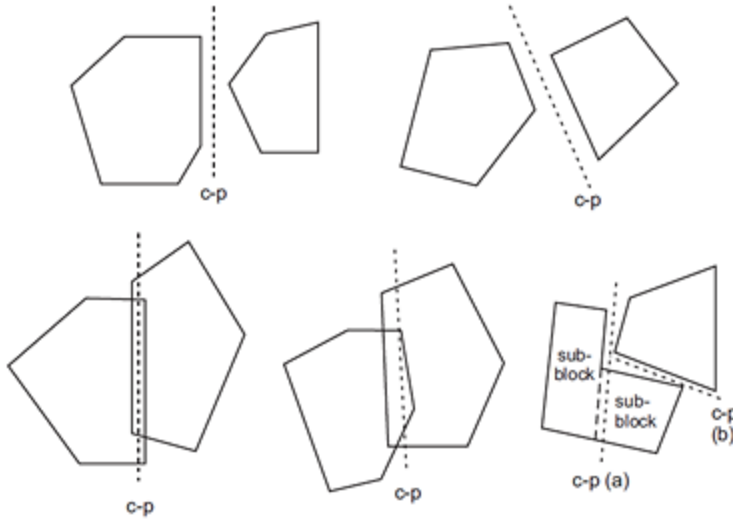
Figure 5.26. Examples of c-p between two blocks in 3DEC

3DEC is based on a dynamic (time-domain) algorithm that solves the equations of motion of the block system by an explicit finite difference method. At each timestep, the law of motion and the constitutive equations are applied. For blocks, sub-contact force-displacement relations are prescribed. The integration of the law of motion provides the new block positions, and therefore the contact-displacement increments (or velocities). The sub-contact force-displacement law is then used to obtain the new sub-contact forces, which are to be applied to the blocks in the next timestep.

The relative velocity across a sub-contact is obtained from the velocity associated with the sub-contact, V_i^V, and the velocity of the corresponding point on the opposing face, V_i^F. If the unit normal, n_i, points from block A to block B, therefore the relative velocity is calculated as:

If the tetrahedral-zone vertex belongs to block A, otherwise it is calculated as:

$$V_i = V_i^F - V_i^V \quad (5.92)$$

The increment in relative displacement at the sub-contact for both rigid and deformable blocks is given by:

$$\Delta U_i = V_i \Delta t \quad (5.93)$$

which can be resolved into normal and shear components along the common-plane as:

$$\Delta U^n = \Delta U_i n_i \quad (5.94)$$

$$\Delta U_i^s = \Delta U_i - \Delta U_i n_i n_j \quad (5.95)$$

The sub-contact displacement increments are used to calculate the elastic force increments. The normal and shear force increments, taking compressive force as positive, are:

$$\Delta F^n = -K_n \Delta U_i^n A_c \quad (5.96)$$

166

$$\Delta F_i^s = -K_s \Delta U_i^s A_c \quad (5.97)$$

where A_c is the area of the sub-contact. The sub-contact area is obtained by assigning to the point a region formed by $1/3$ of the areas of the triangular faces containing the sub-contact and lying on the c-p. The area of the intersection of this region with the other block's faces lying on the c-p is then calculated.

Then, total normal force and shear force vectors are updated for the sub-contact as:

$$F^n := F^n + \Delta F^n \quad (5.98)$$

$$F_i^s := F_i^s + \Delta F_i^s \quad (5.99)$$

5.3.4   Benchmarking Modeling for Intact Rock

Here, it is aimed to numerically model a 100x100x100 m³ homogeneous, isotropic, and elastic block composed of lower granite of Soultz-sous-Forêts geothermal reservoir. The elastic moduli of this granite are already assessed in many literatures such as Vallier et al., 2019, in which Young's modulus and Poisson's ratio are obtained respectively 25 GPa and 0.29. These values are assigned to the numerical rock block of the current section and effective elastic moduli are then determined through uniaxial compressive stress test, confined uniaxial compressive stress test, and true triaxial compressive stress test. Noteworthy that the gravitational effect of the rock is not taken into account.

Uniaxial Compressive Stress Test

In this test, all sides of the block are free to move except the bottom, which is fixed only in the Z-direction. The block is discretized by a tetrahedral with a side size of 5 meters. A 10 MPa compressive stress is applied to the top of the block and the model is let to reach an equilibrium state. It is also assumed that the X-, Y-, and Z-directions are corresponding with principal directions. Arithmetic average values of strain and stress increments throughout the block volume are then extracted from the numerical model in order to assess the effective elastic moduli of the rock block under a uniaxial compressive stress test.

Substituting the values of assigned elastic moduli and applied stress in equations (5.35) and (5.37) will yield -4.000e-04 and 1.160e-04 for vertical and lateral strains, respectively. Numerical average values of strain and stress increments are shown in tables 5.10 and 5.11.

Table 5.10. Average numerical strain increment values and corresponding standard deviations

Strain Increments	Average Numerical Values	Standard Deviation
ZZ-Strain	-4.00e-04	1.29e-08
XX-Strain	1.16e-04	4.58e-09
YY-Strain	1.16e-04	4.33e-09
XY-Strain	1.19e-11	5.46e-10
XZ-Strain	-1.62e-9	7.92e-09
YZ-Strain	-2.68e-09	8.09e-09

Table 5.11. Average stress increment values and corresponding standard deviation

Stress Increments	Average Numerical Values (Pa)	Standard Deviation (Pa)
ZZ-Stress	-1.00e07	3.09e02
XX-Stress	-3.09e01	8.20e01
YY-Stress	-3.09e01	8.43e01
XY-Stress	1.78e-01	7.85e00
XZ-Stress	-2.62e01	4.16e01
YZ-Stress	-4.30e01	5.01e01

Very small standard deviation in above tables indicates that the strain and stress increments distributed in the block zones are centered on the obtained average values and might be consistent to conclude that the estimated average values are good representative of the distributed parameters.

Effective elastic moduli can then be determined by doing some reorder in equations (5.34) and (5.36) so as

$$E_{eff} = \frac{\sigma_{zz_{ave}}}{\varepsilon_{zz_{ave}}} \quad (5.100)$$

$$\vartheta_{eff} = \frac{-\varepsilon_{xx_{ave}}}{\varepsilon_{zz_{ave}}} = \frac{-\varepsilon_{yy_{ave}}}{\varepsilon_{zz_{ave}}} \quad (5.101)$$

By substituting average values of ZZ-, XX-, and YY-Strains and ZZ-Stress of tables 5.1 and 5.2 in equations (5.92) and (5.93), the effective values of elastic moduli yields approximately 25.0 GPa and 0.290. Knowing that the assigned Young's modulus and Poisson's ratio are respectively 25.0 GPa and 0.290, we may determine relative error of estimations for effective elastic moduli in percent as

$$relative\ Error = \frac{numerical-assigned}{assigned} * 100 \quad (5.102)$$

In this way, and by considering 3 significant figures, a negligible relative error for both Young's modulus and Poisson's ratio were obtained.

Confined Uniaxial Compressive Stress Test

In this test, all sides of the block are fixed in the direction of face-normal except the top side. The block is discretized by a tetrahedral with a side size of 5 meters. A 10.0 MPa of compressive stress is applied to the top of the block and the model is let to reach an equilibrium state. It is also assumed that the X-, Y-, and Z-directions are corresponding with principal directions. Arithmetic average values of strain and stress increments throughout the block volume are then extracted from the numerical model in order to assess the effective elastic moduli of the rock block under a confined compressive stress test.

Substituting the values of assigned elastic moduli and applied stress in equations (5.40) and (5.41) results in lateral stresses of -4.1 MPa and the vertical strain of -3.1e-04. Numerical average values of strain and stress increments are shown in tables 5.12 and 5.13. Effective elastic moduli can be obtained by substituting numerical average strain and stress values in equations (5.40) and (5.41) and doing some reorder so as

$$\vartheta = \frac{\sigma_{xx_{ave}}}{\sigma_{xx_{ave}} + \sigma_{zz_{ave}}} = \frac{\sigma_{yy_{ave}}}{\sigma_{yy_{ave}} + \sigma_{zz_{ave}}} \quad (5.103)$$

$$E_{eff} = \frac{1}{\varepsilon_{zz_{ave}}} \left[\sigma_{zz_{ave}} - \vartheta_{eff} \left(\sigma_{xx_{ave}} + \sigma_{yy_{ave}} \right) \right] \quad (5.104)$$

By substituting average values of ZZ-, XX-, and YY-Strains and ZZ-Stress of tables 5.12 and 5.13 in equations (5.103) and (5.104), the effective values of Poisson's ratio and Young's modulus will be 0.290 and 25.0 GPa, respectively; again with negligible relative errors.

Table 5.12. Average strain increment values and corresponding standard deviations

Strain Increments	Average Numerical Values	Standard Deviation
ZZ-Strain	-3.05e-04	7.54e-09
XX-Strain	1.10e-10	1.62e-09
YY-Strain	1.08e-10	2.61e-09
XY-Strain	-2.37e-12	1.75e-09
XZ-Strain	1.02e-09	3.92e-09
YZ-Strain	2.30e-09	4.12e-09

Table 5.13. Average stress increment values and corresponding standard deviation

Stress Increments	Average Numerical Values (Pa)	Standard Deviation (Pa)
ZZ-Stress	-1.00e07	2.71e02
XX-Stress	-4.08e06	1.07e02
YY-Stress	-4.08e06	1.14e02
XY-Stress	-5.34e-02	3.40e01
XZ-Stress	2.09e01	5.03e01
YZ-Stress	4.65e01	5.66e01

Triaxial Compressive Stress

In this test, all sides of the block are free to move except the bottom side, which is fixed only in the z-direction (the direction of face-normal). A 10.0 MPa of compressive vertical stress is applied to the top of the block. XX- and YY- stresses are both equal to 1.00 MPa compressive stress. It is also assumed that the X-, Y-, and Z-directions are corresponding with principal directions. Arithmetic average values of strain and stress increments throughout the block volume are then extracted from the numerical model in order to assess the effective elastic moduli of the rock block under triaxial compressive stress test. Substituting the values of assigned elastic moduli and applied stresses in equations (5.43) to (5.45) yields -3.8e-04 and 8.8e-05 for vertical and lateral strains, respectively. Numerical average values of strain and stress increments are shown in tables 5.14 and 5.15.

Table 5.14. Average strain increment values and corresponding standard deviations

Strain Increments	Average Numerical Values	Standard Deviation
ZZ-Strain	-3.77e-04	1.57e-08
XX-Strain	8.76e-05	5.23e-09
YY-Strain	8.76e-05	4.85e-09
XY-Strain	-7.39e-12	5.85e-10
XZ-Strain	-1.95e-09	6.55e-09
YZ-Strain	-3.25e-09	6.86e-09

Table 5.15. Average stress increment values and corresponding standard deviations

Stress Increments	Average Numerical Values (Pa)	Standard Deviation (Pa)
ZZ-Stress	-1.00e07	3.85e02
XX-Stress	-1.00e06	6.98e01
YY-Stress	-1.00e06	7.38e01
XY-Stress	9.23e-02	7.89e00
XZ-Stress	-3.35e01	4.15e01
YZ-Stress	-5.56e01	5.52e01

Effective elastic moduli can be obtained by substituting numerical average strain and stress values in equations (5.43) to (5.45) and doing some reorder so as

$$\vartheta_{eff} = \frac{\varepsilon_{xx_{ave}}\sigma_{zz_{ave}} - \varepsilon_{zz_{ave}}\sigma_{xx_{ave}}}{\varepsilon_{xx_{ave}}(\sigma_{xx_{ave}} + \sigma_{yy_{ave}}) - \varepsilon_{zz_{ave}}(\sigma_{zz_{ave}} + \sigma_{yy_{ave}})} \quad (5.105)$$

$$E_{eff} = \frac{1}{\varepsilon_{zz_{ave}}}\left[\sigma_{zz_{ave}} - \vartheta_{eff}\left(\sigma_{xx_{ave}} + \sigma_{yy_{ave}}\right)\right] \quad (5.106)$$

By substituting average values of ZZ-, XX-, and YY-Strains and ZZ-Stress of tables 5.14 and 5.15 in equations (5.105) and (5.106), the effective values of Poisson's ratio and Young's modulus will be 0.290 and 25.0 GPa, respectively; with negligible relative errors for Young's modulus and Poisson's ratio.

Sensitivity Analysis on Intact Rock Behavior

One of the most important parameters in modeling using numerical tools such as 3DEC which affects the accuracy of the estimates might be the number of zones in the model or, in the other words, the size of meshing. In 3DEC, the model is discretized to tetrahedral, side size of which in this subsection is going to be changed from reference value of 5 meters (results of which are explained in above subsections) to 4, 10, and finally to 20 meters. It is aimed to assess the sensitivity of the strain and stress increments and finally the estimation of effective elastic moduli against the mesh size change.

Worth to mention that, since the elongations and distortions in a 3D model are independent of each other (Timoshenko and Goodier, 1970) and distortions were negligible in our estimated data set, the sensitivity

analysis carried out on principal strain and stress increments. Figures 5.27 to 5.29 illustrate the relative error evolution of estimated effective moduli in terms of discretization size of the model. Looking at these figures, one may conclude that the effect of mesh size on the accuracy of estimated effective elastic moduli are not significant, however it might be time-effective to discretize the model with tetrahedral of side size of 10 meters, since it has the best accuracy among four defined mesh sizes to the model under all three loading scenarios.
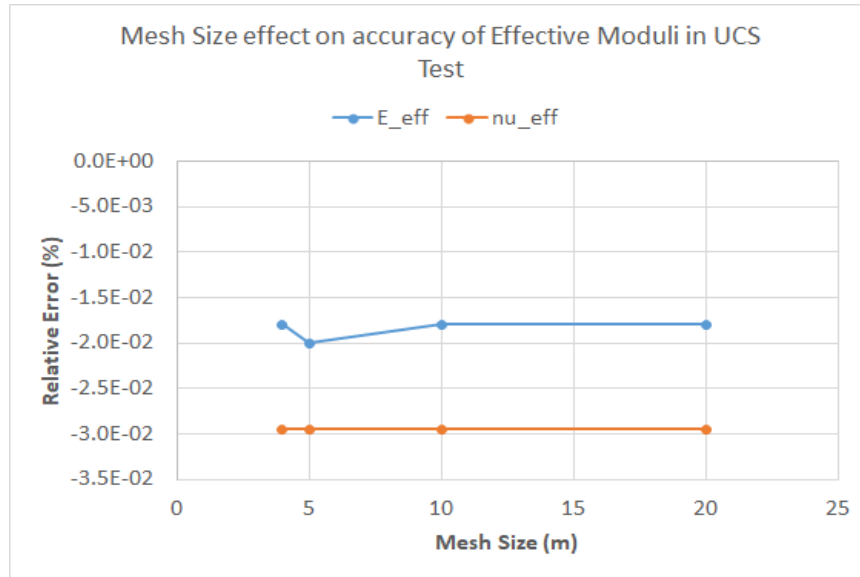
Figure 5.27. Evolution of estimation accuracy of effective elastic moduli against variation of mesh size in uniaxial compressive stress test
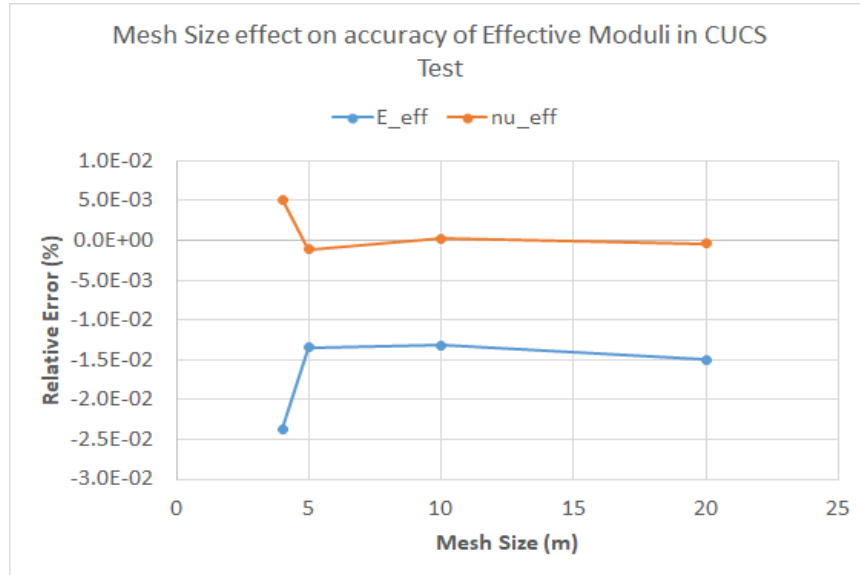
Figure 5.28. Evolution of estimation accuracy of effective elastic moduli against variation of mesh size in confined uniaxial compressive stress test
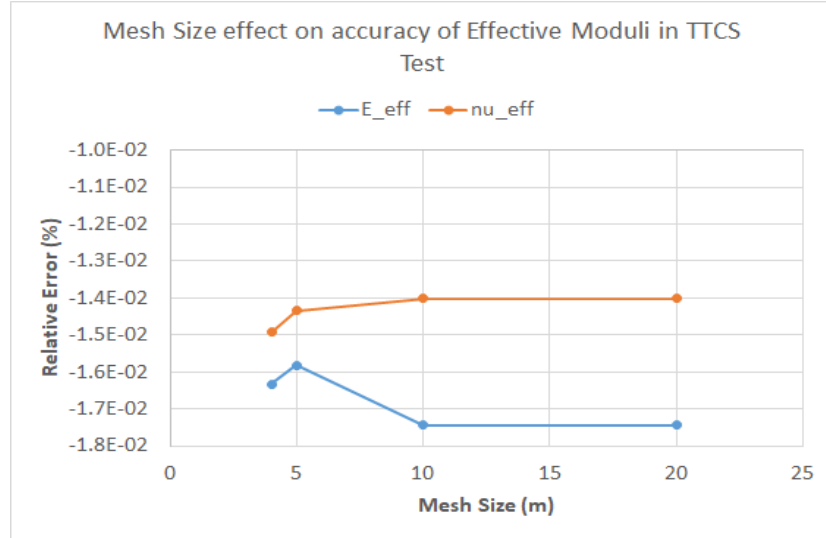
Figure 5.29. Evolution of estimation accuracy of effective elastic moduli against variation of mesh size in true triaxial compressive stress test

5.3.5 Benchmarking Modeling for Rock Block Containing an Infinite Fracture

Here, it is aimed to repeat the numerical tests of subsection 5.3.4 when the block is divided into two identical parts in height by a horizontal infinite fracture as shown in figure 5.23. The elastic properties of the intact rock is as same as those of block in subsection 5.3.4. The fracture's mechanical and physical properties are summarized in table 5.16, after Gentier et al, 2003 and 2005, to evaluate the response of the numerical model to the existence of a fracture and its mechanical reaction to the loading.

Table 5.16. Mechanical and physical properties of the fracture embedded in the intact rock block

Property	Symbol	Value	Unit	Reference
Normal Stiffness	k_n	80.0	(GPa/m)	Gentier et al., 2005
Shear Stiffness	k_s	20.0	(GPa/m)	Gentier et al., 2005
Initial Hydraulic Aperture	h_{ini}	14e-05	(m)	Gentier et al., 2005
Residual Hydraulic Aperture	h_{res}	7.0e-05	(m)	Gentier et al., 2005
Maximum Hydraulic Aperture	h_{max}	12e-03	(m)	Gentier et al., 2005

Analytically, the normal displacement of the fracture under uniaxial compressive stress test is

$$d\delta = \frac{\sigma_n}{k_n} \quad (5.107)$$

which yield fracture closure of -1.25e-04 m under -10.0 MPa of normal stress. Vertical displacement of the intact rock block can be determined using the first term of right-hand side of equation (5.51) as

$$dH_r = \frac{H}{E_r} d\sigma_V = -4.00e - 02 \, m$$

172

Hence, the total vertical displacement of the fractured rock block will be -4.01e-2 m. The vertical strain of the fractured rock block can then be determined by dividing total vertical displacement by sum of intact block height and fracture's initial aperture as -4.01e-04 m.

So, the lateral strain increments will yield 1.2e-04. Below in tables 5.17, the numerical values of average strain and stress increments of the rock mass block for uniaxial compressive stress loading scenarios are summarized.

Table 5.17. Average numerical strain increments and corresponding standard deviations

Parameter	Average Numerical Values	Standard Deviations
ZZ-Strain	-4.00e-04	1.56e-08
XX-Strain	1.16e-04	4.40e-08
YY-Strain	1.16e-04	5.09 e-09

Table 5.18. Average stress increment values and corresponding standard deviations

Stress Increments	Average Numerical Values (Pa)	Standard Deviation (Pa)
ZZ-Stress	-1.00e07	3.89e02
XX-Stress	1.38e01	4.33e01
YY-Stress	1.55e01	2.99e01

Substituting the results of tables 5.17 and 5.18 in equations (5.100) and (5.101) yields effective Poisson's ratio and Young's modulus of 0.290 and 25.0 GPa, respectively, with a negligible relative error.

Now, it is aimed to assess the effect of lateral confinement on the resulting effective elastic moduli of the fractured rock block. For that, like the tests performed on the intact rock, in the first test the lateral displacement of the block is fixed to zero and then, in the second test, a confining compressive stress of - 1.0 MPa is applied to the side faces of the block in X- and Y-directions.

For the first test, the analytical solution is as:

$$\sigma_{xx} = \sigma_{yy} = \frac{\nu}{1-\nu}\sigma_V = -4.08e6\ Pa$$

$$d\delta = \frac{\sigma_n}{k_n} = -1.25e-4\ m$$

$$dH_r = \frac{H}{E_r}\left[d\sigma_V - \vartheta(\sigma_{xx} + \sigma_{yy})\right] = -3.1e-2\ m$$

$$dH_{Total} = dH_r + d\delta = -3.1e-2\ m$$

$$\varepsilon_{zz} = \frac{1}{E_r}\left[d\sigma_V - \vartheta(\sigma_{xx} + \sigma_{yy})\right] = -3.1e-4$$

$$\varepsilon_{xx} = \varepsilon_{yy} = 0$$

Numerical average values of strain and stress increments are shown in tables 5.19 and 5.20.

Table 5.19. Average numerical strain increments and corresponding standard deviations

Parameter	Average Numerical Values	Standard Deviation
ZZ-Strain	-3.05e-04	7.79e-09
XX-Strain	1.53e-10	1.79e-09
YY-Strain	1.53e-10	1.79e-09

Table 5.20. Average stress increment values and corresponding standard deviation

Stress Increments	Average Numerical Values (Pa)	Standard Deviation (Pa)
ZZ-Stress	-1.00e07	2.43e02
XX-Stress	-4.08e06	9.93e01
YY-Stress	-4.08e06	9.94e01

Substituting the results of tables 5.19 and 5.20 in equations (5.103) and (5.104) yields 0.290 and 25.0 GPa respectively for Poisson's ratio and Young's modulus.

For true triaxial compressive stress test, analytical solution yield

$$d\delta = \frac{\sigma_V}{k_n} = -1.25e - 4\ m$$

$$dH_r = \frac{H}{E_r}[d\sigma_V - \vartheta(\sigma_h + \sigma_H)] = -3.77e - 2\ m$$

$$dH_{Total} = dH_r + d\delta = -3.78e - 2\ m$$

$$\varepsilon_{zz} = \frac{1}{E_r}[d\sigma_V - \vartheta(\sigma_h + \sigma_H)] = -3.77e - 4$$

$$\varepsilon_{xx} = \frac{1}{E_r}[d\sigma_H - \vartheta(\sigma_V + \sigma_h)] = 8.76e - 5 = \varepsilon_{yy}$$

Numerical average values of strain and stress increments are shown in tables 5.21 and 5.22.

Table 5.21. Average numerical strain increments and corresponding standard deviations

Parameter	Numerical Value	Standard Deviation
ZZ-Strain	-3.77e-04	1.85e-08
XX-Strain	8.76e-05	5.24e-09
YY-Strain	8.76e-05	6.03e-09

Table 5.22. Average stress increment values and corresponding standard deviation

Stress Increments	Average Numerical Values (Pa)	Standard Deviation (Pa)
ZZ-Stress	-10e06	4.61e02
XX-Stress	-1e06	5.12e01
YY-Stress	-1e06	3.57e01

Substituting the results of tables 5.21 and 5.22 in equations (5.105) and (5.106) yields 0.290 and 25.0 GPa for Poisson's ratio and Young's modulus, respectively.

The true triaxial test will be the only scenario to be investigated afterwards due to the reason that it is more relevant to the rock masses undergoing in-situ stress states compared to the other two loading scenarios. Therefore, a true triaxial test on the above-mentioned rock mass block is designed by applying in-situ stress magnitudes at the depth of 4.7 km of Soultz-sous-Forêts reservoir. For that, the stress magnitudes are determined based on Cornet et al., 2007, equations which yield 118.5, 64, and 112.6 MPa for vertical, minimum and maximum horizontal stresses, respectively. It is also assumed that the in-situ stresses are aligned with principal stress directions and stress variation with depth is negligible through 100 meter of block height. For such true triaxial compressive stress test, analytical solution yield

$$d\delta = \frac{\sigma_V}{k_n} = -1.48e - 3\ m$$

$$dH_r = \frac{H}{E_r}[d\sigma_V - \vartheta(\sigma_h + \sigma_H)] = -2.69e - 1\ m$$

$$dH_{Total} = dH_r + d\delta = -0.271\ m$$

$$\varepsilon_{zz} = \frac{1}{E_r}[d\sigma_V - \vartheta(\sigma_h + \sigma_H)] = -2.69e - 3$$

$$\varepsilon_{xx} = \frac{1}{E_r}[d\sigma_h - \vartheta(\sigma_V + \sigma_H)] = 1.21e - 4$$

$$\varepsilon_{yy} = \frac{1}{E_r}[d\sigma_H - \vartheta(\sigma_V + \sigma_h)] = -2.39e - 3$$

Numerical average values of strain and stress increments are shown in tables 5.23 and 5.24.

Table 5.23. Vertical displacement values, strain increments, and corresponding errors

Parameter	Analytical Values	Numerical Values	Relative Error (%)
ZZ-Strain	-2.69e-03	-2.691e-03	0.0371
XX-Strain	1.21e-04	1.206e-04	0.331
YY-Strain	-2.39e-03	-2.387e-03	0.126

Table 5.24. Average stress increment values and corresponding standard deviation

Stress Increments	Applied Values (Pa)	Average Numerical Values (Pa)	Relative Error (%)
ZZ-Stress	-118.5e06	-118.49e06	0.008
XX-Stress	-64.00e6	-64.00e06	N/A
YY-Stress	-112.6e6	-112.59e06	0.009

Substituting the results of tables 5.14 and 5.15 in equations (5.103) and (5.104) yields

$$\vartheta_{eff} = 0.290$$

$$E_{eff} = 25.0 \, GPa$$

It was found from benchmarking modeling using the uniaxial compressive, confined uniaxial compressive, triaxial compressive, and polyaxial (true triaxial) tests on the block hosting an infinite horizontal dry fracture show that the numerical results have a good agreement with the analytical counterparts as can be observed in tables from 3.8 to 3.15. On the other hand, and comparing the numerical effective elastic moduli with the initially assigned values of 0.290 and 25.0 GPa (respectively for Poisson ratio and Young's modulus) implies that the embedded dry fractures characterized with parameters in table 3.7 does not change the elastic behavior of the fractured rock block in comparison to the intact rock block.

Sensitivity Analysis on Fractured Rock Behavior

In the previous subsection equivalent elastic moduli of a fractured rock block was determined through a true triaxial loading test in which in-situ stress magnitudes at depth of 4.7 km of Soultz-sous-Forêts reservoir was applied to the block. Here, it is aimed to assess the sensitivity of equivalent elastic moduli to some of fracture properties such as orientation, normal and shear stiffnesses.

Orientation of fracture can be generalized to the angle between fracture's normal and direction of maximum principal stress. This will simultaneously take the effect of fracture's dip and dip direction into consideration related to calculation of normal and shear stresses acting on the fracture plane. These two stresses in collaboration with fracture's normal and shear stiffnesses will determine normal and shear displacement of fracture. Noteworthy that shear displacement of fracture planes are assumed to be elastic as long as the shear stress acting on the fracture plane does not exceed the fracture's shear strength (equation 5.50). The shear displacement prior to reaching fracture's shear strength then might be considered as elastic shear displacement, $d\delta_s$, and be expressed as

$$d\delta_s = \frac{d\tau}{k_s} \quad (5.108)$$

in which τ is shear stress acting on the fracture plane and k_s is shear stiffness of the fracture.

Normal displacement of the fracture has been already discussed and can be determined using equation (5.107).

It is obvious that fracture's orientation will affect the magnitude of normal and shear stresses acting on the fracture plane (see Cauchy tetrahedron in figure 5.24) which in turn will have influence on normal and shear displacements of fracture and hence the elastic response of the rock mass block compared to when the fracture was horizontal (in which the normal stress acting on the fracture is as equal as vertical stress, but shear stress is zero).

Here, we have just analyzed sensitivity of equivalent elastic moduli to variation of fracture's dip. According to Cornet, 2015, shear and normal stress acting on a surface in which an eigenvector lies (e.g., changing dip of a fracture) and its normal makes an angle of β with direction of maximum principal stress can be expressed as

$$\sigma_n = \frac{\sigma_1 + \sigma_3}{2} + \frac{\sigma_1 - \sigma_3}{2} cos2\beta \quad (5.109)$$

$$\tau = -\frac{\sigma_1 - \sigma_3}{2} sin2\beta \quad (5.110)$$

Substitution of these stress values in equation (5.109) and (5.110) will yield normal and shear displacement of the fracture, projection of which onto principal direction will be added to displacement magnitudes of intact rock and, therefore, will affect elastic moduli.

Figure 5.30 illustrates a fractured block where the fracture's normal has an angle of β with maximum principal stress and the eigenvector e_2 lies on the fracture plane. So, equations (5.105) and (5.106) are valid for this case. On the other hand, direction cosines of normal and shear displacement in such configuration will be cos (90-β), cos (90), and cos (β) in X-, Y-, and Z-directions, respectively. These direction cosines can be employed for determination of projection of normal and shear displacement components in principal directions.

Figures 3.31 and 3.32 illustrate effective elastic moduli variation against fracture's dip alteration. Effective elastic moduli are determined in two principal directions of I_2 and I_3 by substituting average numerical values of stress and strain in equations (3.74) and (3.75). For this case in which the lateral stresses are not identical, contrary to those which are used to obtain equations (3.74) and (3.75), two more equations are required to determine effective elastic moduli in both I_2 and I_3 directions. Then, we may reformulate aforementioned equations as

$$\vartheta_{eff_{12}} = \frac{\varepsilon_{2ave}\sigma_{1ave} - \varepsilon_{1ave}\sigma_{2ave}}{\varepsilon_{2ave}(\sigma_{3ave} + \sigma_{2ave}) - \varepsilon_{1ave}(\sigma_{1ave} + \sigma_{3ave})} \quad (5.111)$$

$$E_{eff_{12}} = \frac{1}{\varepsilon_{1ave}}\left[\sigma_{1ave} - \vartheta_{eff_{12}}(\sigma_{2ave} + \sigma_{3ave})\right] \quad (5.112)$$

$$\vartheta_{eff_{13}} = \frac{\varepsilon_3\sigma_{1ave} - \varepsilon_{1ave}\sigma_3}{\varepsilon_{3ave}(\sigma_{3ave} + \sigma_{2ave}) - \varepsilon_{1ave}(\sigma_{1ave} + \sigma_{2ave})} \quad (5.113)$$

$$E_{eff_{13}} = \frac{1}{\varepsilon_{1ave}}\left[\sigma_{1ave} - \vartheta_{eff_{13}}(\sigma_{2ave} + \sigma_{3ave})\right] \quad (5.114)$$
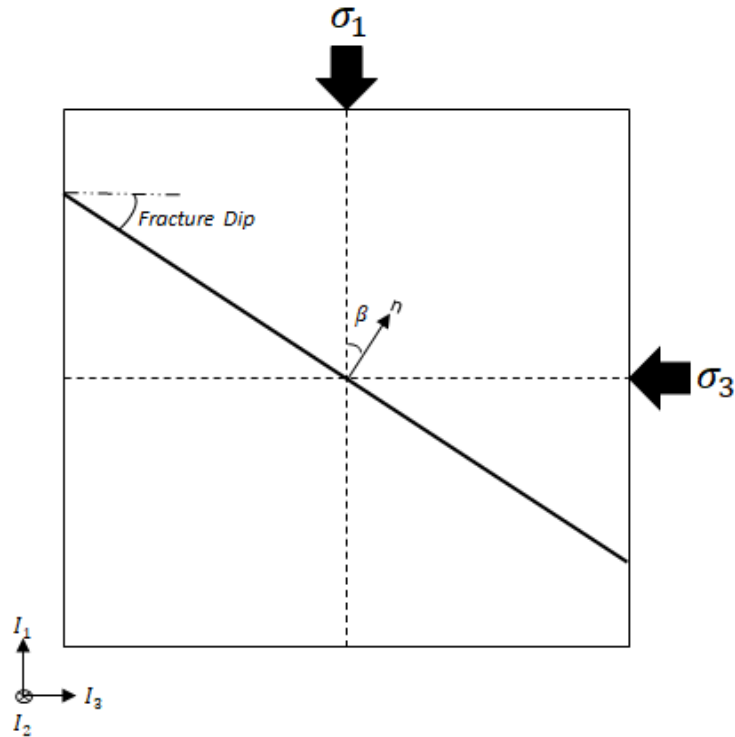
Figure 5.30. Schematic vertical cross section of a fractured rock mass
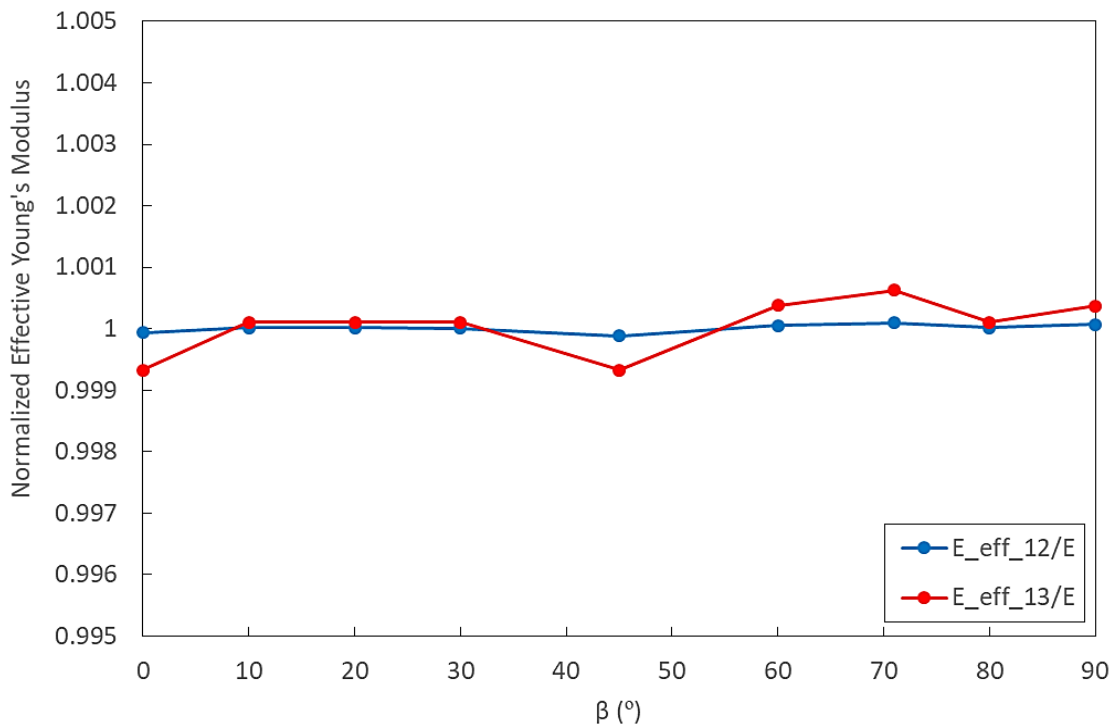
Figure 5.31. Evolution of effective Young's modulus in I_2 and I_3 directions versus fracture dip
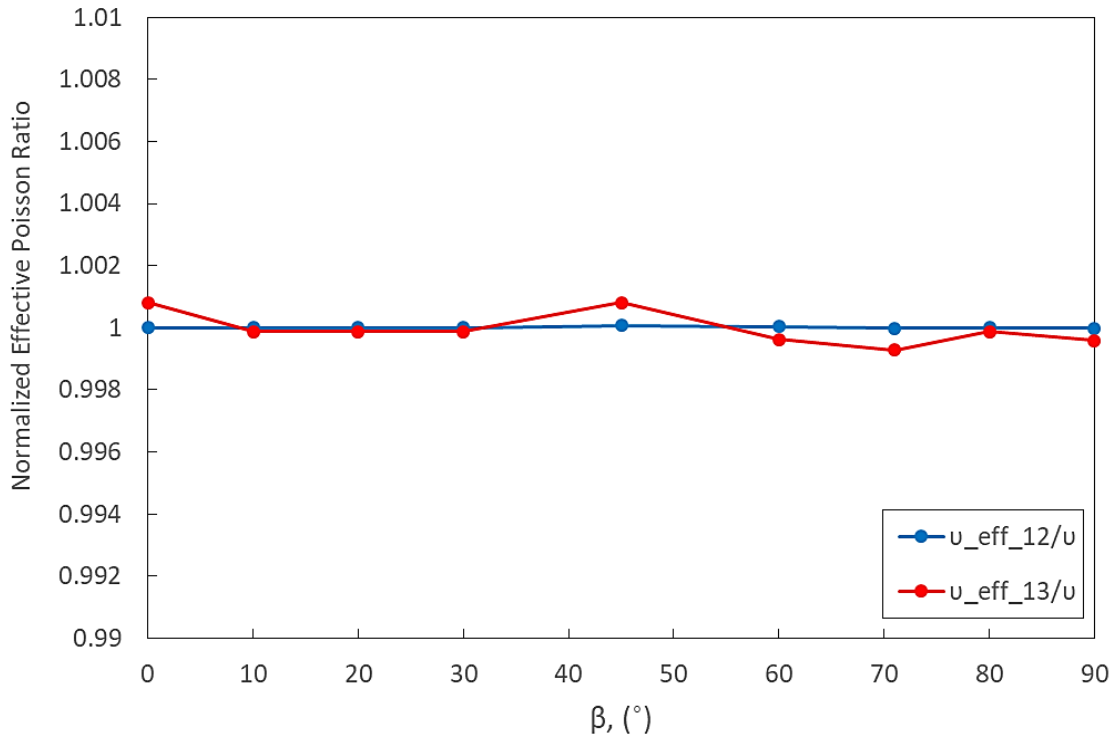
Figure 5.32. Evolution of effective Poisson's ratio in I_2 and I_3 directions versus fracture dip

The results summarized in figures 5.31 and 5.32 reveal that the average effective elastic moduli evolution in I_3 direction is relatively more sensitive to fracture dip variation compared to that in I_2 direction due to the fact that contribution of the fracture's elastic displacement to the total displacement of the block in I_2 direction is approximately zero. It stems from the azimuth of fracture which is zero in this specific case. Generally looking, it seems that the variation of elastic moduli is not meaningful at this test; however, in some cases (e.g., dip of 45° and 70°) show a slight deviation from elastic moduli of the intact rock.

The effect of fracture's azimuth can be assessed by keeping fracture dip on a constant value, e.g. 71°, and changing fracture's azimuth from 0° to 90°. Doing so, yielded the results shown in figures 5.33 and 5.34.
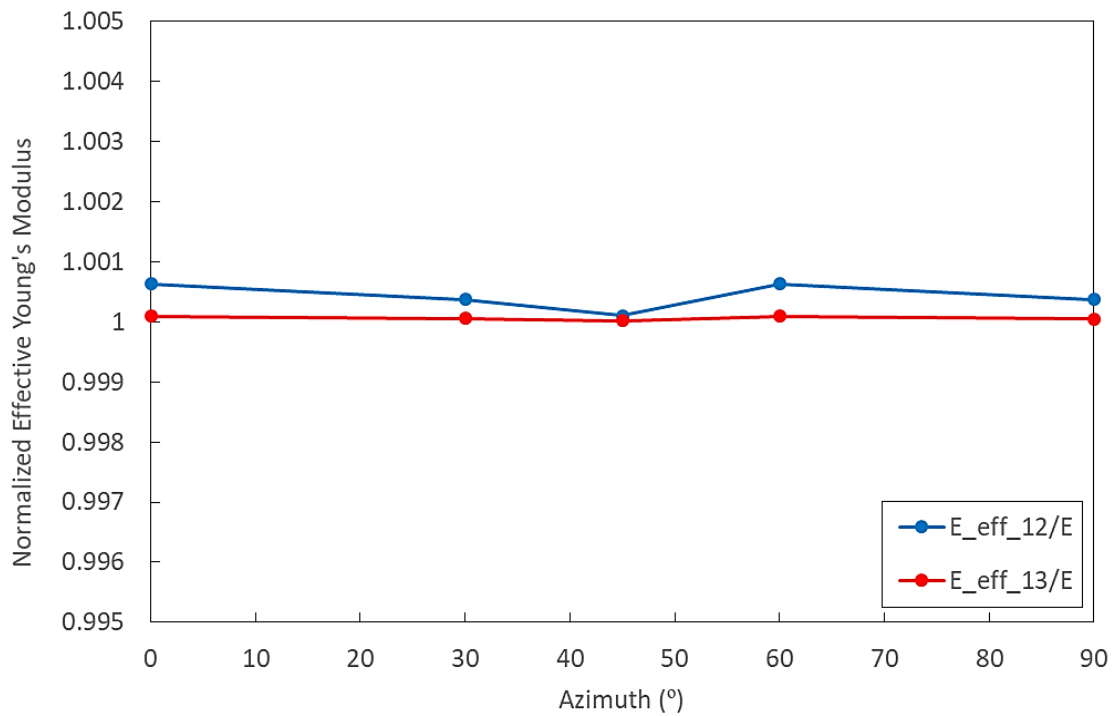
Figure 5.33. Effective Young's modulus evolution in I_2 and I_3 directions versus fracture azimuth
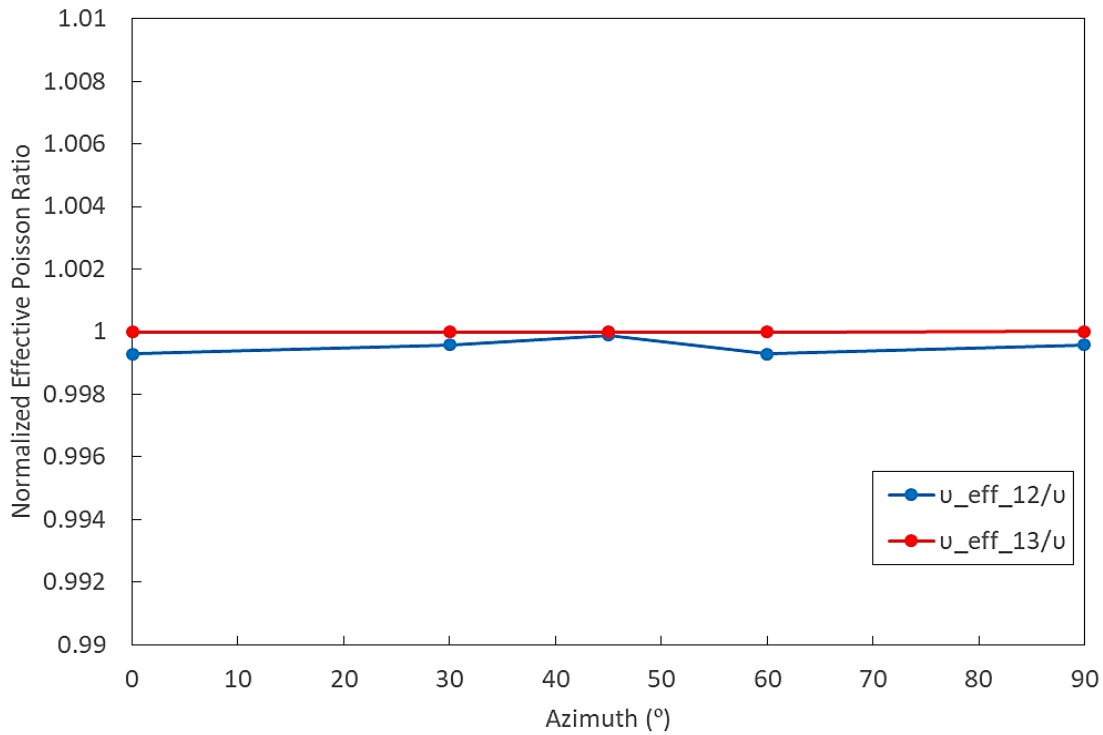
Figure 5.34. Evolution of effective Poisson's ratio in I_2 and I_3 directions versus fracture azimuth

Looking at figures 3.33 and 3.34 reveals that the elastic moduli deviation from the assigned values in I_3 direction is negligible compared to that in I_2 direction. On the other hand, the overall variation of the effective elastic moduli in these tests is not significant.

Based on the conducted sensitivity analysis, it is observed that the fracture characterized as table 5.16 has a negligible influence on the effective elastic moduli of the rock mass regardless of its dip and orientation. In addition to the fracture's dip and orientation, the normal and shear stiffnesses of the fracture may also affect the effective elastic moduli of the fractured rock mass, but this effect has not been investigated in the present work.

5.3.6 Stress-Dependent Fracture Stiffness

In subsection 5.3.5, we assumed that the fracture's normal and shear stiffnesses are constant or independent of applied stress. But, many authors such as Kulhawy, 1975, Goodman, 1976, and Bandis et al., 1983, reported non-linear variation of fracture stiffness depending on the applied normal stress, as explained in subsubsection 5.3.2. Here, we tried to use 3DEC so as to assign non-linear stiffness to the fractures based on equations 5.47 to 5.49. For that, an iterative process is defined based on which the normal and shear stiffnesses of each zone on fracture surface for timestep Δt_i are obtained by replacing local normal and shear stresses on each zone of fracture surface of timestep Δt_{i-1} in equations 5.47 to 5.49. Therefore and benefiting from equation 3.96 to 3.99, the normal and shear stress values for timestep Δt_i were calculated to be used for calculation of normal and shear stiffness for timestep Δt_{i+1} and so on. In equation form and at the timestep Δt_i, for mismatched joint case we have

$$k_n^i = k_{ni} \left[1 - \frac{\sigma_n^{i-1}}{V_m k_{ni} + \sigma_n^{i-1}} \right]^{-2} \quad (5.115)$$

$$\Delta F_n^{i+1} = -k_n^i \Delta U_n^i A_c \quad (5.116)$$

$$F_n^{i+1} = F_n^i + \Delta F_n^{i+1} \quad (5.117)$$

V_m in equation 5.115 is the difference between initial and residual hydraulic aperture. n_j, and R_f data of Soultz granite were not available, therefore in current work those data of dolerite, reported in Bandis et al., 1983, were used instead. k_j is also assumed to be as equal as initial shear stiffness. q parameter in equation 5.48, which is called "stiffness characteristics" (Evans et al., 1992; Zangerl et al., 2008), determined by Zangerl et al., 2008, by compilation of 115 normal closure experiments carried out on natural and artificial fractures in granites. They found "stiffness characteristics" spanning from 720 mm^{-1} for well-mated fractures in the laboratory to 3 mm^{-1} for an in-situ test on an induced or reactivated hydro-fracture isolated in a borehole. This parameter is the slope of logarithm of normal stress versus fracture closure curve for mismatched joints as shown in figure 5.35. According to the compilation of the stiffness characteristic for first loading path of natural fractures in granitic samples summarized in Zangerl et al., 2008, q ranges from 5-244 mm^{-1}, with the majority between 20 and 30 mm^{-1} and the mean of about 88 mm^{-1} (figure 5.36). In the current simulation, we used the mean stiffness characteristic of 88 mm^{-1}. The model geometry and mechanical parameters are summarized in table 3.17.

Table 5.25. Index properties and sampling locations of the samples (Bandis et al., 1983)

Rock materials	Tensile strength σ_t (MPa)	Compressive strength σ_c (MPa)	Young's modulus E_{t50} (GPa)	Unit weight γ(KN/m³)
Slate (Ordovician from Skiddaw Slates—Quarry nr Keswick, Lake District)	14.9	159.0	66.0	27.7
Dolerite (Permo-Carboniferous —natural exposure at Horwick Crags, Teesdale)	17.3	165.0	78.0	29.0
Limestone (Lower Carboniferous —natural exposure, N. Yorks)	10.6	152.0	49.0	27.3
Siltstone (Upper Coal Measures —NCB pit, W. Yorks)	6.3	84.0	28.5	24.2
Sandstone (Lower Coal Measures —Shibden Dale Quarry, W. Yorks)	5.1	78.0	24.0	24.1
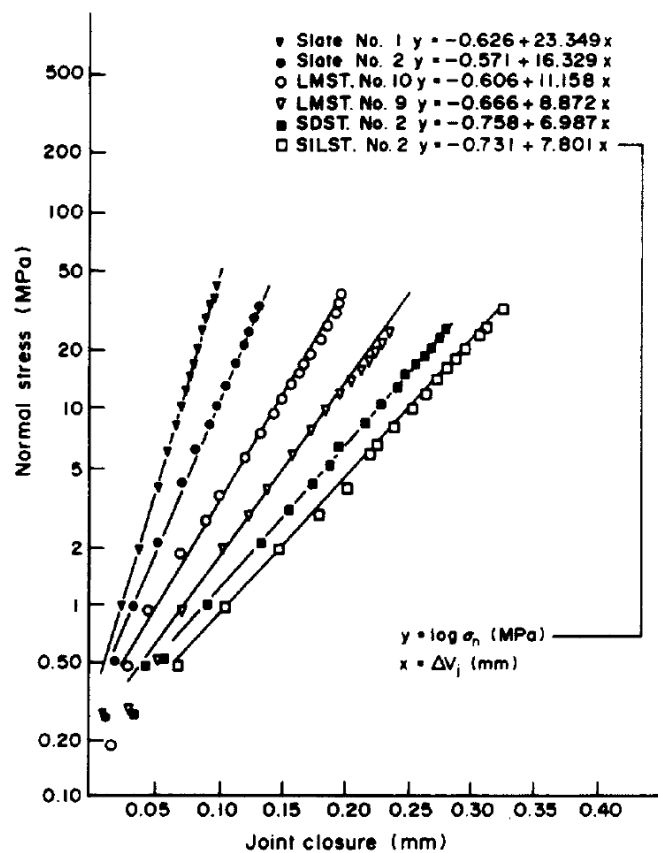
Figure 5.35. Semi-log plots of normal stress versus fracture closure of mismatched joints (Bandis et al., 1983)

182

Table 5.26. Mechanical and physical properties of the model

Parameter	value
Block Height (m)	2
Block Length (m)	1
Block width (m)	1
E (GPa)	40
ν	0.1
Density (kg/m^3)	2680
Fracture Diameter (m)	0.5
Fracture Dip (°)	45
Fracture Dip Direction (°)	90
k_{ni} (GPa/m)	80
k_{si} (GPa/m)	20
Friction Angle (°)	39.0
Cohesive Strength (MPa)	6.5
Initial Hydraulic Aperture (m)	14e-05
Residual Hydraulic Aperture (m)	7.0e-05
Maximum Hydraulic Aperture (m)	12e-03
V_m (m)	7e-05
k_j (MPa/mm)	20
n_j (MPa^2/mm)	0.615
R_f	0.652
q (1/mm)	88

Figure 5.37 shows the model and embedded circular finite fracture. Displacement of the area outside of the circular fracture plane was restricted.
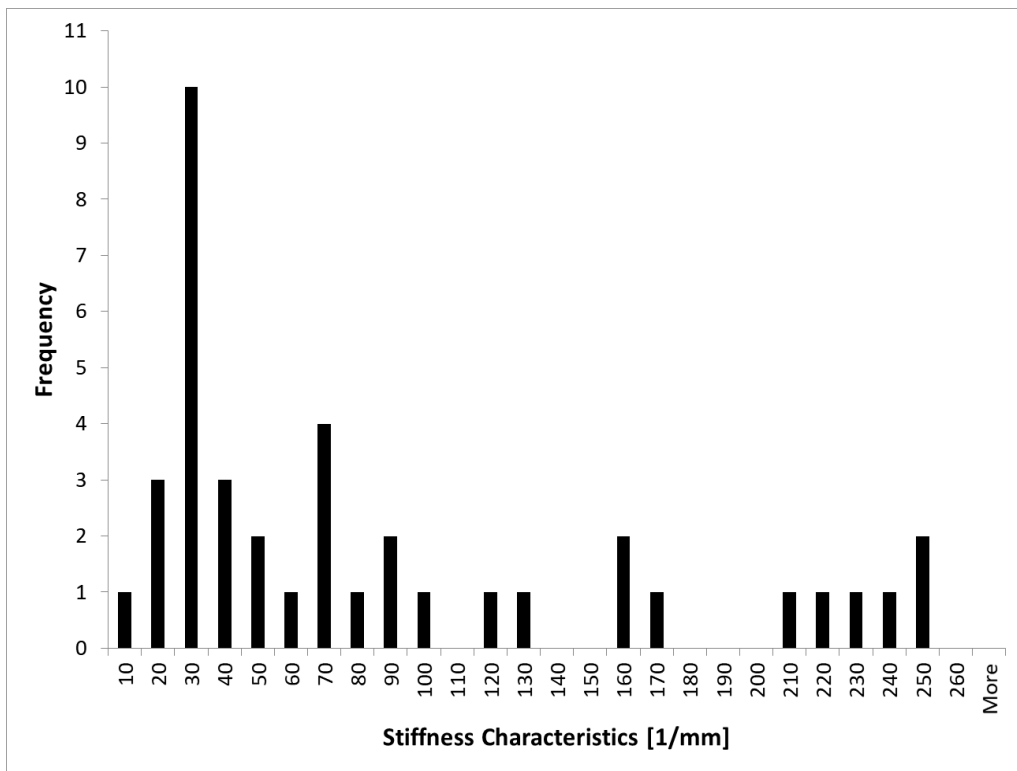
Figure 5.36. Histogram of stiffness characteristic values (for natural fractures in granite) based on Zangerl at al., 2008
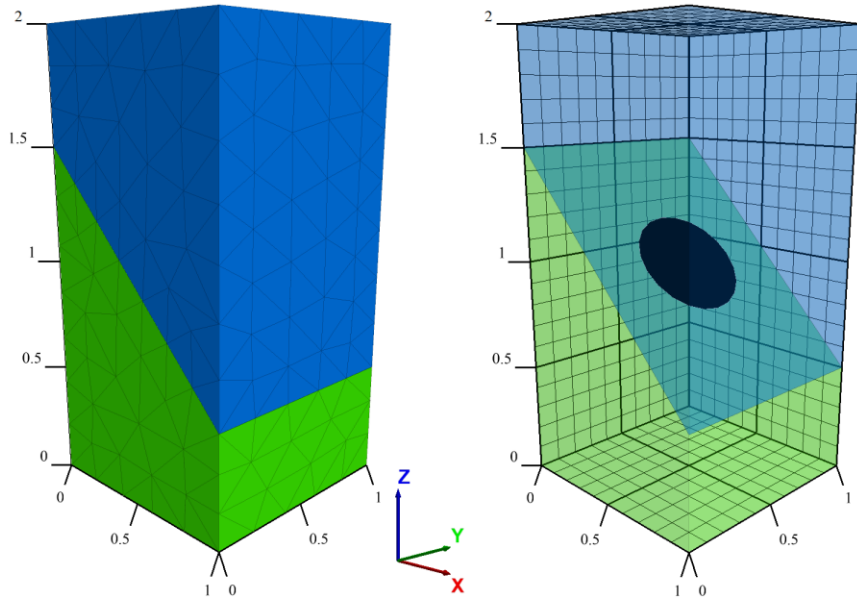
Figure 5.37. Parallelepiped block (1x1x2 m^3) with embedded circular finite fracture (black circular surface with diameter of 0.5 m)

Applying loads to intact rock or fractured rock mass specimens in the laboratory experiments are mainly carried out by two mechanisms of strain (displacement) and stress (load) controlled methods (Alshkane et al., 2017) among other existing alternative methods (e.g., Pan et al., 2006; Shimizu et al., 2010). In the current study, we used a strain-controlled loading mechanism considering the fact that in 3DEC/UDEC

184

applying a displacement (*d*) boundary condition is only possible by defining velocity (*V*) boundary condition for a time (*t*) increment (*V=d/t*) (Itasca, 2016). To avoid detrimental inertial shocks to the model it is essential to keep the loading velocity small or to increase the loading velocity slowly (Alshkane et al., 2017). But, keeping loading velocity small will cause time-consuming numerical computations. To overcome this problem, a FISH (programming language used by Itasca numerical tools) algorithm is provided by Itasca (Itasca, 2016) to impose strain-controlled loading boundary conditions. This servo-control mechanism adjusts loading velocity based on the value of "maximum unbalanced force" in order to avoid internal shock. So, the FISH algorithm of Itasca was used to apply a downward constant normal velocity of 1e-04 m/s for 100 numerical steps and stop loading to check the total vertical displacement on top of the model reached the assigned displacement limit. In consequence, a vertical compressive stress applied to the top of the block shown in figure 5.37. Verification tests stopped when the axial displacement at the top of the block reached 5e-4 m (half of a millimeter). At each loading step, the average values of shear and normal stresses acting on the fracture plane were iteratively extracted and the associated values of k_n and k_s were calculated based on equations 5.47 or 5.48 and 5.49. These new stiffness values were then assigned to the fracture for the next loading step so as to obtain normal and shear displacements of the fracture using equations 5.109 and 5.110. The results were then compared to the analytical displacement magnitudes obtained as

$$d\delta_n = \frac{\sigma_n V_m}{k_{ni} V_m + \sigma_n} \quad (5.117)$$

$$d\delta_n = (log(\sigma_n) - p)/q \quad (5.118)$$

$$d\delta_s = \frac{\tau}{k_{si}(1 - (\tau/\tau_{ult}))} \quad (5.119)$$

for, respectively, normal displacement in interlocked joints, normal displacement in mismatched joints, and shear displacement. *p* in equation 5.118 is antilog of initial normal stress which was equal to 0.15 MPa in Bandis et al., 1983. This *p* value is in fact the normal stress after which Bandis et al., 1983, have characterized the mismatched joint stiffness. In the current study we assumed that fracture stiffness for the normal stress ranging from zero to *p* were equal to initial value of normal stiffness (k_{ni}) as is observed in figure 5.39. Figures 5.38 and 5.39 are comparisons between analytical and numerical variation of normal displacement in terms of normal stress for interlocked and mismatched joints, respectively. Figure 5.40 is variation of shear displacement in terms of shear stress acting on the fracture plane. As it can be seen from the figures, there is a good agreement between the results of numerical and analytical calculations, however the numerical shear displacement for a given shear stress shows a small deviation from analytical results which might be caused by the fact that τ_{ult} in equation 5.112 is a parameter which depends on the condition of the sample under direct shear test that has not reached residual shear strength (which needs more displacement). On the other hand, ultimate shear strength is more than residual shear strength but less than peak shear strength and is unique in each test depending on the situation of the test and sample (Barton, personal communication). Here, we assumed τ_{ult} to be equal with multiplication of static friction coefficient to the normal stress.
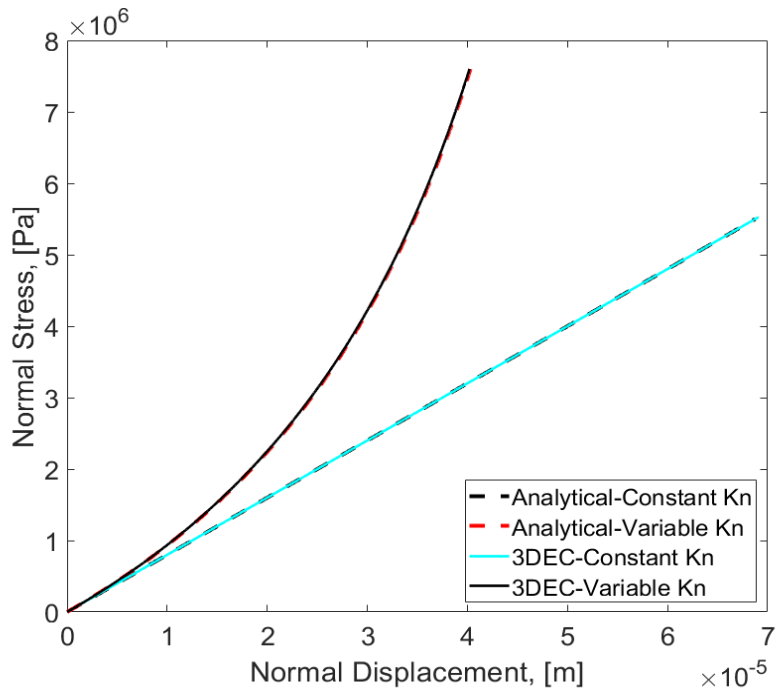
Figure 5.38. Fracture normal stress versus normal displacement for interlocked joint type
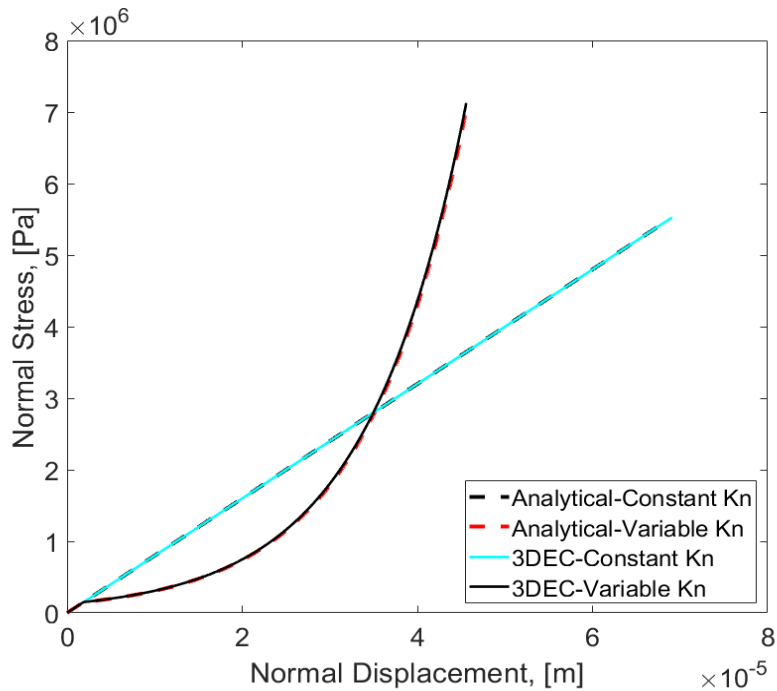
Figure 5.39. Fracture normal stress versus normal displacement for mismatched joint type
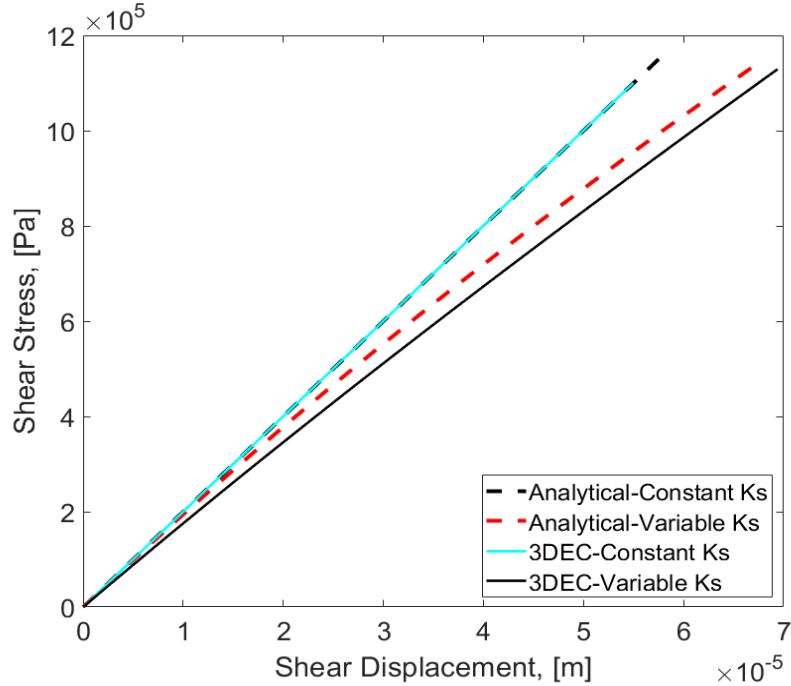
Figure 5.40. Fracture shear stress versus shear displacement

The developed code was then slightly reformed by using normal and shear stress values of tetrahedral zones in equations 5.47 or 5.48 and 5.49 instead of average values of them acting on the fracture plane. This reformed code was then applied to a DFN containing two fractures to qualitatively validate it for the cases where a set of fractures are embedded in the model. For that, a block of 100x100x100 m^3 hosting two circular finite size fractures was created and underwent the same loading mechanism as that used above for a single fracture model. The block and embedded two fractures are shown in figure 5.41. The fractures are F1 and F2 on which the evolution of normal and shear stiffness versus normal stress were investigated. The results are illustrated in figures 5.42 to 5.43, where, qualitatively, it can be seen that the stress-dependent fracture stiffnesses are deviated from their constant counterparts; representing non-linear stress-dependent fracture stiffness as described by Bandis et la., 1983.
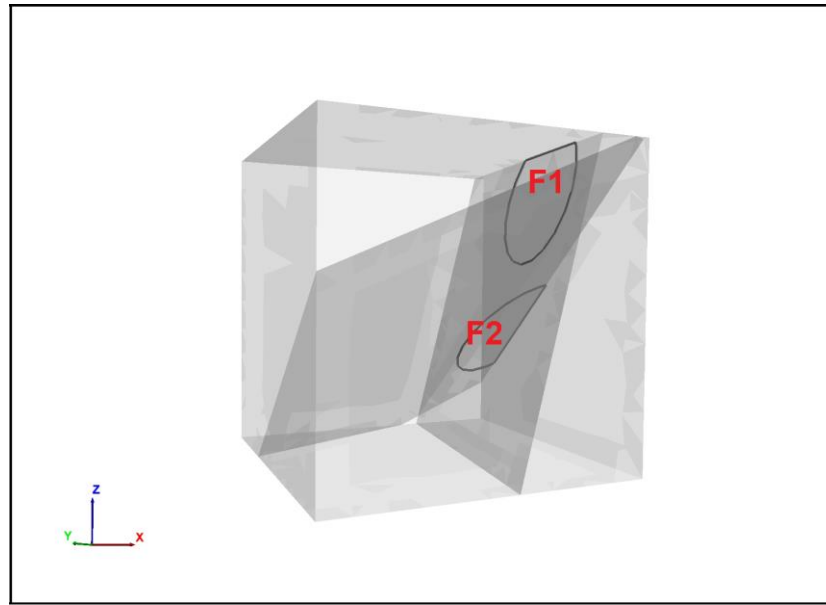
Figure 5.41. Schematic 3-D view of 100x100x100 m³ block and two finite size fractures (F1 and F2)
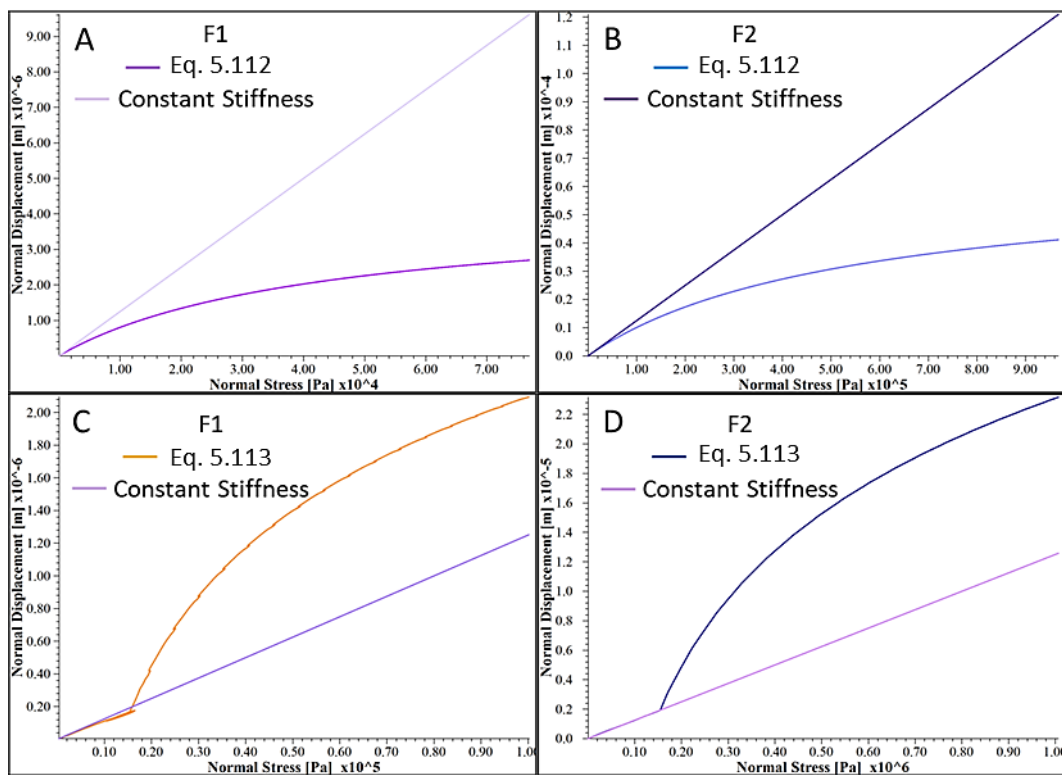
Figure 5.42. Comparison of F1 and F2 fractures' normal displacement versus normal stress for constant and stress-dependent fracture stiffness parameter (Eq. 5.112 to 5.113); interlocked joints (A and B), mismatched joints (C and D)

188
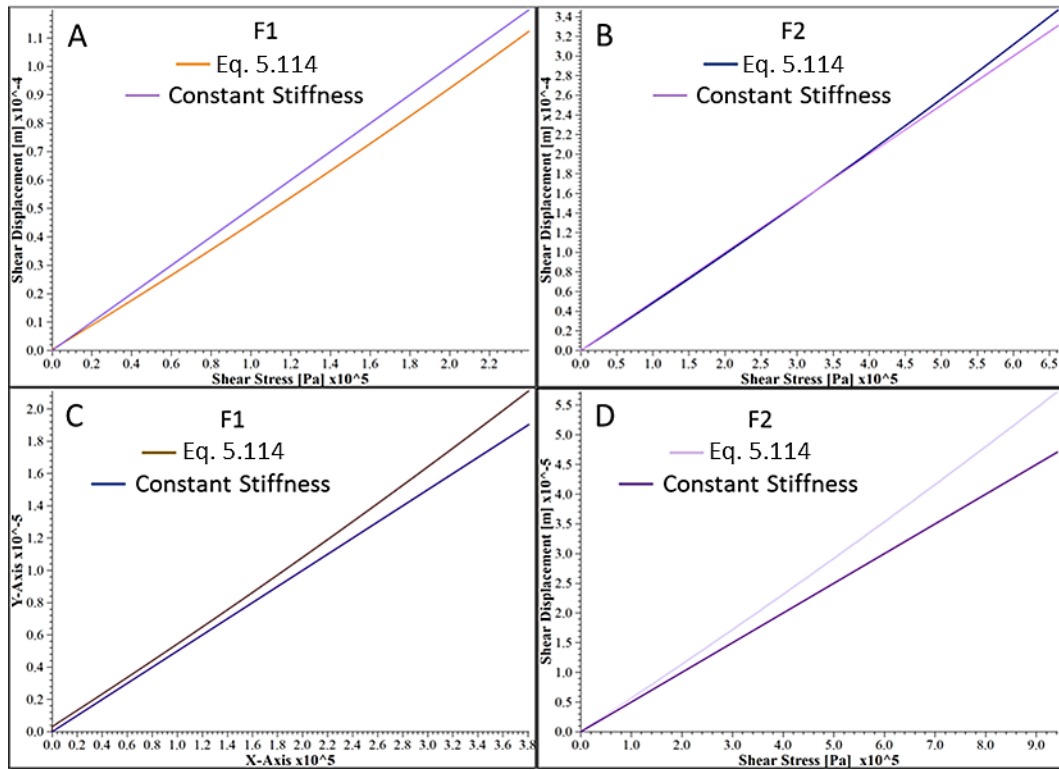
Figure 5.43. Comparison of F1 and F2 fractures' shear displacement versus shear stress for constant and stress-dependent fracture stiffness parameter (Eq. 5.114); interlocked joints (A and B), mismatched joints (C and D)

5.3.7 Effective Elastic Moduli of the Fractured Rock Mass

Here, the DFN example generated in section 5.2.1 was embedded in the intact, homogeneous, isotropic rock block of 100x100x100 m³ in order to simulate fractured rock mass block of Soultz-sous-Forêts. 4500 fractures generated by the numerical DFN example cut intact rock into small blocks of deformable materials with E and v of 40 GPa (Villeneuve et al., 2018) and 0.1 (Sausse, 2002). Importing such DFN (shown in figure 5.44) into the intact rock block of 100x100x100 m³ creates a fractured rock mass such as figure 5.45.
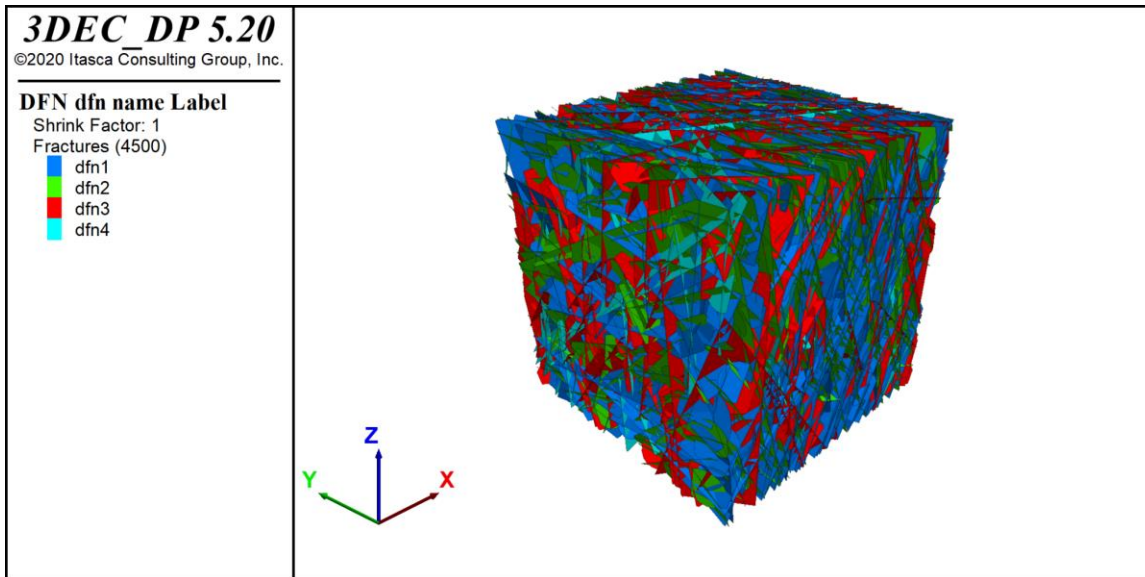
Figure 5.44. Numerical DFN example composed of 4500 fractures with diameters ranging from 10 to 3000 m
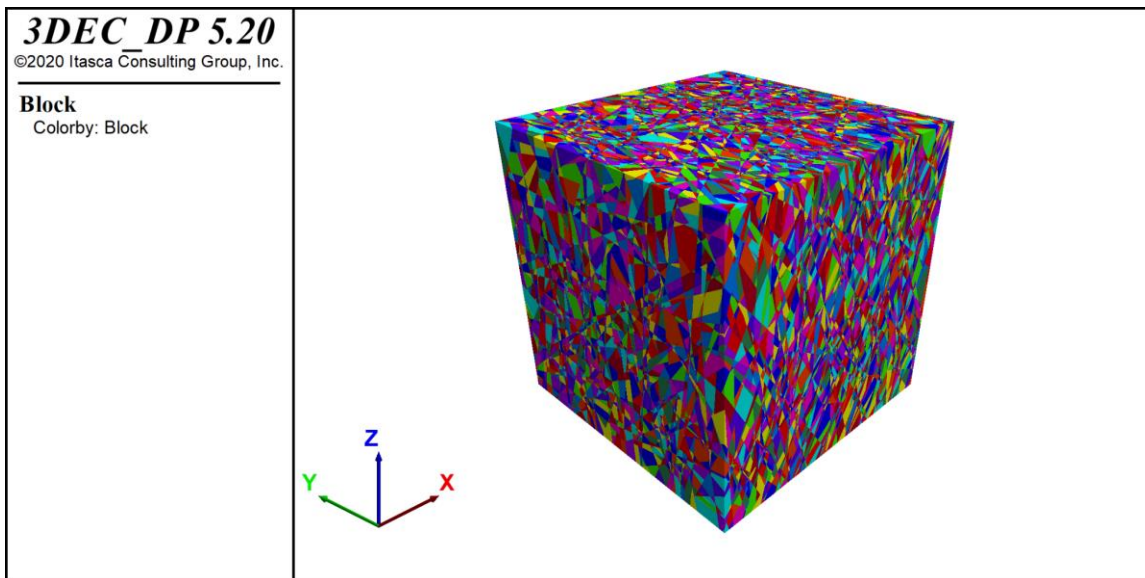
Figure 5.45. Rock block with side size of 100x100x100 m^3 fractured with numerical DFN example shown in figure 5.44

Three models of fractured rock mass were created by assigning constant (case 1), mismatched (case 2), and interlocked (case 3) fracture stiffnesses to the fractures of the DFN in models. The boundaries of models (except the bottom of the block that was set to be fixed in the Z-direction at all simulations) were subjected to three stress levels of 1) 10%, 2) 50%, and 3) 100% of in-situ stress state derived from Soultz-sous-Forêts geothermal reservoir at a depth of 4.7 km. The applied in-situ stress field was computed based on equations in Cornet et al., 2007, where orientation of maximum horizontal stress was stated 170±10°, but here we assumed that it is 180°; thus, the applied stresses in X-, Y-, and Z-directions could be considered as principal stresses of, respectively, S_3, S_2, and S_1. In other words, the principal stress frame of reference is aligned with the Cartesian frame of reference. After reaching an equilibrium at each stress level (initial state), four stress perturbation modes (secondary state) were applied to the models. In the three stress perturbation

190

modes, the models were subjected to initial stress state and then, respectively, 10%, 1% of the principal stress values, and a 1 MPa of isotropic stress values were applied to the boundaries of the cubic block. The fourth perturbation mode was a 1 MPa of isotropic stress values applied to the initial state of the models which were first subjected to the isotropic stresses equal to the S_1 at each stress level. These modes are summarized in table 5.27.

Table 5.27. Summary of simulation scenarios

Stress Level	Fracture Stiffness	Initial Loading	Stress Perturbation Mode
1) 10% of in-situ stress field at 4.7 km	a) Constant stiffness	In-situ stress field	1) 10% of in-situ stress field
2) 50% of in-situ stress field at 4.7 km	b) Stress dependent Stiffness (Interlocked Joints)	In-situ stress field	2) 1% of in-situ stress field
		In-situ stress field	3) 1 MPa of isotropic triaxial stress
3) 100% of in-situ stress field at 4.7 km	c) Stress dependent Stiffness (Mismatched Joints)	Isotropic triaxial S_1	4) 1 MPa of isotropic triaxial stress

By convergence of each loading step (both initial and secondary loadings) the average values of stress and strain components over zones of the blocks were measured. Subtraction of secondary state components from those of the initial state were utilized to obtain effective values of Young's modulus and Poisson ratio for each simulation. In this study, it was aimed to estimate effective elastic moduli of homogenized fractured rock mass in order to evaluate P-wave velocity variation in the fractured medium of interest. Therefore, a grid search algorithm was developed to compute optimum values of elastic moduli for which the difference between components of the resulting and the computed stress tensors were minimum. In other words, the least-square method was defined as equation (5.120) aiming to minimize the sum of squared residuals.

$$F = \sum(\sigma_{ij}^{comp} - \sigma_{ij}^{num})^2, \quad i,j = 1,2,3 \quad (5.120)$$

The six components of the computed stress tensor were obtained by substituting of numerical strain tensor components on Hooke's law equation introduced for isotropic material subjected to polyaxial loading (equations 5.114-5.116) and doing grid search on Lame's coefficients (λ and G) so as to find the Optimum λ and G for which the computed stress component was closest to the numerically obtained stress. The range of λ and G was defined from zero to 20 GPa with 10000 steps between the minimum and the maximum at each axis of the grid. Optimum λ and G were then utilized to calculate the corresponding Young's modulus and Poisson ratio using equations 5.117 and 5.118.

$$\sigma_{ij} = (\lambda + 2G)\varepsilon_{ij}\delta_{ij} + \lambda\varepsilon_{ij}\delta_{ij} + \lambda\varepsilon_{ij}\delta_{ij} = \lambda\varepsilon_v + 2G\varepsilon_{ij}, \quad i,j = 1,2,3 \quad (5.121)$$

$$\sigma_{ij} = 2G\varepsilon_{ij}, \quad i,j = 1,2,3 \ \& \ i \neq j \quad (5.122)$$

$$\varepsilon_v = \sum \varepsilon_{ij}\delta_{ij} \quad , \qquad i,j = 1,2,3 \quad (5.123)$$

$$E = \frac{(3\lambda+2G)G}{\lambda+G} \quad (5.124)$$

$$v = \frac{\lambda}{2(\lambda+G)} \quad (5.125)$$

At which σ, ε, G, λ, ν, and E are, respectively, stress, strain, shear modulus, lambda, Poisson ratio, and Young's modulus. δ_{ij} is Kronecker delta that is zero when $i \neq j$ and is 1 when $i = j$. ε_v is volumetric strain.

Applying above mentioned loading scenarios on the generated fractured rock mass models encountered with a problem that is common in loading of fractured rock mass blocks using 3DEC. This problem stems from the volume of geomaterial surrounded by the fracture planes that, in some cases, are small such that their loading yields zero or negative volume and interrupts numerical computations.

To overcome this issue, the author tried some solutions offered by the Itasca CG such as eliminating the blocks having small volume in a given range (e.g., less than 1e-6 m³), but the efforts were unsuccessful in spite of investing an abundant amount of time. Therefore, the DFN built in section 5.1.1 was reformed so as to decrease the probability of zero/negative volume occurrence in the fractured rock block. For that, fracture density was decreased by one tenth of the density introduced in section 5.1.1 and distribution of orientation and position of fractures was changed to uniform distribution. Doing so, the resulting DFN (shown in figure 5.46) composed of 418 fractures with *a* exponent of 3.0, l_{min} and l_{max} of 10 and 3000 m, respectively. Embedding that DFN into the intact rock block of 100x100x100 m³ created the fractured rock mass block which is shown in figure 5.47.
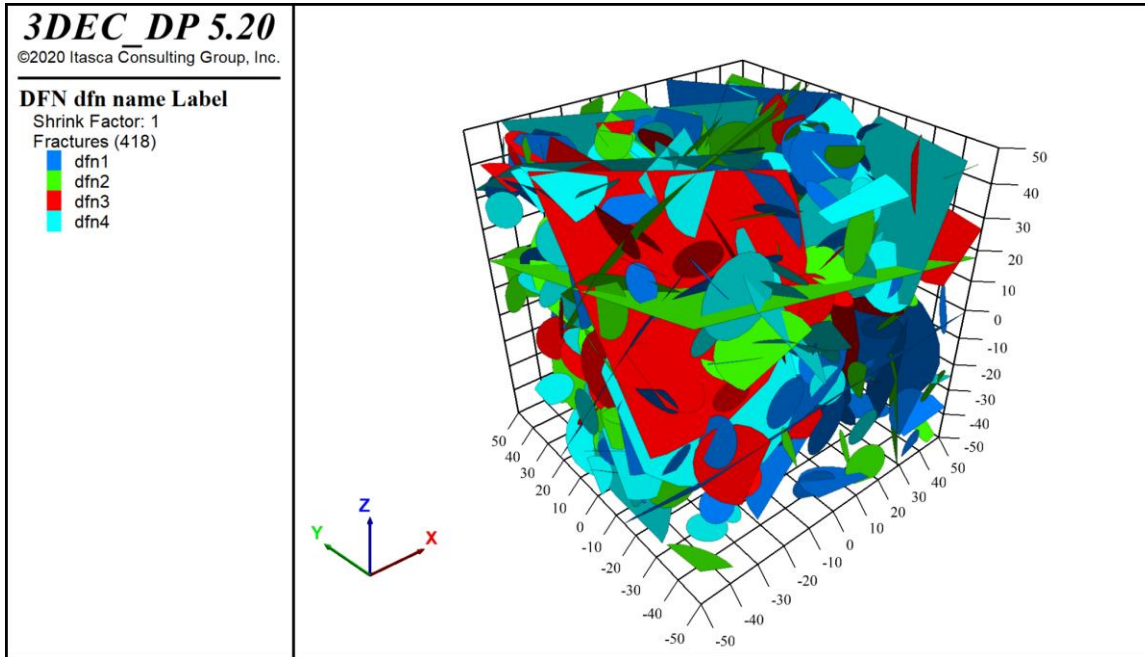

Figure 5.46. Fictitious DFN composed of 418 fractures with diameters ranging from 10 to 3000 m
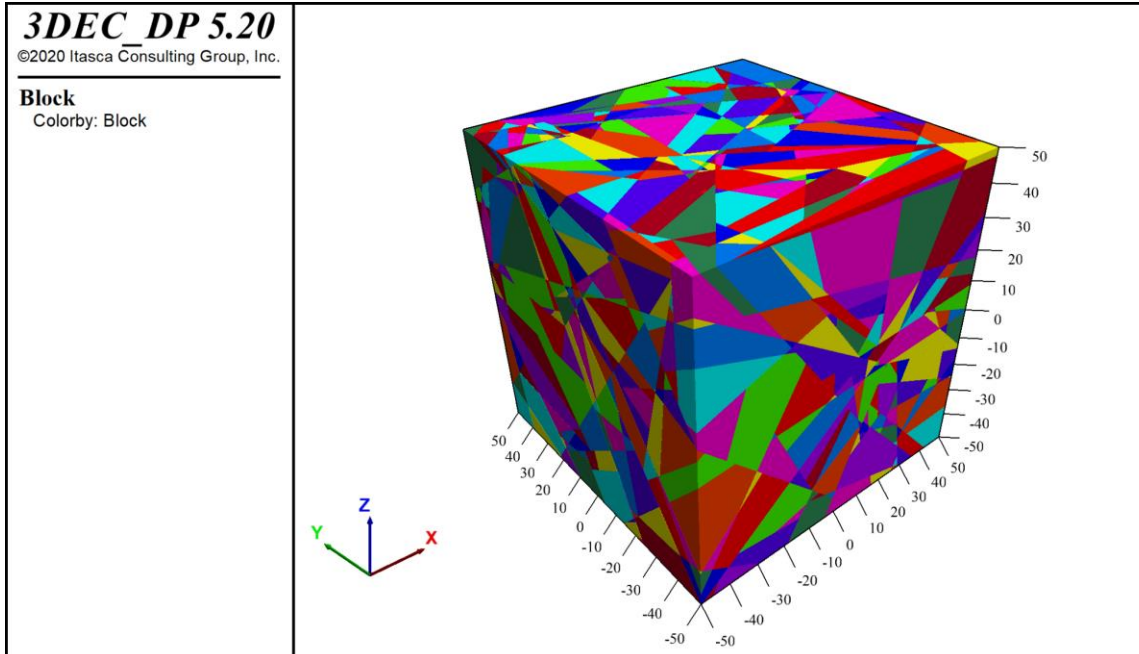
Figure 5.47. Rock block with side size of 100x100x100 m^3 fractured with fictitious DFN of figure 5.46

Constant, mismatched, and interlocked cases of fractured rock mass models were generated and the loading scenarios were applied and effective elastic moduli were estimated by using the previously explained grid search method. As an example, for the interlocked case of fractured rock mass at the third stress level undergoing the second stress perturbation mode, the effective Young's modulus and Poisson ratio of 39.91 GPa and 0.1 were obtained for which the least square value was 3.73e8. The resulting effective elastic moduli of the fractured rock were then normalized by intact rock's elastic moduli (E=40 GPa and ν=0.1). A total number of 72 simulations were carried out at this step, from which 36 effective values of Young's modulus and Poisson Ratio were derived as shown in figure 5.48.

It can be seen in the figures 5.48 that the effective elastic moduli of the fractured rock mass in most of the cases are not significantly different from those of the intact rock. It might be due to the fact that fracture density in the models were not high enough to change mechanical behavior of the fractured rock mass. Assuming that this expression about fracture density is valid and having a closer look at the graphs in figure 5.48, one may deduce that the results of the second stress perturbation mode are consistent in all stress levels.
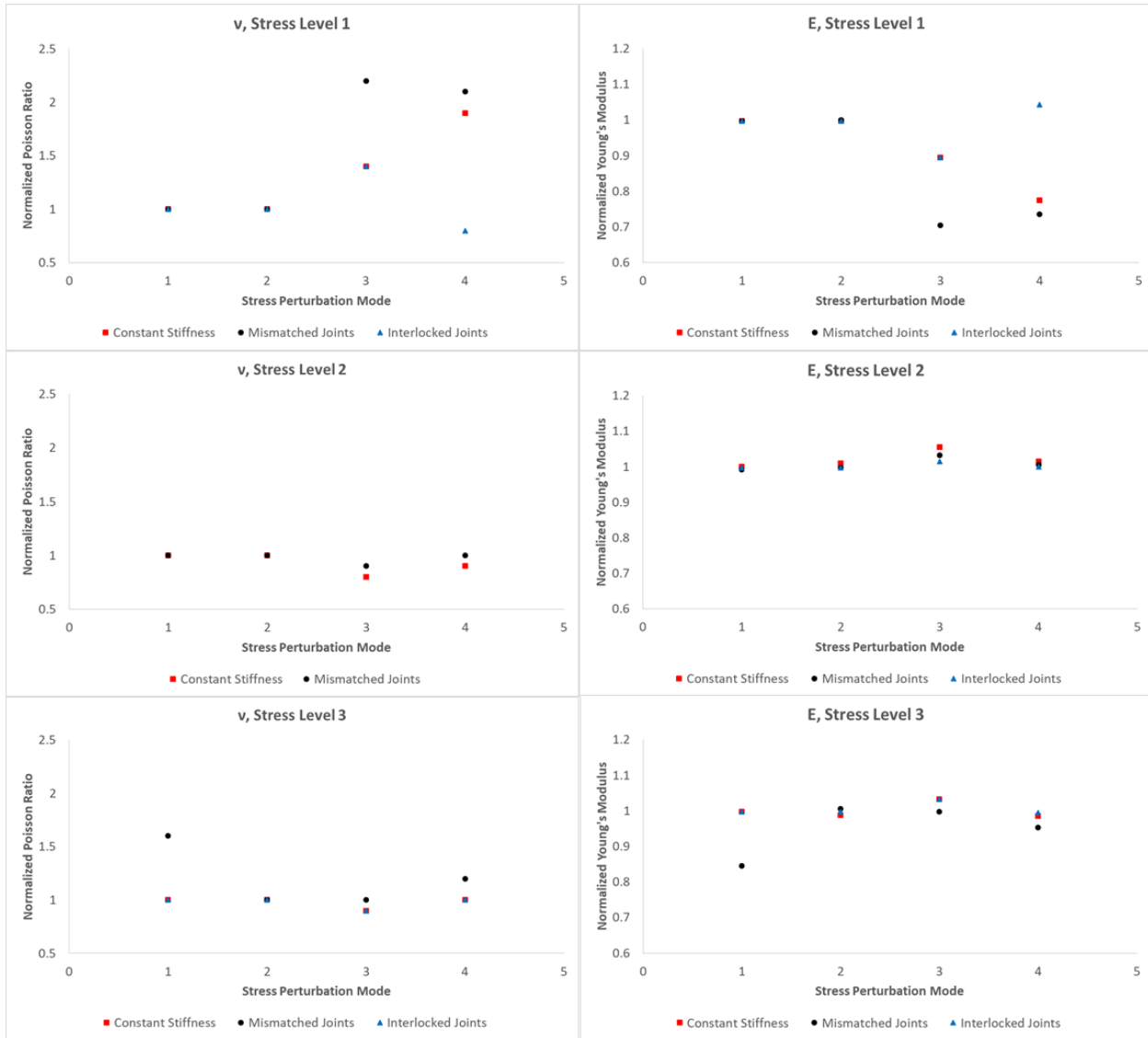
Figure 5.48. Normalized Poisson ratio and Young's modulus in three fractured models for four stress perturbation modes in three stress levels

Many authors (e.g., Walsh, 1965; Vakulenko and Kachanov, 1971; Salganik, 1973; Bruner, 1976; Hoenig, 1979; Gottesmann et al., 1980; Hudson, 1980 & 1981, 1986; Kachanov, 1980 & 1987; Henyey and Pomphery, 1982; Horii and Nemat-Naser, 1983; Case, 1984; Zimmerman, 1984 & 1985; Aboudi and Benveniste, 1987; Kachanov, 1993; Sayers and Kachanov, 1991 & 1995; Schoenberg and Sayers, 1995; Grechka and Kachanov, 2006; Gueguen and Kachanov, 2011) investigated influence of discontinuities and cracks on elastic moduli of materials. Zimmerman, 1985, and Jaeger et al., 2007, summarized most common methods of no-interaction, self-consistent, and differential scheme as below, respectively,

$$\frac{E_0}{E} = 1 + \frac{16(10-3\nu_0)(1-\nu_0^2)\alpha}{45(2-\nu_0)} \quad (5.126)$$

$$\frac{E}{E_0} = 1 - \frac{16}{9}\alpha \quad (5.127)$$

194

$$\frac{E}{E_0} = e^{-\frac{16}{9}\alpha} \qquad (5.128)$$

at which α is fracture density parameter computed as $\Sigma a^3/V$ where a is fracture radius and V is the volume of the specimen in the study. E_0 and v_0 are intact rock's Young's modulus and Poisson ratio, and E is effective moduli of rock mass.

In order to assess the influence of fracture density on the estimated effective elastic moduli, five more DFN samples consist of 50, 100, 200, 500, and 1000 fractures were embedded in the modeled intact rock block and were subjected to stress perturbation mode of 2; again in all three stress levels and by assigning all three fracture stiffness variations. The results were then compared to the outcomes of methods such as no-interaction (Walsh, 1965), self-consistent (Budiansky and O'Connell, 1976), differential scheme (Hashin, 1988) and finally the method introduced by Davy et al., 2018, as explained in section 5.3.2, where the equation (5.91) (effective medium theory) is used in combination with equation (5.80) solved for polyaxial loading mechanism to compute effective elastic moduli at the fractured rock mass. These comparisons are demonstrated in figures 5.49 to 5.51 for three stress levels. The X-axis of these graphs is fracture density defined as $\rho = Na^3/V$ in which N is the number of fractures in the DFN, a is the fracture radius, and V is the model volume being studied.
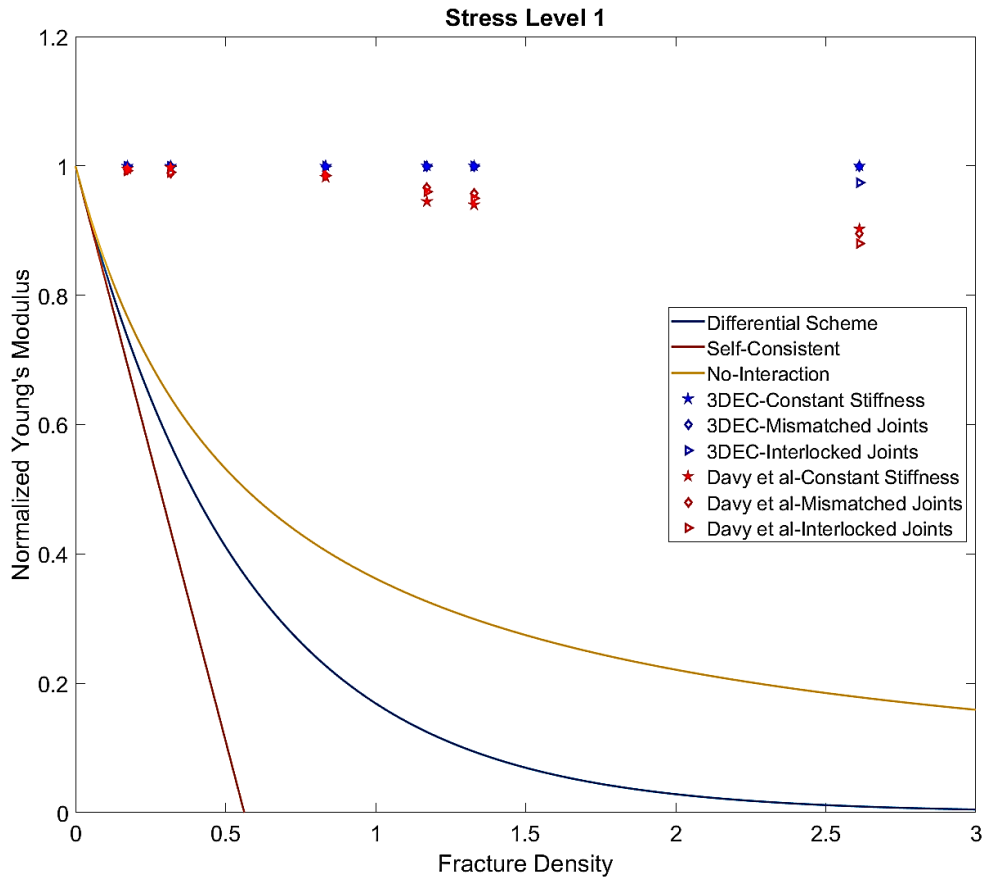
Figure 5.49. Comparison of the normalized Young's modulus obtained from 3DEC to those of no-interaction, differential scheme, self-consistent, and Davy et al., 2018 methods for three fractured models underwent the first stress level and the second stress perturbation mode

195
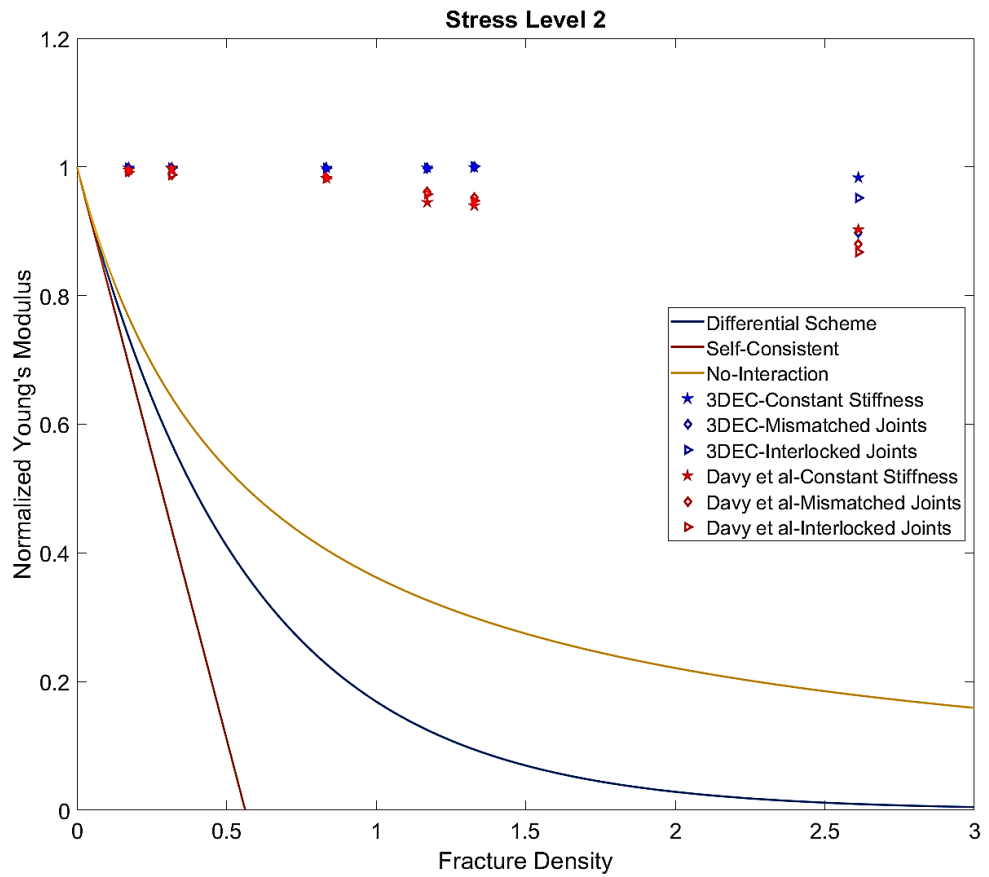
Figure 5.50. Comparison of the normalized Young's modulus obtained from 3DEC to those of no-interaction, differential scheme, self-consistent, and Davy et al., 2018 methods for three fractured models underwent the second stress level and the second stress perturbation mode
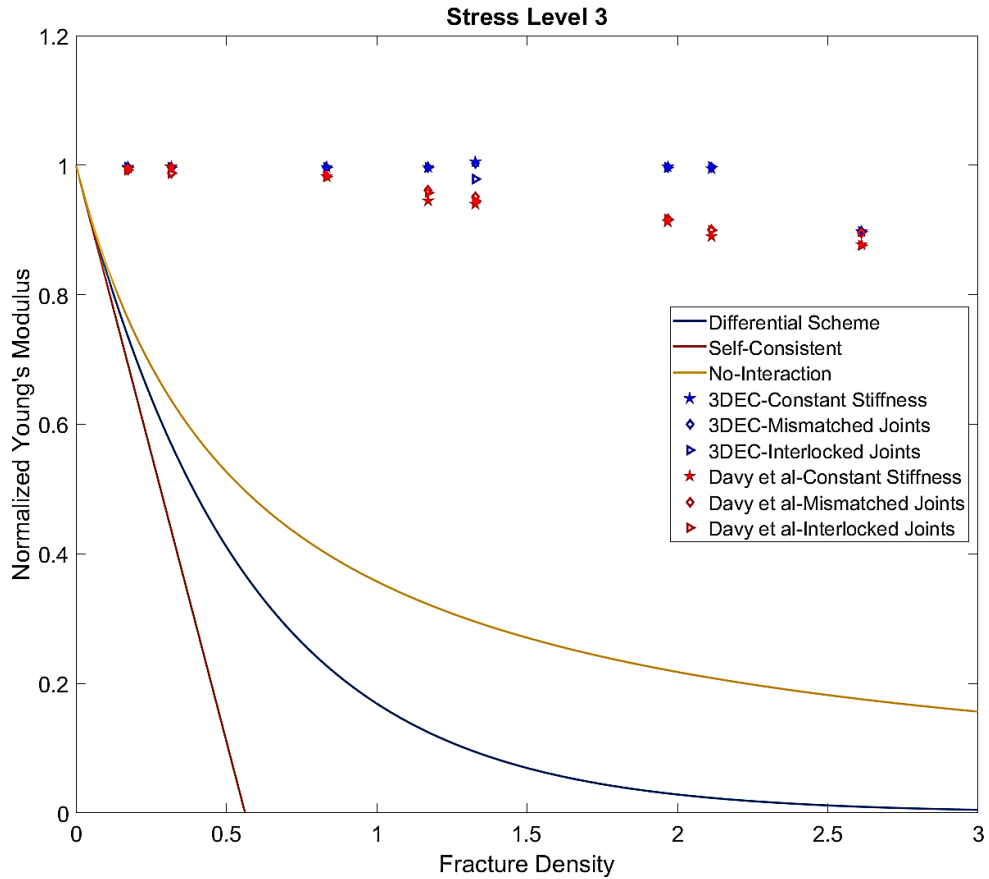
Figure 5.51. Comparison of the normalized Young's modulus obtained from 3DEC to those of no-interaction, differential scheme, self-consistent, and Davy et al., 2018 methods for three fractured models underwent the third stress level and the second stress perturbation mode

Three methods of differential scheme, self-consistent, and no-interaction are based on the stored elastic strain energy of Eshelby, 1957. The simplest approach to obtain energy perturbation in a fracture/void containing medium caused by confining/shear stress is to neglect fracture-fracture/ pore-pore interaction and calculate the effect of each fracture/pore as if it were an isolated fracture/pore in an infinite intact rock, and then sum up all these energy perturbations for all fractures/pores. This simplification causes significant divergence of results of three above mentioned from those of Davy et al., 2018, and 3DEC. Another drawback to the three aforementioned methods is their incapability to consider the stress perturbation generated by presence of the fracture/pore in the intact rock; which can evolve the direction and magnitude of the remote stress field in the vicinity of the fracture/pore (Darcel et al., 2021). I can also add another drawback to these methods as their incapability to take into account the remote stress field as well as fracture stiffness parameter; but only considering the crack density parameter.

As it can be seen from the figures 5.49 to 5.51, the Davy et al., 2018, results are closest to those of 3DEC. The reason is that this method considers the remote stress field, fracture's orientation relative to the applied remote stress field, and fracture stiffness parameters. But, the differences as shown in figures 5.52 to 5.54, may result from the fact that Davy et al., 2018, does not take into account the stress perturbation caused by

fractures and also fracture interactions; so that an early stage decrease as well as overestimated effective moduli can be seen in the graphs.
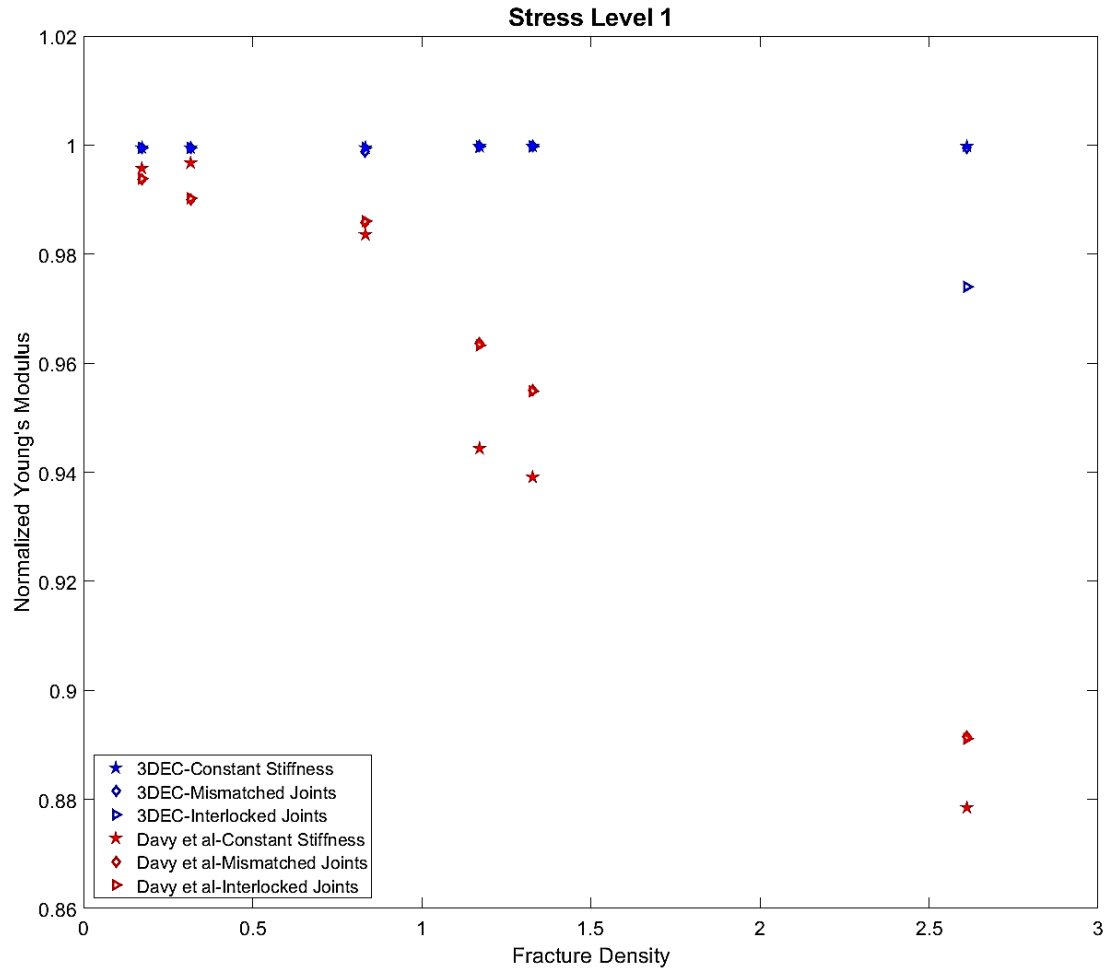
Figure 5.52. Evolution of the normalized numerical and analytical effective Young's modulus versus fracture density parameter in the three fractured models underwent the first stress level and the second stress perturbation mode
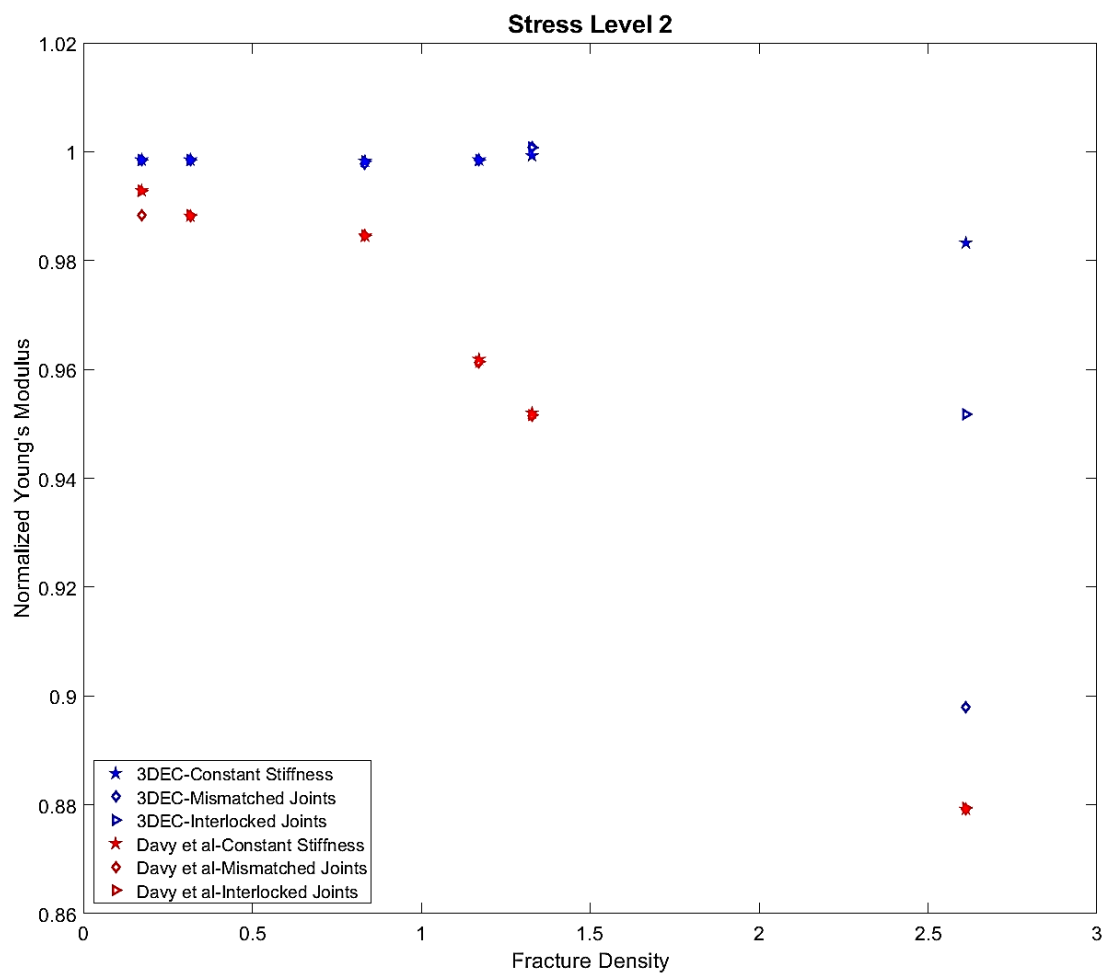
Figure 5.53. Evolution of the numerical to analytical ratio of effective Young's modulus versus fracture density parameter in the three fractured models underwent the second stress level and the second stress perturbation mode

199
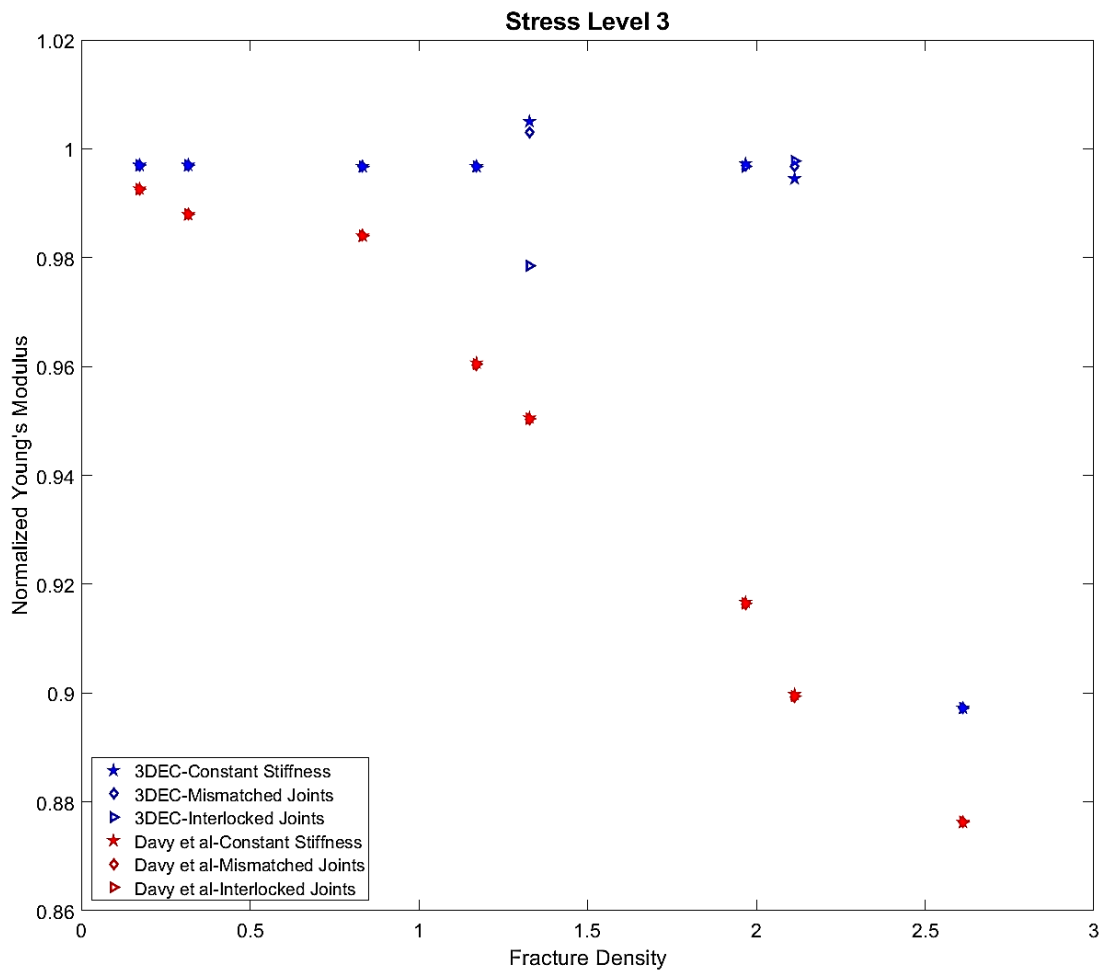
Figure 5.54. Evolution of the numerical to analytical ratio of effective Young's modulus versus fracture density parameter in the three fractured models underwent the third stress level and the second stress perturbation mode

It can also be seen from Figures 5.52 to 5.54 that at all three stress levels, the deviation from the moduli of elasticity of the intact rock in the 3DEC results occurred at a fracture density of 2.6. On the other hand, this deviation occurred at the first stress level only in the interlocked joints model, but in all three models (constant stiffness, mismatched joints, and interlocked joints) at the second and third stress levels.

In addition, at the third stress level, the rock mass hosting fractures, whose normal stiffness is characterized by the interlocked joints relation (equation 5.47), the effective elastic moduli of fractured rock deviates from that of intact rock at fracture density of 1.3. The effective moduli of the remaining two cases, i.e., rock masses containing fractures with constant and mismatched stiffness values, were then evaluated for two fracture density values between 1.3 and 2.6 to find the density at which the elastic modulus deviation occurs. It was observed that for fracture densities of approximately 1.9 and 2.2, there was no significant deviation in the effective moduli.

A closer look at the results of Davy et al. in Figures 5.52-54 also shows that as the stress level increases, the effect of stress-dependent fracture stiffness decreases, such that Davy et al.'s effective Young's modulus at stress levels 2 and 3 are almost superimposed, in contrast to stress level 1. This is only observed in the numerical results at stress level 3.

200

The Poisson ratio variations for the numerical fractured rock mass models were also compared to those obtained based on the analytical method of Davy et al., 2018. Figures 5.55 to 5.57 show the normalized Poisson ratio variation as a function of the fracture density parameter for stress levels of 1, 2, and 3, respectively. The deviation in the numerical Poisson ratio values of the fractured rock mass models only occurs at a fracture density parameter of 2.6, which is similar to the effective Young's modulus.
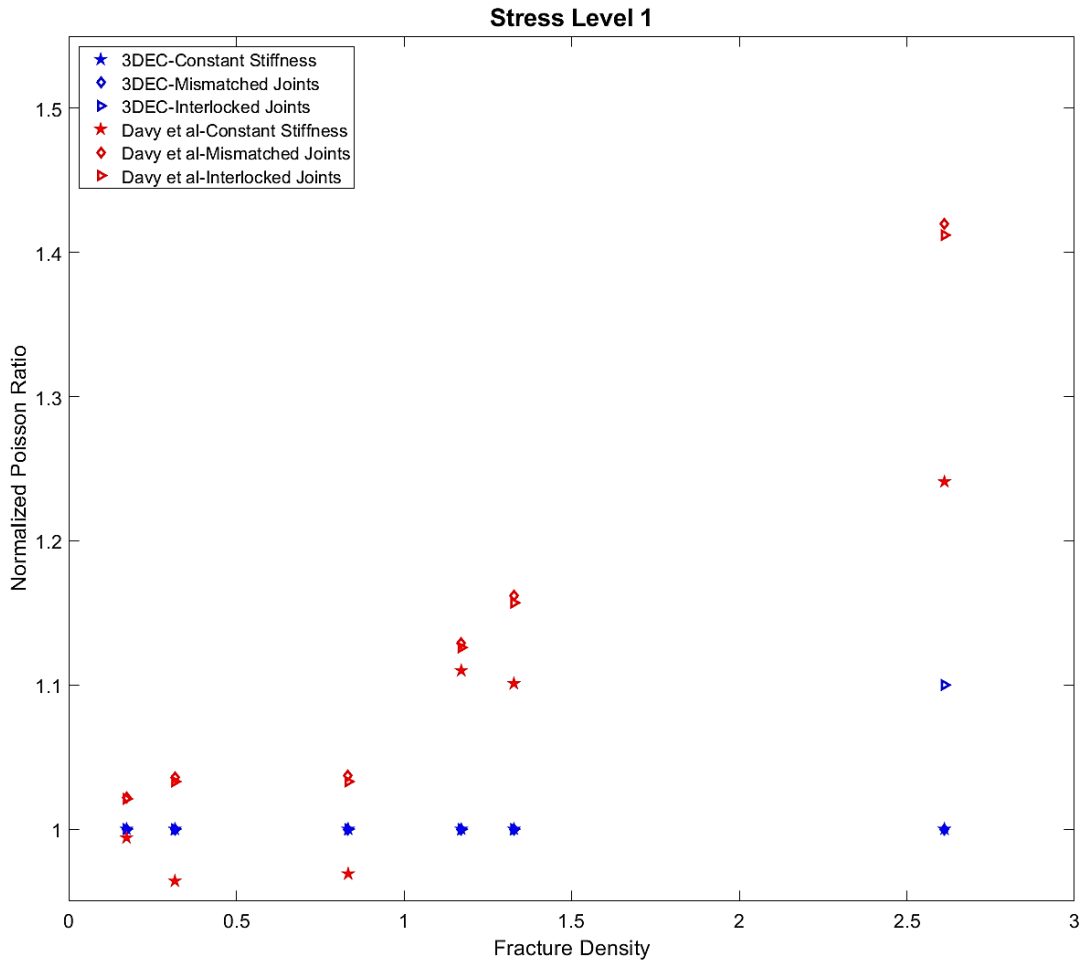
Figure 5.55. Evolution of the normalized numerical and analytical effective Poisson ratio versus fracture density parameter in the three fractured models underwent the first stress level and the second stress perturbation mode
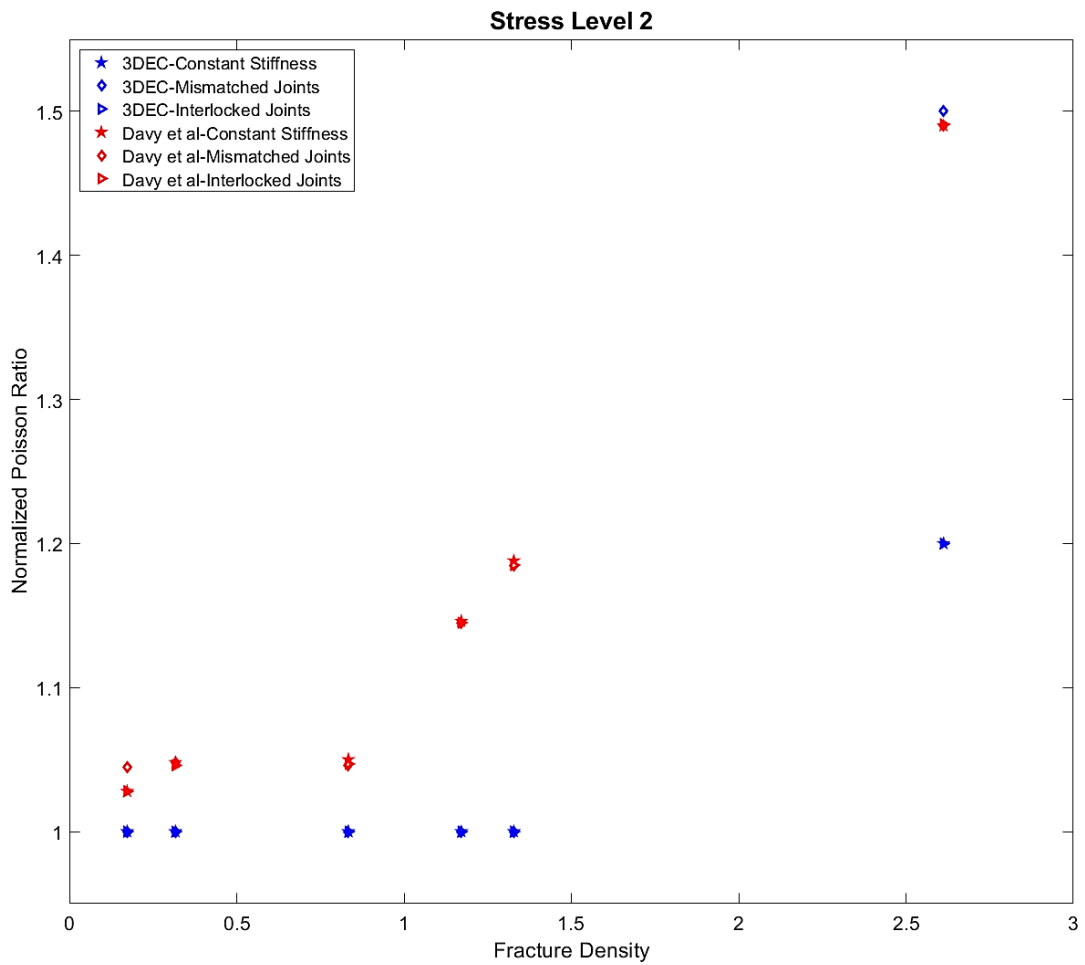
Figure 5.56. Evolution of the normalized numerical and analytical effective Poisson ratio versus fracture density parameter in the three fractured models underwent the second stress level and the second stress perturbation mode
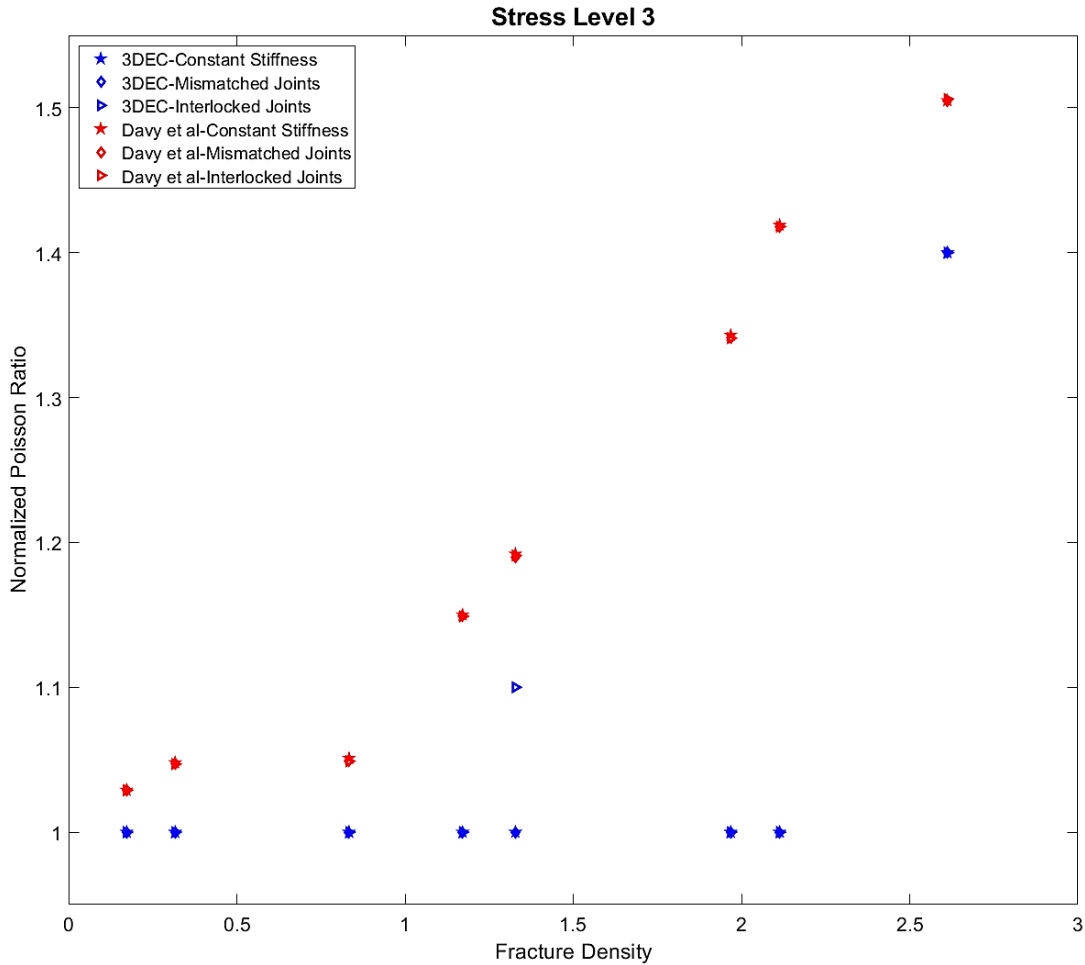
Stress Level 3

Figure 5.57. Evolution of the normalized numerical and analytical effective Poisson ratio versus fracture density parameter in the three fractured models underwent the third stress level and the second stress perturbation mode

5.3.8 P-wave Velocity Variation

As already stated, the objective of the present work was to characterize observed P-wave velocity variation in the fractured medium of Soultz-sous-Forêts when the stress-dependent fracture stiffness described by Bandis et al., 1983, were taken into account. Assuming that the rocks are at rest under in-situ stress state implies that the problems in rock mechanics are static. However, in some situations such as natural earthquakes or man-made seismicity, the generated stress perturbations are dynamic and their propagation has to be considered as waves (Jaeger et al, 2007). In such examples, dynamic theory of linear elasticity can be used to analyze the stresses and the resulting displacements; and the generated waves which are governed by the laws of linear elasticity and propagate through the medium, are known as seismic waves (Jaeger et al., 2007). Three types of waves are body waves, surface waves, and free oscillations (Stacey and Davis, 2008). The body waves are two kinds of compressional (P-wave) and shear (S-wave) (Stacey and Davis, 2008; Cornet, 2015). Seismic wave propagation depends on the mechanical characteristics of the medium through which they travel (Cornet, 2015). The velocity of this travel in an isotropic, homogeneous, and linearly elastic medium for P-waves are

$$V_P = \sqrt{\frac{E(1-\nu)}{(1+\nu)(1-2\nu)\rho}} \quad (5.129)$$

where ρ is the bulk density of the medium. Therefore, the elastic moduli of the medium (ν and E) are utilized to evaluate P-wave velocity in the medium of interest. These values for the generated synthetic fractured mediums of the current study, were previously estimated using the developed grid search algorithm in section 5.3.7 and were used here to evaluate P-wave velocity through the models. Bulk density of the intact rock was already opted from literature as 2680 kg/m³, but for the synthetic fractured media of this project bulk density varied depending on the fracture density. An approximate solution was deployed to estimate rock mass bulk density in which the total fracture surface per unit volume (often named p_{32}, Dershowitz and Herda, 1992) multiplied to the initial hydraulic aperture of fractures in order to approximately compute the void volume throughout the rock block. Figure 5.58 illustrates the ratio of void volume divided by bulk volume versus fracture density.
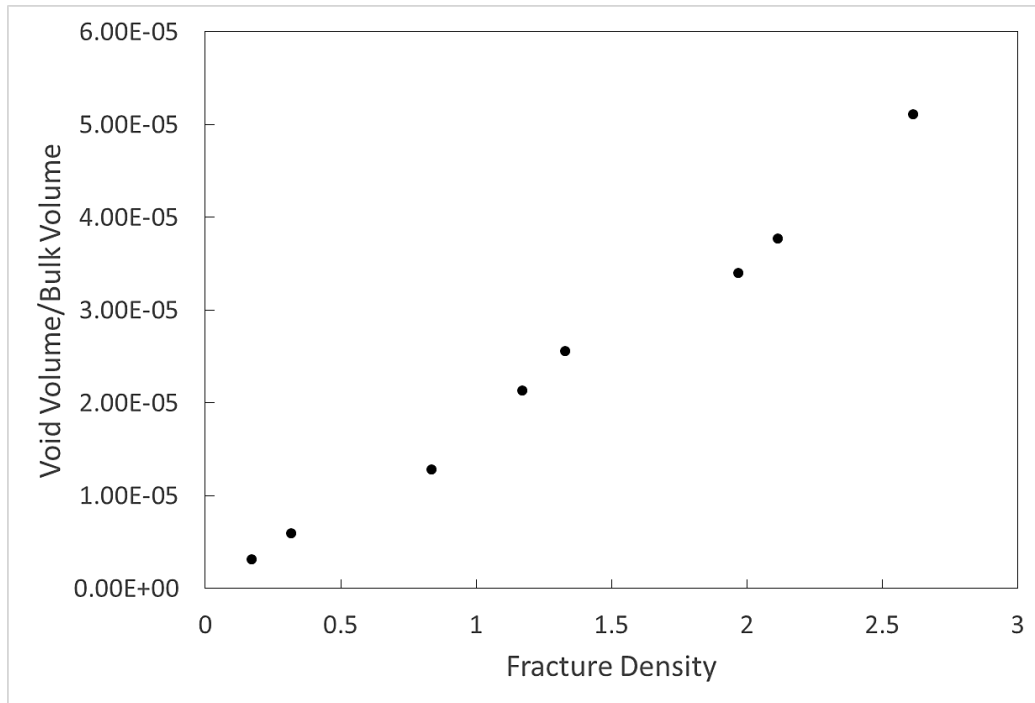
Figure 5.58. Evolution of the ratio of void volume to bulk volume versus fracture density

The void volume was then multiplied to the bulk density of the intact rock so as to obtain the mass corresponding to the computed void volume. This mass had to be subtracted from the total mass of the intact rock block (i.e., 2680*100³=2.68e9 kg) to obtain the solid mass of the block. The resulting mass was then divided by the block volume (i.e., 100x100x100 m³) to achieve the approximate bulk density of the fractured rock mass (figure 5.59).
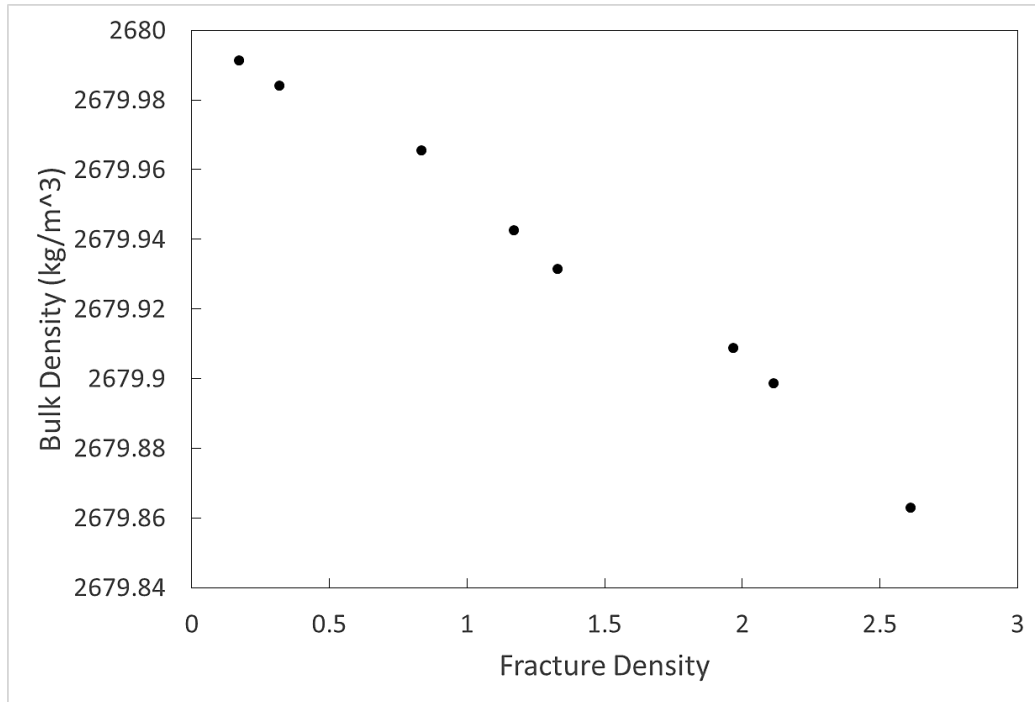
Figure 5.59. Evolution of the bulk density versus fracture density

This density was substituted in equation 5.128 to evaluate P-wave velocity in the fractured medium. By replacing the elastic moduli of the intact rock and its bulk density in equation 5.129, P-wave velocity in the intact rock yielded 3.9 km/s. This velocity is by far slower than that measured at Soultz-sous-Forêts fractured reservoir with approximately 5.5-5.8 km/s according to the literature (Place et al., 2010; Calo et al., 2011; Cornet, 2012; Calo and Dorbath, 2013; Cauchie et al., 2020). Worth to note the difference between static and dynamic elastic moduli. The elastic stiffness obtained from elastic wave velocities in conjunction with density is commonly referred to as dynamic moduli. Conversely, static moduli describe the elastic stiffness or the slope of the stress-strain curve that relates deformation to applied stress in a quasi-static loading scenario (Fjaer et al, 2008).

The obtained P-wave velocity through fractured rock models was then normalized to the P-wave velocity through intact rock and plotted against the fracture density parameter as shown in Figures 5.60 through 5.62 for three different stress levels. Figures 5.60 to 5.62 reveal that, at all three stress levels, the propagation velocity of P-wave through the rock mass follows the same pattern as effective elastic moduli illustrated in figures 5.52 to 5.57. Assuming that the 0.01 variation in the P-wave velocity is negligible (normalized P-wave velocity of 1 ∓ 0.01), it can be concluded that the numerical scheme at stress level 1 is independent of the fracture density parameter, contrary to the analytical method of Davy et al., 2018, while at stress levels 2 and 3, some deviations in the P-wave velocity are visible at fracture density 2.6. Similar to the evolution of Young's modulus as a function of stress level, the difference in the normalized P-wave velocity between the three fracture stiffness models of constant, mismatched, and interlocked vanishes as the stress level increases in both the numerical and analytical methods.
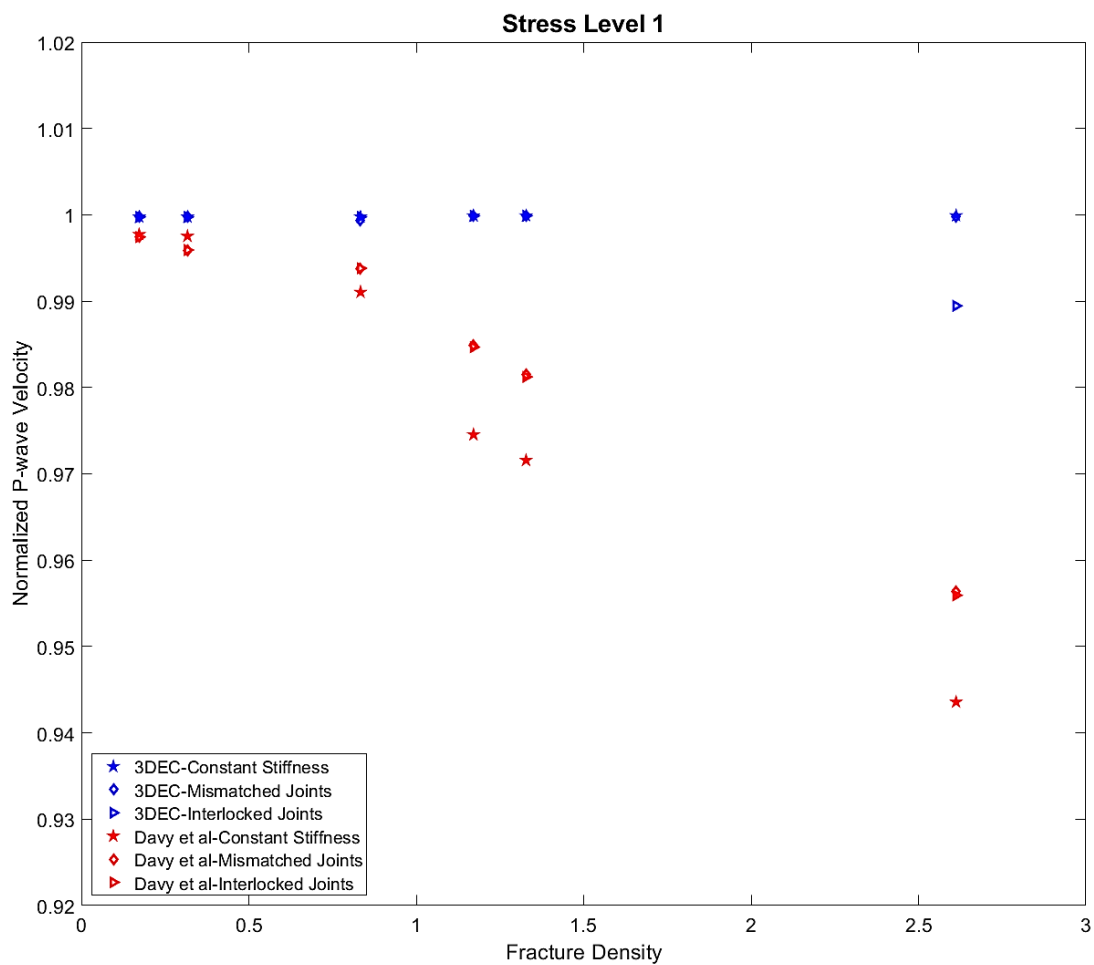
Figure 5.60. Normalized P-wave velocity variation versus fracture density parameter in the three fractured models underwent the first stress level and the second stress perturbation mode
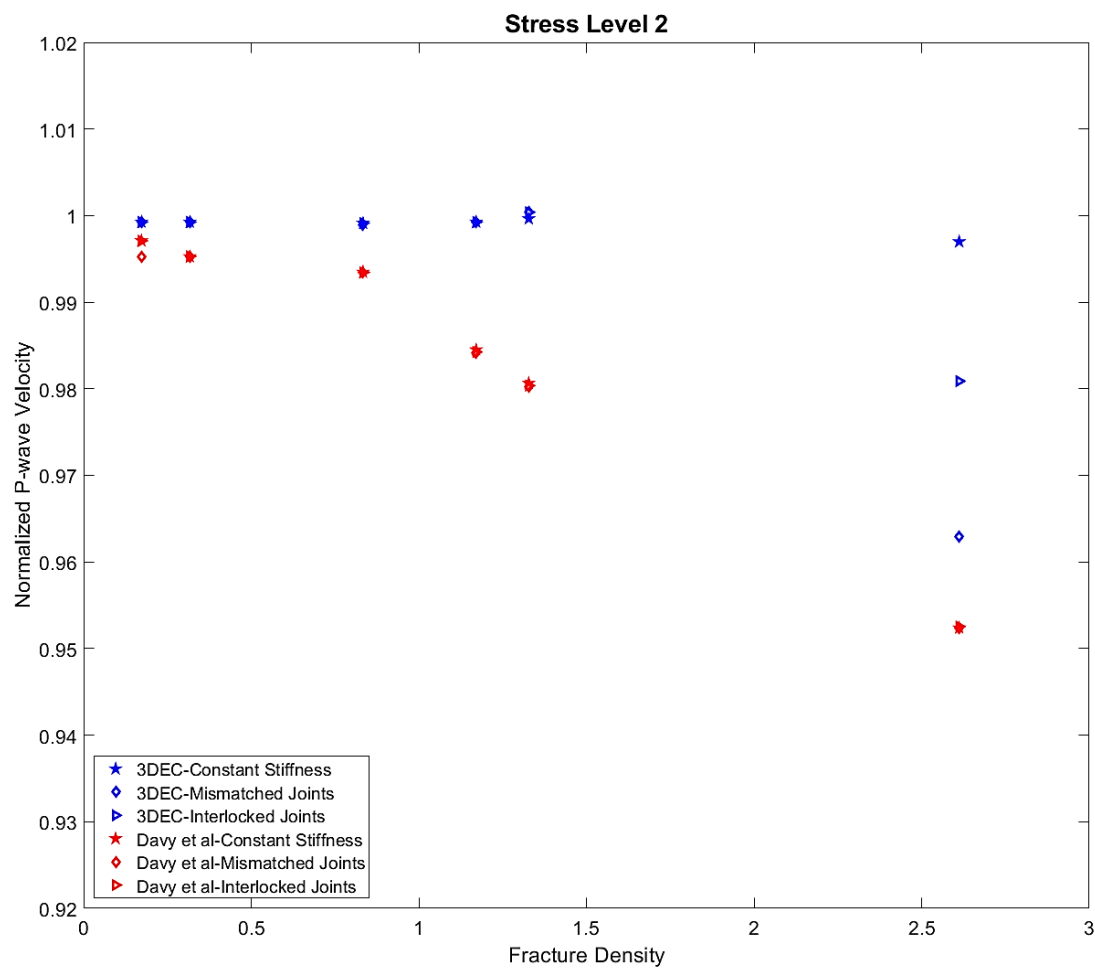
Figure 5.61. Normalized P-wave velocity variation versus fracture density parameter in the three fractured models underwent the second stress level and the second stress perturbation mode
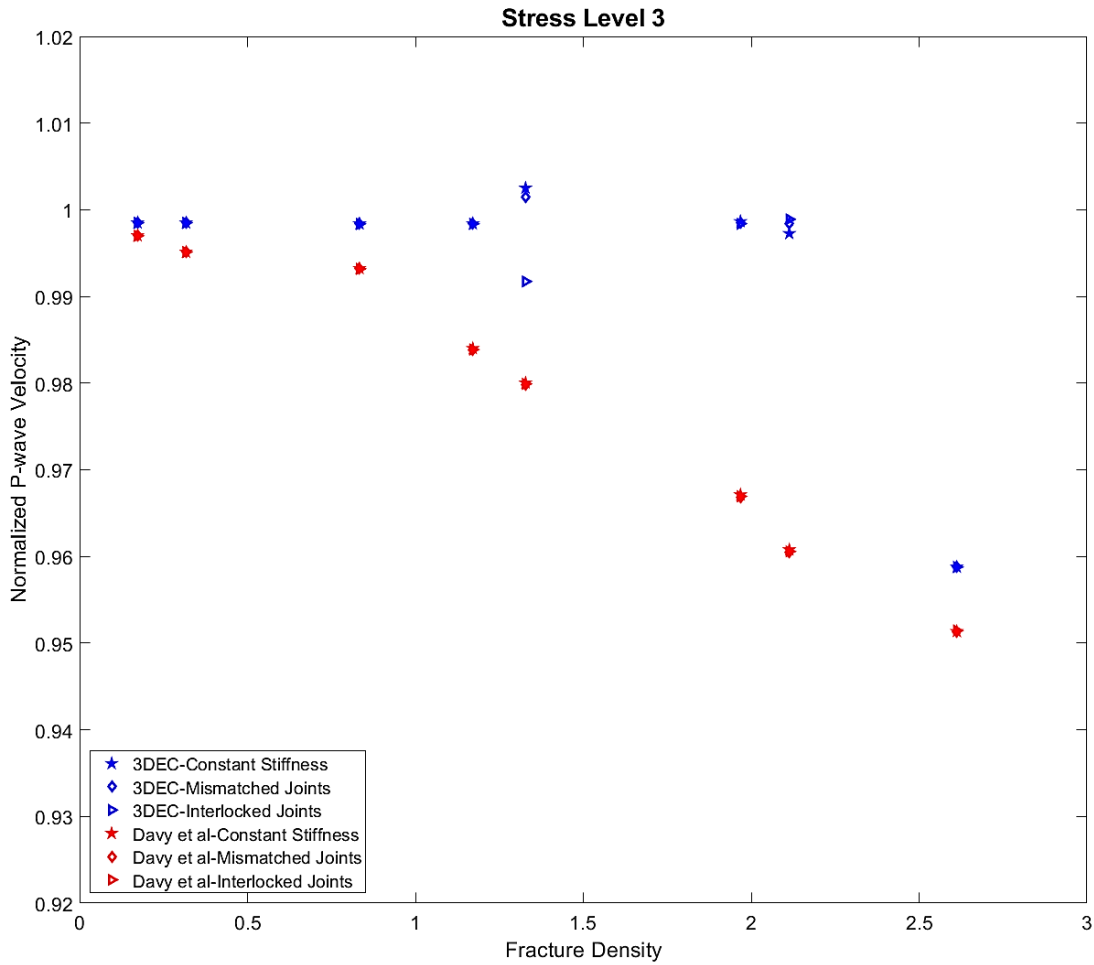
Figure 5.62. Normalized P-wave velocity variation versus fracture density parameter in the three fractured models underwent the third stress level and the second stress perturbation mode

Figure 5.63 demonstrates variation of the normalized P-wave velocity in response to the applied stress level for both analytical and the numerical methods. As can be seen from this figure, the Davy et al. results (red triangles in Figure 5.63) at all three stress levels show approximately consistent variation in normalized P-wave velocity versus applied stress level with a range of approximately [1.00, 0.95]; showing a quasi-stress independent trend, or in other words, a depth independent trend. This behavior is in contrast to the numerical results (blue points in Figure 5.63) which vary from a range of [1.00, 0.99] at the first stress level to a range of about [1.00, 0.96] at the second and third stress levels.
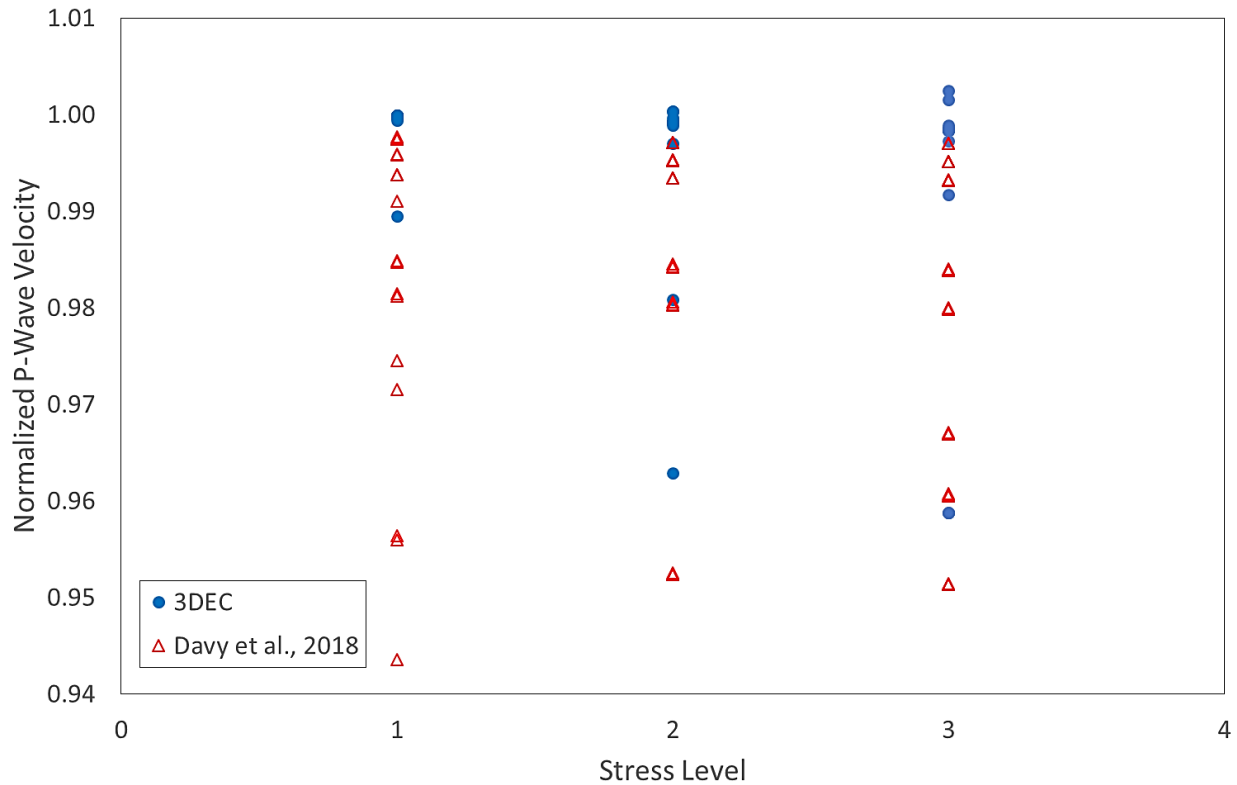
Figure 5.63. Variation of normalized P-wave velocity versus stress level for all fracture densities

5.4 Conclusion

At this chapter, the scaling of the fracture network of Soultz-sous-Forêts (Valley, 2007; Massart et al., 2010, Afshari Moein et al., 2019 and 2021) is adopted to numerically realize the stochastic DFN of the study field using 3DEC. A numerical DFN containing 4500 fractures with length (diameter) range of 10 to 3000 m, power law length distribution exponent of 3.0, and uniform spatial distribution of fractures was generated in a cubic domain of $100 \times 100 \times 100$ m^3 at which the fracture orientations were adopted from Valley, 2007, work. This DFN was then inserted into a homogeneous, isotropic, and elastic intact rock block so as to create a fractured rock mass block of $100 \times 100 \times 100$ m^3. Three models of the rock mass blocks were created based on the type of normal and shear stiffness values assigned to the fractures of DFN. These three models were: i) hosting fractures with constant normal and shear stiffness, ii) hosting fractures with interlocked normal stiffness and stress-dependent shear stiffness, and iii) hosting fractures with mismatched normal stiffness and stress-dependent shear stiffness.

Generated rock mass blocks were then located at three different in-situ stress levels (stress level 1, 2, and 3) and underwent four various stress perturbation modes (mode 1, 2, 3, and 4) in order to evaluate effective elastic moduli and P-wave velocity variation in each case. Due to the high number of fractures in the used DFN, the fractured rock mass model contained some blocks with very small volume magnitudes which tend to be zero or negative when undergoing in-situ stress state as well as stress perturbation phase. To overcome this issue, the DFN was simplified by decreasing the fracture number (from 4500 to about 420 fractures) as well as switching from non-uniform distribution of fracture orientation (introduced by Valley, 2007) to the

uniform distribution. Inserting such DFN into the intact rock block generated a fractured rock block that was then put under various loading scenarios so as to estimate effective elastic moduli. The results showed that for the used DFN the second stress perturbation mode had the most consistent outcomes.

After that and with the aim of assessing fracture density influence on the effective elastic moduli, a set of fractured models were created hosting 50, 100, 200, 400, 500, 600, 700, and 1000 fractures; each of which containing three different models distinguished by the assigned fracture stiffness (constant or stress-dependent) and subjected to a secondary stress perturbation mode at all three stress levels. The numerical results showed that among all assigned DFN examples, the effective moduli of the rock mass deviated from that of the intact rock only when the fracture number of the DFN was 1000 (i.e., fracture density parameter of 2.6), whereas in the analytical method of Davy et al. this deviation occurred at lower fracture density values.

The P-wave velocity through the generated rock mass examples was also obtained based on the calculated elastic moduli and then normalized to the P-wave velocity in the intact rock block. The resulting figures, analogous to the effective elastic moduli, showed that the deviation in the numerical P-wave velocity occurred only when the number of fractures in the DFN was 1000 (i.e., fracture density parameter of 2.6), while it occurred at lower fracture density parameters in the analytical model. In addition, it was also found that the difference in normalized P-wave velocity between the three fracture stiffness models of constant, mismatched, and interlocked vanishes as the stress level increases in both numerical and analytical methods, however, this phenomenon occurs at the second and third stress levels in the analytical model but at the third stress level in the numerical scheme.

The difference between the analytical and numerical results might be justified by the effect of fracture interaction and corresponding stress perturbation in the rock mass models, which is inherently accounted for in the 3DEC calculation but not in the analytical model (Davy et al., 2018).

Chapter 6

6   Conclusion

This research aimed to numerically characterize the origin of observed P-wave velocity variation during hydraulic stimulation of GPK2 well. Occurrence of this P-wave velocity anomaly was faster and more extended compared to that usually happens during a classical fluid diffusion process, as noted by Calo et al., 2011. These P-wave velocity changes were also observed at large scale (~1 km), which suggest that large scale elastic moduli of the reservoir rock had changed rapidly.

First phase of the present work was to address the timing aspect of the observation. It was aimed at understanding the pressure migration during this hydraulic stimulation process by simulating it using 3DEC. It was found that the fluid pressure migrates in time and space following a process controlled by fracture opening rather than fluid pressure. A very rapid migration of fluid pressure was observed, with a much higher effective diffusivity (~13 m^2/s) than that classically observed at Soultz-sous-Forêts (~0.05 m^2/s; see e.g. Shapiro et al., 2002). This rapid process is compatible with the results of Calo et al. who observed a migration of over 1000 m in 3 hours. So, for the time effect, we have highlighted a process consistent with observation.

In the second phase, it was purposed to explore the large scale value of the elastic moduli at Soultz-sous-Forêts reservoir and analyze its sensitivity to stress perturbations in order to understand how pressure changes studied in the first phase would impact P-wave velocity. It was found that large scale elastic moduli through fractured rock mass deviates from that of intact rock in the conditions of high fracture density parameter. Furthermore, investigation of related P-wave velocity as a function of the applied stress level revealed that it is almost independent of the applied stress level.

Considering the low permeability medium addressed by Weidler et al. (2002), in addition to the existence of a fluid pressure/fracture opening front that propagates along the fracture faster than fluid diffusion in the fracture surrounding medium, as demonstrated in this study, it can be stated that the overpressure generated by the injected fluid in the fracture acts as an additive component to the confining pressure of the rock mass, instead of playing the role of pore pressure enhancement. In this situation, and according to the literature already mentioned, especially Todd and Simmons (1972), any increase in confining pressure can cause an increase in P-wave velocity.

Further research is required to fully answer the thesis question. For example, the process highlighted in the first phase could also have implications for the magnitude of pressure perturbation away from the well, or it would be interesting to add fluid pressure to the second phase simulations in order to study the effect of pore pressure on P-wave velocity variation.

References

Aboudi, J., Benveniste, Y., 1987. The effective moduli of cracked bodies in plane deformations. Eng. Frac. Mech. 26, 171–184.

Ackerman, R.V., Schlische, R.W., 1997. Anticlustering of small normal faults around larger faults. Geology 25, 1127–1130.

Afshari Moein, M.J., Bar, K., Valley, B., Genter, A., Sass, I., 2021. Depth-Dependent Scaling of Fracture Patterns Inferred from Borehole Images in GPK3 and GPK4 Wells at Soultz-sous-Forêts Geothermal Site. Presented at the World Geothermal Congress 2020+1, Reykjavik, Iceland.

Afshari Moein, M.J., Valley, B., Evans, K.F., 2019. Scaling of Fracture Patterns in Three Deep Boreholes and Implications for Constraining Fractal Discrete Fracture Network Models. Rock Mech. Rock Eng. 52, 1723–1743. https://doi.org/10.1007/s00603-019-1739-7

Alshkane, Y.M., Marshall, M.A., Stace, L.R., 2017. Prediction of strength and deformability of an interlocked blocky rock mass using UDEC. J. Rock. Mech. Geothec. Eng. 9, 531–542.

Amadei, B., Goodman, R., 1981. A 3-D constitutive relation for fractured rock masses. Studies in App. Mech. Part B, 249–268. https://doi.org/10.1016/B978-0-12-066266-1.50001-6

Anderson, E.W., 1905. The dynamics of faulting. Transactions of the Edinburgh Geological Society 8, 387–402.

Angelier, J., 2002. Inversion of earthquake focal mechanisms to obtain the seismotectonic stress IV-a new method free of choice among nodal planes. Geophys. J. Int. 150, 588–609. https://doi.org/10.1046/j.1365-246X.2002.01713.x

Arrowsmith, S.J., Eisner, L., 2006. A technique for identifying microseismic multiplets and application to the Valhall field, North Sea. Geophysics 71, V31–V40.

Bandis, S.C., Lumsden, A.C., Barton, N.R., 1983. Fundamentals of Rock Joint Deformation. Int. J. Rock Mech. 20, 249–268.

Barth, A., Wenzel, F., Langenbruch, C., 2013. Probability of earthquake occurrence and magnitude estimation in the post shut-in phase of geothermal projects. J Seismol 17, 5–11.

Barton, C.C., 1995. Fractal analysis of scaling and spatial clustering of fractures, in: Fractals in the Earth Science (Edited by C. C. Barton and P. R. LaPointe). Plenum, pp. 141–178.

Barton, C.C., Gott, C.B., Montgomery, J.R., 1986. Fractal scaling of fracture and fault maps at Yucca Mountain, southern Nevada (abstract). Eos Trans. AGU 67, 1295.

Barton, C.C., Hsieh, P., 1989. Physical and hydrological flow properties of fractures, Field Trip Guidebook T385. ed. AGU, Washington D. C.

Barton, C.C., Larsen, E., 1985. Fractal geometry of two-dimensional fracture networks at Yucca Mountain, southwestern Nevada, (edited by O. Stephannso). Presented at the International Symposium on Fundamentals of Rock Joints, Centek, Lulefi, Sweden, pp. 77–84.

Barton, N.R., Lien, R., Lunde, J., 1974. Engineering classification of rock masses for the design of tunnel support. Rock Mechanics 6, 189–236. https://doi.org/10.1007/BF01239496

Batchelor, G.K., 2012. An Introduction to Fluid Dynamics. Cambridge University Press.

Bear, J., 1988. Dynamics of Fluids in Porous Media. Dover Publications.

Beran, M.J., 1967. Statistical Continuum Theories. Wiley Interscience, London and New York.

Berkowitz, B., Adler, P.M., 1998. Stereological analysis of fracture network structure in geological formations. J. Geophys. Res. 103, 15339–15360.

Berkowitz, B., Scher, H., Silliman, S.E., 2000. Anomalous transport in laboratory-scale, heterogeneous porous media. Water Resour. Res. 36, 149–158.

Bieniawski, Z., 1978. Determining rock mass deformability: Experience from case histories. Int. J. Rock Mech. Min. Sci. Geomech. Abstr. 15, 237–247. https://doi.org/10.1016/0148-9062(78)90956-7

Bieniawski, Z., 1973. Engineering classification of jointed rock masses. Civil Engineer in South Africa 15, 335–344.

Blöcher, G., Cacace, M., Jacquey, A.B., Zang, A., Heidbach, O., Hofmann, H., Kluge, C., Zimmermann, G., 2018. Evaluating micro-seismic events triggered by reservoir operations at the geothermal site of groß schönebeck (Germany). Rock Mech Rock Eng 51, 3265–3279.

Biot, M.A., 1962. Mechanics of deformation and acoustic propagation in porous media. J. appl. Phys. 33, 1482–1498.

Bonnet, E., Bour, O., Odling, N.E., Davy, P., Main, I., Cowie, P., Berkowitz, B., 2001. Scaling of frcture system in geological media. Reviews of Geophys. 39, 347–383.

Borgos, H.G., Cowie, P.A., Dawers, N.H., 2000. Practicalities of extrapolating one-dimensional fault and fracture size-frequency distributions to higher-dimensional samples. J. Geophys. Res. 105, 28377–28391.

Bott, M.H.P., 1959. The mechanics of oblique slip faulting. Geological Magazine 96, 109–117. https://doi.org/10.1017/S0016756800059987

Bour, O., 1997. Transferts de fluides dans les milieux fractures: Effets d'echelle. Geosci. Rennes, Univ. of Rennes, Rennes, France.

Bour, O., Davy, P., 1999. Clustering and size distribution of fault patterns: Theory and measurements. Geophys. Res. Lett. 26, 2001–2004.

Bour, O., Davy, P., 1998. On the connectivity of three-dimensional fault networks. Water Resour. Res. 34, 2611–2622.

Bour, O., Davy, P., 1997. Connectivity of random fault networks following a power law fault length distribution. Water Resour. Res. 33, 1567–1583.

Bour, O., Davy, P., Darcel, C., Odling, N.E., 2002. A statistical scaling model for fracture network geometry, with validation on a multiscale mapping of a joint network (Hornelen Basin, Norway). J. Geophys. Res. 107, ETG-4-1-ETG-4-12. https://doi.org/10.1029/2001JB000176

Bourouis, S., Bernard, P., 2007. Evidence for coupled seismic and aseismic fault slip during water injection in the geothermal site of Soultz (France), and implications for seismogenic transients. Geophys. J. Int. 169, 723–732.

Brady, B.H.G., Cramer, M.L., Hart, R.D., 1985. Preliminary analysis of a loading test on a large basalt block. Int. J. Rock Mech. Min. Sci. Geomech. Abstr. 22, 345–348.

Brown, E.T., Hoek, E., 1978. Trends in relationships between in situ stresses and depth. Int. J. Rock Mech., 15, 211–25.

Bruner, W.M., 1976. Comment on 'seismic velocities in dry and saturated cracked solids' by Richard J. O'Connell and Bernard Budiansky. J. Geophys. Res. 81, 2573–2576. https://doi.org/10.1029/JB081i014p02573

Budianski, R., O'Connell, R.J., 1976. Elastic Moduli of cracked solid. Int. J. Solids Struct. 12, 81–97.

Cai, M., Horii, H., 1993. A Constitutive Model and FEM Analysis of Jointed Rock Masses. Int. J. Rock Mech. Min. Sci. Geomech. Abstr. 30, 351–359.

Cai, M., Horii, H., 1992. A constitutive model of highly jointed rock masses. Mech. Mater. 13, 217–246.

Calò, M., Dorbath, C., 2013. Different behaviours of the seismic velocity field at Soultz-sous- Forˆets revealed by 4-D seismic tomography: case study of GPK3 and GPK2 injection tests. Geophys. J. Int. 194, 1119–1137. https://doi.org/10.1093/gji/ggt153

Calò, M., Dorbath, C., Cornet, F.H., Cuenot, N., 2011. Large-scale aseismic motion identified through 4-D P-wave tomography. Geophys. J. Int. 186, 1295–1314. https://doi.org/10.1111/j.1365-246X.2011.05108.x

Carbotte, S.M., Mc Donald, K.C., 1994. Comparison of seafloor tectonic fabric at intermediate, fast, and super fast spreading ridges' Influence of spreading rate, plate motions, and ridge segmentation on fault patterns. J. Geophys. Res. 99, 13609–13631.

Case, E.D., 1984. The effect of microcracking upon the Poisson's ratio for brittle materials. J. Mater. Sci. 19, 3702–3712.

Cauchie, L., Lengline, O., Schmittbuhl, J., 2020. Seismic asperity size evolution during fluid injection: case study of the 1993 Soultz-sous-Forˆets injection. Geophys. J. Int. 221, 968–980.

Childs, C., Walsh, J.J., Watterson, J., 1990. A method for estimation of the density of fault displacements below the limits of seismic resolution in reservoir formations, in North Sea Oil and Gas Reservoirs II, (edited by A. T. Buller et al.), in: North Sea Oil and Gas Reservoirs—II. Springer, Dordrecht, pp. 309–318.

Chiles, J.P., 1988. Fractal and geostatistical methods for modeling of a fracture network,. Math. Geol. 20, 631–654.

Cornet, F.H., 2015. Elements of Crustal Geomechanics. Cambridge University Press.

Cornet, F.H., 2012. The relationship between seismic and aseismic motions induced by forced fluid injections. Hydrogeo. J. 20, 1463–1466.

Cornet, F.H., Bérard, T., Bourouis, S., 2007. How close to failure is a granite rock mass at a 5km depth? Int. J. Rock Mech. Min. Sci. 44, 47–66. https://doi.org/10.1016/j.ijrmms.2006.04.008

Cornet, F.H., Helm, J., Poitrenaud, H., Etchecopar, A., 1997. Seismic and Aseismic Slips Induced by Large-scale Fluid Injections. Pure appl. geophys. 150, 563–583.

Cornet, F.H., Julien, Ph., 1989. Stress Determination from Hydraulic Test Data and Focal Mechanisms of Induced Seismicity. Int. J. Rock Mech. Min. Sci. Geomech. Abstr. 26, 235–248.

Cowie, P.A., Scholz, C.H., Edwards, M., Malinverno, A., 1993a. Fault strain and seismic coupling on mid-ocean ridges. J. Geophys. Res. 98, 17911–17920.

Cowie, P.A., Vanneste, C., Sornette, A., 1993b. Statistical physics model for the spatiotemporal evolution of faults. J. Geophys. Res. 98, 21809–21822.

Cruden, D.M., 1977. Describing the size of discontinuitie. Int. J. Rock Mech. Min. Sci. Geomech. Abstr. 14, 133–137.

Cuenot, N., Dorbath, C., Dorbath, L., 2008. Analysis of the microseis-micity induced by fluid injection in the Hot Dry Rock site of Soultz-sous-Forˆets (Alsace, France): implications for the characterization of the geothermal reservoir properties. Pure appl. Geophys. 165, 1–32.

Cundall, P.A., 1987. Distinct Element Models of Rock and Soil Structure, in: Analytical and Computational Methods in Engineering Rock Mechanics. London: George Allen and Unwin., pp. 129–163.

Cundall, P.A., Strack, O.D.L., 1979. A Discrete Numerical Model for Granular Assemblies. Geotechnique 29, 47–65.

Dagan, G., 1993. Higher-order correction for effective permeability of heterogeneous isotropic formations of lognormal conductivity distribution. Transp. Porous Media 12, 279–90.

Darcel, C., Bour, O., Davy, P., 2003a. Cross-correlation between length and position in real fracture networks. Geophys. Res. Lett. 30, 1650. https://doi.org/10.1029/2003GL017174

Darcel, C., Bour, O., Davy, P., 2003b. Stereological analysis of fractal fracture networks. J. Geophys. Res. 108, 2451.

Darcel, C., Le Goc, R., Doolaeghe, D., Ghazal, R., Davy, P., 2021. Rock mass effective properties from a DFN approach Phase 1 – Elastic properties (No. R-20-05).

Darot, M., Reuschle, T., 2000. Acoustic wave velocity and permeability evolution during pressure cycles on a thermally cracked granite. Int. J. Rock Mech. Min. Sci. 37, 1019–1026.

Davy, P., 1993. On the frequency-length distribution of the San Andreas fault system. J. Geophys. Res. 98, 12141–12151.

Davy, P., Darcel, C., Le Goc, R., Mas Ivras, D., 2018. Elastic Properties of Fractured Rock Masses With Frictional Properties and Power Law Fracture Size Distributions. J. Geophys. Res. Solid Earth 123. https://doi. org/10.1029/2017JB015329

Davy, P., Le Goc, R., Darcel, C., Bour, O., de Dreuzy, J.R., Munier, R., 2010. A likely universal model of fracture scaling and its consequence for crustal hydromechanics. J. Geophys. Res. 115, B10411. http://dx.doi.org/10.1029/2009JB007043

Davy, P., Sornette, A., Sornette, D., 1992. Experimental discovery of scaling laws relating fractal dimensions and the length distribution exponent of fault system. Geophys. Res. Lett. 19, 361–363.

Davy, P., Sornette, A., Sornette, D., 1990. Some consequences of a proposed fractal nature of continental faulting. Nature 348, 56–58.

Deng, Q., Blöcher, G., Cacace, M., Schmittbuhl, J., 2021. Hydraulic Difusivity of a Partially Open Rough Fracture. Rock Mech. Rock Eng. 54, 5493–5515.

Dershowitz, W.S., Herda, H.H., 1991. Interpretation of fracture spacing and intensity. Presented at the The 33rd U.S. Symposium on Rock Mechanics (USRMS), ARMA, New Meico-USA.

Dezayes, C., Genter, A., Gentier, S., 2004. Fracture Network of the EGS Geothermal Reservoir at Soultz-sous-Forêts (Rhine Graben, France). GRC Transactions 28, 213–218.

Dezayes, C., Genter, A., Hooijkaas, G.R., 2005. Deep-Seated Geology and Fracture System of the EGS Soultz Reservoir (France) based on Recent 5km Depth Boreholes. Presented at the World Geothermal Congress, Antalya, Turkey.

Dezayes, C., Genter, A., Valley, B., 2010a. Structure of the low permeable naturally fractured geothermal reservoir at Soultz. Comptes Rendus Geoscience 342, 517–530.

Dezayes, C., Genter, A., Valley, B., 2010a. Overview of the Fracture Network at Different Scales Within the Granite Reservoir of the EGS Soultz Site (Alsace, France). Presented at the World Geothermal Congress, International Geothermal Association., Bali, Indonesia, p. 13.

Dezayes, C., Genter, A., Velley, B., 2010b. Overview of the Fracture Network at Different Scales Within the Granite Reservoir of the EGS Soultz Site (Alsace, France). Presented at the World Geothermal Congress, Bali, Indonesia.

Dorbath, L., Cuenot, N., Genter, A., Frogneux, M., 2009. Seismic response of the fractured and faulted granite of Soultz-sous-Forˆets (France) to 5 km deep massive water injections. Geophys. J. Int. 177, 653–675. https://doi.org/10.1111/j.1365-246X.2009.04030.x

Elrod, H.G., 1979. A general theory for laminar lubrication with Reynolds roughness. J. of Lubrication Tech. 101, 8–14.

Eshelby, J.D., 1957. The determination of the elastic field of an ellipsoidal inclusion, and related problems. Proc. of the Royal Soci. London. Series A. Math. & Phys. Sci. 241, 376–396.

Eshelby, J.D.E., 1959. The elastic field outside an ellipsoidal inclusion. Proc. of the Royal Soci. London. Series A. Math. & Phys. Sci. 252, 561–569. https://doi.org/10.1098/rspa.1959.0173

Evans, K.F., 2005. Permeability creaion and damage due to massive fluid injections into granite at 3.5 km at Soultz: 2. Critical stress and fracture strength. J. Geophys. Res. Solid Earth 110.

Evans, K.F., Kohl, T., Rybach, L., Hopkirk, R.J., 1992. The effects of fracture normal compliance on the long term circulation behaviour of a hot dry rock reservoir: a parameter study using the new fully-coupled code fracture. GRC Transactions 16, 449–456.

Falconer, K., 1990. Fractal Geometry: Mathematical Foundations and Applications. John Wiley & Sons Ltd., New York.

Feder, J., 1988. Fractals. Plenum, New York.

Fjaer, E., Holt, R.M., Horsrud, P., Raaen, A.M., Risnes, R., 2008. Petroleum related rock mechanics, 2nd ed. Elsevier.

Fletcher, J.B., Sykes, L.R., 1977. Earthquakes related to hydraulic mining and natural seismic activity in western New York state. J. geophys. Res. 82, 3767–3780.

Fouche, O., Diebolt, J., 2004. Describing the geometry of 3D fractures systems by correcting for linear sampling bias. Math. Geology 36, 33–63.

Genter, A., 1989. le granite de Soultz-Sous-Forêts (Bas Rhin, France). Fracturation naturelle, altérations hydrothermales et interactions eau-roche. Orléans University, BRGM, France.

Genter, A., Castaing, C., Dezayes, C., Tenzer, H., Traineau, H., Villemin, T., 1997. Comparative analysis of direct (core) and indirect (borehole imaging tools) collection of fracture data in the Hot Dry Rock Soultz reservoir (France). J. Geophys. Res. 102, 15419–15431.

Gentier, S., Genter, A., Sanjuan, B., Bourgine, B., Dezayes, C., Hosni, A., Breton, J.P., Nicol, N., Quinquis, J.P., Crouzet, C., Braibant, G., Brach, M., Moussay, A., Foucher, J.C., Jouin, F., 2003. "Hot Dry Rock" Project; Soultz-sous-Forets (No. RP-52730-FR). BRGM, France.

Gentier, S., Rachez, X., Dezayes, C., Blaisonneau, A., Genter, A., 2005. How to Understand the Effect of the Hydraulic Stimulation in Terms of Hydro-Mechanical Behavior at Soultz-sous-Forêts (France). GRC Transactions 29.

Gephart, J.W., Forsyth, D.W., 1984. An improved method for determining the regional stress tensor using earthquake focal mechanism data – application to the San-Fernando earthquake sequence. J. Geophys. Res. Solid Earth. https://doi.org/10.1029/JB089iB11p09305

Gertsch, L.S., 1995. Three-dimensional fracture network models from laboratory-scale rock sample. Int. J. Rock Mech. Min. Sci. Geomech. Abstr. 32, 85–91.

Gervais, F., Genter, S., 1991. Threedimensional geometrical description of the fracture pattern of a stratified rock mass (edited by W. Wittke). Presented at the International Congress on Rock Mechanics, Aachen, Germany, pp. 237–240.

Goodman, R.E., 1976. Methods of Geological Engineering in Discontinuous Rocks. West Publishing, New York.

Gottesman, T., Hashin, Z., Brull, M.A., 1980. Effective elastic moduli of cracked fiber composites, in: Advances in Composite Materials. Presented at the International Conference on Composite Materials 3, Oxford, pp. 749–758.

Grechka, V., Kachanov, M., 2006. Effective elasticity of fractured rocks: A snapshot of the work in progress. Geophysics 71, W45–W58.

Gudmundsson, J.S., 2000. Fracture dimensions, displacements and fluid transport. J. Struct. Geology 22, 1221–1231. https://doi.org/10.1016/S0191-8141(00)00052-3

Guéguen, Y., Kachanov, M., 2011. Effective elastic properties of cracked rocks—An overview, in: Mechanics of Crustal Rocks, Y. Leroy & F. Lehner (Eds.). Springer, Vienna, pp. 73–125.

Haenel, R., 1983. Geothermal investigations in the Rhenish Massif, in: Fuchs, K., von Gehlen, K., Mälzer, H., Murawski, H., Semmel, A. (Eds) Plateau Uplift. Springer, Berlin, Heidelberg. https://doi.org/10.1007/978-3-642-69219-2_29

Hakami, E., 1989. Water Flow in Single Rock Joints. Luleå Univ. Tech., Luleå, Sweden.

Hardebeck, J.L., Shearer, P.M., 2003. Using S/P Amplitude Ratios to Constrain the Focal Mechanisms of Small Earthquakes. Bul. Seismo. Soci. America 93, 2434–2444.

Hardebeck, J.L., Shearer, P.M., 2002. A New Method for Determining First-Motion Focal Mechanisms. Bul. Seismo. Soci. America 92, 2264–2276.

Harris, C., Franssen, R., Loosveld, R., 1991. Fractal analysis of fractures in rocks: the Cantor's Dust method-comment. Tectonophysics 198, 107–111. https://doi.org/10.1016/0040-1951(91)90135-F

Hart, R.D., 1991. An introduction to Distinct Element Modeling for Rock Engineering. Pergamon Press, Oxford, New York, Seoul, Tokyo.

Hasegawa, E., Izuchi, H., 1983. On the steady flow through a channel consisting of an uneven wall and a plane wall. Bul. Jap. Soc. Mech. Eng. 26, 514–20.

Hashin, Z., 1988. The differential scheme and its application to cracked materials. J. of the Mech. and Phys. of Soli. 36, 719–734. https://doi.org/10.1016/0022-5096(88)90005-1

Hashin, Z., 1983. Analysis of composite materials. J. App. Mech. 50, 481–505.

Hatton, C.G., Main, I.G., Meredith, P.G., 1993. A comparison of seismic and structural measurements of fractal dimension during tensile subcritical crack growth. J. Struct. Geol. 15, 1485–1495.

Hentschel, H.G.E., Proccacia, I., 1983. The infinite number of generalised dimensions of fractals and strange attractor. Physica D. 8, 435–444.

Henyey, F.S., Pomphrey, N., 1982. Self-consistent moduli of a cracked solid. Geophys. Res. Lett. 9, 903–906.

Hiramatsu, Y., Yamanaka, H., 2002. Scaling law between corner frequency and seismic moment of microearthquakes: Is the breakdown of the cube law a nature of earthquakes? Geophys. Res. Lett. 29. https://doi.org/10.1029/2001GL013894

Hoek, E., 1994. Strength of rock and rock masses. ISRM News Journal 2, 4–16.

Hoek, E., Diederichs, M.S., 2006. Empirical estimation of rock mass modulus. Int. J. Rock Mech. Min. Sci. 43, 203–215. https://doi.org/10.1016/j.ijrmms.2005.06.005

Hoek, E., Kaiser, P.K., Bawden, W.F., 1995. Support of underground excavations in hard rock. CRC Press.

Hoenig, A., 1979. Elastic moduli of a non-randomly cracked body. Int. J. Soli. Struct. 15, 137–154.

Horii, H., Nemat-Nasser, S., 1983. . Overall moduli of solids with microcracks: Load-induced anisotropy. J. of the Mech. and Phys. of Soli. 31, 155–171.

Hudson, J.A., 1986. A higher order approximation to the wave propagation constants for a cracked solid. Geophys. J. R. Astr. Soc. 87, 265–274.

Hudson, J.A., 1981. Wave speeds and attenuation of elastic waves in material containing cracks. Geophys. J. R. Astr. Soc. 64, 133–150.

Hudson, J.A., 1980. Overall properties of a cracked solid. Math. Proc. Comb. Phil. Soc. 88, 371–384.

Hudson, J.A., Priest, S.D., 1983. Discontinuity frequency in rock masses. Int. J. Rock Mech. Min. Sci. Geomech. Abstr 20, 73–89.

Hudson, J.A., Priest, S.D., 1979. Discontinuities and rock mass geometry. Int. J. Rock Mech. Min. Sci. Geomech. Abstr. 16, 339–362.

Huet, C., 1990. Application of variational concepts to size effects in elastic heterogeneous bodies. J. Mech. Phys. Solids 38, 813–841.

Itasca (3DEC Software User Manual), 2016. . Itasca Consulting Group, Inc., Minnesota, USA.

Jackson, P., Sanderson, D.J., 1992. Scaling of fault displacements from the Badajoz-Cordoba shear zone, SW Spain. Tectonophysics 210, 179–190.

Jaeger, J.C., Cook, N.G.W., Zimmerman, R.W., 2007. Fundamentals of rock mechanics, 4th Edition. ed. Blackwell.

Jin, L., Zoback, M.D., 2017. Fully coupled nonlinear fluid flow and poroelasticity in arbitrarily fractured porous media: A hybriddimensional computational model. J. Geophys. Res. Solid Earth 122, 7626–7658.

Johnston, J.D., McCaffrey, K.J.W., 1996. Fractal geometries of vein systems and the variation of scalingrelationships with mechanism. Journal of Structural Geology 18, 349–358. https://doi.org/10.1016/S0191-8141(96)80055-1

Julien, Ph., Cornet, F.H., 1987. Stress determination from aftershocks of the Compania-Lucania earthquake of November 23, 1980. Annales Geophysicae 5B, 289–300.

Kachanov, M., 1993. Elastic solids with many cracks and related problems. Advances in Applied Mechanics 30, 259–445.

Kachanov, M., 1987. Elastic solids with many cracks: A simple method of analysis. Int. J. Soli. Struct. 23, 23–43. https://doi.org/10.1016/0020-7683(87)90030-8

Kachanov, M., 1980. Continuum model of medium with cracks. J. Eng. Mech. Division 106. https://doi.org/10.1061/JMCEA3.0002642

Kachanov, M., Sevostianov, I., 2013. Effective properties of heterogeneous materials. Springer, Netherlands.

Kagan, Y.Y., 1997. Seismic moment-frequency relation for shallow earthquakes: Regional comparison. J. Geophys. Res. 102, 2835–2852.

Kee, G., Rummel, F., 1993. Hydrofrac stress data for the European HDR research project test site Soultz-sous-Forets. Int. J. Rock Mech. Min. Sci. Geomech. Abst. 30, 973–976.

King, G.C.P., 1983. The accommodation of large strains in the upper lithosphere of the Earth and other solids by selfsimilar fault system. Pure Appl. Geophy. 12, 761–815.

Kolbel, T., Genter, A., 2017. Enhanced Geothermal Systems: The Soultz- sous- Forêts Project, in: Towards 100% Renewable Energy. Springer Proceedings in Energy. https://doi.org/10.1007/978-3-319-45659-1_25

Kranz, R.L., Frankel, A.D., Engelder, T., Scholz, C.H., 1979. The Permeability of Whole and Jointed Barre Granite. Int. J. Rock Mech. Min. Sci. Geomech. Abst. 16, 225–34.

Kulhaway, F.H., 1975. tress-deformation properties of rock and rock discontinuities. Engineering Geology 8, 327–350.

Le Ravalec, M., Guéguen, Y., 1996. High and low frequency elastic moduli for a saturated porous/cracked rock – Differential self consistent and poro-elastic theory. Geophysics 61, 1080–1094.

Lemos, J., 1987. Distinct Element Model for Dynamic Analysis of Jointed Rock with Application to Dam Foundations and Fault Motion (PhD Thesis). University of Minnesota, USA.

Lengline, O., Boubacar, M., Schmittbuhl, J., 2017. Seismicity related to the hydraulic stimulation of GRT1, Rittershoffen, France. Geophys. J. Int. 208, 1704–1715.

Lengline, O., Lamourette, L., Vivin, L., Cuenot, N., Schmittbuhl, J., 2014. Fluid-induced earthquakes with variable stress drop. J. Geophys. Res. Solid Earth 119, 8900–8913. https://doi.org/10.1002/2014JB011282

Li, J., Kuleli, H.S., Zhang, H., Nafi Toksoz, M., 2011a. Focal mechanism determination of induced microearthquakes in an oil field using full waveforms from shallow and deep seismic networks. Geophysics 76, WC87–WC101. https://doi.org/10.1190/GEO2011-0030.1

Li, J., Zhang, H., Kuleli, H.S., Nafi Toksoz, M., 2011b. Focal mechanism determination using high-frequency waveform matching and its application to small magnitude induced earthquakes. Geophys. J. Int. 184, 1261–1274. https://doi.org/10.1111/j.1365-246X.2010.04903.x

Lockner, D.A., Byerlee, J.D., Walsh, J.B., 1977. Changes in seismic velocity and attenuation during deformation of granite. J. Geophys. Res. 82, 5374–5378. https://doi.org/10.1029/JB082i033p05374

Main, I.G., 1996. Statistical physics, seismogenesis, and seismic hazard,. Rev. Geophy. 34, 433–462.

Mandelbort, B., 1984. Les objets fractals : Forme, hasard et dimension, 2nd ed. Flammarion, Paris.

Mandelbort, B., 1982. The Fractal Geometry of Nature. W. H. Freeman, New York.

Marrett, R., 1996. Aggregate properties of fracture populations. J. Struct. Geol. 18, 169–178.

Marrett, R., Allmendinger, R., 1991. Estimates of strain due to brittle faulting: Sampling of fault population. J. Struct. Geol. 13, 735–738.

Massart, B., Paillet, M., Henrion, V., Sausse, J., Dezayes, C., Genter, A., Bisset, A., 2010. Fracture Characterization and Stochastic Modeling of the Granitic Basement in the HDR Soultz Project (France). Presented at the World Geothermal Congress, International Geothermal Association, Bali, Indonesia, p. 7.

Maury, J., Cornet, F.H., Dorbath, L., 2013. A review of methods for determining stress fields from earthquakes focal mechanisms; Application to the Sierentz 1980 seismic crisis (Upper Rhine graben). Bull. Soc. géol. France 184, 319–334.

Mavko, G., Vanorio, T., 2010. The influence of pore fluids and frequency on apparent effective stress behavior of seismic velocities. Geophysics 75, N1–N7.

Michael, A.J., 1984. Determination of stress from slip data: Faults and folds. J. Geophys. Res. Solid Earth 89, 11517–11526. https://doi.org/10.1029/JB089iB13p11517

Michael, A.J., 1987b. Stress rotation during the Coalinga aftershock sequence. J. Geophys. Res. Solid Earth 92, 7963–7980.

Michael, A.J., 1987a. Use of focal mechanisms to determine stress: a control study. J. Geophys. Res. Solid Earth 92, 357–368. https://doi.org/10.1029/JB092iB01p00357

Moriya, H., Nakazato, K., Niitsuma, H., Baria, R., 2002. Detailed Fracture System of the Soultz-sous-Forêts HDR Field Evaluated Using Microseismic Multiplet Analysis. Pure appl. geophys. 159, 517–541.

Murphy, H., Huang, C., Dash, Z., Zyvoloski, G., White, A., 2004. Semi-analytical Solutions for Fluid Flow in Rock Joints with Pressure-Dependent Openings. Water Resour. Res. 40.

Neuzil, C.E., Tracy, J.V., 1981. Flow through fractures. Water Resour. Res. 17, 191–9.

Nordgren, R.P., n.d. Propagation of a vertical hydraulic fracture. Soc. Pet. Eng. J. 12, 306–314.

Nur, A., 1982. The origin of tensile fracture lineament. J. Struct. Geol. 4, 31–40.

O'Connell, R.J., Budianski, R., 1974. Seismic velocities in dry and saturated cracked solids. J. Geophys. Res. 79, 5412–5426. https://doi.org/10.1029/JB079i035p05412

Oda, M., 1988. A method for evaluating crack geometry on the mechanical behaviour of cracked rock masses. Mechanics of Materials 2, 163–171.

Ohtake, M., 1974. Seismic activity induced by water injection at Matsushiro, Japan. J. Phys. Earth 22, 163–176.

Okubo, P.G., Aki, K., 1987. Fractal geometry in the San Andreas fault system. J. Geophys. Res. 92, 345–355.

Oron, A.P., Berkowitz, B., 1998. Flow in rock fractures: The local cubic law assumption re-examined. Water Resour. Res. 34, 2811–24.

Pan, P.Z., Feng, X.T., Hudson, J.A., 2006. Numerical simulations of Class I and Class II uniaxial compression curves using an elasto-plastic cellular automaton and a linear combination of stress and strain as the control method. Int. J. Rock Mech. Min. Sci. 43, 1109–1117.

Parotidis, M., Shapiro, S.A., Rothert, E., 2004. Back front of seismicity induced after termination of borehole fuid injection. Geophys. Res. Lett. 31.

Patir, N., Cheng, H.S., 1978. An average flow model for determining effects of threedimensional roughness on partial hydrodynamic lubrication. J. of Lubrication Tech. 100, 12–17.

Perkins, T.K., Kern, L.R., 1961. Widths of hydraulic fractures. J. Pet. Technol. 13, 937–947.

Pickering, G., Peacock, D.C.P., Sanderson, D.J., Bull, J.M., 1997. Modeling tip zones to predict the throw and length characteristics of faults. Am. Assoc. Pet. Geol. Bull. 81, 82–99.

Piggott, A.R., 1997. Fractal relations for the diameter and trace length of disc-shaped fractures. J. Geophys. Res. 102, 18121–18125.

Place, J., Diraison, M., Naville, C., Geraud, Y., Schaming, M., Dezayes, C., 2010. Decoupling of deformation in the Upper Rhine Graben sediments. Seismic reflection and diffraction on 3-component Vertical Seismic Profiling (Soultz-sous-Foreˆts area). Comptes Rendus Geoscience 342, 575–586.

Place, J., Sausse, J., Marthelot, JM., Diaraison, M., Geraud, Y., Naville, C., 2011. 3-D mapping of permeable structures affecting a deep granite basement using isotropic 3C VSP data. Geophys. J. Int. 186, 245–263. https://doi.org/10.1111/j.1365-246X.2011.05012.x

Poupinet, G., Ratdomopurbo, A., Coutant, O., 1996. On the use of earthquake multiplets to study fractures and the temporal evolution of an active volcano. Annali di Geofisica. https://doi.org/10.4401/ag-3968

Pouya, A., Ghoreychi, M., 2011. Determination of rock mass strength properties by homogenization. Int. J. Num. Anal. Meth. Geomech. 25, 1285–1303. https://doi.org/10.1002/nag.176 hal-00576675

Priest, S.D., Hudson, J.A., 1981. Estimation of discontinuity spacing and trace length using scanline survey. Int. J. Rock Mech. Min. Sci. Geomech. Abstr. 18, 183–197.

Reches, Z., 1986. Network of shear faults in the field and in experiment, in Fragmentation, Form and Flow in Fractured Media, edited by R. Englman and Z. Jaeger. Ann. Isr. Phys. Soc 8, 42–51.

Renshaw, C.E., 1995. On the relationship between mechanical and hydraulic apertures in rough-walled fractures. J. Geophys. Res. Solid Earth 100, 629–36.

Rice, J.R., 1992. Fault stress states, pore pressure distributions, and the weakness of the san andreas fault. Int. Geophys. 51, 475–503.

Rouleau, A., Gale, J.E., 1985. Statistical characterization of the fracture system in the Stripa granite, Sweden. Int. J. Rock Mech. Min. Sci. Geomech. Abstr. 22, 353–367.

Rozhko, A.Y., 2010. Role of seepage forces on seismicity triggering. J. Geophys. Res. Solid Earth 115.

Rummel, F., 1991. Physical properties of the rock in the granitic section of Borehole GPK1, Soultz-sous-Forêts. Geother. Sci. Tech. 3, 199–216.

Salganik, R.L., 1973. Mechanics of bodies with many cracks. Mekhanika Tverdogo Tela 8, 149–158.

Sausse, J., 2002. Hydromechanical properties and alteration of natural fracture surfaces in the Soultz granite (Bas-Rhin, France). Tectonophysics 348, 169–185.

Sausse, J., Dezayes, C., Dorbath, L., Genter, A., Place, J., 2010. 3D model of fracture zones at Soultz-sous-Forêts based on geological data, image logs, induced microseismicity and vertical seismic profiles. Comptes Rendus Geoscience 342, 531–545. https://doi.org/10.1016/j.crte.2010.01.011

Sayers, C.M., Kachanov, M., 1995. . Microcrack-induced elastic wave anisotropy of brittle rocks. J. of Geophys. Res. 100, 4149–4156. https://doi.org/10.1029/94JB03134

Sayers, C.M., Kachanov, M., 1991. A simple technique for finding effective elastic constants of cracked solids for arbitrary crack orientation statistics. Int. J. of Soli. and Struc. 27, 671–680.

Schmittbuhl, J., 2018. Modeling P-wave velocity variations related to aseismic slip in a fractured reservoir.

Schoenberg, M., Sayers, C.M., 1995. Seismic anisotropy of fractured rock. Geophysics 60, 204–211. https://doi.org/10.1190/1.1443748

Scholz, C.H., Cowie, P., 1990. Determination of total strain from faulting using slip measurement. Nature 346, 837–838.

Segall, P., Lu, S., 2015. Injection-induced seismicity: Poroelastic and earthquake nucleation efects. J Geophys Res Solid Earth 120, 5082–5103.

Shapiro, S.A., Audigane, P., Royer, J.J., 1999. Large-scale in situ permeability tensor of rocks from induced microseismicity. Geophys J Int 137, 207–213.

Shapiro, S.A., Huenges, E., Borm, G., 1997. Estimating the crust permeability from fluid-injection-induced seismic emission at the KTB site. Geophys. J. Int 131, F15–F18.

Shapiro, S.A., Kruger, O.S., Dinske, C., 2013. Probability of inducing given-magnitude earthquakes by perturbing finite volumes of rocks. J. Geophys. Res. Solid Earth 118, 3557–3575. https://doi.org/10.1002/jgrb.50264

Shapiro, S.A., Rothert, E., Rath, V., Rindschwentner, J., 2002. Characterization of fluid transport properties of reservoirs using induced microseismicity. Geophysics 67, 212–220.

Shimizu, H., Koyama, T., Ishida, T., Chijimatsu, M., Fujita, T., Nakama, S., 2010. Distinct element analysis for Class II behavior of rocks under uniaxial compression. Int. J. Rock Mech. Min. Sci. 47, 323–333.

Silliman, S.E., 1989. Interpretation of the difference between aperture estimates derived from hydraulic and tracer tests in a single fracture. Water Resour. Res. 25, 2275–83.

Simmons, G., Brace, W., 1965. Comparison of static and dynamic measurements of compressibility of rocks. J. Geophys. Res. 70, 5649–5656. https://doi.org/10.1029/JZ070i022p05649

Simpson, D.W., Leith, W.S., Scholz, C.H., 1988. Two types of reservoir induced seismicity. Bull. seism. Soc. Am. 78, 2025–2040.

Singh, B., 1973. Continuum characterization of jointed rock masses: Part I—The constitutive equations. Int. J. Rock Mech. Min. Sci.

Skjente, E., Hensen, Q., Gudmundsson, J.S., 1999. High-velocity flow in a rough fracture. J. Fluid Mech. 383, 1–28.

Sneddon, I.N., Lowengrub, M., 1969. Crack problems in the classical theory of elasticity. Wiley and sons, New York.

Sornette, A., Davy, P., Sornette, D., 1993. Fault growth in brittleductile experiments and the mechanics of continental collisions. J. Geophys. Res. 98, 12111–12139.

Sornette, D., Sornette, A., 1999. General theory of the modified Gutenberg-Richter law for large seismic moments. Bull. Seismol. Soc. Am. 89, 1121–1130.

Stacey, F.D., Davis, P.M., 2008. Physics of the Earth, 4th ed. Cambridge University Press.

Talwani, P., Acree, S., 1985. Pore pressure diffusion and the mechanism of reservoir-induced seismicity. Pageoph 122, 947–965.

Timoshenko, S.P., Goodier, J.N., 1970. Theory of Elasticity, Third Edition. ed, Engineering Mechanics Series. McGraw Hill.

Todd, T., Simmons, G., 1972. Effect of Pore Pressure on the Velocity of Compressional Waves in Low-Porosity Rocks. J. Geophys. Res. 77, 3731–3743.

Trimmer, D., Bonner, B., Heard, H.C., Duba, A., 1980. Effect of Pressure and Stress on Water Transport in Intact and Fractured Gabbro and Granite. J. Geophys. Res. Solid Earth 85, 7059–71.

Tsay, R.Y., Weinbaum, S., 1991. Viscous flow in a channel with periodic cross-bridging fibers: exact solutions and Brinkman approximation. J. Fluid Mech. 226.

Turcotte, D.L., 1992. Fractals and Chaos in Geology and Geophysics. Cambridge University Press, New York.

Turcotte, D.L., 1986. A fractal model for crustal deformation. Tectonophysics 132, 261–269.

Vakulenko, A.A., Kachanov, M., 1971. Continuum model of medium with cracks. Mekhanika Tverdogo Tela 4, 159–166.

Valley, B., 2007. The relation between natural fracturing and stress heterogeneities in deep-seated crystalline rocks at Soultz-sousForêts (France). ETH Zurich, Switzerland.

Vallier, B., Magnenet, V., Schmittbuhl, J., Fond, C., 2019. Large scale hydro-thermal circulation in the deep geothermal reservoir of Soultz-sous-Forêts (France). Geothermics 78, 154–169. https://doi.org/10.1016/j.geothermics.2018.12.002

Velley, B., Evans, K.F., 2007. Stress state at Soultz-sous-Forêts to 5 km depth from wellbore failure and hydraulic observations. Presented at the Workshop on Geothermal Reservoir Engineering, Stanford University, Stanford, California, USA.

Vermilye, J., Scholz, C., 1995. Relation between vein length and aperture. Journal of Structural Geology 17, 423–434. https://doi.org/10.1016/0191-8141(94)00058-8

Vicsek, T., 1992. Fractal Growth Phenomen. World Sci., River Edge, N. J.

Villeneuve, M.C., Heap, M.J., Kushnir, A.R., Qin, T., Baud, P., Zhou, G., Xu, T., 2018. Estimating in situ rock mass strength and elastic modulus of granite from the Soultz-sous-Forêts geothermal reservoir (France). Geothermal Energy 6. https://doi.org/10.1186/s40517-018-0096-1

Walsh, J.B., 1981. Effect of Pore Pressure and Confining Pressure on Fracture Permeability. Int. J. Rock Mech. Min. Sci. Geomech. Abstr. 18, 429–435.

Walsh, J.B., 1965. The effect of cracks on the compressibility of rock. J. Geophys. Res. 70, 5249–5257. https://doi.org/ 10.1029/JZ070i002p00381

Walsh, J.J., Watterson, J., Yielding, G., 1991. The importance of small-scale faulting in regional extension. Nature 391–393.

Wang, H.F., n.d. Theory of linear poroelasticity with applications to geomechanics and hydrogeology. Princeton University Press, Princeton.

Weidler, R., Gerard, A., Baria, R., Baumgartner, J., Jung, R., 2002. Hydraulic and micro-seismic results of massive stimulation test at 5 km depth at the European Hot-Dry-Rock test site Soultz, France. Presented at the 27th Workshop on Geothermal Reservoir Engineering, Stanford, California, USA, pp. 95–100.

Westway, R., 1994. Quantitative analysis of population of small faults. J. Struct. Geol. 16, 1256–1273.

Witherspoon, P.A., Wang, J.S.Y., Iwai, K., Gale, J.E., 1980. Validity of Cubic Law for fluid flow in a deformable rock fracture. Water Resour. Res. 16, 1016–1024.

Yin, J.M., Cornet, F.H., 1994. Integrated stress determination by joint inversion of the hydraulic tests and focal mechanisms. Geophys. Res. Lett. 21, 2645–2648.

Yin, Z., Huang, H., Zhang, F., Zhang, L., Maxwell, S., 2020. Three-dimensional distinct element modeling of fault reactivation and induced seismicity due to hydraulic fracturing injection and backflow. J. Rock. Mech. Geothec. Eng. 12, 752–767.

Zangerl, C., Evans, K.F., Eberhardt, E., Loew, S., 2008. Normal stiffness of fractures in granitic rock: A compilation of laboratory and in-situ experiments. Int. J. Rock Mech. Min. Sci. 45, 1500–1507.

Zimmerman, R.W., 1985. The effect of microcracks on the elastic moduli of brittle materials. J. of Mater. Sci. Let. 4, 1457–1460.

Zimmerman, R.W., 1984. Elastic moduli of a solid with spherical pores: New self-consistent method. Int. J. Rock Mech. Min. Sci. Geomech. Abstr 21, 339–343.

Zimmerman, R.W., Bodvarsson, G.S., 1996a. Hydraulic conductivity of rock fractures. Transp. Porous Media 23, 1–30.

Zimmerman, R.W., Bodvarsson, G.S., 1996b. Hydraulic conductivity of rock fractures. Transp. Porous Media 23, 1–30.

Zimmerman, R.W., Kumar, S., Bodvarsson, G.S., 1991. Lubrication theory analysis of the permeability of rough-walled fractures. Int. J. Rock Mech. Min. Sci. Geomech. Abstr. 28, 325–31.

Zimmerman, R.W., Yeo, I.W., 2000. Fluid Flow in Rock Fractures: From the Navier-Stokes Equations to the Cubic Law, in: Dynamics of Fluids in Fractured Rocks. American Geophysical Union, Washington, pp. 213–324.

Appendix A1

Numerical and analytical results of mechanical benchmarking

A) For the cases for which the gravity was not taken into account:
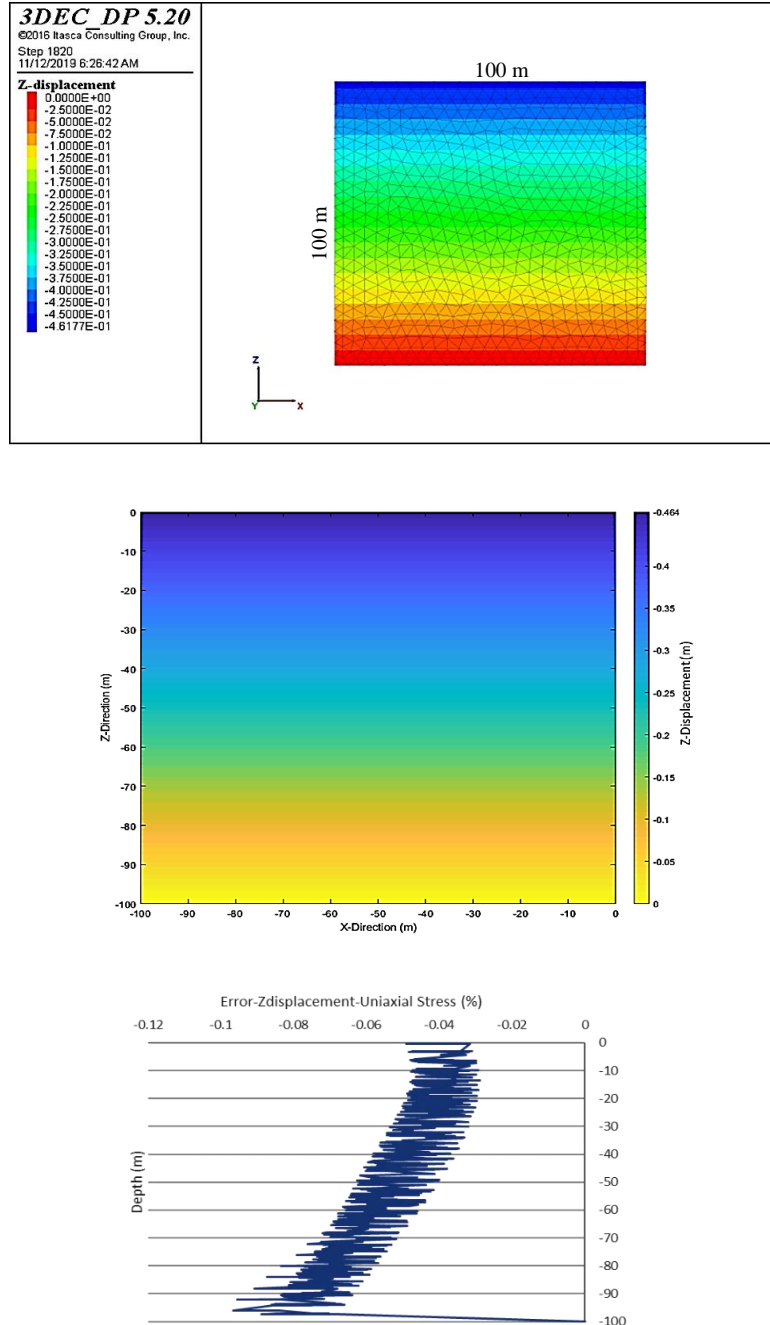
Figure A1.1. Numerical (upper) and analytical (middle) vertical displacement magnitudes and corresponding error (lower) in Uniaxial Stress case
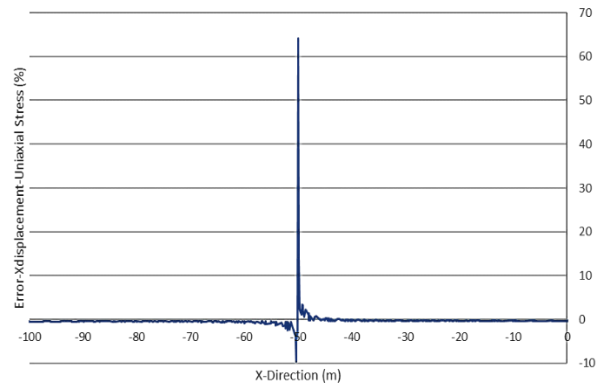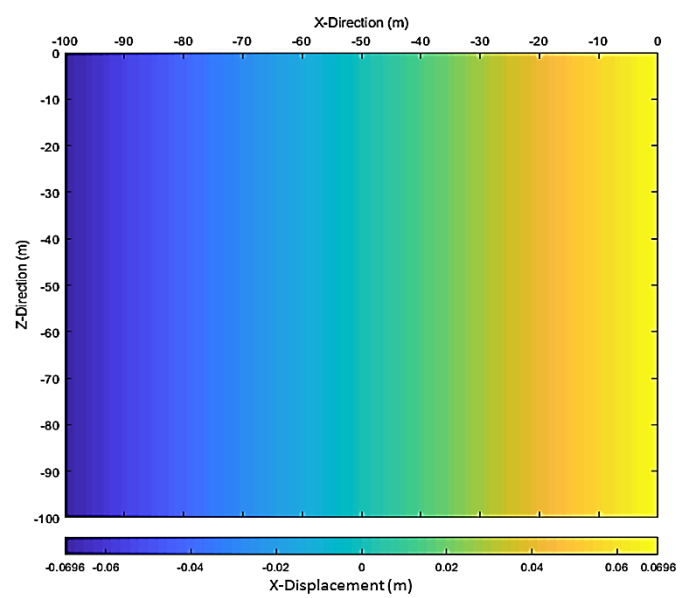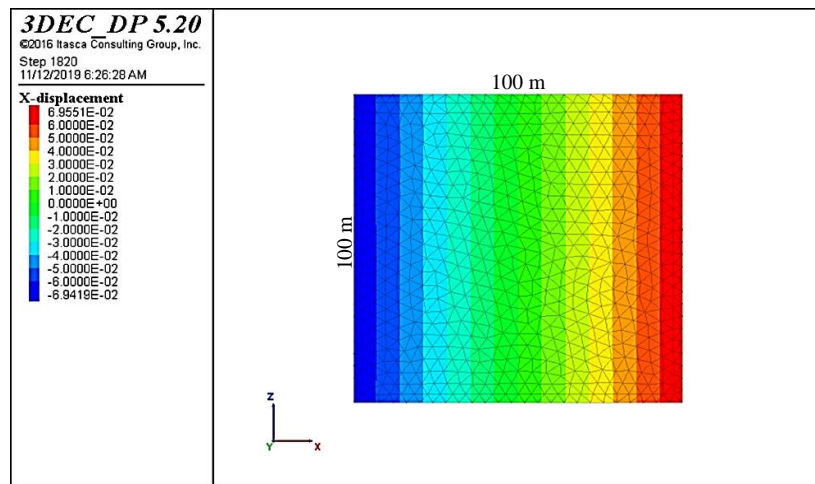
Figure A1.2. Numerical (upper) and analytical (middle) lateral displacement magnitudes in X-direction and corresponding error (lower) in Uniaxial Stress case
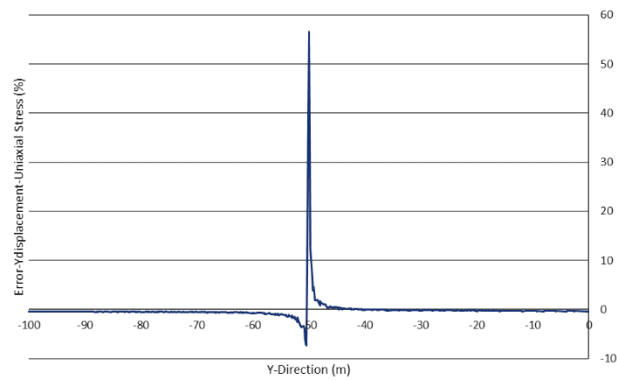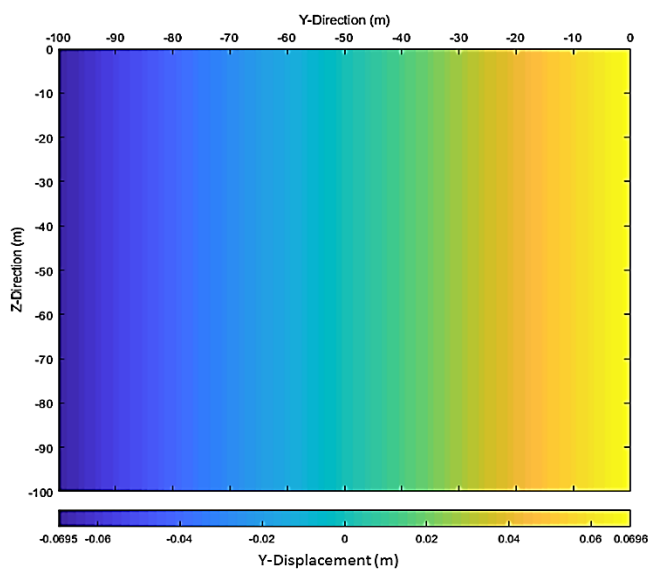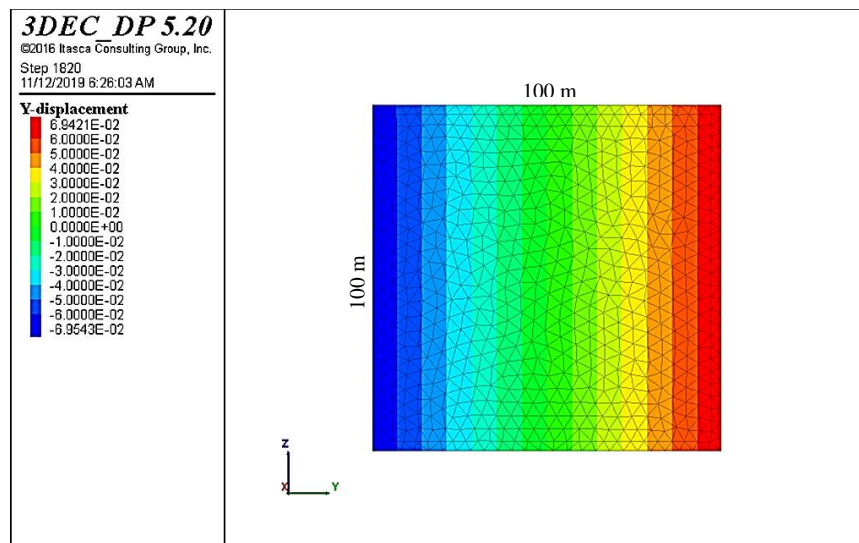
Figure A1.3. Numerical (upper) and analytical (middle) lateral displacement magnitudes in Y direction and corresponding error (lower) in Uniaxial Stress case
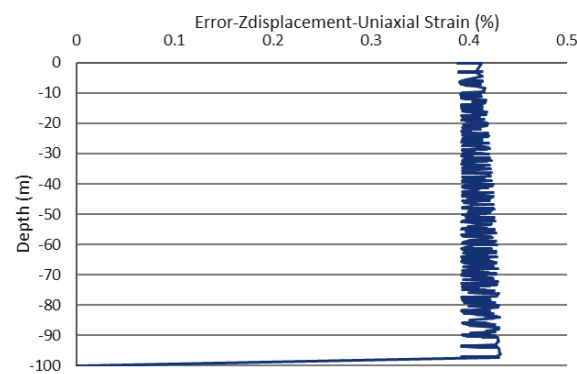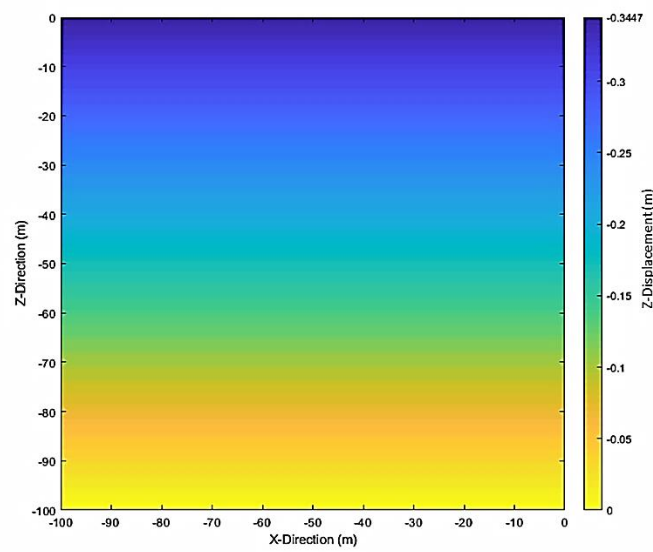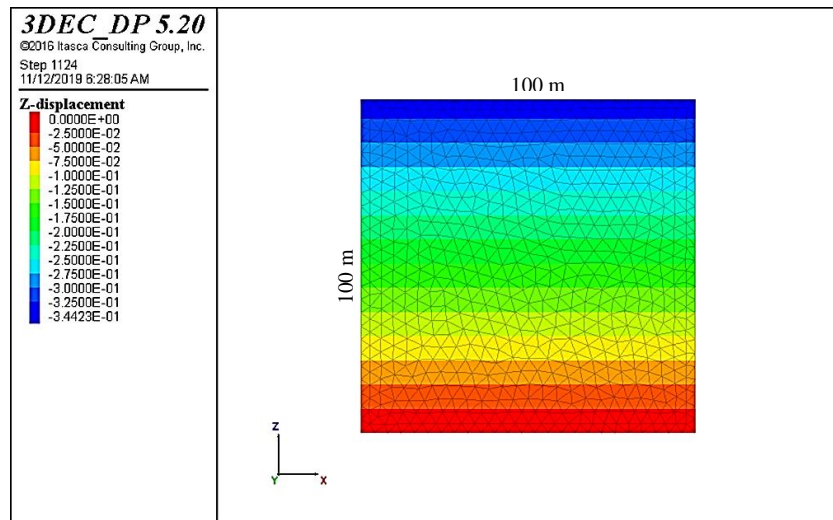
Figure A1.4. Numerical (upper) and analytical (middle) vertical displacement magnitudes and corresponding error (lower) in Uniaxial Strain case
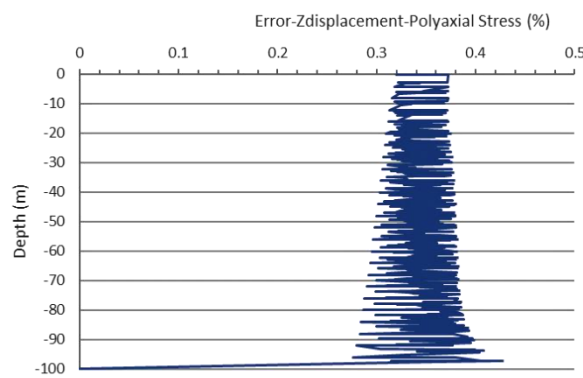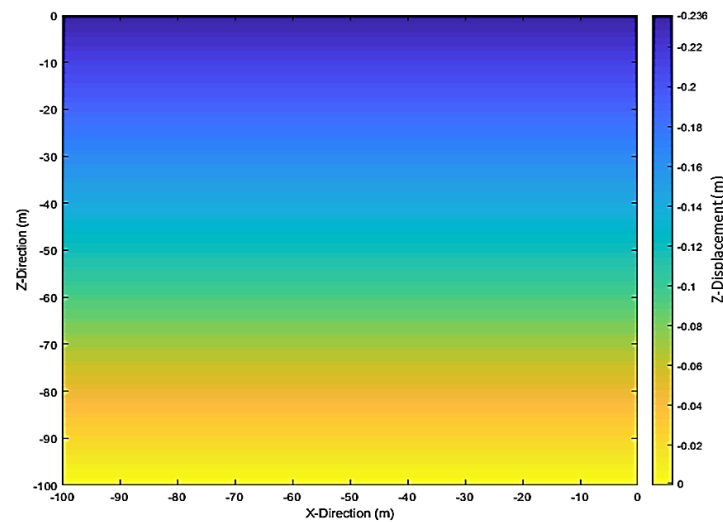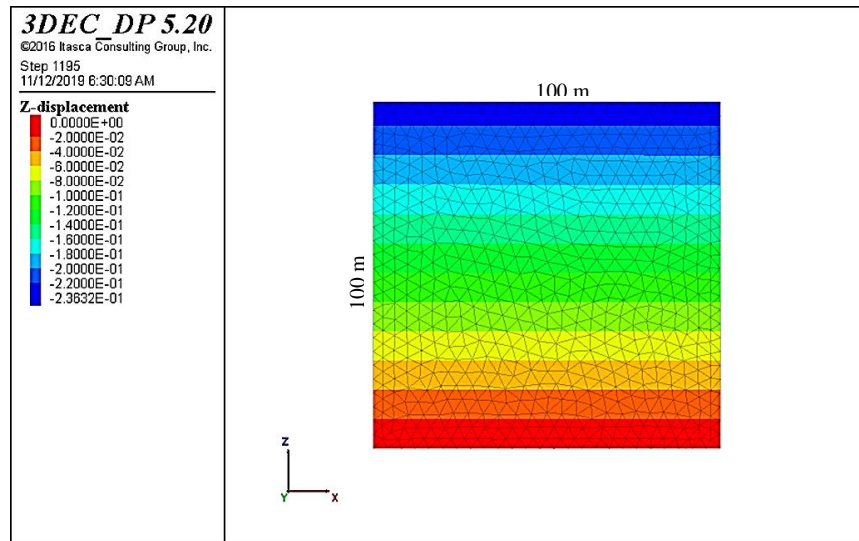
Figure A1.5. Numerical (upper) and analytical (middle) vertical displacement magnitudes and corresponding error (lower) in Polyaxial Stresses case
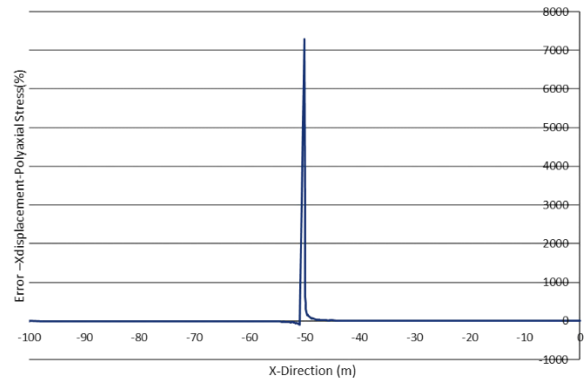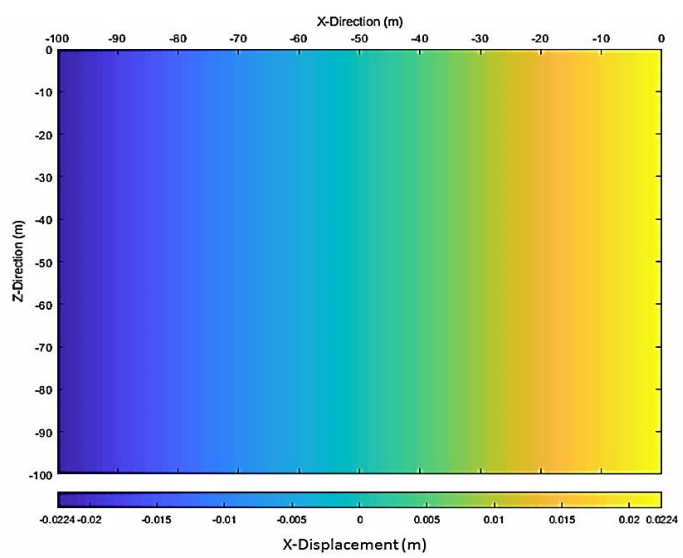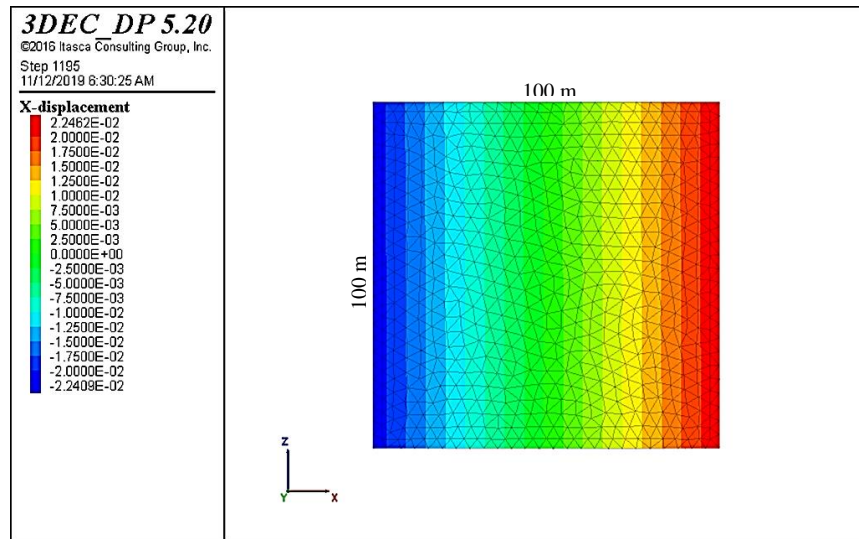
Figure A1.6. Numerical (upper) and analytical (middle) lateral displacement magnitudes in X direction and corresponding error (lower) in Polyaxial Stresses case

232
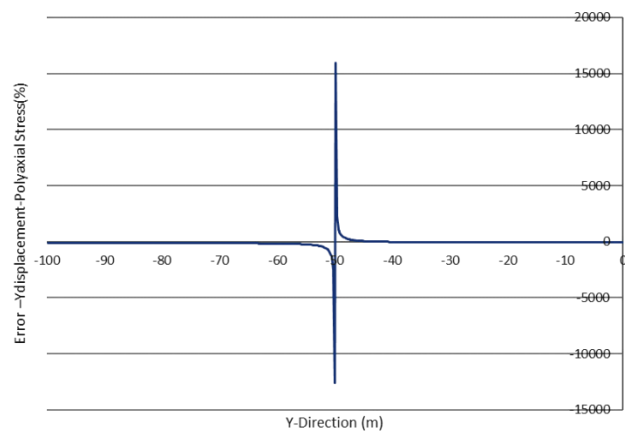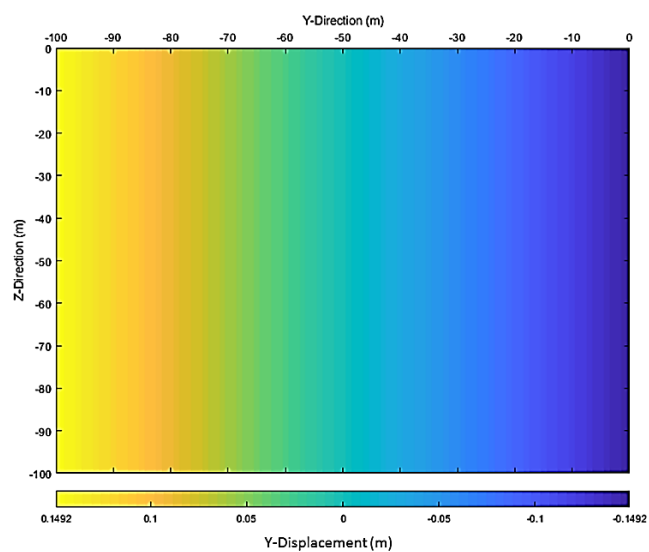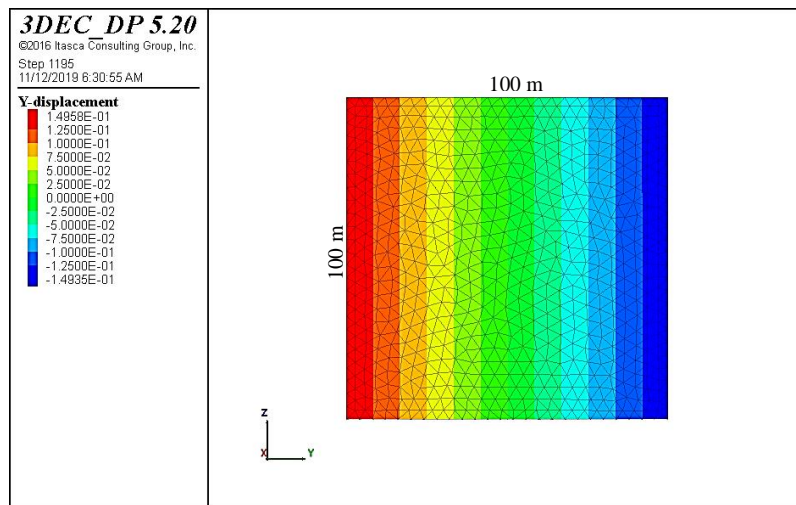
Figure A1.7. Numerical (upper) and analytical (middle) lateral displacement magnitudes in X direction and corresponding error (lower) in Polyaxial Stresses case

B) For the cases in which the gravity was taken into account:
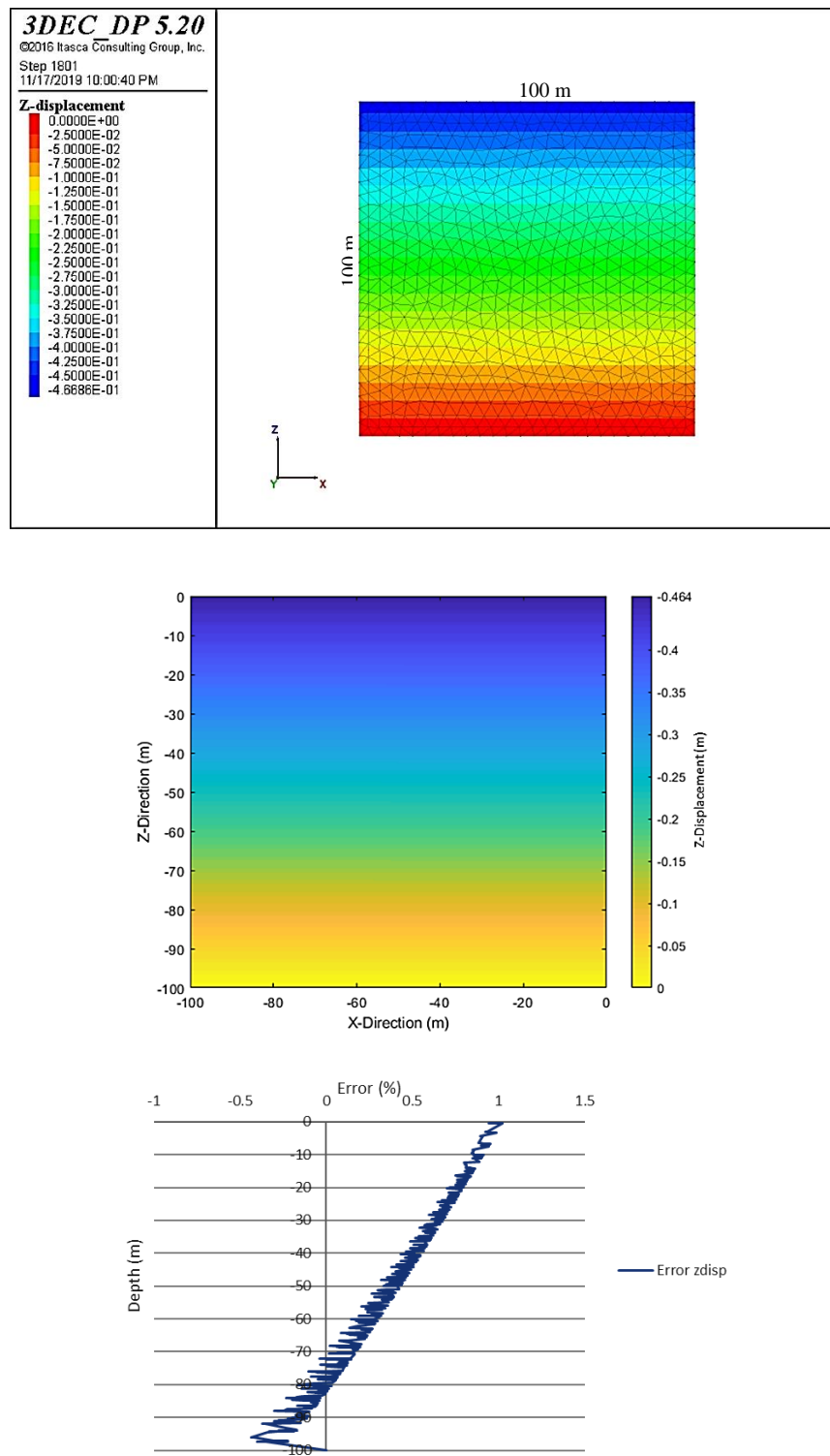

Figure A1.8. Numerical (upper) and analytical (middle) vertical displacement magnitudes and corresponding error (lower) in Uniaxial Stress case
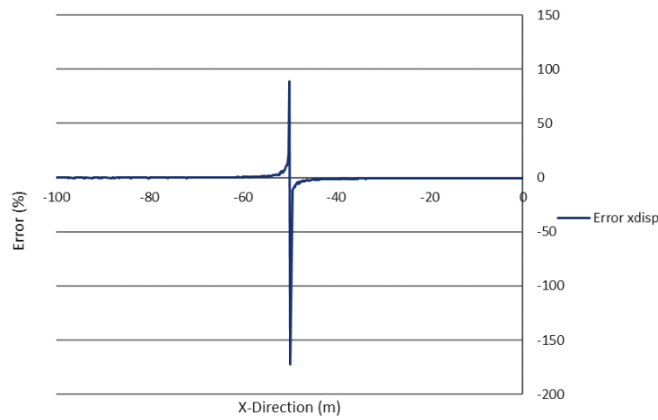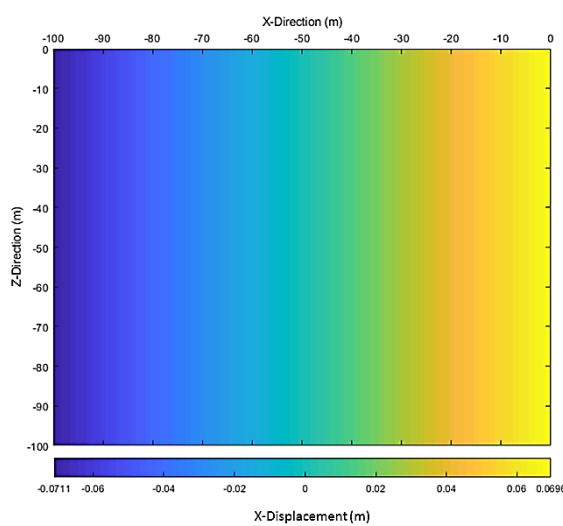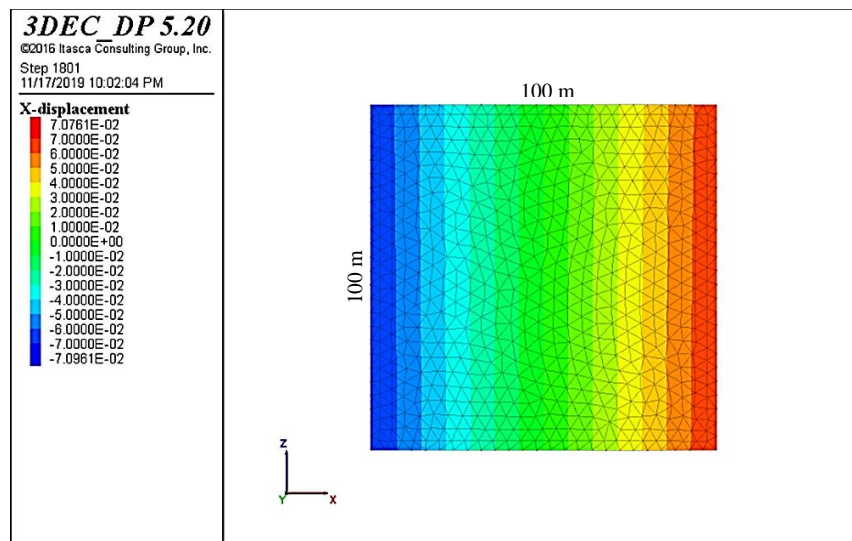
Figure A1.9. Numerical (upper) and analytical (middle) lateral displacement magnitudes in X direction and corresponding error (lower) in Uniaxial Stress case
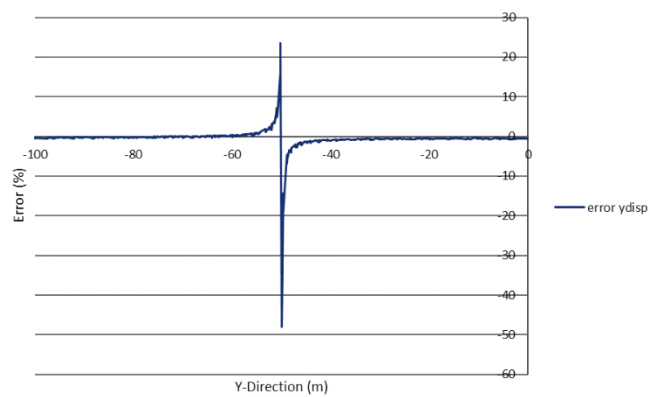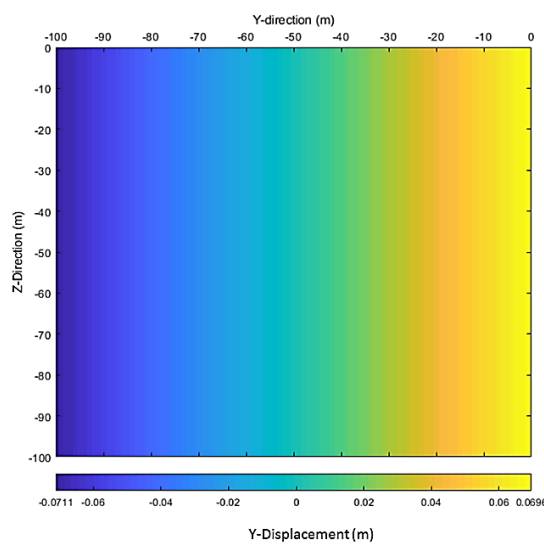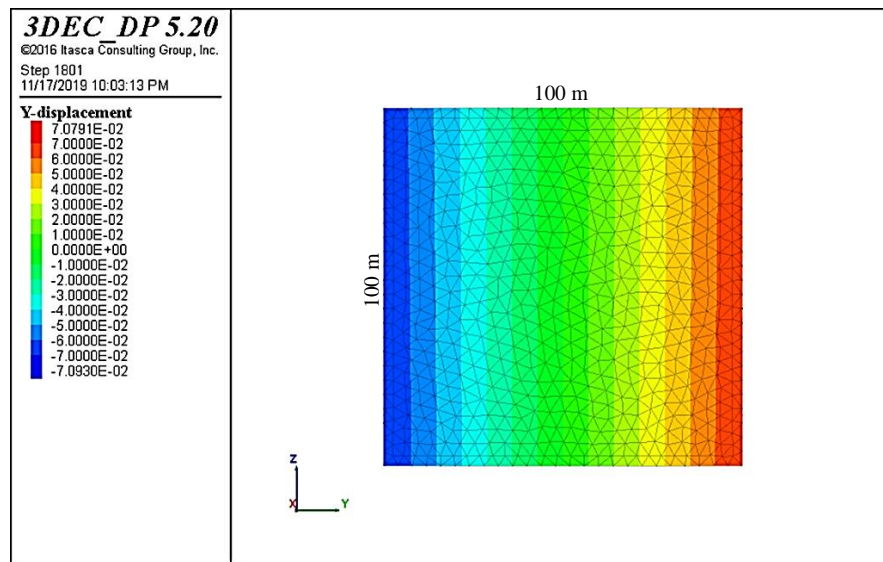
Figure A1.10. Numerical (upper) and analytical (middle) lateral displacement magnitudes in Y direction and corresponding error (lower) in Uniaxial Stress case
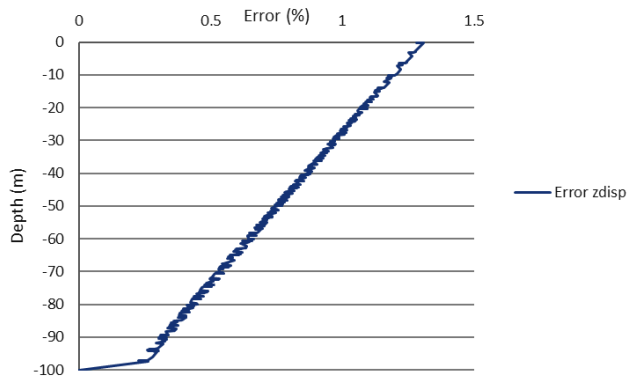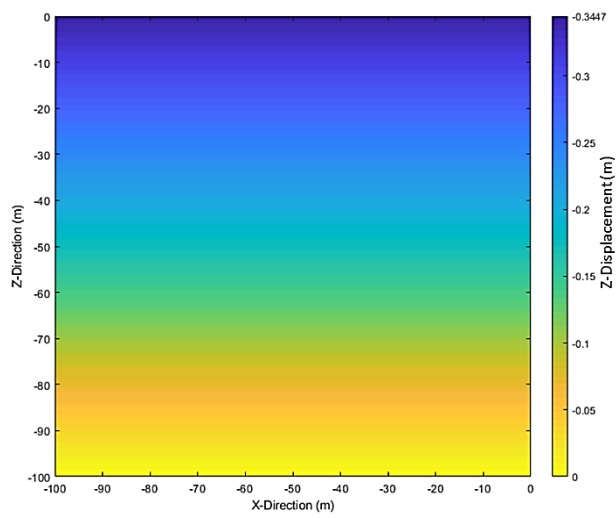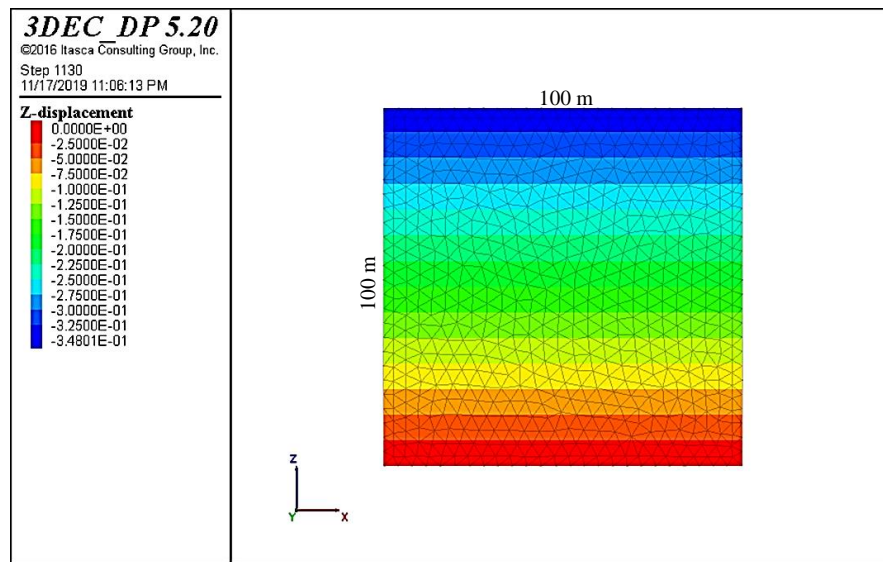
Figure A1.11. Numerical (upper) and analytical (middle) vertical displacement magnitudes and corresponding error (lower) in Uniaxial Strain case
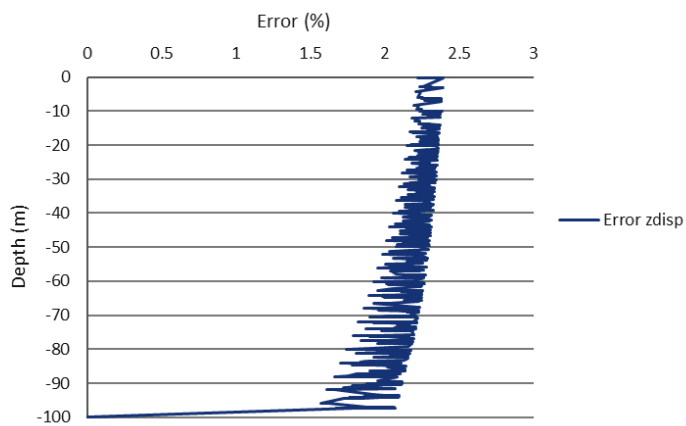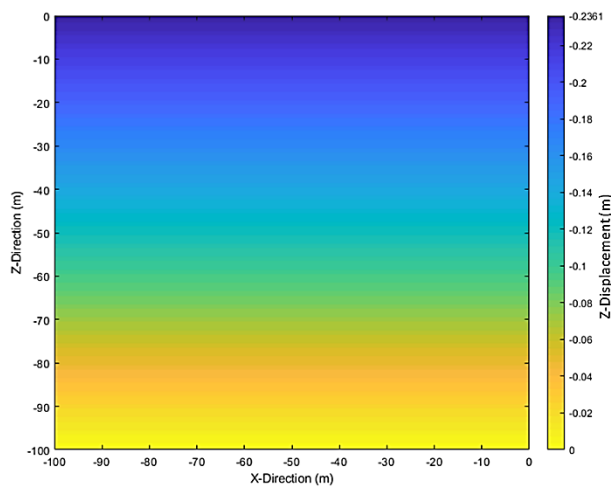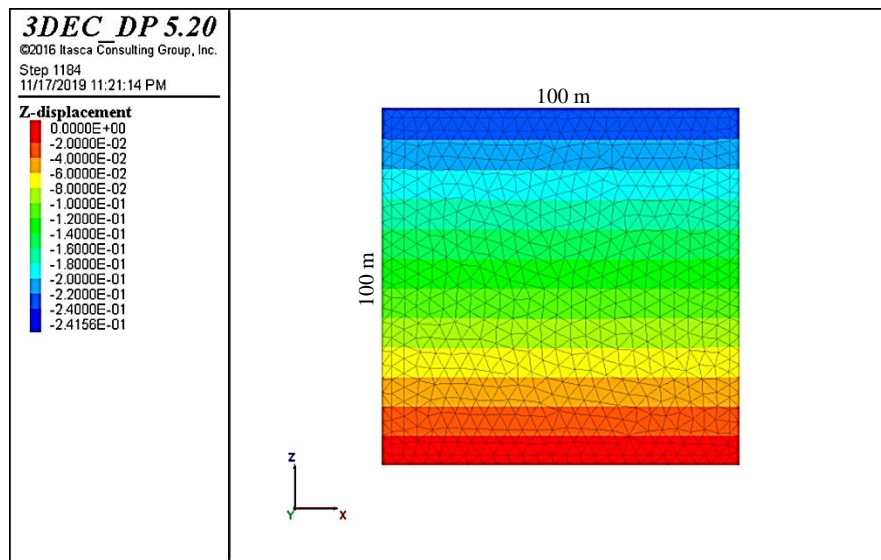
Figure A1.12. Numerical (upper) and analytical (middle) vertical displacement magnitudes and corresponding error (lower) in Polyaxial Stresses case
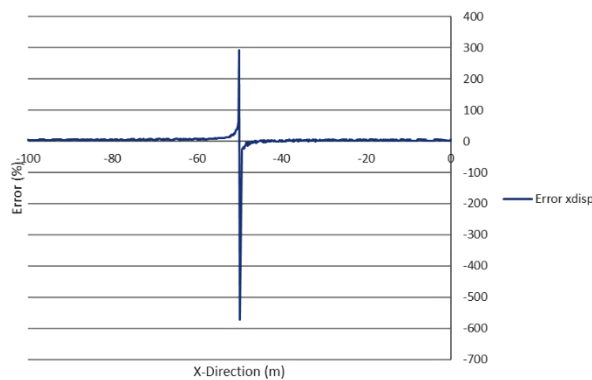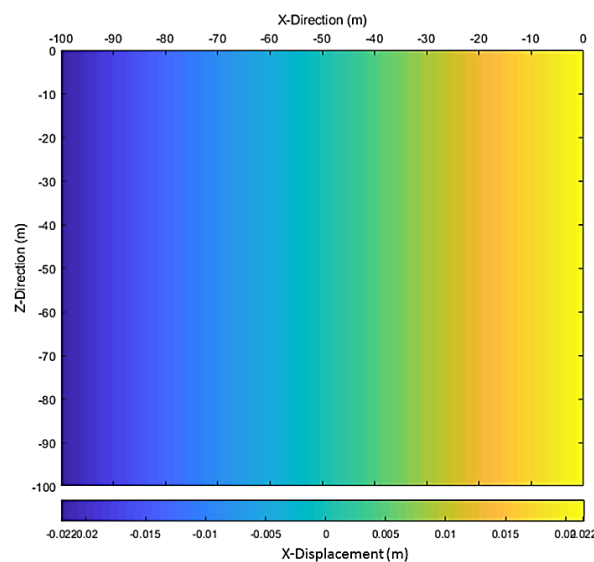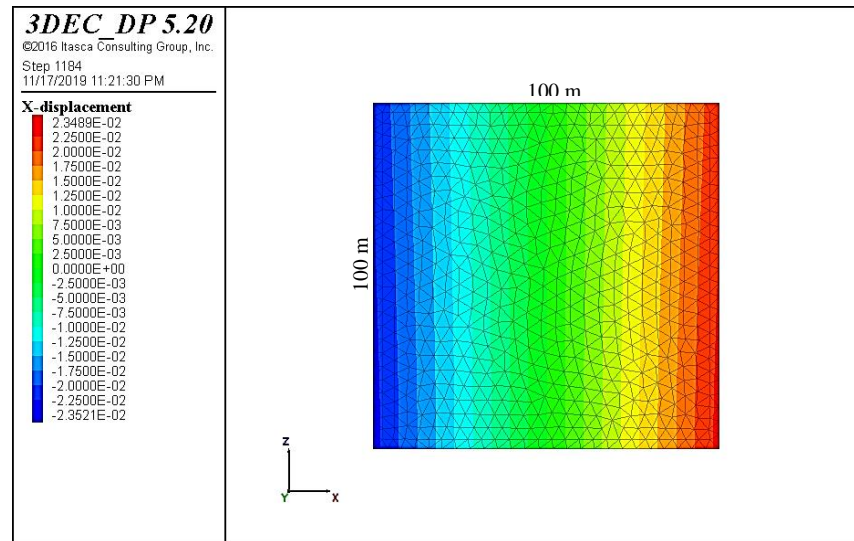
Figure A1.13. Numerical (upper) and analytical (middle) lateral displacement magnitudes in X direction and corresponding error (lower) in Polyaxial Stresses case
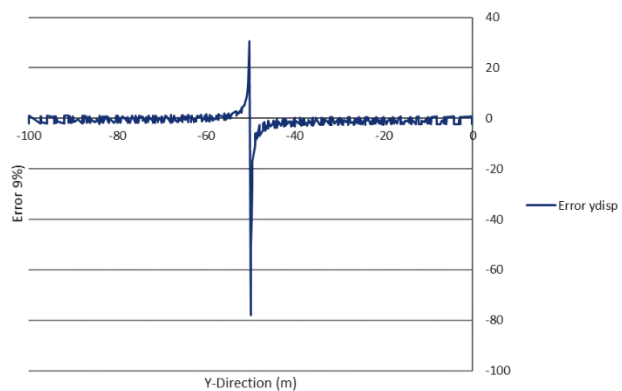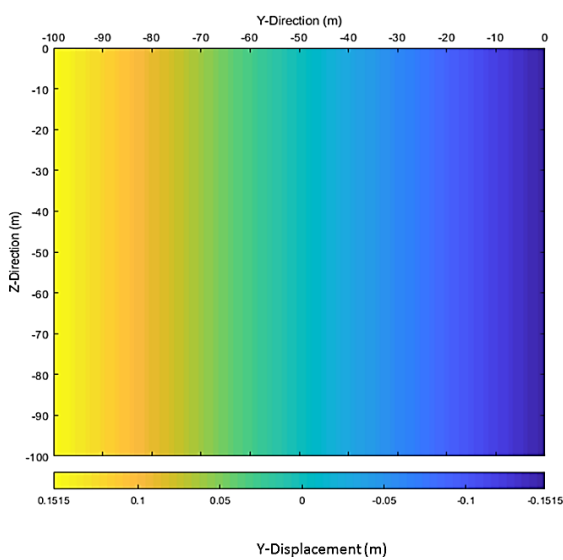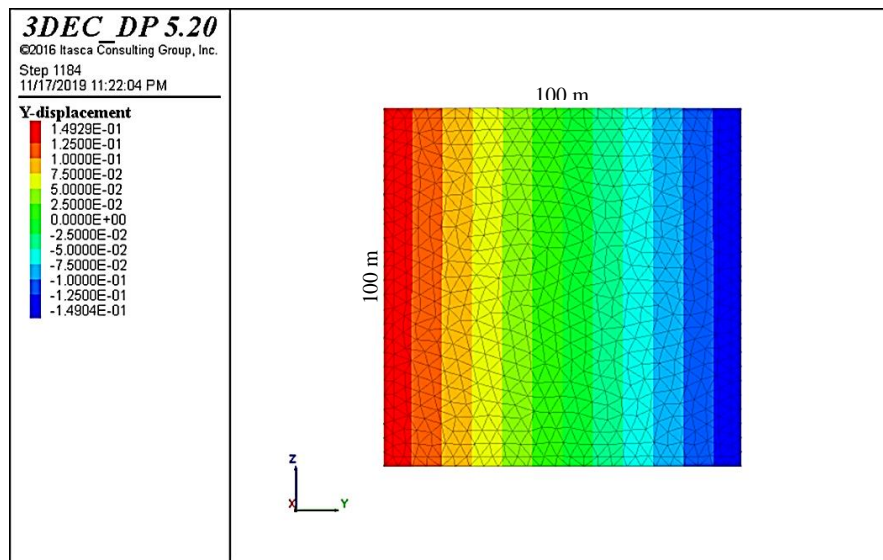
Figure A1.14. Numerical (upper) and analytical (middle) lateral displacement magnitudes in Y-direction and corresponding error (lower) in Polyaxial Stresses case

Appendix A2

Simulation results using "Fast Flow" option of 3DEC

Here, we are trying to illustrate some of the results for which the "fast flow" option of the 3DEC is used to simulate the 24 hours of fluid injection into the center of the fault of 3 km diameter. As already stated, the final result such as maximum WHP or the results of sensitivity analysis was approximately identical with the results where the "fast flow" option is not utilized, but the process of approaching to those results was different. For example, the fluid pressure evolution in time exhibited a waveform oscillation when using "fast flow" option while this curve showed a smooth increase to the maximum pressure in the simulations without using "fast flow" option. Figure A2.1 is an example of pressure oscillation at injection point for the reference case. This waveform oscillation showed a time period of 5.7 hours along the injection duration as illustrated in figure A2.2 which is fast Fourier transform (FFT) of spectra shown in figure A2.1.
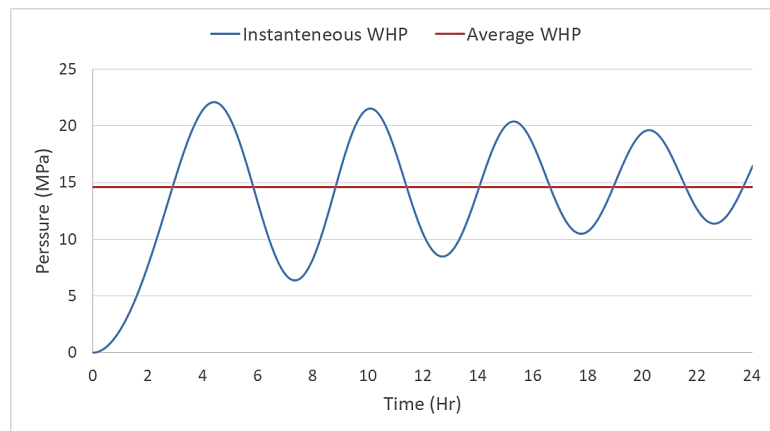

Figure A2.1. Numerical WHP oscillation at injection point of approximately 4.7 km; the average value of the oscillating WHP of 14.6 MPa has good agreement with field observation of WHP being approximately 11-12 MPa
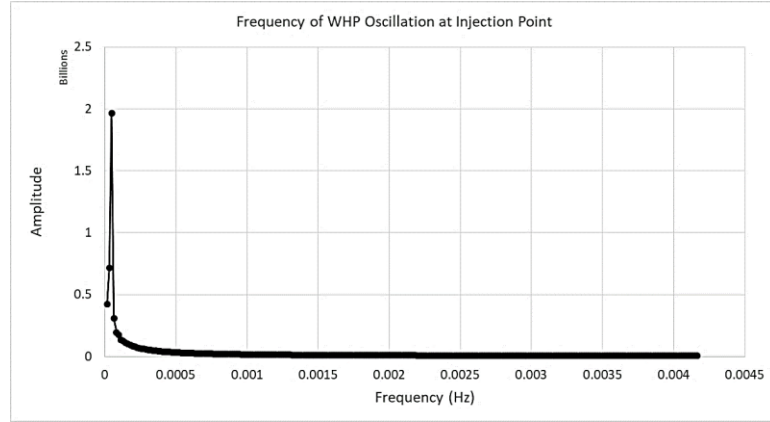

Figure A2.2. FFT of instantaneous WHP oscillation at injection point shown in figure A2.1; spectrum frequency is about 48.8e-6 Hz which yields to a time period of about 5.7 hours

The same oscillation behavior was also observed for fluid pressure evolution at other measuring points along the fracture diameter as can be seen from figure A2.3. The time period of the spectra at all the measuring points illustrated the same value of 5.7 hours by doing FFT on the waveform observations.

241
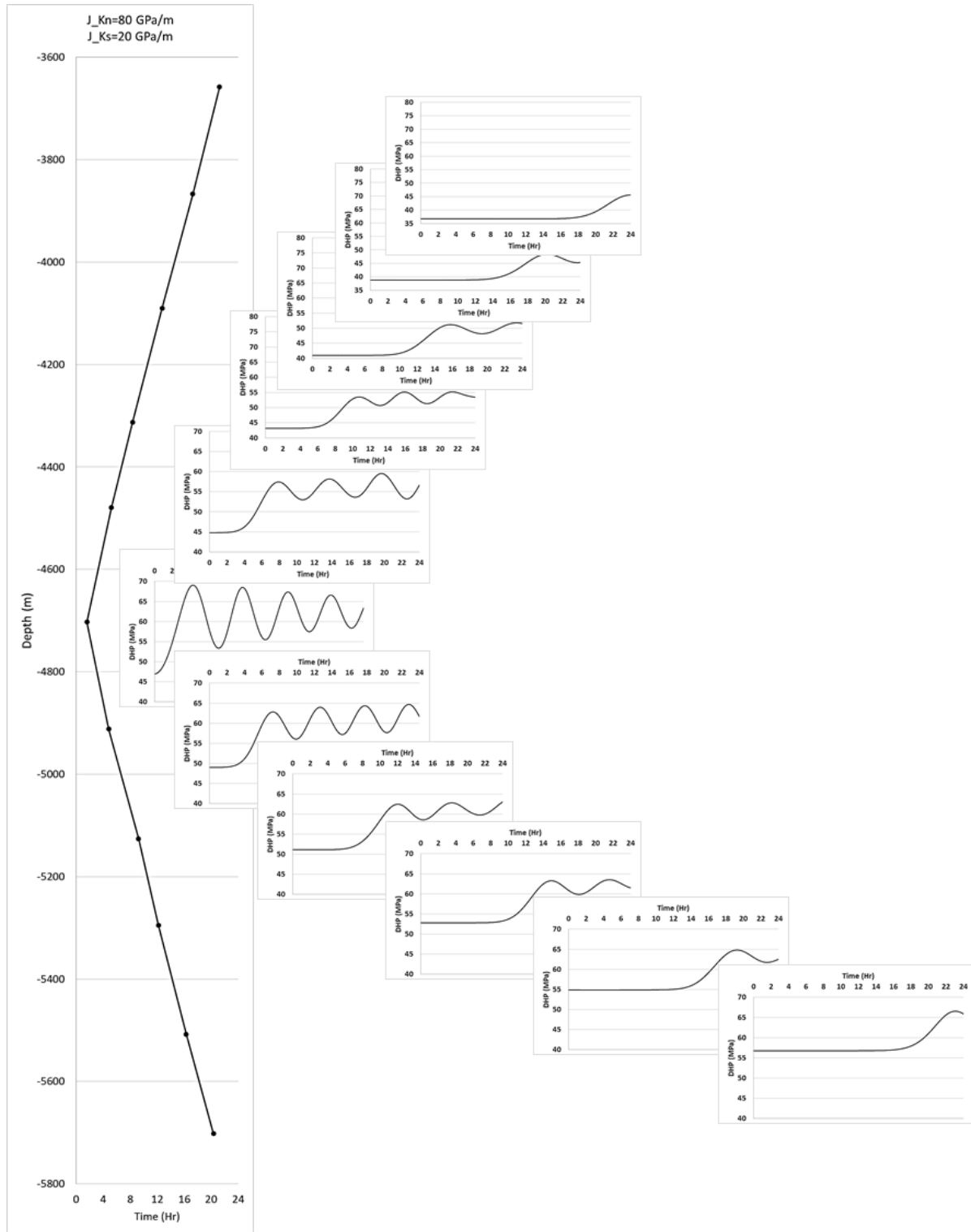
Figure A2.3. Pressure front migration from injection point at about 4.7 km to the top and bottom of the fracture; the linear pressure propagation with depth in the left-hand side sub-figure is caused by a wrong strategy in picking the pressure build-up onset time at sampling points, however the pressure evolution in time at all sampling points exhibited oscillation behavior as at injection point

These type of observations were also detected for fracture aperture opening along the fracture. The same time-period for oscillations and the same waveform propagation. These results were then explored that are sensitive to the magnitude of fluid time-step in numerical calculations. In figure A2.4, the impact of fluid timestep on pressure evolution in time is demonstrated. As can be seen in the figure, the decrease of the fluid timestep decreases the waveform oscillation of the pressure curve, however the final value for the maximum WHP is approximately the same. This is in fact the main opportunity that the "fast flow" option offers to the users of 3DEC when simulating a fully coupled hydro-mechanical process; the fast convergence of the model to a final result with minimum magnitude of error. But, if the process of this convergence is important to the user, it might be affected by the "fast flow" option even if the user limits the fluid-timestep to a lower value as equal as the timestep automatically calculated and used by the 3DEC when doing simulation without using "fast flow" option.
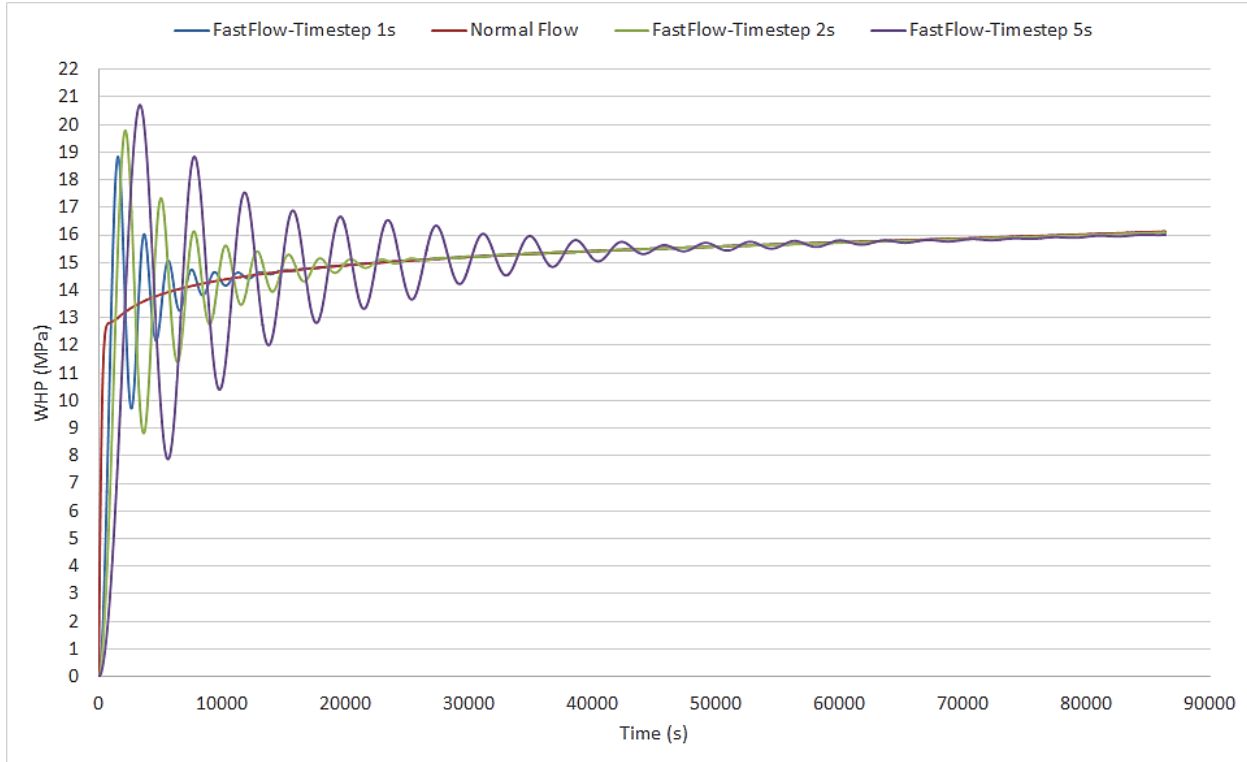

Figure A2.4. Comparison of fluid pressure evolution in time at injection point for normal flow and fast-flow with different fluid timesteps; as it can be seen, the maximum value of the WHP is identical for all cases, but the process of convergence to that maximum value is different between normal flow and fast-flow options where there is not any oscillation in normal flow calculations contrary to the fast-flow calculations

It is worth to note that, the upper bound for fluid time-step can be controlled by the user of 3DEC; so that, if the automatically calculated fluid timestep by 3DEC is more than that of assigned by the user, then it will not pass beyond. Using this possibility, we tried to compensate the oscillation behavior of the fluid pressure curves by assigning 5 s, 2 s, and finally 1 s as upper bound to fluid timestep (initially it was 10 second in calculation of the results shown in figure A2.1 and A2.3) and found that the oscillation behavior has not been completely removed, however the amplitude of oscillation decreased a bit and convergence of the curve to the smooth line towards the maximum value happened at earlier times as can be seen from figure A2.4. Furthermore, and importantly, the fluid timestep of 1 second is in fact close to the timestep automatically calculated by 3DEC in normal flow

run (the red curve in figure A2.4), but still there was a significant difference between the curves of normal flow and fast-flow with 1 second of fluid timestep (blue curve in figure A2.4).

The set of sensitivity analyses carried out on the fracture's hydromechanical behavior using fast-flow option were also illustrated the same conclusion as those of normal flow calculations. The results can be found in below figures from A2.5 to A2.14 where the fracture's normal stiffness has the most effect on the mechanical behavior of the no-slip fracture.
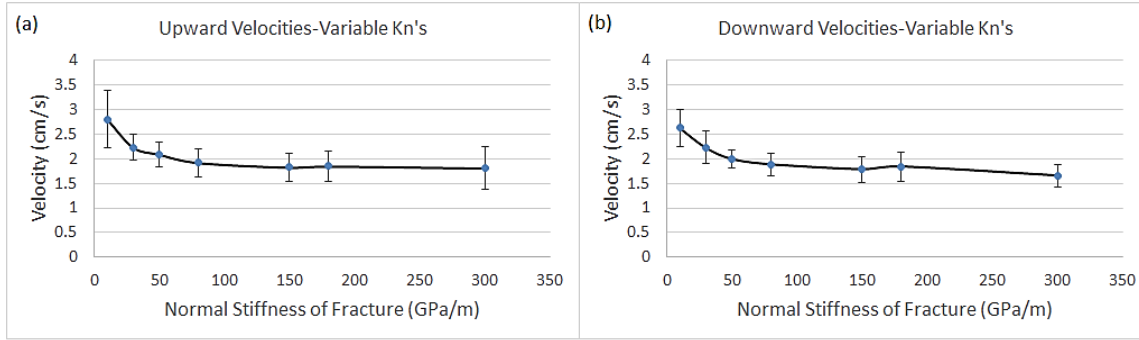

Figure A2.5. The pressure propagation velocity versus normal stiffness of the fracture for (a) upward propagation and (b) downward propagation, for the cases with fixed K_s; it can be seen in the figures that the velocity decreases by increase of normal stiffness from 10 to 80 GPa/m, but after that the velocity variation is not significant.
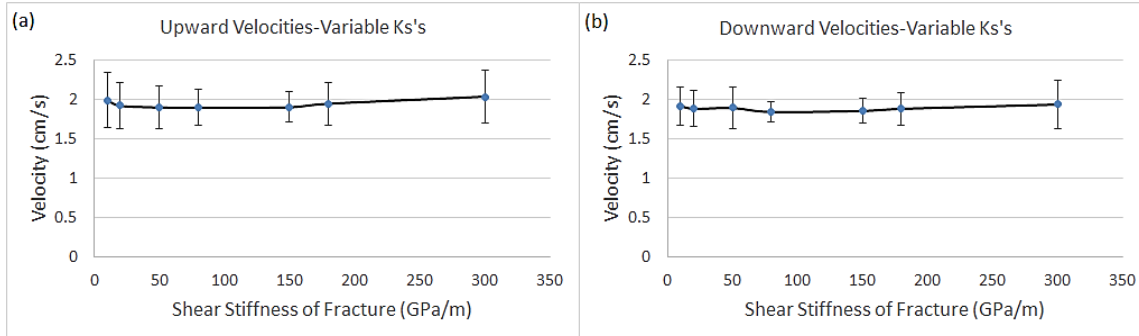

Figure A2.6. The pressure propagation velocity versus normal stiffness of the fracture for (a) upward propagation and (b) downward propagation, for the cases with fixed K_n; it can be seen in the figures that there is not a meaningful variation in the pressure propagation velocities of normal stiffness from 10 to 300 Gpa/m
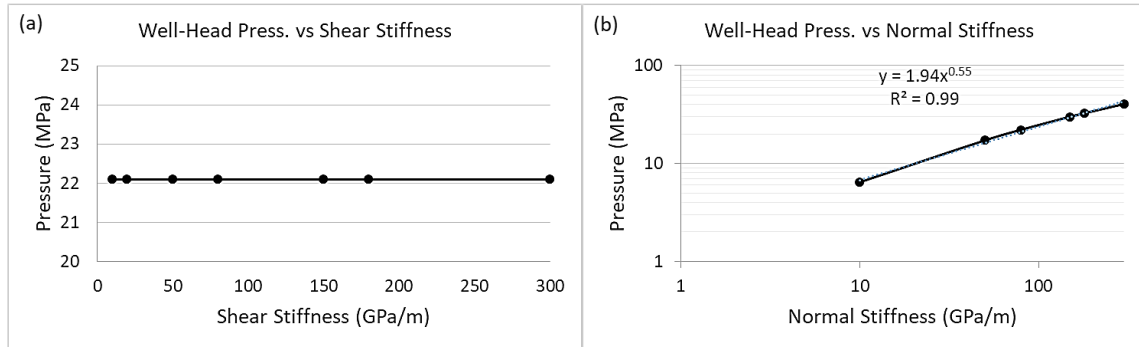

Figure A2.7. Maximum WHP evolution at injection point versus (a) shear stiffness and (b) normal stiffness of the fracture

244
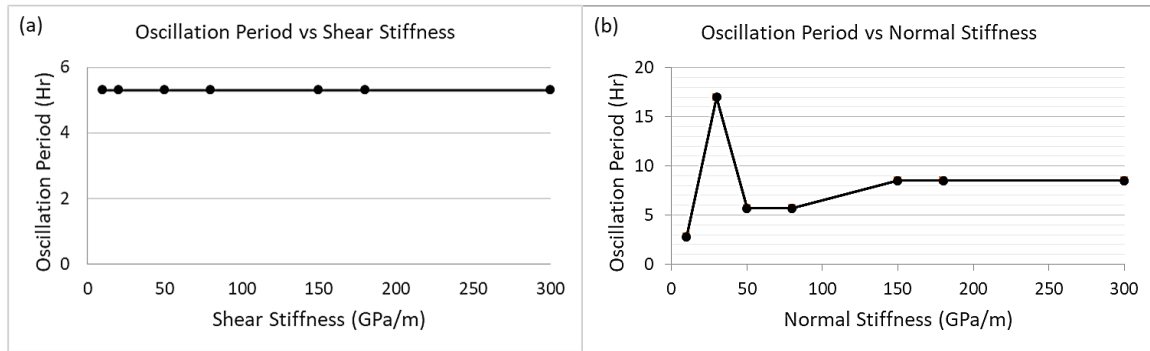
Figure A2.8. Oscillation period evolution versus (a) shear stiffness and (b) normal stiffness of the fracture
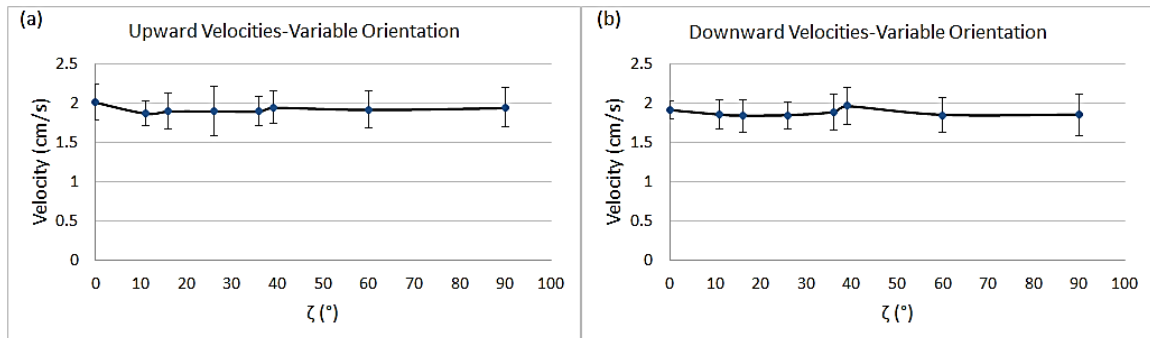

Figure A2.9. Upward (a) and downward (b) pressure propagation velocities versus different angles between fracture strike and direction of the maximum horizontal stress
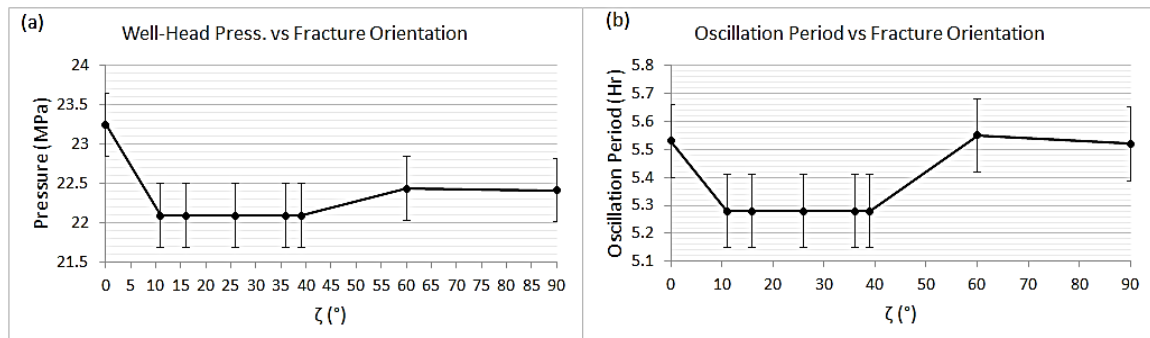

Figure A2.10. WHP (a) and oscillation period (b) variations versus different angles between fracture strike and direction of the maximum horizontal stress
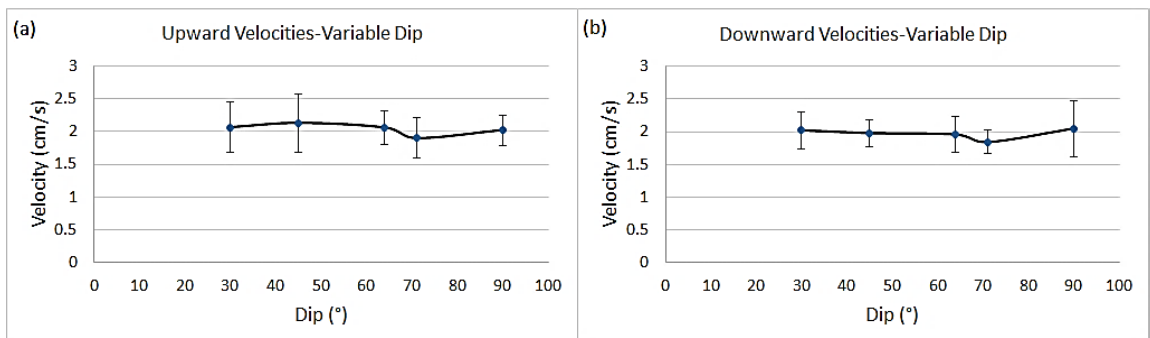

Figure A2.11. Upward (a) and downward (b) pressure propagation velocities versus fracture dip

245
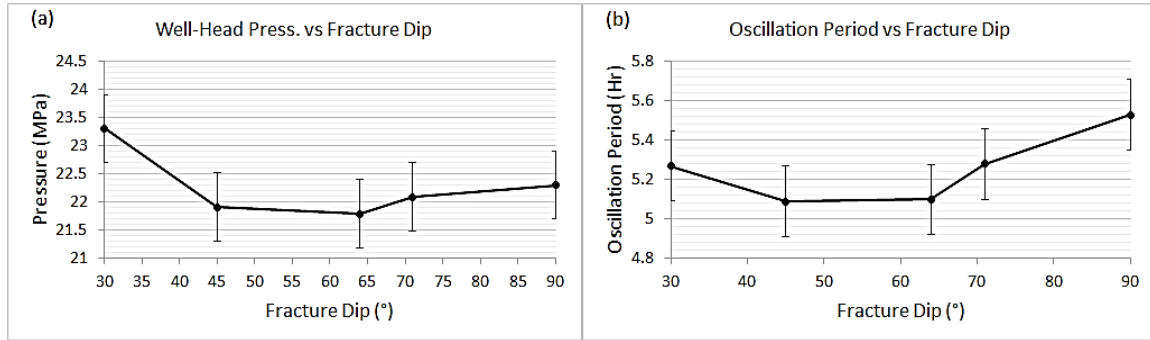
Figure A2.12. WHP (a) and oscillation period (b) variations versus fracture dip
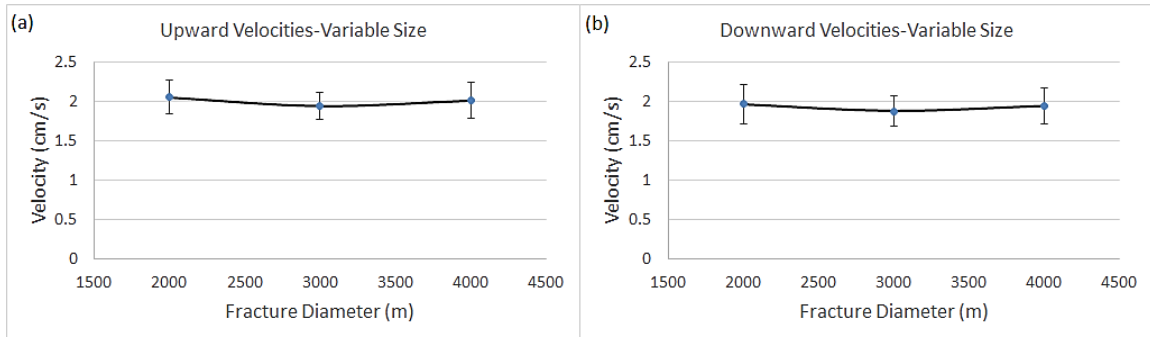
Figure A2.13. Upward (a) and downward (b) pressure propagation velocities versus fracture size
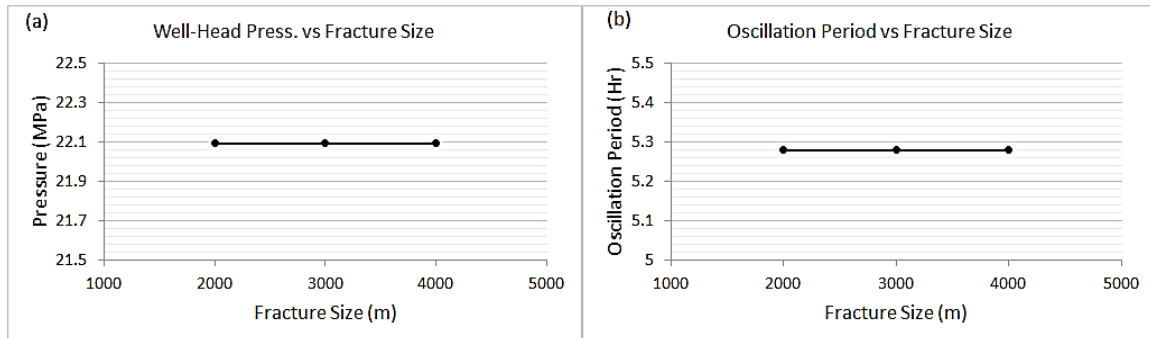
Figure A2.14. WHP (a) and oscillation period (b) variations versus fracture size

Having all these results in hand, it might be of crucial importance to run a reference model of the problem using both options of normal flow calculation and fast-flow calculations to compare the target results of simulation to have a solid conclusion regarding the type of flow calculation desired to be opted according to the requirements of the project. This, hence, will help the modeler to save the time budget of the project by minimizing the time spend on the wrong choose of modeling strategy and method.

246

Résumé en français suivi des mots-clés en français

Insérer votre résumé en français (1000 caractères maximum) suivi des mots-clés en français

 Insér Cette recherche vise à caractériser numériquement l'origine de la variation de vitesse de l'onde P observée pendant la stimulation hydraulique du puits GPK2. L'apparition de cette anomalie de vitesse des ondes P a été plus rapide et plus étendue que celle qui se produit habituellement au cours d'un processus classique de diffusion des fluides, comme l'ont noté Calo et al. en 2011. Ces changements de vitesse des ondes P ont également été observés à grande échelle (~1km), ce qui suggère que les modules élastiques à grande échelle de la roche réservoir ont changé rapidement.

La première phase du présent travail a consisté à étudier l'aspect temporel de l'observation. Elle visait à comprendre la migration de la pression au cours de ce processus de stimulation hydraulique en la simulant à l'aide de 3DEC. Il a été constaté que la pression du fluide migre dans le temps et l'espace suivant un processus contrôlé par l'ouverture des fractures plutôt que par la pression du fluide. Une migration très rapide de la pression de fluide a été observée, avec une diffusivité effective beaucoup plus élevée (~13 m2/s) que celle classiquement observée à Soultz-sous-Forêts (~0,05 m2/s ; voir par exemple Shapiro et al., 2002). Ce processus rapide est compatible avec les résultats de Calo et al. qui ont observé une migration de plus de 1000 m en 3 heures. Ainsi, pour l'effet temps, nous avons mis en évidence un processus compatible avec l'observation.

Dans la deuxième phase, il était prévu d'explorer la valeur à grande échelle des modules élastiques du réservoir de Soultz-sous-Forêts et d'analyser sa sensibilité aux perturbations des contraintes afin de comprendre comment les changements de pression étudiés dans la première phase auraient un impact sur la vitesse des ondes P. Il a été constaté que les modules élastiques à grande échelle ont un impact sur la vitesse des ondes P. Il a été constaté que les modules élastiques à grande échelle à travers la masse rocheuse fracturée s'écartent de ceux de la roche intacte dans les conditions d'un paramètre de densité de fracture élevé. En outre, l'étude de la vitesse des ondes P en fonction du niveau de contrainte appliqué a révélé qu'elle est presque indépendante du niveau de contrainte appliqué.

Des recherches supplémentaires sont nécessaires pour répondre pleinement à la question de la thèse. Par exemple, le processus mis en évidence dans la première phase pourrait également avoir des implications sur l'ampleur de la perturbation de la pression loin du puits, ou il serait intéressant d'ajouter une pression de fluide aux simulations de la deuxième phase afin d'étudier l'effet de la pression interstitielle sur la variation de la vitesse de l'onde P.

Mots clés : Réservoirs géothermiques, stimulation hydraulique, glissement asismique, vitesse des ondes P, écoulement des fluides, réseau de fractures discrètes, modélisation numérique

Direction de la **recherche**
et de la **valorisation**
Collège **doctoral**
Université de Strasbourg

Résumé en anglais suivi des mots-clés en anglais

Insérer votre résumé en anglais (1000 caractères maximum) suivi des mots-clés en anglais

This research aimed to numerically characterize the origin of observed P-wave velocity variation during hydraulic stimulation of GPK2 well. Occurrence of this P-wave velocity anomaly was faster and more extended compared to that usually happens during a classical fluid diffusion process, as noted by Calo et al., 2011. These P-wave velocity changes were also observed at large scale (~1km), which suggest that large scale elastic moduli of the reservoir rock had changed rapidly.

First phase of the present work was to address the timing aspect of the observation. It was aimed at understanding the pressure migration during this hydraulic stimulation process by simulating it using 3DEC. It was found that the fluid pressure migrates in time and space following a process controlled by fracture opening rather than fluid pressure. A very rapid migration of fluid pressure was observed, with a much higher effective diffusivity (~13 m2/s) than that classically observed at Soultz-sous-Forêts (~0.05 m2/s; see e.g. Shapiro et al., 2002). This rapid process is compatible with the results of Calo et al. who observed a migration of over 1000 m in 3 hours. So, for the time effect, we have highlighted a process compatible with observation.

In the second phase, it was purposed to explore the large scale value of the elastic moduli at Soultz-sous-Forêts reservoir and analyze its sensitivity to stress perturbations in order to understand how pressure changes studied in the first phase would impact P-wave velocity. It was found that large scale elastic moduli through fractured rock mass deviates from that of intact rock in the conditions of high fracture density parameter. Furthermore, investigation of related P-wave velocity as a function of the applied stress level revealed that it is almost independent of the applied stress level.

Further research is required to fully answer the thesis question. For example, the process highlighted in the first phase could also have implications for the magnitude of pressure perturbation away from the well, or it would be interesting to add fluid pressure to the second phase simulations in order to study the effect of pore pressure on P-wave velocity variation.

Keywords : Geothermal Reservoirs, Hydraulic Stimulation, Asesimic Slip, P-wave Velocity, Fluid Flow, Discrete Fracture Network, Numerical Modeling